UNIVERSITAT POLITÈCNICA DE CATALUNYA BARCELONATECH

Novel assessment of unintentional islanding operations in distribution networks

by

Alexandre Serrano-Fontova

PhD program in Electrical Engineering

A Novel Assessment of Unintentional Islanding operations in Distribution Networks

Doctoral thesis by:

Alexandre Serrano-Fontova

Thesis advisor:

Ricard Bosch, Pau Casals-Torrens

A dissertation submitted in partial satisfaction of the requirements for the degree of Doctor of Philosophy in Electrical Engineering by the

UNIVERSITAT POLITECNICA DE CATALUNYA

Barcelona, March 2020

Universitat politecnica de catalunya

Departament d'Enginyeria Elèctrica

Av. Diagonal 647. Pl.1

08028 Barcelona

Primera impressió Març 2020

To my family and gaston

Acknowledgements

First of all, I would like to thank my thesis advisors Dr. Ricard Bosch and Dr. Pau Casals for their absolute willingness to help during these years. A PhD thesis implies hard work, but frankly, I have thoroughly enjoyed all this time. Both of you have been dedicated and committed to this task, and perhaps more importantly, you have driven me to achieve something I would never have imagined. I will always be grateful for that. Indeed, I've been fortunate to find someone like you to share this passion for the electrical power systems. It is worth mentioning that this thesis has been carried part-time whilst working full-time at an electrical company, which has forced me to research during afternoons, nights and weekends. Honestly, Ricard and Pau have understood perfectly this situation and supported me in dealing with this issue. As far as I am concerned, our relationship does not finish with this thesis. Instead, it is the beginning of a new stage where we can work together towards new research projects.

I also want to thank Prof. Juan Antonio Martinez, for all his help. Sincerely, each suggestion, advice or comment, has made me improve. I wish to continue collaborating and researching with him. Juan, thank you very much. It has been an honour to learn from you!

Since this islanding operation has been identified in the distribution network where I was working and has been the starting point of this thesis, I would like to thank all my colleges at the DSO who, in one way or another, supported me in collecting the data. A special mention to Miquel Jordana and Jon Aguirre from Ormazabal, for those fruitful discussions we had, even still in the early stages. Moreover, the debate that I had about this transient with Prof. Math Bollen in the panel session of my first conference (ICREPQ, Málaga 2017), helped me in finding a way to structure this assessment.

During this time, I have been working as an assistant professor at ETSEIB, where I discovered a new way of enjoying with electrical engineering. I would thank Prof. Samuel Galcerán, who gave me the chance of becoming a teacher. Also, thank all other fellows who helped me during lab lessons.

Under no circumstances would I have achieved this thesis, if it wasn't for my parents and family. They had supported me, especially during hard times, when I needed them the most. While I'm writing these words, a lot of memories come to my mind. Especially, at the beginnings when my father introduced me in the electrical engineering field. On the other hand, those who unfortunately are not present deserve some words of thanks. I am pretty sure that all of you would have enjoyed this thesis as much as I have done.

Finally, the last words are dedicated to my close friends, to whom I sent a warm embrace. Thank you so much for being there!

List of publications

Journal Publications:

Alexandre Serrano-Fontova, Pau Casals-Torrens and Ricard Bosch, "Power Quality disturbances assessment during unintentional Islanding scenarios. A contribution to voltage sag studies. *Energies* 2019, 12(16), 3198 doi: 10.3390/en12163198.

Pau Casals-Torrens, Juan A. Martinez-Velasco, **Alexandre Serrano-Fontova** and Ricard Bosch, "Assessment of unintentional islanding operations in distribution networks with large induction motors. *Energies* 2020, 13(2), 345 doi:10.3390/en13020345.

Alexandre Serrano-Fontova, Pau Casals-Torrens, Juan A. Martinez-Velasco and Ricard Bosch, "A new islanding detection method for unintentional islanding scenarios". (Submitted to *IEEE Trans. on Power Delivery*)

Conference Publications:

Alexandre Serrano-Fontova, Pau Casals-Torrens and Ricard Bosch, "A novel voltage sag approach during unintentional islanding scenarios: A survey from real recorded events. *ICREPQ 19'*, Tenerife (Spain), April 2019, n.17, July 2019, doi: 10.24084/repqj17.215

Ricard Bosch**,** Pau Casals-Torrens and **Alexandre Serrano-Fontova**, "The influence of the self-excited induction machine into the electrical grid under instability situation-Real case measurement. *ICREPQ 17'*, Málaga (Spain), April 2017, n.15, April 2017, doi: 10.24084/repqj15.280.

Ricard Bosch**,** Pau Casals-Torrens, J. Alvarez-Florez, and **Alexandre Serrano-Fontova**", Hybrid gas-electrical power & heavy duty propulsion: Test platform. *IAMU 17'*, Barcelona (Spain), October, 2018.

Awards and recognitions:

- **BEST POSTER AWARD** at ICREPQ 17' Málaga (Spain).
- **Best PhD Thesis proposal**. Grant received by the Catalonian College of engineers. Barcelona June 2017.

Other Publications derived from the thesis:

Mr Antonio Herrero, Jesús Álvarez-Flórez, Pau Casals-Torrens, Ricard Bosch, and **Alexandre Serrano-Fontova.** "The Five main Stability Criteria for Marine Power Generation Plants". (Submitted to *Engineering Failure Analysis-Elsevier)*

Bosch R., Pau Casals-Torrens and **Alexandre Serrano-Fontova.** "Els inicis de l'electricitat a Catalunya, el present i el futur: Història hidroelèctrica de Seròs amb la "Canadenca". *X Jornades d'Arqueologia Industrial de Catalunya.* Vic, Desembre 2016.

Abstract

This thesis aims to investigate an unexpected islanding operation (IO) which has been identified in a real distribution network. The process of recording and processing the data obtained from the field measurements in the distribution network (DN) has been the starting point of this research. It has to be underlined that this IO raised a problem and became a major challenge for the distribution operator. Therefore, the aim of this thesis is twofold; solving a real problem as well as further enhance the current research studies about IOs in DNs. IOs have been object of study during the recent years due to the rapid proliferation of the distributed generation (DG) within the so-called smart grids (SGs). Commonly, the power of these DG resources ranges between hundreds of kW and few MW and are allocated at either low voltage or medium voltage levels. One of the significant issues that these resources are raising is, undoubtedly, the IOs. These situations occur when a portion of the grid operates in parallel with the main grid following a disconnection. Thereby IOs, where the DG is energising the grid after a CB opening, must be identified and tripped in the minimum time possible. Failure to do so, the list of hurdles may include; power quality (PQ) disturbances (e.g., frequency and voltage out of range), a safety hazard for the network personnel or out-of-phase reclosings. That is the reason why the research towards the anti-islanding protection methods has elicited great interest.

Fundamentally, the substantial improvement of this thesis lies in the fact that, in this IO, there are no DG resources, but large induction motors. In fact, the grid remains energised after the CB disconnection due to the induction motors (IMs) which transiently, act as generators. The island begins with the CB operation and ends when the CB recloses the circuit to restore the electrical supply. This rapid reclosing operation is widely adopted in DNs to avoid manual operations in self-extinguished faults and typically ranges between 0.5 and 1s. Given the fact that usually IOs are originated in the presence of DG, indeed, this IO is utterly unexpectedly for the DSO.

Due to the phenomenon mentioned above, the specific goals of this thesis are described down below:

1. The first goal of this thesis focuses on developing a model suitable for validation purposes. To make a proper model validation, the simulations results obtained with this model will be compared with those obtained from field measurements. Thus, once the model has been validated, a thorough investigation regarding the most influential factors will be carried out.
2. The second goal of this thesis falls within the scope of the PQ. During the IO mentioned above, a new voltage sag topology is observed. Consequently, the efforts will be focused on modelling this new type of sag.
3. The third goal of this thesis emerges from the protective point of view. Once the IO has been defined and characterised, the need for identifying and preventing it becomes the main concern. In such a way, the third pillar of the thesis is targeted at implementing a suitable tool to prevent this particular IO. Besides, this new tool will be compared with the currently available methods for ID developed for scenarios with DG.

Resum

Aquesta tesi te com a objectiu investigar una operació en illa no intencional, que ha set identificada en una xarxa de distribució real. El procés de registre i processament de les dades obtingudes a partir de les mesures de camp en la xarxa de distribució, ha estat el punt de partida d'aquesta investigació. Cal subratllar que aquesta operació en illa va plantejar un problema i es va convertir en un repte important per l'operador de distribució. Per tant, l'objectiu d'aquesta tesi és doble; resoldre un problema real, així com millorar els estudis de recerca actuals sobre les illes no intencionals en xarxes de distribució elèctrica. El fenomen de les illes dins una xarxa elèctrica, han estat objecte d'estudi durant els darrers anys a causa de la ràpida proliferació de la generació distribuïda. Habitualment, la potència d'aquests recursos distribuïts oscil·la entre centenars de kW i pocs MW i s'assignen a nivells de baixa tensió o mitja tensió. Una de les qüestions importants que plantegen aquests recursos és, sens dubte, les illes. Aquestes situacions es produeixen quan una part de la xarxa elèctrica funciona en paral·lel amb la xarxa principal després d'una desconnexió. Per això, les illes no intencionals es donen quan la generació distribuïda energitza la xarxa després de la obertura d'un interruptor. Principalment, l'objectiu es identificar aquesta situació i desconnectar dites fonts en el mínim temps possible. En el cas de que això no succeeixi, els següents disturbis poden produir-se; pertorbacions de la qualitat de potència (PQ) (per exemple, freqüència i tensió fora del rang), un perill per a la seguretat del personal de la xarxa o bé reconnexions fora de fase. Aquesta és la raó per la qual la investigació vers els mètodes de protecció "anti-islanding" han despertat un gran interès.

Essencialment, la millora substancial d'aquesta tesi rau en el fet que, en aquesta illa, no hi ha recursos energètics distribuïts, sinó grans motors d'inducció. Així, la xarxa elèctrica continua energitzada després de la desconnexió del interruptor a causa dels motors d'inducció, que actuen de forma transitòria com a generadors. L'illa comença amb l'obertura del interruptor i finalitza quan aquest tanca el circuit per restablir el subministrament elèctric. Aquesta operació de reconnexió ràpid es freqüent en xarxes de distribució per evitar operacions manuals en faltes temporals i generalment oscil·la entre 0,5 i 1s. Tenint en compte que generalment les illes tenen l'origen en presència de generació distribuïda , realment, la illa elèctrica objecte d'aquesta tesi és inesperada per l'operador de distribució.

A causa del fenomen esmentat anteriorment, els objectius específics d'aquesta tesi es descriuen a continuació:

1. El primer objectiu d'aquesta tesi se centra a desenvolupar un model adequat per la validació. Per fer una validació adequada del model, es compararan els resultats de les simulacions obtinguts amb aquest model amb els obtinguts de les mesures de camp. Així, un cop validat el model, es durà a terme una investigació completa sobre els factors més influents.

2. El segon objectiu d'aquesta tesi entra dins de l'àmbit d'aplicació del PQ. Durant l'esmentada illa, s'observa una nova topologia de forat de tensió. En conseqüència, els esforços se centraran en modelar aquest nou tipus de forat.

3. El tercer objectiu d'aquesta tesi s'emmarca en el punt de vista de proteccions. Un cop definida i caracteritzada l'illa, la necessitat d'identificar-la i prevenir-la esdevé la principal preocupació. D'aquesta manera, el tercer pilar de la tesi té com a objectiu la implementació d'una eina adequada per prevenir aquesta particular illa. A més, es compararà aquesta nova eina amb els actuals mètodes utilitzats per a identificar les illes en escenaris amb generació distribuïda.

Table of contents

Acknowledgements I

List of Publications III

Abstract V

Resum VII

1 Introduction, concept and objectives 1

1.1 Power systems overview 1

1.2 Power distribution networks 4

1.2.1. DNs general structure and configurations 4

1.2.2. DNs elements and systems applications 11

1.3 Thesis background 14

1.4 Steps of the thesis 15

1.5 Thesis Objectives 16

1.6 Document structure 16

1.7 References 18

2 State of the art 21

2.1 Motor bus transfers 21

2.2 Islanding operations in DNs 23

2.2.1 Overview 23

2.2.3 Intentional islanding operations 23

2.2.4 Unintentional islanding operations 25

2.3 Power quality 26

2.3.1 PQ Fundamentals 26

2.3.2 PQ disturbances classification 26

2.3.3 Voltage sag features 28

2.4 Islanding detection methods 30

2.4.1 The need for detecting the islanding operations 30

2.4.2 General classification 30

2.4.3 Passive-based methods 31

2.4.4 Active-based methods 32

2.4.5 HIDM Overview 32

2.5 Conclusions 32

2.6 References 33

3 Voltage sags review 39

3.1 Voltage sags with constant magnitude 39
3.1.1 Voltage sag general classification 39
3.1.2 Voltage sags with abrupt recovery 43
3.1.3 Voltage sags with discrete recovery 46
3.1.4 Transformers influence on voltage sags 52
3.1.5 Effects of the type of grounding 54
3.1.6 Phase-angle jump 58
3.2 Voltage sags with a non-constant magnitude 59
3.3 Conclusions 62
3.4 References 62
4 Islanding operation: Theoretical analysis 65
4.1 Introduction 65
4.2 Electrical network under investigation 65
4.3 System components modelling 67
4.3.1 Introduction to modelling guidelines 67
4.3.2 Distribution lines 67
4.3.3 Transformers 68
4.3.4 Induction motors mathematical model 68
4.3.5 Protective devices 76
4.3.6 Load models 77
4.3.7 Three-phase Model adopted 80
4.4 IM behaviour during the fault 80
4.4.1 Introduction 80
4.4.2 Transient behaviour during the fault 81
4.4.3 Influence of the fault-type 85
4.4.4 Clearing time influence 86
4.5 Islanding operation 86
4.5.1 Overview 86
4.5.2 IM Mathematical model during the island 88
4.5.3 Islanding influential factors 92
4.6 Conclusions 92
4.7 References 93
5 Simulations 97
5.1 Introduction 97
5.2 Hypothesis and considerations 98
5.3 Effects of feeder loads and its load model 98
5.3.1 Simulations for different load scenarios 98

5.3.2 Load models impact 108
5.4 Type of fault and clearing time influence 108
5.5 Reclosing time influence 113
5.6 Impact of the load torque 114
5.7 Permanent-faults 116
5.8 Conclusions 120
6 Field measurements 123
6.1 Introduction 123
6.2 Event I 124
6.3 Event II 128
6.4 Event III 128
6.5 Event IV 128
6.6 Event V 132
6.7 Event VI 132
6.8 Event VII 137
6.9 Summary of events 137
7 Model validation 140
7.1 General criteria 140
7.2 Validation of Event I 141
7.3 Validation of Event II 141
7.4 Validation of Event III 147
7.5 Validation of Event IV 147
7.6 Validation of Event V 147
7.6 Modelling features discussion 148
7.7 Conclusions 150
8 Voltage sags during the island 153
8.1 Introduction 153
8.2 Main features of the new voltage sag type 153
8.3 Novel voltage sag magnitude: Analytical expression 154
8.4 Voltage sag duration and recovery 155
8.4.1 Voltage duration 155
8.4.2 Voltage recovery 156
8.5 Voltage sag magnitude: Simulation results 156
8.5.1 Overview 156
8.5.2 Simulation results 157
8.6 Voltage sag validation 167
8.7 Conclusions 167

9 Islanding detection 170
9.1 Introduction 170
9.2 Passive-based methods review 171
9.3 HIDM features 172
9.3.1 Overview 172
9.3.2 Directional criterion 173
9.3.3 Input, outputs and intermediate variables 174
9.3.4 Architecture 175
9.3.5 Time constraints in islanding detection 180
9.4 Simulations 180
9.4.1 Overview 180
9.4.2 Tripping times for different feeder load scenarios 181
9.4.3 Tripping times for different types of faults 187
9.4.4 Testing the NDZ capabilities of the HIDM 193
9.5 Conclusions 200
9.6 References 201
10 General Conclusions and future work 204
10.1 General conclusions 204
10.2 Future work 206

List of Tables

Table 2.1: Power Quality disturbances summary 27
Table 3.1: Voltage sags general classification 40
Table 3.2: Summary of the voltage sags general classification. 40
Table 3.3: Angles for voltage sags C, D, F and G 41
Table 3.4: Symmetrical components of the voltage sags. 42
Table 3.5: Voltage recovery for SLG and LL faults 44
Table 3.6: Voltage recovery for LLG faults 46
Table 3.7: Voltage recovery for LLL and LLLG faults. 51
Table 3.8: Influence of transformers winding connection 52
Table 3.9: Transformers shift influence 54
Table 4.1: Test system parameters 66
Table 4.2: Induction motor data 76
Table 4.3: Over-current relay parameters. 77
Table 4.4: Feeder A loads rated value 78
Table 4.5: Voltage sags grouping 86
Table 5.1: Summary of the simulated scenarios for different feeder loads value 104
Table 5.2: Parameters of the simulated faults. 108
Table 5.3: Summary of the simulation results to evaluate the fault influence. 112
Table 5.4: Summary of values for different reclosing times. 113
Table 5.5: Summary of the measurements obtained from simulations. 114
Table 5.6: Data of the simulated faults. 116
Table 6.1: A selected list of the real occurred events 124
Table 6.2: Summary of the main values of the recorded events. 138
Table 7.1: Parameters of the PLL_1. 149
Table 7.2: Parameters of the PLL_2. 149
Table 8.1: Summary of the voltage sag parameters for each simulated scenario 149
Table 8.2: List of the occurred events with the voltage sag magnitude coefficient 149
Table 9.1: Parameters used in the passive-based ID methods 173
Table 9.2: State variables for ID. 175
Table 9.3: Tripping times of subsection 9.4.2 182
Table 9.4: Tripping times of subsection 9.4.3 188
Table 9.5: Summary of the tripping times for islanding and non-islanding events. 194

List of figures

Figure 1.2: Power systems general structure with DGs. 4
Figure 1.3: Primary distribution substations with single bus. 5
Figure 1.4: Primary substations with single bus. 6
Figure 1.5: Substation with main bus transfer configuration. 7
Figure 1.6: Substation with breaker-and-a-half configuration 7
Figure 1.7. Substation with double-breaker-double-bus. 8
Figure 1.8: Typical Distribution network with radial configuration. 9
Figure 1.9: Distribution network configuration with open-loop configuration. 9
Figure 1.10: Distribution network scheme with DG units. 10
Figure 1.11: Secondary distribution substation configurations. 10
Figure 2.1: Power system stability classification. 25
Figure 2.2: An example of voltage sag and voltage swell. 28
Figure 2.3: Main characteristics of a voltage sag. 30
Figure 3.1: Test system with three voltage levels to represent sag types. 39
Figure 3.2: Types of voltage recovery. Abrupt (Dashed line), Discrete (Solid line). 43
Figure 3.3: Voltage waveform of sags type B, C and D. 45
Figure 3.4: Phasor representation of sags type B, C and D. 45
Figure 3.5: Phasor representation of sags type E_1-E_2. 47
Figure 3.6: Phasor representation of sags type F_1-F_2. 48
Figure 3.7: Phasor representation of sags type G_1-G_2. 48
Figure 3.8: Voltage waveform for a LLG fault at location I. 49
Figure 3.9: Phase voltage waveform for sags type $A_1$and A_2. 50
Figure 3.10: Phase voltage waveform for sags type A_3, A_4 and A_5. 50
Figure 3.11: Voltage sag phasor representation for a LLLG fault. (a) Sag A_1, (b) Sag A_2 and (c) Sag A_3. 52
Figure 3.12: Phasor representation of the voltage sags considering transformer shifting. 53
Figure 3.13: Comparison between solid and resistance-grounded networks for a SLG. 56
Figure 3.14: Comparison between LL and LLG faults in resistance-based grounding grids. 57
Figure 3.15: Detailed comparison between the sags produced by LL and LLG faults. 58
Figure 3.16: Phase-angle jump comparison for different fault locations. 59
Figure 3.17: Voltage sag for a three-phase fault considering induction motors contribution. 60
Figure 3.18: Voltage sag due to transformer energisation. 61
Figure 3.19: Voltage sag due to induction motor starting. 61
Figure 4.1: One-line diagram of the test system under study. 66
Figure 4.2: Induction machine model in the abc-reference frame 69
Figure 4.3: Electrical model of the induction machine in dq components. 73
Figure 4.4: Electrical model of the induction machine in dq components in stator reference. 74
Figure 4.5: Electrical model of the induction machine for steady-state analysis. 75
Figure 4.6: Time-current curves of overcurrent relays. 77
Figure 4.7: Load profile at PCC_1 with the time of occurrence of some events. 79
Figure 4.8: Three-phase Matlab/Simulink implementation of the test system. 80
Figure 4.9: Single-line representation of the test system under study. 81
Figure 4.10: Equivalent circuit of the test system. 82
Figure 4.11: Thévenin equivalent seen by the IM stator. 82
Figure 4.12: Thévenin equivalent seen by the IM magnetisation branch. 83
Figure 4.13: Flowchart to obtain the transient behaviour of the IM during the voltage sag. 84
Figure 4.14: Phase-voltage comparison scenarios with and without IMs. 87
Figure 4.15: Phase voltage comparison scenarios with and without IMs. 87

Figure 4.16: Electromagnetic torque developed by the IM. 88
Figure 4.17: Flowchart to obtain the transient behaviour of the IM during islanding..... 89
Figure 4.18: Single-line diagram of reduced test system before islanding..... 91
Figure 4.19: Single-line diagram of the reduced scheme of the system during islanding. 91
Figure 5.1: Voltage and current measured at PCC_1. 99
Figure 5.2: Voltage and frequency measurements obtained from scenario I. 100
Figure 5.3: Voltage and frequency measurements obtained from scenario II. 100
Figure 5.4: Voltage and frequency measurements obtained from scenario III. 101
Figure 5.5: Voltage and frequency measurements obtained from scenario IV. 101
Figure 5.6: Voltage and frequency measurements obtained from scenario V. 102
Figure 5.7: Voltage and frequency measurements obtained from scenario VI. 102
Figure 5.8: Voltage and frequency measurements obtained from scenario VII. 103
Figure 5.9: Voltage and frequency during the island for all simulated scenarios. 103
Figure 5.10: IM mechanical speed comparison between scenarios II, III, IV and V. 105
Figure 5.11: Comparison between torques in scenarios II, III, IV and V. 105
Figure 5.12: Active-power comparison between scenarios II, III, IV and V. 106
Figure 5.13: Frequency and IM rotor speed in per unit comparison. 106
Figure 5.14: Voltage, active-power and reactive-power for the three type of load models. 107
Figure 5.15: Voltage and frequency for the three types of load models. 107
Figure 5.16: Simulated scenarios with fixed clearing time. 109
Figure 5.17: Voltage and frequency comparison of the simulated scenarios with fixed clearing time. 109
Figure 5.18: Voltage and frequency of scenario V. 110
Figure 5.19: Voltage and frequency of scenario VI. 111
Figure 5.20: Voltage and frequency of scenario VII. 111
Figure 5.21: Voltage and frequency of scenario VIII. 112
Figure 5.22: Voltage, IM speed and frequency during the IO for several reclosing times. 113
Figure 5.23: Voltage and frequency comparison between scenarios with different load torque values. 115
Figure 5.24: Speed and torque comparison between scenarios with different load torques. 115
Figure 5.25: Voltage, frequency and IM mechanical speed of permanent fault-scenario I. 117
Figure 5.26: Voltage, frequency and IM mechanical speed of permanent fault-scenario II. 117
Figure 5.27: Voltage, frequency and IM mechanical speed of permanent fault-scenario III. 118
Figure 5.28: Voltage, frequency and IM mechanical speed of permanent fault-scenario IV. 118
Figure 5.29: Voltage, frequency and IM mechanical speed of permanent fault-scenario V. 119
Figure 6.1: Event I – Measurements at PCC_1 for a SLG fault at node 8. 125
Figure 6.2: Event I - Measurements at PCC_2 for a SLG fault at node 8. 126
Figure 6.3: Event II - Measurements at PCC_2 for a SLG between nodes 6 and 7. 127
Figure 6.4: Event III – Measurements at PCC_2 for a Permanent fault at node 8. 129
Figure 6.5: Event IV – Measurements at PCC_2 for a SLG in a midpoint in Line 5. 130
Figure 6.6: Event V – Measurements at PCC_2 for a SLG at node 7. 131
Figure 6.7: Event VI – Measurements at PCC_1 for a SLG at Line L6. 133
Figure 6.8: Event VI – Measurements at node 9 for a SLG at Line L6. 134
Figure 6.9: Event VI – Measurements at PCC_2 for a SLG at node at line L6. 135
Figure 6.10: Event VII – Measurements at PCC_2 for a SLG at node at Node 5. 136
Figure 7.1: Validation of Event I. 142
Figure 7.2: Validation of Event II. 143
Figure 7.3: Validation of Event III. 144
Figure 7.4: Validation of Event IV. 145
Figure 7.5: Validation of Event V. 146
Figure 7.6: PLL Blocks of the Matlab model. 148

Figure 8.1: Voltage sag analytical function for a given b parameter. 155
Figure 8.2: Comparison between the voltage sag analytical expression and simulation results. 157
Figure 8.3: Results obtained from Scenario IV of subsection 5.3.1 in Chapter 5. 159
Figure 8.4: Voltage sag magnitude analytical function and simulations of scenario IV..... 159
Figure 8.5: Results obtained from Scenario V of subsection 5.3.1 in Chapter 5. 160
Figure 8.6: Voltage sag magnitude analytical function and simulation of scenario V..... 160
Figure 8.7: Results obtained from Scenario VI of subsection 5.3.1 in Chapter 5. 161
Figure 8.8: Voltage sag magnitude analytical function and simulations of scenario VI..... 161
Figure 8.9: Results obtained from Scenario VI of subsection 5.3.1 in Chapter 5. 162
Figure 8.10: Voltage sag magnitude analytical function and simulation of scenario VI. 162
Figure 8.11: Island caused by a LLL fault. 164
Figure 8.12: Island caused by a LLG fault. 164
Figure 8.13: Island caused by a LL fault. 165
Figure 8.14: Island caused by a LLLG fault. 165
Figure 8.15: Voltage sag magnitude analytical expression for different reclosing times. 166
Figure 9.1: Flowchart to compute the state variables and the pattern for islanding detection. . 173
Figure 9.2: Graphical representation of the adopted directional protection. 174
Figure 9.3: Seven-level HIDM. 176
Figure 9.4: Matlab model with the proposed HIDM. 177
Figure 9.5: Matlab implementation of the seven-level HIDM block. 177
Figure 9.6: Scheme of the UVP/OVP protection. 178
Figure 9.7: Scheme of the UFP/OFP protection. 178
Figure 9.8: Scheme of ROCOF protection. 178
Figure 9.9: Scheme for ROCOV protection. 179
Figure 9.10: ROCOP and ROCOQ protections. 179
Figure 9.11: Voltage and frequency from simulations of subsection 9.4.2. 182
Figure 9.12: Tripping times for Case 1 of subsection 9.4.2. 183
Figure 9.13: Tripping times for Case 2 of subsection 9.4.2. 183
Figure 9.14: Tripping times for Case 3 of subsection 9.4.2. 184
Figure 9.15: Tripping times for Case 4 of subsection 9.4.2. 184
Figure 9.16: UVP/OVP and ROCOV protections results for case 2 in subsection 9.4.2. 185
Figure 9.17: UFP/OFP and ROCOF protections results for case 2 in subsection 9.4.2. 185
Figure 9.18: ROCOP and ROCOQ protections results for case 2 in subsection 9.4.2. 186
Figure 9.19: Directional criterion protection results for case 2 in subsection 9.4.2. 186
Figure 9.20: Voltage, mechanical speed and frequency from simulations of subsection 9.4.3. 188
Figure 9.21: Tripping times for Case 1 of subsection 9.4.3. 189
Figure 9.22: Tripping times for Case 2 of subsection 9.4.3. 189
Figure 9.23: Tripping times for Case 3 of subsection 9.4.3 190
Figure 9.24: Tripping times for Case 4 of subsection 9.4.3. 190
Figure 9.25: UVP/OVP and ROCOV protections results for case 2 in subsection 9.4.3. 191
Figure 9.26: UFP/OFP and ROCOF protections results for case 2 in subsection 9.4.3. 191
Figure 9.27: ROCOP and ROCOQ protections results for case 2 in subsection 9.4.3. 192
Figure 9.28: Directional criterion protection results for case 2 in subsection 9.4.3. 192
Figure 9.29: Tripping times for case 1 of subsection 9.4.4 194
Figure 9.30: Tripping times for case 2 of subsection 9.4.4. 195
Figure 9.31: Tripping times for case 3 of subsection 9.4.4 195
Figure 9.32: Tripping times for case 4 of subsection 9.4.4. 196
Figure 9.33: Tripping times for case 5 of subsection 9.4.4 196
Figure 9.34: Tripping times for case 6 of subsection 9.4.4. 197
Figure 9.35: Tripping times for case 7 of subsection 9.4.4. 197

Figure 9.36: Tripping times for case 8 of subsection 9.4.4. 198
Figure 9.37: UVP/OVP and ROCOV protections results for case 2 of subsection 9.4.4. 198
Figure 9.38: UFP/OFP and ROCOF protections results for case 2 of subsection 9.4.4. 199
Figure 9.39: ROCOP and ROCOQ protections results for case 2 of subsection 9.4.4. 199
Figure 9.40: Directional criterion protection results for case 2 of subsection 9.4.4. 200

Nomenclature

AC	Alternating Current
DC	Direct Current
HV	High Voltage
MV	Medium Voltage
LV	Low Voltage
IMs	Induction machines
CB	Circuit breaker
PQ	Power Quality
DG	Distributed Generation
SI	Standard Inverse
VI	Very inverse
EI	Extremely inverse
IEEE	Institute of electrical and electronics engineers
DN	Distribution Network
SCADA	Supervisory control and data acquisition
DSO	Distribution Operator
TSO	Transmission Operator
SG	Smart Grid
XLPE	Cross-linked polyethylene
ID	Islanding Detection
IO	Islanding Operation
UVP/OVP protection	Under and over-voltage protection
ROCOF-ROCOV	Rate of change of frequency and voltage
UFP/OFP protection	Under and over-Frequency protection
ROCOP-ROCOQ	Rate of change of Active and reactive-Powers
VSR	Vector surge relay
HIDM	Hybrid Islanding Detection Method
NDZ	Non-detection Zone
H	Inertia in seconds
D	Damping coefficient
J	Inertia in $kg \cdot m^2$
SLG fault	Single-line-to-ground fault
LL fault	Phase-to-phase fault
LLG fault	Line-to-line-to-ground fault
LLL fault	Three-phase fault
LLLG fault	Three-phase-to-ground fault
Rf	Resistance fault
Z_{feeder}	MV feeder impedance
Z_{source}	Main grid impedance
PLL	Phase-Locked Loop
PCC	Point of common coupling
RMS	Root mean square
COMTRADE	Common Format for Transient Data Exchange (IEEE format)

Chapter 1

Introduction, concept and objectives

1.1 Power systems overview

Conceptually, power systems can be defined as the set of elements required to supply electrical power to the costumers. As a whole, power systems can be seen as a chain where several agents take part of it and interact between them. To understand the present power systems structure, a brief recall regarding its beginnings becomes crucial. Indeed, the electrical networks have evolved tremendously from its beginning at the end of the XIX century. At first, the electrical networks were formed by power plants linked with the supply centres with low distances, fed through direct current (DC) at a voltage of 100 V with very low power in the range of hundreds of kW. Years later, with the invention of the alternating current (AC) and the implementation of power transformers, the electrical energy was transmitted through long distances, where the voltage increased to the hundreds of kV and the transmitted power increased to the MW. Thus, in 1922 the first 245 kV transmission line was inaugurated, this voltage level has been increasing until today. In more or less extent, the electric energy systems have developed equally for all countries, converging towards a very similar structure and configuration [1.1]. However, each electrical network may have a particular configuration.

As a rule of thumb, the aforementioned electrical chain is composed of electrical generation, a transmission system, distribution networks and lastly the costumers. Meanwhile, production centres have to produce the required amount of electrical energy required by the costumers, transmission and distribution networks are designed to connect both agents. Furthermore, these two magnitudes (i.e., the amount of generated and consumed energy) have to be properly balanced. Since generators produce electricity at low voltage levels in the range of few kV, this voltage has to be increased through a step-up transformer and after that, the latter is connected with the transmission system. The transmission networks is used interconnect the major part of the electricity generation plants with the major part of the distribution substations. Typically, the transmission system operates with a meshed configuration (i.e., with a closed-loop configuration), that is, the network is fed by more than once source. Therefore, HV substations can be supplied by different generation centres simultaneously. Commonly, HV substations are highly automated and are protected with a high degree of redundancy in order to assure high reliability. Detailed information about the full range of configurations in an HV substation, see [1.2-1.3]. In these substations, high-capacity power transformers are allocated so as to evacuate the high amount of energy. The operation and maintenance of the transmission system, as well as the coordination

between generation and consumption, is under the responsibility of the transmission operators (TSOs).

The subsequent step in the electrical chain is the subtransmission system, which hangs from the previously mentioned transmission system at HV levels, and subtransmission systems can be seen as the connection between the HV substations with the distribution primary substations. Even though, presently is still not clear if these assets belong to the transmission network or instead, to the distribution networks.

Distribution networks (DNs) hang from the previously mentioned subtransmission systems, which operate at lower levels. Although only two different voltage levels are theoretically defined (HV and LV levels), in practical engineering, the concept medium voltage (MV) is widely used. DNs encompasses two types of distribution systems, named primary and secondary distribution systems. The first distinction is aimed at connecting the subtransmission levels (e.g., Lines between 66 and 132 kV) with the secondary distribution system which operate at MV levels (e.g., between 11 and 25 kV). Therefore the transformers allocated at the primary substations operate between HV and MV (e.g., 132-66 / 11-25 kV). Afterwards, the so-called MV grid is connected through the LV networks at the secondary distribution substations where the voltage reduction takes place (e.g., step-down transformers of 25/0.4 kV are widely used). Costumers are the last step of the electrical chain and are supplied by the LV networks. Even though different configurations and voltage levels may vary depending on the country, commonly, low voltages are around 0.4 kV and its configuration is mainly radial. The main difference between LV networks rises in the type of grounding. In Section 1.2, the configurations and parts of these distribution networks (DNs) will be showed and briefly discussed. The DN is operated by the distribution operator (DSO), who is responsible for the grid planning, operation and its maintenance. Figure 1.1 shows the typical configuration of an electrical power system where the previously mentioned agents are depicted. As can be drawn from this Figure, the power flow is unidirectional and is all supplied by the transmission levels.

Focusing on DNs, its degree of automation and observability used to be lower than the one implemented in the transmission systems. Nonetheless, in the recent years, due to the emerging challenges that DNs are facing such as the integration of dispersed generation or the increasing interest in the power quality, they are transitioning to full automated grids. On the other hand, the LV networks are less automated than the MV are, which makes them weaker. Nevertheless, they are also experiencing noticeable changes, especially due to the rapid proliferation of the rooftop PV generation and also due to the implementation of the smart meters [1.4-1.5]. Even though, as has been stated before, the huge amount of generated electricity is transmitted to the consumption centres through the HV transmission lines and its substations, this fact is changing recently with the proliferation of the so-called distributed generation (DG). These power plants are usually based on renewable energies (e.g., mini-hydraulic, photovoltaic or wind power), range between hundreds of kW to few MW and are connected to the different voltage levels of DNs. At the early beginnings, these resources were seen as a threat to the network, given the changes that these plants will rise, and indeed, these DG units have changed the way classical DNs were operated. Among the issues that have appeared, it is relevant to highlight the change in the protective coordination [1.8], and the reverse in the power flow [1.9].

On the other hand, it has been demonstrated that these DG units can provide valuable advantages such as losses reduction and voltage improvement [1.6-1.7]. As a consequence of this dispersed generation, the resulting electrical system is shown in Figure 1.2. As can be seen, the power system depicted in Figure 1.1 has suffered major changes.

Costumers are the last step of the electrical chain, and the electrical loads represent them. Depending on the load profile, the following classification is done: (i) industrial, (ii) commercial

and (iii) residential. The first group, have a large rate of power and high load profile, the second group typically have a high rate of power and consumption per area (kW/m^2 and kWh/m^2) and lastly, the third group has a low rate of power and the rate of consumption is below the commercial one. The (i) group, depending on its power rate, can be either connected to the subtransmission grid or to the MV grid, the (ii) and (iii) are typically connected to the LV grid. In addition to the load profile classification, if the type of load voltage-dependence is considered, the following distinction can be done; (i) constant impedance loads, (ii) constant power loads and (iii) constant current loads. Lastly, it is worthwhile to note that, the previous loads have been assumed linear, nevertheless, with the appearance of the electronically-interfaced devices (i.e., devices fed through AC/DC converters) the non-linear loads are increasing.

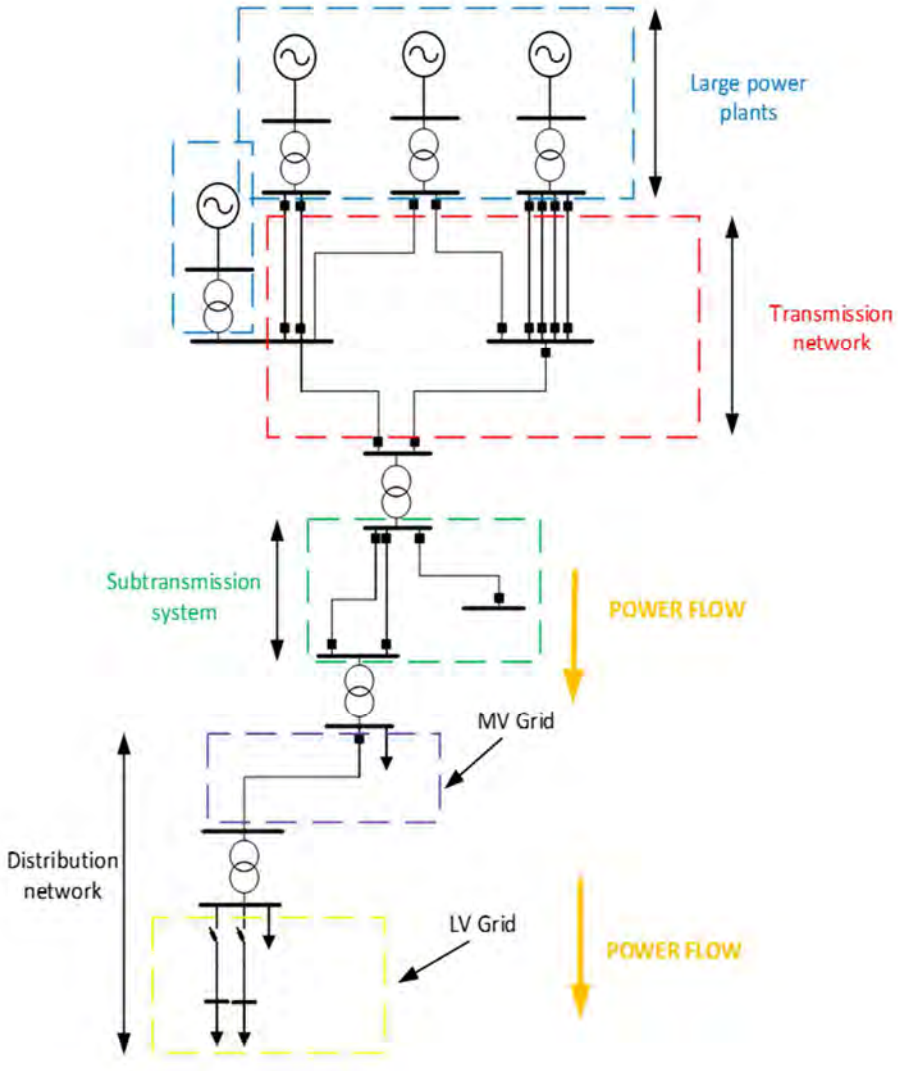

Figure 1.1: Power systems general structure.

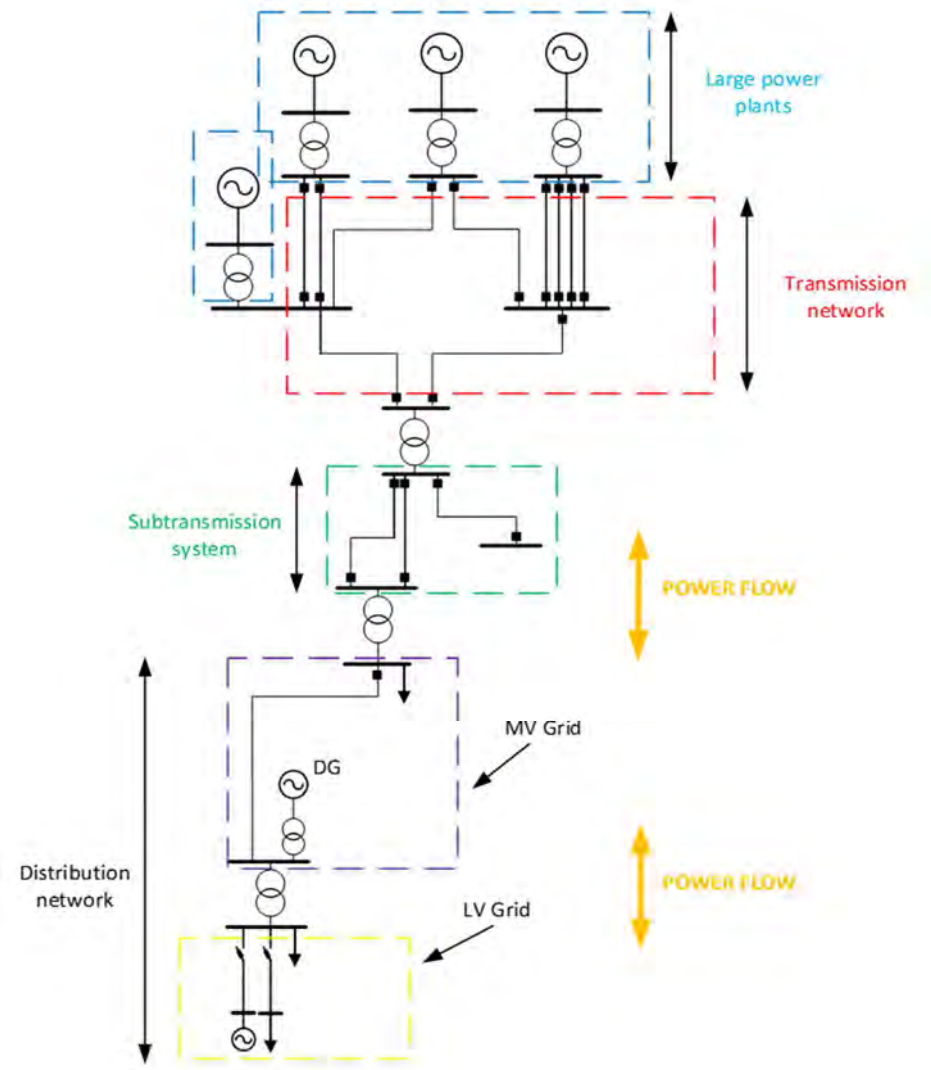

Figure 1.1: Power systems general structure with DGs.

1.2 Power distribution networks

1.2.1. DNs general structure and configurations

Distribution substations

As stated in the previous subsection, distribution networks hang from the subtransmission levels and the step-down HV/MV transformers allocated at the substations reduce the voltage level between the subtransmission system and MV network. Therefore, once the DNs structures have been defined (i.e., primary and distribution systems), this section will list the most common types of substations configurations and its main features. In general, these substations are equipped with measurements devices, protective equipment (e.g., circuit breakers, switches, potential transformers, current transformers or surge arresters), communication devices and automation systems. Commonly, the substation configuration depends, to a large extent, on where they are located (i.e, rural, suburban or urban) and regardless of the type of configuration these substations can be fed by one, two or more lines and can have one, two or even three transformers in exceptional occasions. It is worthwhile to note that regardless of the type of substation, the MV

configuration (i.e., the secondary side of the transformer) may vary. The first type is composed by only one main bus and one transformer, the second is known as split bus and is formed by two transformers and the third is composed by a main bus and has a tie-switch which guarantees the continuity of supply in case one transformer fails. Thus, Figure 1.3a shows single transformer configuration and Figure 1.3b shows double transformer with split configuration. Thirdly, even though double MV bus is not the most common scheme, this configuration can be found especially in urban substations with large amount of clients and uninterruptible supplies.

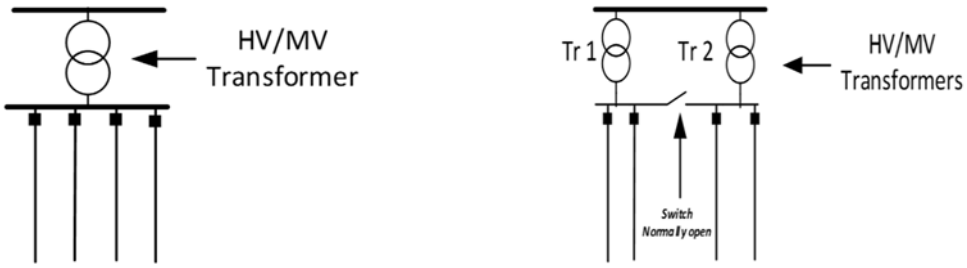

a) Single MV bus b) Split configuration for MV bus

Figure 1.2: Primary distribution substations with single bus.

The most common substations schemes for HV/MV voltage reduction, are listed down below:

- Single bus
- Sectionalized single bus
- Main and bus transfer
- Ring
- Breaker-and-a-half
- Double-breaker-double-bus

For a more detailed explanation about these configurations and other substation configurations, see [1.2].

Single bus

This substation configuration is the simplest one and is formed by one bus which connects the HV grid lines with the HV/MV transformer. The main disadvantage of this configuration is the low level of reliability where, in case a transformer or bus fails, it implies the loss of the whole electrical supply. The MV lines which hang from the substation will experience an interruption. Figure 1.4a show this configuration. Note, that this configuration can be fed with one or two HV lines and can allocate one or two transformers.

Sectionalized single bus

This configuration is the evolution of the previously described single bus substation. The main feature and advantage is the possibility of splitting the main bus, therefore, if in the substation a bus fault occurs, it can operate with one circuit breaker and one transformer, thus increasing the level of operations in case a fault occurs. Thus, by operating the central tie-switch, this type of structure improves reliability, enhances the single bus configuration and allows the isolation of the main bus for maintenance tasks. On the other hand, the cost is increased in regards to the single bus. Figure 1.4b shows this configuration.

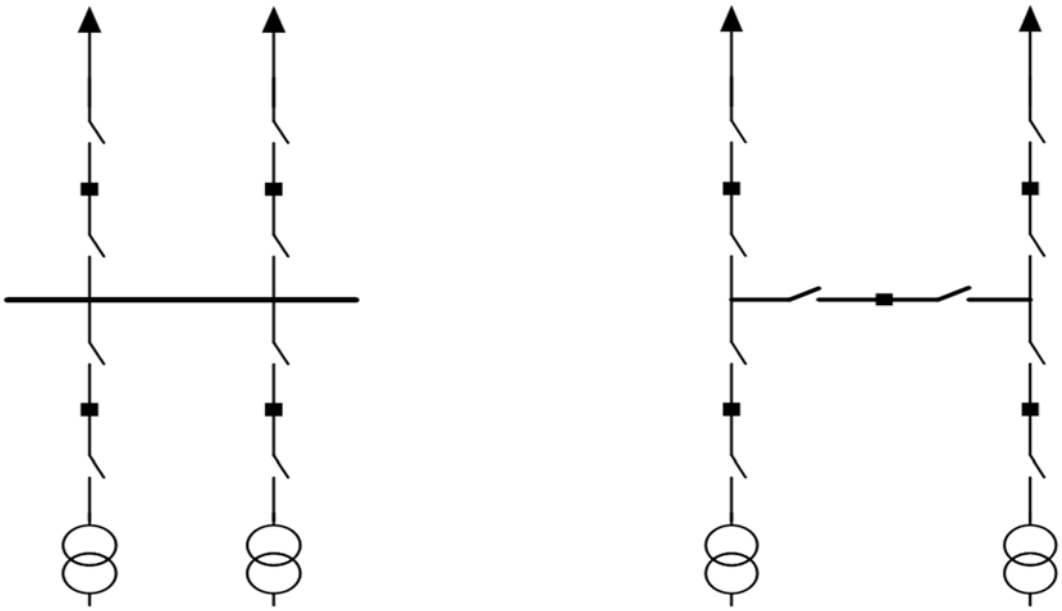

a) Single bus b) Sectionalized single bus

Figure 1.3: Primary substations with single bus.

Main and bus transfer

A main and a bus transfer configuration consists of two independent buses, where one acts as the main bus which is fed by the HV lines and, two switches and a circuit breaker (CB) protect the transformer. The main bus and the second bus are connected through the interconnection CB equipped with two switches. In case a circuit breaker has to be removed or put out of service, this can be accomplished by taking advantage of this bypass tie-switch. This configuration requires two switches for each HV line and each transformer, in Figure 1.5, an example of a double bus with bypass switch is depicted. Concerning the previous configuration, the main advantage is the reliability increasing, whereas the main disadvantage is that its cost is also increased.

Ring

Ring configuration is an extension of the sectionalised bus substation and is formed by interconnecting the two open ends with a CB. This configuration creates a loop where two switches and a CB protect each section. The main advantage of this configuration is that in the case of transformer or circuit breaker failure, this section can be isolated and the substation continues operating. In case a bus fault occurs, with this configuration, the two circuit breakers of the faulted side clears the fault without interrupting the power supply. Figure 1.6 shows this substation scheme. As for the sectionalised bus configuration, the main advantages of these substations are the high reliability in case of outages, and the flexibility to perform maintenance tasks. On the contrary, the cost increases due to the required number of switches and CBs.

Breaker-and-a-half

The breaker-and-a-half configuration is composed of two buses which are connected both CBs and switches.

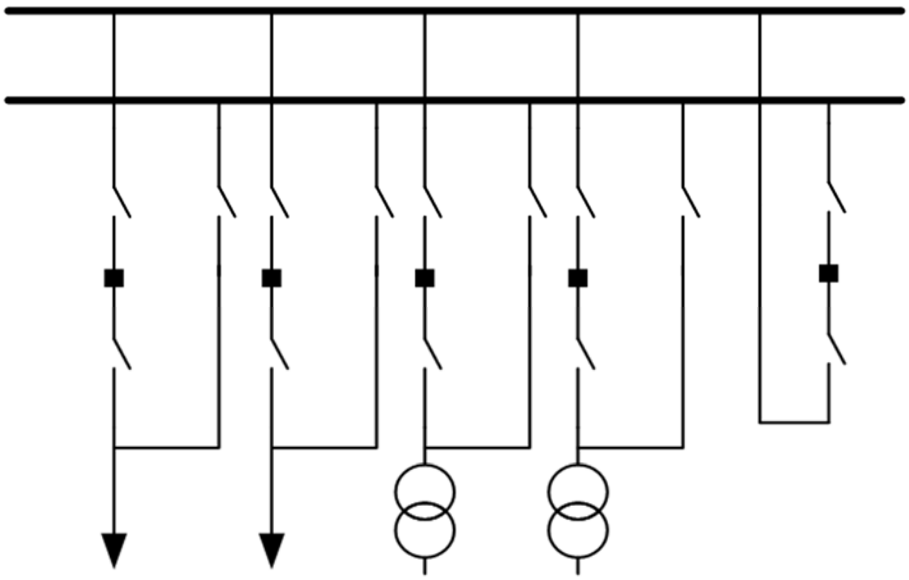

Figure 1.4: Substation with main bus transfer configuration.

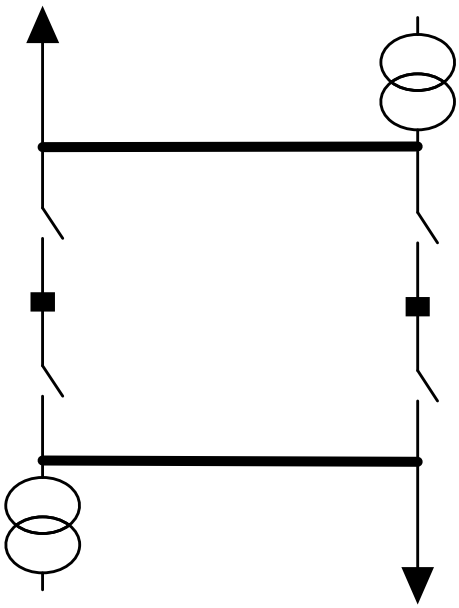

Figure 1.5: Substation with breaker-and-a-half configuration

Usually, for each high voltage line and transformer, there are two switches and one CB. In each side, three circuit breakers are allocated. Thereby, the reason why this substation is called breaker-and-a-half is that each side (either HV line or transformer) has one CB and share the second one. This configuration provides high flexibility in case a CB has to be replaced and guarantees full protection during this task. Besides, bus faults do not produce any substation outage. The pros and cons of this configuration are the high flexibility, high reliability, the chance of remove either circuit breakers or bus for maintenance with no interruption, however, the cons are the high price and the protective coordination between circuit breakers (i.e., the shared circuit breaker which both high voltage line and the transformer). This configuration with two HV lines and two transformer positions is shown in Figure 1.6.

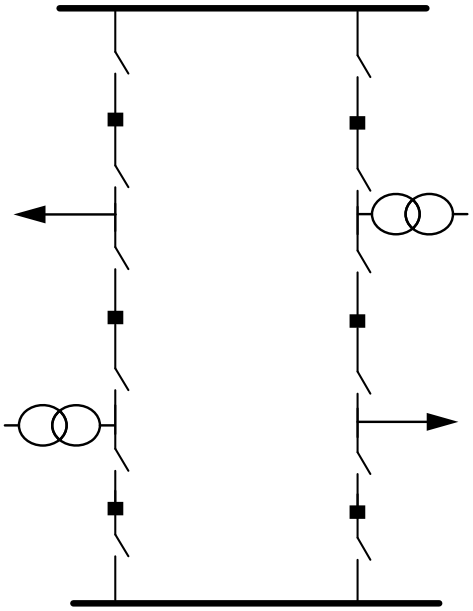

Figure 1.6. Substation with double-breaker-double-bus.

Double breaker-double bus

This substation configuration is probably the most complex, essentially, because of the number of switches and CBs. As for the three previous configurations, this substation has two main buses which generally energised. For each circuit of the substation, there are two CBs, thereby, any of them can be removed without interrupting the electrical supply. Each branch between the two buses allocates either an HV line or a transformer position. Figure 1.7 shows this configuration with two HV lines and two transformers. Undoubtedly, among all the listed substations configurations, this is the one which provides more reliability, however, is the most expensive due to the number of switches and CBs.

Primary distribution systems

Primary distribution systems can be either single-feeder which means that there is only one MV line or a multi-feeder when several lines hang from the substation. As an example, a typical DN configuration is shown in Figure 1.8. In the latest, an open-loop configuration can be made if two or more feeders can be connected. However, Figure 1.9 shows the configuration of the feeders, where the normally open switch is closed. An essential factor to take into consideration in the open-loop configuration is the high reliability. Commonly, each feeder which hangs from the HV/MV is protected by a CB with an overcurrent function implemented, whereas fuses protect the lateral branches. Note however, that this configuration can be different if the grid contains DGs, as an example, see the network layout of Figure 1.10.

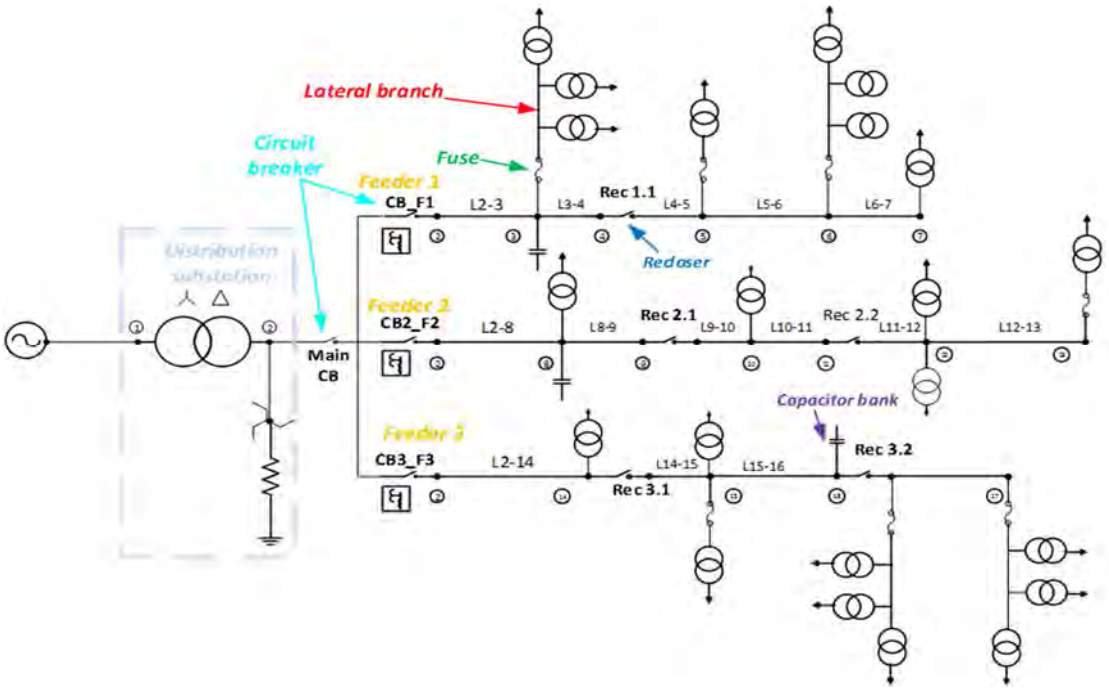

Figure 1.7: Typical Distribution network with radial configuration.

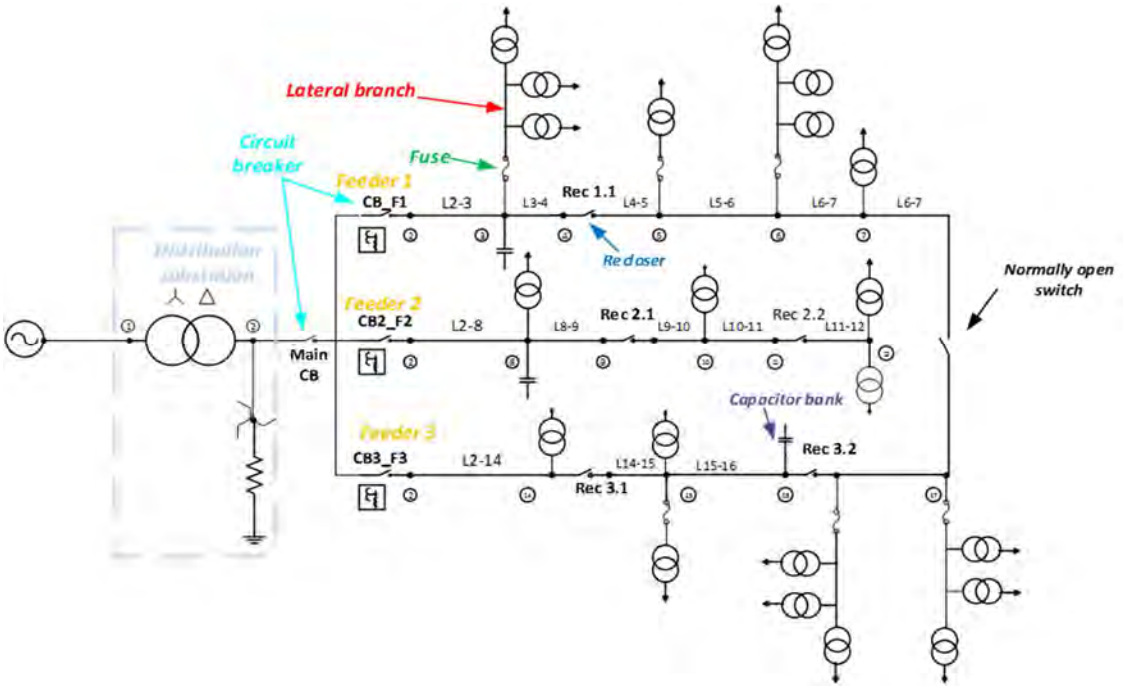

Figure 1.8: Distribution network configuration with open-loop configuration.

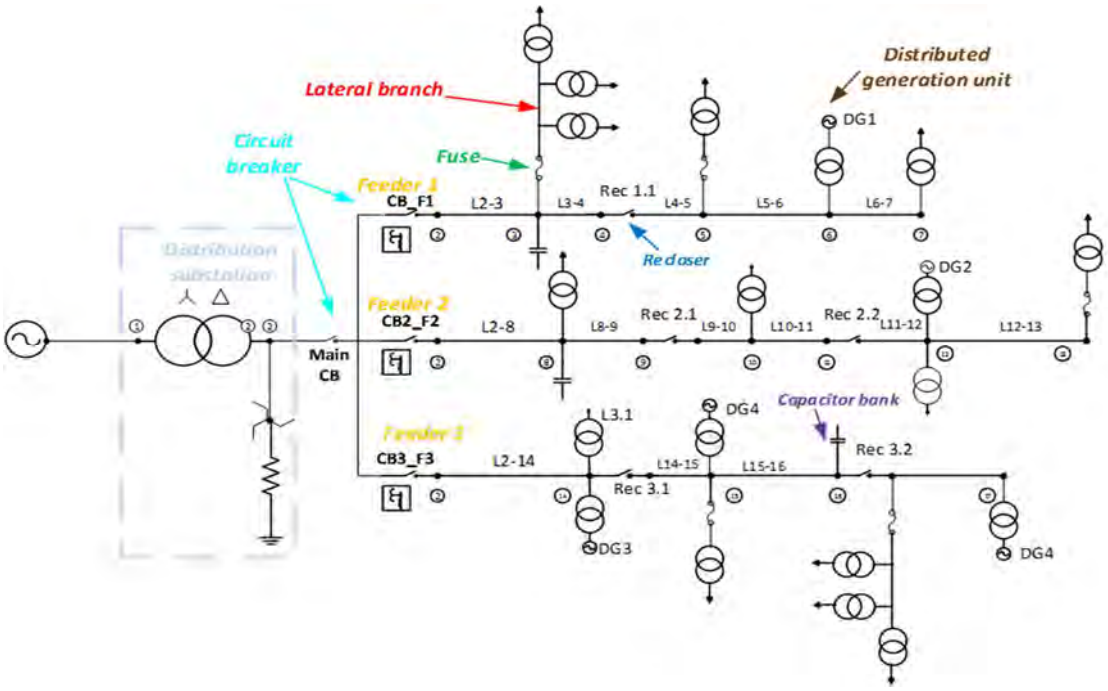

Figure 1.9: Distribution network scheme with DG units.

Secondary distribution systems

Secondary distribution systems are the part of the grid which hang from the MV/LV substations, and as stated before, its configuration will vary depending on how important is the load's power continuity. Accordingly, the major part of the LV grid is operated radially, while, for consumers where the power cannot be interrupted (e.g., hospitals, large factories, large buildings) a spot configuration is selected. In Figure 1.11a, the typical radial LV grid configuration is showed; meanwhile, a spot configuration is shown in Figure 1.11b. Fuses protect the LV feeders which hang from theses substations.

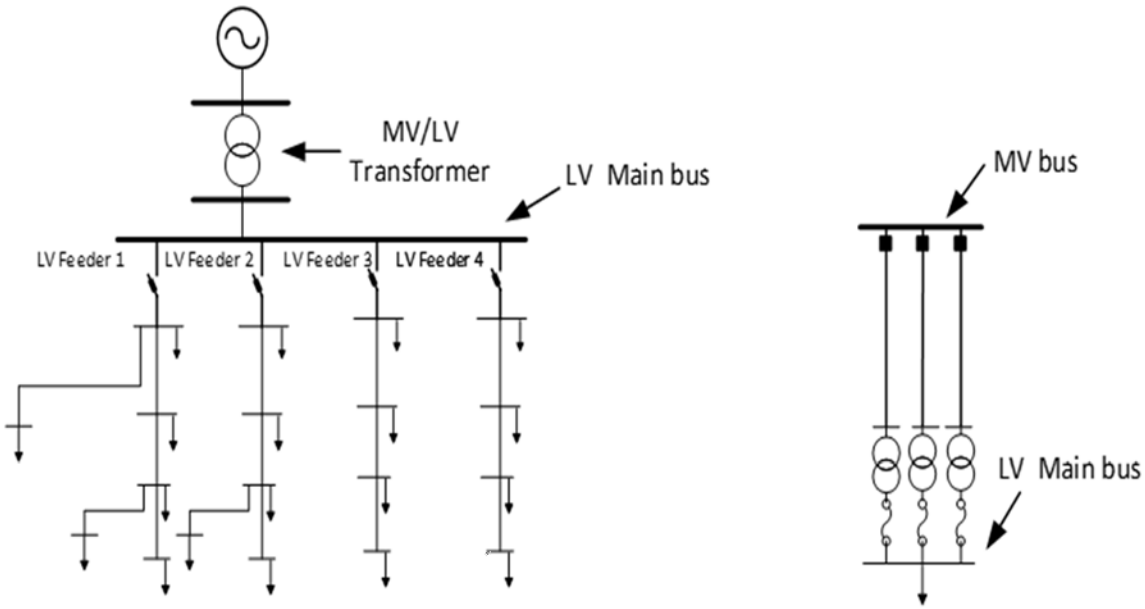

a) Radial multi-feeder LV grid

b) Spot configuration of a LV grid

Figure 1.10: Secondary distribution substation configurations.

1.2.2. DNs elements and systems applications

The elements that compose a DN can be classified into three main types; the inherent elements of the DN, which are focused on transmitting the power between primary and secondary substations. Distribution lines (i.e., they can be either over-head wires or cables) and transformers are the main components of this group.

The second group of devices is focused on providing reliability and safety. This group includes elements such as relays, CBs, switches, sectionalizers, reclosers, fuses or surge arresters. Besides, the coordinated between those elements becomes crucial. Additionally, other elements such as voltage regulators, capacitor banks or inductances can be found along the DN to provide reactive support for voltage support.

The third category of elements is focused on measurement, operation and grid monitoring. Measurement devices are, at the same time, composed by elements such as potential transformers, current transformers, power quality analysers and smart meters. The electrical measurements sensed by the previously mentioned tools are typically collected with a remote terminal unit (RTU) and transmitted to the monitoring systems taking advantage of a communication system (e.g., GSM, GRPS, or optic fibre). Finally, software systems such as SCADA or state estimators manage the data obtained from the obtained field measurements. The latter has aroused great interest during the last decade and have provided successful results to detect missoperations.

Lines

Lines are designed to transmit power along the grid. These lines can be either an overhead line or a cable depending on its configuration. Mainly, distribution lines along urban areas are typically composed of cables, whereas overhead lines are the most used type in suburban and rural areas. Meanwhile, overhead lines are based on aluminium; cable lines are insulated with polymers such as XLPE or EPR. A detailed modelling regarding lines in power systems is done in [1.10]. Furthermore, a comprehensive study of electrical lines modelling for transient studies can be found in [1.11].

Transformers

Transformers are one of the most critical elements of an electrical system and are used to adjust the voltage level to the desired value; thus, it can be used to increase or decrease (i.e., step-up and step-down transformers) the voltage level through its electromagnetic fields between windings. They transfer power through its windings without changing the frequency. Transformers can be categorised by the number of windings and its connection, the core configuration (e.g., three-limb core, five-limb core or three single-phase transformer), the transformation ratio, the power rating, its clock ratio between windings, and the type of cooling. ANSI/IEEE-Std. C57.12 provides useful data regarding transformers characteristics and tests [1.12]. The main characteristics of a transformer are supplied by the manufacturer and showed in the rating plate. Usually, the main features are as follows: its ratio between winding voltages, the rated apparent power, the short-circuit impedance and its losses. In [1.13-1.14], a comprehensive evaluation of transformer models for transient studies is carried out.

Circuit breaker

A circuit breaker is a switching element designed to energise or de-energise a circuit; therefore, it can interrupt the electrical current. The circuit breaker is defined by its breaking capacity in steady-state as well as under fault conditions. This current interruption can be done to protect the grid against disturbances or to carry out maintenance tasks. Presently, several types of the circuit breakers are available, among them, SF6 CB, vacuum CB or oil CB. For a thorough analysis

regarding the types of CBs and its capabilities, see [1.15]. Overall, in MV networks, the breaking capacity during steady-state operation of these devices is around a maximum value of 800 A, while during short-circuit, the breaking capacity is approximately 20 kA.

Relay

The main goal of a relay is to drive the circuit breakers or other switching devices. This device performs the task of preventing abnormal situations in the grid (e.g., short-circuits, over-voltages, etc.). These devices have the capability of generating a trip and send it to the CB in case a threshold has been exceeded. The thresholds and settings of each relay depend on the desired protective function (e.g., over-current relays, voltage relays, frequency relays, etc.). In general, radial distribution networks are equipped with overcurrent relays to protect the grid against short circuits or over-loads [1.16].

Nevertheless, depending on the type of grounding and the type of network (i.e., radial or meshed), this overcurrent protection has to be replaced by a more complex protective system. Particularly, in the presence of DG units, voltage and frequency relays are widely used. In the further sections, the main types of relays used in distribution networks will be assessed.

Recloser

A recloser is a protective device which is allocated along the grid and has the capability of interrupting currents. In case a fault occurs, it de-energise the circuit, and after a preset reclosing time, it attempts to re-energise it to restore the supply. If this operation is unsuccessful, few more reclosing operations are typically implemented (e.g., between three and four reclosing operations at different time rates is a commonly used procedure). If these attempts proved to be unsuccessful because the fault is permanent, the circuit remains opened isolating the faulted section. The breaking capability of these devices can be similar to those adopted in circuit breakers. It is essential to highlight that, reclosing function can also be implemented in a relay, see manufacturers data [1.17].

Sectionalizer

Essentially, a sectionalizer is a protective device which acts as a slave of a master device, which can be either a circuit breaker or a recloser. Therefore, the principal goal of these devices is the fault location. A typical procedure implemented in sectionalizers for fault location and isolation in MV DNs is described as follows. Firstly, it counts the number of faults and interruptions (i.e., a short-circuit and its subsequent CB opening). Secondly, and depending on the desired time, between two of the aforementioned reclosing operations, it orders the switch opening to isolate the faulty section. Note, however, that during normal operation, sectionalizers are capable of interrupting less current than circuit breakers. For instance, in MV networks, regardless of the voltage level, commonly the breaking capacity of sectionalizers during normal operation is between 200 and 600 A. These devices proved to be useful to locate and isolate the fault in DNs.

Switch

A switch is used to isolate a faulted section of an electrical network. Mainly, the difference between a CB and a switch is its breaking capacity. Meanwhile, the CB can interrupt high fault currents; this switch can only interrupt low current levels. As mentioned earlier, they are especially useful to isolate faults when the upstream CB has previously de-energised the circuit.

Fuse

Unlike the other protective devices such as CB, reclosers or sectionalizers, fuses are only designed for over-current protection. Fuses are formed by a piece of wire which melts when current exceeds

a particular threshold. The most common fuses curves can be seen in [1.18]. For reliability purposes, these protective devices are not recommended and are used to protect laterals and secondary branches in the MV distribution network. Indeed, based on a cost-effective solution, fuses are widely adopted in secondary distribution substations to protect LV lines.

Potential transformer

A potential transformer is used for measurement purposes, it usually is formed by a common core and its main aim is to adapt the voltage level of the grid to a low voltage level suitable for devices such as relays and meters. More detailed data of these transformers can be found in [1.19].

Current transformer

Current transformers are used in measurement and protection purposes. Unlike potential transformers, these devices are used to reduce the current level that flows through the primary winding. These transformers have a ratio between the primary winding and the secondary winding. The primary winding is connected in series with the wires, and the secondary is connected to the protective relay or measurement unit. Presently, different topologies of current transformers are available; some of them are designed to avoid line de-energisation (e.g., open-core CT). The relationship between primary and secondary is kept fixed. See manufacturer data in [1.20].

Power quality analyser

As a general definition, a power quality analyser is aimed at measuring a wide range of parameters for power quality assessments. The most common power quality disturbances are as follows: voltage sags/swells, voltage interruptions, flicker, transient over-voltages, harmonics, voltage and current unbalances or even frequency deviations, an extensive analysis of power quality disturbances can be found in [1.21-1.22]. Presently, the use of these devices is gaining importance among utilities to record system disturbances. Depending on its accuracy, they can be classified as class A or B, see the measurements requirements in the standard UNE-EN 61000-4-30.

Capacitor bank

Capacitor banks are used to provide reactive power to the grid and help to improve the power factor of end-users. Even though three-phase capacitor banks are the most commonly adopted in DNs, single-phase capacitor banks may also be found in single-phase LV networks. Due to the power factor correction, they help to improve the voltage drop and losses. These devices usually are allocated in either the primary substations (i.e., at the MV bus of the substation) or at the secondary distribution systems (i.e., at the primary side of the MV/LV distribution transformer). A comprehensive investigation regarding the optimum allocation of capacitor banks in DNs can be found at [1.23].

Smart meter

Smart meters are measurement devices and the main difference with regards the typical ones is its capability of transmitting the data through the distribution network wires. Indeed, the power line communication (PLC) system, is one of the most commonly adopted solution by DSOs. Additionally, they are prepared for bidirectional measurements and can register events such as power failure or detect over/under-voltages in steady-state. In the modern power systems, these devices are a valuable asset for the DSO to carry out other functionalities such as voltage control, demand-response, DG dispatching control or network losses evaluation (either technical or non-technical). Lastly, in smart grids, these devices can be crucial to improve the current load shedding procedures. An excellent example of smart meters project can be seen in [1.22].

Voltage regulators

Voltage regulation can be done by using a transformer equipped with a tap changer of a specific apparent power capacity, which allows the user to modify the ratio by changing the number of turns. Usually, the addition or removal coils is done in the primary winding (i.e., the higher voltage winding). Thus, by switching the taps, the voltage drop can be reduced.

In the recent years, as a result of the electronically-interfaced devices, the voltage control is done with several flexible alternating current transmission systems (FACTS) devices such as static var compensators (SVC) (it that can be either a capacitor or a reactor) or static synchronous compensator (STATCOM). These devices are electronically-interfaced capacitors or even reactors connected to the grid through a voltage source converter (VSC); thereby, the injection of reactive power can be controlled by its thyristors. For more information about this voltage compensation, see [1.24].

SCADA

Conceptually SCADA (System control and data acquisition) systems are implemented for real-time monitoring. This control can be implemented through a communication system which receives the signals (i.e., bus voltages, line currents, system frequency, circuit breakers state, etc.) from in-field measurement and protection devices. These data is sensed, collected and stored into a database. The stored data can be evaluated and classified by the SCADA main program and allows the DSO to analyse the state of the grid as well as evaluate prescribed events. SCADA systems are beneficial for DN dispatching tasks.

State estimators

State estimators have represented one of the most noteworthy achievements in the power systems control, especially during the recent years in the so-called smart grids. The input of this tool is the obtained data from the SCADA, which in turn, it has been collected from field measurements. The state estimators main goal is to detect ill-conditioned measurements and false alarms; thus, it estimates the grid from local measurements. For more detailed information regarding state estimators, see [1.25].

1.3 Thesis background

DNs in rural areas are those who are more vulnerable and are more exposed to contingencies due to the environment and due to the low level of redundancy. Typically, DNs are operating in radial configuration and are protected by CBs and reclosers which are driven by over-current relays. Hence, if a fault occurs (e.g., it can be either short-circuits or over-loads), after the clearing time, the circuit is de-energised. As mentioned earlier, following this operation, in order to avoid manual operations and time-consuming posting of employees, the recloser will attempt to re-energise the circuit on several occasions to restore the electrical supply. Therefore, the costumers located downstream of the faulted section are expected to experience a voltage sag before the fault is cleared, and a supply interruption once the CB has opened the circuit. However, if a source is acting in parallel with the main grid during the reclosing time, instead of an interruption, an islanding operation (IO) can occur. To date, these IOs were expected only in the presence of distributed generation (DG) units, which following the CB disconnection, they continue energising this portion of the network.

However, unexpectedly, and IO was observed in a DN with no DG units. This fact, undeniably, raised a problem for the DSO accentuated by a considerable amount of consumers complaints.

Crucially, this was the starting point of the undertaken research. This being the case, the first steps focused on locating the source of this unexpected IO and analyse the occurred events which, given the situation, it was not a trivial issue.

As a general matter, the background of this thesis lies in solving a major problem identified in a real DN located in Spain.

1.4 Steps of the thesis

As derived from the previous section, essentially, this thesis has been oriented at solving a real problem identified in a DN located in Spain. Although the main pillars of the thesis have been detailed in the abstract, this section will list a detailed point-by-point summary of the main stages. Particularly, during the research period, the following steps have been carried out:

1. Carry out an in-depth analysis of the recorded field measurements.
    - Collect the data from relays.
    - Extract this data from Comtrade files.
    - Analyse of the origin of the events.
    - Determine the origin of this IO.
    - Classify each event depending on its duration and characteristics.
2. Preliminary characterisation of the transient.
    - Characterise the main features of the islanding.
    - Accurately identify the different stages of the IO. Thus, considering the pre-fault, during-fault, the IO and the recovery process.
    - Preliminary discussion concerning the possible influential factors of this IO.
    - Study the possible effects of the IO into the grid and costumers.
3. The development of the model
    - Evaluate the Matlab/Simulink capabilities for the transient simulation.
    - Analyse the main characteristics of the network components.
    - Select the most appropriate model for each grid component.
    - A comparison between the model and the real system was investigated.
    - The last step focused on load modelling. Given the fact that its pattern is random in time, to obtain successful results, the trial and error method had been used.
4. Simulations with the implemented model
    - Once the model has been created, the first preliminary simulations were performed.
    - After preliminary attempts, a successful wide range of scenarios were simulated (See Chapter 5).
    - Analyse the obtained results from the simulations.
    - A comparison between the simulation results and those obtained from in-field results has been performed. From this comparison, the exact location of the faults occurred in the grid proved feasible. Given the fact that with voltage and current measurements in only two locations (PCC_1 and PCC_2, See Figure 4.1 in Chapter 4) it is complicated to locate a fault. However, by making this comparison, this location is successfully obtained.
    - Simulate the IO with different feeder load scenarios.
    - Simulate the islanding operations by adding different load torque values.

- Simulation with different types of faults so as to observe its effects on the island.
- Simulate several reclosing times with both permanent and non-permanent faults.

5. Model validation
   - Carry out a comparison between the real occurred events and simulation results, which is achieved by comparing both voltage and frequency measurements separately.
   - Test the accuracy of the developed model.
6. Voltage sag assessment
   - A review of the main power quality disturbances.
   - A general survey of the voltage sags state of the art.
   - Establish the main features of the proposed voltage sag that is observed during the island.
   - Define the analytical expression that follows this voltage sag.
   - Validate the proposed analytical expression of the sag magnitude taking advantage of the real occurred events.
7. Anti-islanding evaluation
   - A brief review of the currently available islanding detection (ID) methods.
   - Test the available methods for DG islanding detection.
   - Describe the principles of the proposed algorithm.
   - Demonstrate the efficiency of this method in ID as well as the incapability of the current ID methods for several particular scenarios.
   - Test the hybrid islanding detection method for both islanding and non-islanding events.

1.5 Thesis Objectives

Fundamentally, the main goals of this thesis can be summarised in three main points, which are listed down below:

- The first objective of this thesis is the development of the required model to validate the recorded field measurements where the islanding operation has been identified.
- The second goal is the assessment of the voltage sags that occur during the islanding operation object of study.
- The third goal of this thesis is the implementation of a suitable tool to prevent the islanding operation which has been previously evaluated, modelled and validated.

1.6 Document structure

This thesis is structured in 10 chapters, as follows:

Chapter 2

The second chapter describes the state of the art of each key issue of this thesis. Thus, the first part will describe state of the art in IOs, the main types and its principal features. The second part is aimed at introducing the main fundamentals of the power quality, which falls within the second

key issue of this thesis. Lastly, the third part makes a review of the currently available islanding detection methods and introduce the basic principle of the islanding detection criterion implemented in this thesis.

Chapter 3

The third chapter reviews the current literature about voltage sags. In this chapter, the voltage sags will be divided into two main types; the ones with constant magnitude (i.e., originated by short-circuits) and ones with non-constant magnitude (i.e., voltage sags originated by the contribution of induction motors, caused by motors starting or transformers energisation).

Chapter 4

The fourth chapter seeks to address the theoretical analysis of the IO. In this chapter, the following aspects are analysed; (i) the origin of the islanding operation and its contributory factors, (ii) the equations of the system before the fault, (iii) during the fault and, (iv) during the IO. Besides, this chapter describes the main features of the three-phase Matlab/Simulink implemented model. Mainly, this chapter describes the modelling guidelines followed to validate this transient.

Chapter 5

Chapter 5 provides the results obtained from simulations and describes the critical aspects of each group of simulations. Since each influential factor has grouped simulations, this Chapter will also be divided according to these factors. Therefore, this chapter is divided into four subparts according to every influential factor, which are the following; the feeder loads value and its model, the motor load torque, the type of fault that caused the IO and the reclosing time.

Chapter 6

This Chapter is principally focused on show and discuss the field measurements. For the sake of brevity, this part will only show and discuss seven events from the available events in the database. It is worthwhile to note that this selection of the recorded events, provides a sufficiently representative sample to characterise the IO object of study.

Chapter 7

This chapter compares the simulations obtained in Chapter 5 with the field measurements from the real occurred events. The validation of this model transient will be carried out comparing both voltage and frequency separately. Additionally, an in-depth discussion regarding the appropriateness of the adopted model and its accuracy is presented.

Chapter 8

Chapter 8 assesses the voltage sag that occurs during the IO and details its main features. However, the crucial aspect of this Chapter is the characterisation of the non-constant magnitude of this sag. A validation between simulations and field measurements can fulfil the validity of the proposed voltage sag analytical expression.

Chapter 9

Chapter 9 is aimed at detailing the main characteristics of the new islanding detection tool that has been implemented to prevent the unintentional IO described in the previous Chapters. This tool has also been tested for both islanding and non-islanding events.

Chapter 10

Lastly, Chapter 10 contains the main conclusions derived from this thesis as well as includes some suggestions for future work.

1.7 References

[1.1] A. Gómez-Expósito, A. J. Conejo, and C. Cañizares, *Electric Energy Systems*, vol. 17. 2008.

[1.2] N. Care, "Distribution substations," *J. Inst. Electr. Eng.*, vol. 6, no. 66, pp. 348–351, 1960.

[1.3] K. P. Brand, J. Kopainsky, and W. Wimmer, "Topology-based interlocking of electrical substations," *IEEE Trans. Power Deliv.*, vol. 1, no. 3, pp. 118–126, 1986.

[1.4] M. H. J. Bollen, Y. Yang, and F. Hassan, "Integration of distributed generation in the power system - a power quality approach," *2008 13th Int. Conf. Harmon. Qual. Power*, pp. 1–8, 2008.

[1.5] E. N. Azadani, C. Canizares, and K. Bhattacharya, "Modeling and stability analysis of distributed generation," in *IEEE Power and Energy Society General Meeting*, 2012.

[1.6] H. L. Willis, *Power Distribution Planning Reference Book*. 2004.

[1.7] H. L. Willis and H. L. Willis, "Basic DG Cases: Schedule and Operating Characteristics," in *Distributed Power Generation*, 2018, pp. 385–407.

[1.8] V. A. Papaspiliotopoulos, G. N. Korres, V. A. Kleftakis, and N. D. Hatziargyriou, "Hardware-In-the-Loop Design and Optimal Setting of Adaptive Protection Schemes for Distribution Systems with Distributed Generation," *IEEE Trans. Power Deliv.*, vol. 32, no. 1, pp. 393–400, 2017.

[1.9] J. C. M. Vieira, W. Freitas, W. Xu, and A. Morelato, "An investigation on the nondetection zones of synchronous distributed generation anti-islanding protection," *IEEE Trans. Power Deliv.*, vol. 23, no. 2, pp. 593–600, 2008.

[1.10] J. A. Martinez-Velasco, *Power System Transients - Parameter Determination*. CRC Press, 2017.

[1.11] J. A. Martinez, B. Gustavsen, and D. Durbak, "Parameter Determination for Modeling System Transients-Part I: Overhead Lines," *IEEE Trans. Power Deliv.*, vol. 20, no. 3, pp. 2038–2044, 2005.

[1.12] IEEE, *IEEE Standard for General Requirements for Liquid-Immersed Distribution, Power, and Regulating Transformers*. 2016.

[1.13] J. A. Martinez and B. A. Mork, "Transformer modeling for low-and mid-frequency transients-a review," *IEEE Trans. Power Deliv.*, vol. 20, no. 2, pp. 1625–1632, 2005.

[1.14] W. L. A. Neves and H. W. Dommel, "Saturation Curves of Delta-Connected Transformers from Measurements," *IEEE Trans. Power Deliv.*, vol. 10, no. 3, pp. 1432–1437, 1995.

[1.15] J. A. Martinez, J. Mahseredjian, and B. Khodabakhchian, "Parameter Determination for Modeling System Transients--Part VI: Circuit Breakers," *IEEE Trans. Power Deliv.*, vol. 20, no. 3, pp. 2079–2085, 2005.

[1.16] Ł. Huchel and H. H. Zeineldin, "Planning the Coordination of Directional Overcurrent Relays for Distribution Systems Considering DG," *IEEE Trans. Smart Grid*, 2016.

[1.17] "ekor.RCI-Recloser.Ormazabal."[Online].Available: https://www.ormazabal.com/sites/default/files/descargas/ca-419-en-1603.pdf.

[1.18] S. Santoso and T. A. Short, "Identification of fuse and recloser operations in a radial distribution system," *IEEE Trans. Power Deliv.*, vol. 22, no. 4, pp. 2370–2377, 2007.

[1.19] P. Systems, R. Subcommittee, P. Systems, and E. Committee, *IEEE Recommended Practice for the Design of Reliable Industrial and Commercial Power Systems (Gold Book)*, vol. 1997. 1998.

[1.20] IEEE, *IEEE Buff Book 242™ IEEE Recommended Practice for Protection and Coordination of Industrial and Commercial Power System.* 2001.

[1.21] M. Pérez-Donsión and F. T. Oliveira, "Voltages in the network and inside industrial plants. Case of PSA-vigo," *Reneable and Energy Power Quality Journal*, vol. 17, pp. 567–572, 2019.

[1.22] M. Pérez-Donsión and S. Álvarez-Lorenzo, "Influence of the power quality instrument class on the accurate of the PQ measurement," *Renewable Energy and Power Quality Journal*, vol. 1, no. 4, pp. 391–395, 2006.

[1.23] A. Sendin, I. Berganza, A. Arzuaga, A. Pulkkinen, and I. H. Kim, "Performance results from 100,000+ PRIME smart meters deployment in Spain," in *2012 IEEE 3rd International Conference on Smart Grid Communications, SmartGridComm 2012*, 2012, pp. 145–150.

[1.24] J. Dixon, L. Morán, J. Rodríguez, and R. Domke, "Reactive power compensation technologies: State-of-the-art review," in *Proceedings of the IEEE*, 2005, vol. 93, no. 12, pp. 2144–2163.

[1.25] C. Gómez-Quiles, A. Gómez-Exposito, and A. De La Villa Jaén, "State estimation for smart distribution substations," *IEEE Trans. Smart Grid*, vol. 3, no. 2, pp. 986–995, 2012.

Chapter 2

State of the art

2.1 Motor bus transfers

The guiding principle of this thesis is the transient behaviour of the induction motor which following a disconnection, transiently, behaves as a generator. This transient has been object of study in the industry practice when a motor is transferred from one bus to another, see [2.1-2.3]. At the beginnings, what concerned most was the higher torques that occur during these bus transfers, in [2.3] a specific ratio (Volts per hertz) value of 1.33 has been established to achieve successful reclosing operations when carrying out these transfers.

Since these transfers were very fast (i.e., typically less than ten cycles), these studies considered that the mechanical motor speed remains constant during the process, which cannot be considered in the present study.

Other works concerning motor bus transfers have been focused on developing several tools to prevent these undesired out-of-phase reclosing operations, see for instance, [2.4-2.5]. Particularly, in [2.5], the main goal is to estimate the angle and voltage magnitude of the motor bus before the other source is connected.

In-depth research has been carried out by the IEEE Task Force, see the report in [2.6]. In motor bus transfers, two main type categories can be distinguished; closed transition or open transition, where the fundamental difference lies in the type the paralleling. Thus, the closing transition involves a brief paralleling between sources, whereas the open transition does not operate with both sources. Among the techniques in the closed transition, the hot-parallel transfer is the most common; meanwhile, within the open transition, the fast, residual and long-time procedures are widely implemented in the industry. Take into consideration that if the new source is not paralleled, the instant when the motor is disconnected is crucial. The period between the motor disconnection and the other source connection, the motor is acting as a generator.

Hot-Parallel transfer

In this technique, the new source feeds the motor before for the old source is tripped to avoid supply interruption, and during a brief period of time (between 100 ms and 200 ms), both sources supply energy to the motor. The main advantage of this method is that no transients occur, however, due to the paralleling, if a fault occurs during this transfer, this can overstress the system components due to the rise in the short-circuit power.

Fast simultaneous transfer

This technique belongs to the open transition method and is based on tripping the old source and reconnect the new one at the same instant. Due to the delay between both CBs, either a brief unintentional paralleling or brief islanding may occur depending on which breaker trips first. In this technique, the deviation between voltage, frequency and angle between sources used to be small since two stiff sources are reclosed. Among the unsupervised reclosing operations, this bus transfer technique is the fastest one.

Fast sequential transfer

The operating principle of this technique is very similar to the previous one, nevertheless, in this technique, the new source is tripped, and as soon as these CB has started the process (i.e., typically one or two cycles), the new source CB is connected. Thus, in this method, a supervised command is implemented to track the state of the CB of the first source. However, if the reclosing is unsupervised, several issues may occur, see the results obtained in [2.3]. On the other hand, if the process is supervised by a closed command, which can dynamically block the fast transfer just after the main source (i.e., the first one) is disconnected, even if a fault occurs during the process, a change in angle or voltage is detected.

Residual transfer and long-time transfer

This technique aims to wait until the motor bus voltage falls below a preset value, typically 0.25 pu; therefore, the reclosing transient will be similar to the one experienced in a motor energisation. In this technique, the angle is not taken into consideration. This technique is the third faster among the open transition methodologies. The main advantage is that no commands or advanced tools are required to fulfil such a task. However, the main disadvantage of this reclosing procedure is the fact that the industrial process is almost stopped; therefore, the motors may need a restart. Note also, that depending on the motor inertia, the load torque and its type, voltage in the motor bus will decay slowly, which will make the process time-consuming. As an example, if no loads are connected to the same busbar, and the motors are rotating with low load torque, this process may take between seconds and a few minutes.

In-phase transfer

This technique offers the possibility of avoiding a fast transfer as well as avoid a supply interruption during a residual or even long time reclosing procedure. Thus, the command to reclose the CB and connect the motor bus to the new source waits until 0 degrees of phase coincidence regardless of the slip frequency or the voltage magnitude difference (i.e., the difference between the motor bus and the new source). Since the motor bus frequency is decaying following its de-energization, this technique requires advanced tools to measure the angle in both sides. Here, CBs are assumed to open in four-cycles, and a variance of one cycle can produce errors in the predicted angle. Therefore, due to the fact that CBs interrupt the alternating current (AC) at zero crossing, depending on the rate-of-change-of-frequency (ROCOF) in the busbar, a half cycle or even one cycle delay can produce an angular error. Fortunately, the angular difference that can occur during this process is assumed as an acceptable error, see [2.3]. A practical discussion regarding how to carry out as well as practical experiences of how to carry out such transfers is done in [2.6].

2.2 Islanding operations in DNs

2.2.1 Overview

An islanding operation can be defined as a parallel operation between the main utility and an isolated area due to either a fault or a maintenance task. Several categories may be used to classify such operations; the first distinction is between intentional and unintentional; the second one is referred to long term and short term. When a part of the grid is isolated, the mismatch between the power delivered by the sources and the local loads that remain in the isolated part plays a pivotal role in the purpose of maintaining system stability within the islands [2.7]. According to IEEE Std. 1547 during unintentional islanding operations, distributed generation (DG) must be disconnected within 2 s for slight voltage and frequency deviations, and in 0.16 s for significant variations [2.8]. Several detailed studies have been carried out to prevent islanding operations in DNs in the presence of DG; see. Several authors have studied (intentional or unintentional) islanding operations under different contexts; see, for instance, [2.9-2.10].

2.2.3 Intentional islanding operations

This type of IO has been object of study in several research articles [2.11-2.12], where the island is created utilising a multi-machine system and considering a wide range of generators. Mostly, these islands have been designed to maintain stability and avoid catastrophic blackouts for wide-area power systems. Stability is a crucial issue in wide-area power systems, in [2.13], the power system stability definition and classification is done. Figure 2.1 shows the main categories and magnitudes that are analysed in power systems stability. From [2.13], it is quite clear that each contingency has to be analysed separately, however, it is also true that a large contingency in one magnitude can produce a collapse to another one. For instance, even though frequency and voltage stabilities are analysed separately, major disturbances in one variable may lead to another variable collapse and as a consequence, entail a major blackout, an excellent report can be found in [2.14]. As stated before, the main aim of the intentional islands is to avoid major blackouts, for example, in [2.15] the causes of several occurred blackouts are thoroughly investigated. The equilibrium between active-power generation and active-power loads has to be maintained and is a crucial indicator (minimum power imbalance), nonetheless, other factors such as generator coherency has to be also taken into account [2.16-2.17].

Although the intentional islands have been thoroughly investigated for wide area, in the recent years the investigation of intentional islanding operations to avoid interruptions and enhance the distribution networks reliability is gaining prominence [2.18-2.19]. In these situations, the distributed generation allocated along the distribution networks is of utmost importance.

That being said, a brief recall of the stability concerning the main magnitudes are detailed down below:

Rotor angle stability

The *rotor angle stability* is the generators ability to remain in synchronism after being affected by a disturbance. The equilibrium between the electromagnetic torque and mechanical torque is the main concern to maintain the generators in synchronism. During a disturbance, an imbalance between torques occur, thereby, depending on factors such as; generators inertia, the type of fault, the clearing time, and the severity of the disturbance itself, may lead generators to lose synchronism. Transient stability has been widely analysed in [2.20]. Recently, the proliferation of renewable energies such as solar farms or wind parks, have reignited a fruitful debate about

the effects of such generators into the traditional synchronous system, see [2.21-2.22]. Depending on the disturbance severity, we have the following classification:

1. Small disturbances of angle stability (e.g., either inter-are or local oscillations).
2. Transient stability (e.g., due to large disturbance).

The first distinction has been assessed in [2.23], whereas the second type has been object of study in [2.24-2.25].

Frequency stability

The *frequency stability* is the ability to maintain stable frequency following an imbalance between the amount of generation and load. Whereby, deviations between active power generation (P_G) and active power loads (P_L) can be absorbed by the kinetic energy stored in the rotor-synchronous generators with inertia constant (H) and the damping constant (D) respectively. In electrical power systems, a frequency deviation is highly linked with lack of generation reserve [2.26]. Depending on its duration, frequency disturbances can be either short term or long term. Crucially, a three-stage procedure is established to address a frequency deviation, this procedure is detailed in chapter 9 of [2.13], and a brief resume is described as follows:

- First control: In this group, little deviations are considered and normally the required times for taking actions is between 2 and 20 seconds. This control is not responsible of restoring the reference value of the frequency, the reference is kept constant. This response is based on local actions.
- Second control is related to wide-area with a multi-machine system and involves the operation of the generation dispatching. The timing for this control is between 20 seconds and 2 minutes. The aim of this control is to keep the balance between generation and load.
- The tertiary control is responsible of address large frequency deviations. This control can order an increase or decrease generation reference to all generation levels. Normally, this control, takes place when the first and the second failed to restore the system frequency. Furthermore, this control considers not only active-power readjusting but also voltage and reactive-power control.

More details about wide-area frequency control in Spain can be found in [2.28].

Voltage stability

Voltage stability is highly linked with the reactive power, thus, imbalances in reactive power between generators and loads may evolve to voltage instability. It is seen in several studies that following a large disturbance, injections of reactive power (i.e., it can be either inductive or capacitive) helped the system to recover. As stated in the introduction, in some particular occasions, voltage instability can cause frequency excursions, see [2.29-2.30].

Depending on the severity of the occurred contingency and its duration, voltage stability can be classified in two categories; small disturbance and large disturbance. Commonly, small disturbances are related to insufficient damping of oscillations or even a little oscillation of the prime mover, especially if there is no governor or the excitation is constant system. Meanwhile, the largest disturbances are mainly due to short-circuits where the system is not capable of supplying the amount of reactive power, this assessment is done in [2.31].

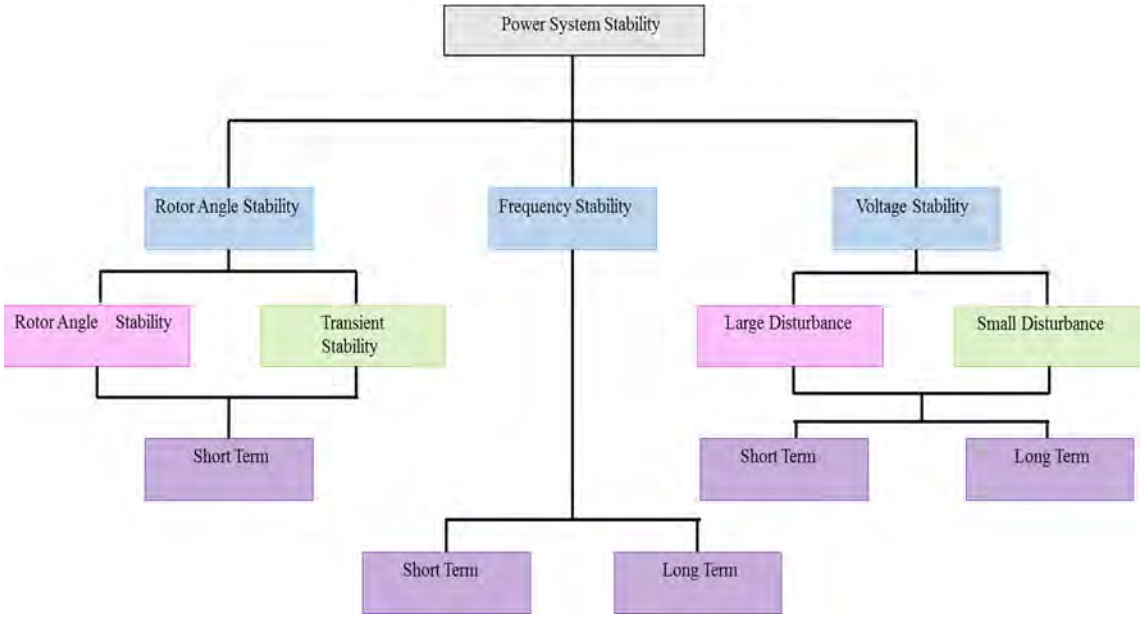

Figure 2.1: Power system stability classification.

2.2.4 Unintentional islanding operations

Unlike the IOs evaluated in the previous section, this part is aimed at describing the ones that are not planned. Mainly, non-planned islanding operations occur at the distribution networks when the distributed generation (DG) units remain energising the grid after the main CB has opened the circuit. Typically, in order to prevent these islands and avoid protective misscoordinations, DSO codes compel the DG resources to trip if a fault occurs.

Based on the previous premise, an essential aspect of any ID study is the capability of the protective devices to detect the island quickly; commonly, within 200 to 400 ms after the loss of mains have occurred [2.32]. The list of hurdles in case of failure to trip may include; PQ disturbances [2.33] (e.g., frequency and voltage out of range), a safety hazard for the network personnel, or a damaging effect due to the out-of-phase reclosing. The increasing demand for detecting IOs have led to implementing islanding detection (ID) methods in coordination with the electric power system protection. Since the survivability of these islands depends on the mismatch between generation and load, in cases with low imbalances, frequency and voltage will remain stable. Therefore, this fact makes the task of detecting the island more challenging. In Section 2.3, a review of the available techniques to identify these undesirable operations is done.

It is essential to highlight the fact that the IO that is assessed in the present thesis falls within this type (i.e., unintentional IO). As mentioned earlier, it occurs when the utility CB opens the circuit, and the induction motors act as generators energising the grid until this CB recloses to restore the supply (e.g., Typically between 0.5 and 1 s).

2.3 Power quality

2.3.1 PQ Fundamentals

Although the term Power Quality is widely used, several definitions can be found in the literature about this concept. Thus, the term power quality is defined by the IEEE in the std. 1100-2005 [2.34] and IEC has also defined this concept in [2.35]. However, *M.H.J Bollen* [2.36], established the following definitions:

- "The quality of voltage can be defined as the variation with regards its ideal form (in sinusoidal waveform and constant amplitude)"
- "The quality of current can be defined as the variation with regards its ideal form (in sinusoidal waveform and constant amplitude)"
- "The power quality encompasses both voltage and current quality"

Having said all that, the quality of power is seen as a matter of reliability and quality in terms of the electrical power that is delivered to the customer. Each deviation from a pre-established value, which is understood as an acceptable, is considered a disturbance.

Over the last decade, power quality (PQ) attracted the attention of the scientific community, while presently, monitoring PQ disturbances has become a crucial task for distribution operators (DSOs) being one of the issues of major concern. Since the DNs supply power to the costumers, monitoring the occurring events has become essential; therefore, the smart meters allocated at each customer node will play a pivotal role [2.37]. Regarding the measurement and monitoring of PQ disturbances, several standards have been published within the EN-61000 series; these standards fall within the electromagnetic compatibility field. Particularly, EN61000-4-30 defines how to measure PQ disturbances and makes a distinction in the measurement accuracy. A relevant summary and interpretation of these standards are given in References [2.38].

Furthermore, other research has been focused on how to identify the different type of disturbances from occurred events; for instance, see references [2.39-2.40]. Once PQ disturbances are detected, classifying them and compressing them into separate events is a challenging task and requires advanced tools; see references [2.41-2.42]. Some authors have considered fuzzy logic or neural networks to classify them [2.43], some others proceed based on clustering the data depending on its origin from offline and prescribed events, and lastly, certain studies have focused on real-time classification, which results in a successful classification; for instance, see reference [2.44].

It is understood that PQ is one of the major concerns for DSOs, and probabilistic studies have been carried out to evaluate the grid reliability with statistical and stochastic assessments. Such studies have concluded that protective devices and the weakness of the grid, as well as the type of loads, are crucial factors when carrying out PQ studies. Besides, with the growing interest in distributed generation (DG) and smart grids, their influence on the PQ field is currently under investigation, see [2.45-2.46].

2.3.2 PQ disturbances classification

Before a classification is done, four parameters such as; frequency, amplitude, waveform and symmetry can serve as reference frames for the following classification. All PQ disturbances are summarized in the standard EN-50160, where current disturbances are not considered. This standard defines disturbances as two types: (i) continuous phenomena (e.g., long-time disturbances in the range between ms and minutes), such as voltage drops, voltage swells or frequency oscillations; and (ii) short-duration disturbances such as voltage interruptions, voltage

Table 2.1: Power Quality disturbances summary.

Disturbance Category	**Subcategory**	**Duration**	**Amplitude**
Transients	Surge	50 ns -1 ms	-
Transients	Oscillating	0.3 ms – 50 ms	-
Short duration disturbances	Interruptions	10 ms – 1 m	<0.1 pu
Short duration disturbances	Voltage sags*	10 ms – 1 m	0.1 - 0.9 pu
Short duration disturbances	Voltage swells*	10 ms – 1 m	1.0 - 1.8 pu
Long duration disturbances	Long interruptions	Steady-state	0 pu
Long duration disturbances	Under-voltages	Steady-state	0.1 - 0.9 pu
Long duration disturbances	Over-voltages	Steady-state	1.1 - 1.2 pu
Voltage unbalance	-	Steady-state	0.5 - 2 %
Waveform distortion	DC component	Steady-state	0 - 0.1 %
Waveform distortion	Harmonics	Steady-state	0 - 20 %
Waveform distortion	Interharmonics	Steady-state	0 - 2.0 %
Waveform distortion	Notches	Steady-state	-
Waveform distortion	Noise	Steady-state	0 - 1 %
Flicker	-	Flashing	-
Frequency deviation	-	< 10 s	+/- 10 Hz

* See an example of both sag and swell in Figure 2.2

sags, voltage swells, and over-voltage transients (e.g., short-term disturbances in the range between μs to ms). These disturbances are also summarised in Table 2.1.

Among all PQ disturbances, voltage sags have been the object of study for many years. At first, voltage sags were assumed to be rectangular. Afterwards, it was demonstrated that this was not strictly true, and the type of recovery, as well as the phase-angle-jump, played a significant role [2.47]. It is relevant to highlight the characterisation done by *M.H.J. Bollen* in [2.48]. Furthermore, immunity tests and studies of electrical devices' behaviour towards voltage sags have been thoroughly analyzed in Reference [2.50], where the effects of the voltage sags are evaluated. In this direction, several standards have been published; for instance, EN 61000-3-2 (limits for harmonic current emissions, less than 16 A), EN-61000-4-34 (immunity test for high current equipment, more than 16 A), and voltage sags with statistical results are summarized in IEC-61000-2-8. Considering that electrical device sensitivity is an aspect of utmost importance, immunity tests for voltage sags and interruptions are still under study.

Even though standard indices for reliability such as standard average interruption frequency index (SAIFI), standard average interruption duration index (SAIDI) or the reliability curves published by the information technology industry council (ITIC) have been defined, each country has its own regulations regarding the number of interruptions or their duration [2.51]. To deal with voltage sags effects, well-known equipment such as dynamic voltage restorers or uninterruptible power supply devices are used [2.52].

Mainly, the origin of voltage sags in DNs and transmission networks (TNs) are faults; given their random nature in time and location, their magnitude, type and recovery can change along the grid. A fault in the system can produce either a voltage sag or an interruption, depending on where the fault originates; that is, depending on the type of network and configuration which is feeding the fault. Thereby, if several lines are feeding the fault, and if we assume that each one has its own CB, the faulted line/section will experience an interruption, whereas the adjacent section will experience a voltage sag.

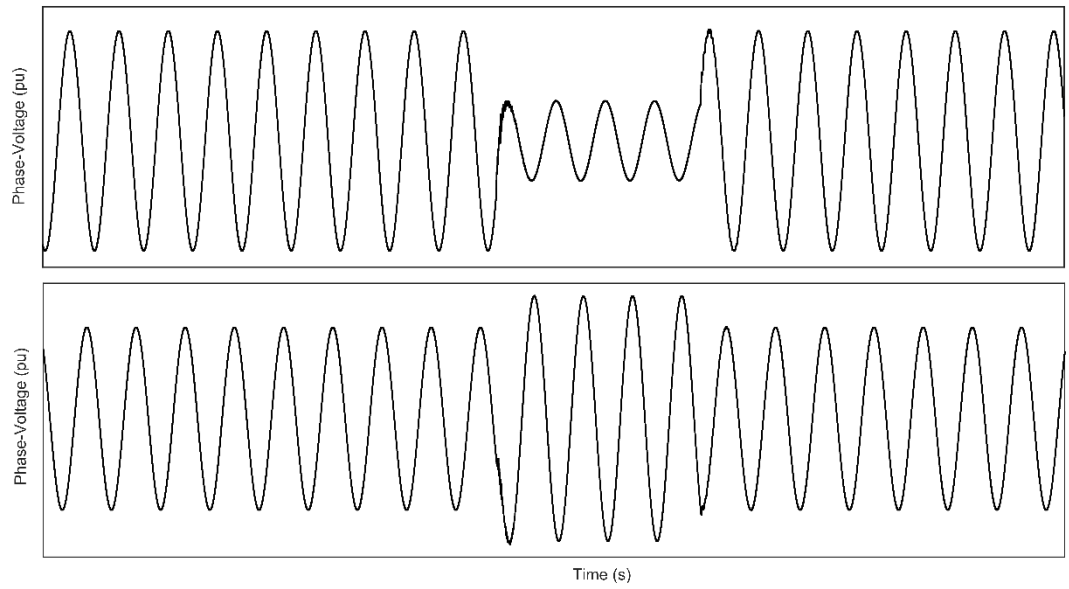

Figure 2.2: An example of voltage sag and voltage swell.

2.3.3 Voltage sag features

Since voltage sags are a short-duration reduction of the root-mean-square (RMS) voltage, it can be said that their characterisation depends on (i) their magnitude (i.e, voltage characteristic), (ii) their duration, (iii) their type, (iv) the type of recovery, (v) the phase-angle-jump, and (v) their origin. Nevertheless, the origin of the voltage sag will, in fact, dictate its type and its recovery. Moreover, voltage sags can change their type and become evolutionary voltage sags because the fault conditions can change (i.e., faults can evolve from one type of fault to another during the same event). Other parameters such as the point-on-wave in both the initiation and the recovery have been the object of study in Reference [2.53]. Besides this, an interesting analysis is done by Bastos et al. in Reference [2.54].

On the other hand, the data extracted from a measured sag are gained from the sag type characteristic voltage (i.e., the complex voltage) and by the positive-negative factor as published in References [2.55]. Particularly, according to Reference [2.56], there is a need to compress the three-phase voltage sag event into a single event, which is still under study by the IEEE project group P1159.2. Furthermore, a two-type contribution has been made in Reference [2.57]. To obtain the main characteristics from a measured voltage sag, relevant methods are available in the literature, among which are the following:

1. Complex voltage: This method uses symmetrical components to evaluate the type of sag; thus, comparing the angle between the definite sequence and the negative sequence, the sag type is obtained. The voltage characteristic is computed with the complex sum and difference of the positive and negative sequence-voltage.

2. RMS voltage: These algorithms use the RMS voltage as input; thus, the computation of the six RMS values of the phase-to-phase and phase-to-neutral voltages is proposed. Therefore, the voltage characteristic, the voltage sag type and the positive-negative factor are extracted from these six voltage time-domain values.

3. Advanced features: Within this group, a considerable number of studies have been published, and the main aim is to extract features from the voltage waveform considering a wide range of measurements and classify them with an algorithm that helps to compress the data. From all studies, the most appropriate methods are summarised in Reference [2.58]. Furthermore, *Cai et al.* in Reference [2.59] developed a mapping strategy for multiple disturbances.

In Reference [2.60], the authors focus on voltage sag characterisation; a general distinction is made considering balanced and unbalanced voltage sags originating from faults (i.e., short-circuits). Nonetheless, in this study, other sources of voltage sags, such as induction or synchronous motors during their starting process, are considered. Moreover, further classification is included in Reference [2.48], where the voltage sag produced during transformer energisation is evaluated.

Previously, in faults originated by short-circuits, between the fault inception and the fault recovery, the voltage characteristic has been considered constant, and therefore the voltage sag has been considered rectangular; see Figure 1. However, this voltage characteristic may not be constant during the voltage sag and non-rectangular voltage sags may occur; for instance, see Figure 3 of Reference [2.48]. One reason for this voltage characteristic increasing or decreasing during the fault could be that the impedance seen from the source changes during the disturbance. Another cause for a decrease in the residual voltage during a non-rectangular voltage sag can occur in the presence of IMs. In such a way, immediately following a fault, the IMs tend to contribute towards the fault (e.g., roughly one or two cycles) so that the drawn current decreases in time and the voltage value also decreases; this phenomenon is thoroughly detailed in Reference [2.61].

To summarize, the studied sources of voltage sags are listed as follows:

- Short-circuits (constant retained voltage);
- Motors start—either synchronous or induction motors (non-constant retained voltage);
- Transformer energization (non-constant retained voltage);
- Short-circuits in the presence of IMs (non-constant retained voltage);

This subsection will show the main characteristics of voltage sags graphically in order to compare these parameters with the proposed voltage sag of the subsequent Section 8 where a novel voltage sag topology will be presented. Although the voltage sag representation of Figure 1 is not innovative, this figure and its analysis are necessary to highlight the improvement made with the proposed voltage sag as the object of study.

In Figure 2.3, the three principal magnitudes are shown in different plots. The first plot depicts the phase voltage waveform of the faulted phase. In this waveform, the beginning and the end of the fault can be observed as well as the point-on-wave in both the initiation and clearing (these two points are within two circles in the voltage waveform). The retained voltage—that is, the magnitude of the voltage sag—is shown in the second plot of Figure 2.3, and lastly, the phase-angle-jump is observable in the third plot of the same figure. For this particular event, the duration is 300 ms, and it originated due to a single-line-to-ground fault (SLG), which belongs to voltage sag type A in the characterization done by *M.H.J Bollen* in [2.36], the retained voltage is 0.12 pu, and the phase-angle-jump is −30 degrees, which means that the grid is predominantly inductive.

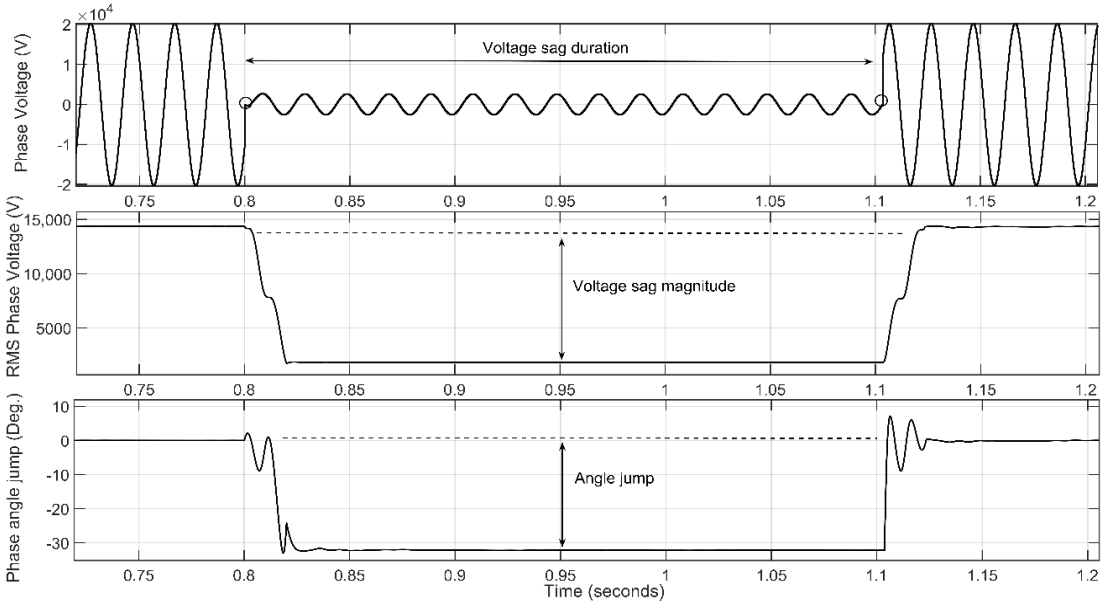

Figure 2.3: Main characteristics of a voltage sag.

2.4 Islanding detection methods

2.4.1 The need for detecting the islanding operations

As has been pointed out previously, if a source continues energising a portion of the electrical grid after CB has cleared a fault and it is acting in parallel with the main grid, this is known an IO. The DSO intends to avoid these scenarios. If this IO is not identified, the following issues can occur: (i) the power quality during the island is not guaranteed, (ii) the out-of-phase reclosing due to the mismatch between the frequency and voltage magnitude between sources (i.e., the main grid and the island), (iii) the protective misscoordination because the DG can continue feeding a permanent fault following the CB action and lastly, (iv) the grid remains energised which becomes a significant hazard for the personnel. Due to the mentioned previous issues, there is a need to detect the islanding operations and disconnect these sources as soon as possible. That is the reason why utilities compel to disconnect the DG in case any disturbance occurs. The subsequent subsection defines the general classification concerning ID methods. Note that the currently available methods are only posed for scenarios with DG, which differs from the present case where large induction motors cause the IO.

2.4.2 General classification

As exposed above, the need to identify these IO, fostered the implementation of the so-called ID methods, which are targeted at tripping the sources responsible for such IO. Generally, ID methods can be classified into three main groups: (i) passive-based methods, (ii) active-based methods, and (iii) communication-based methods.

The first group is based on local measurements. The priority is to prevent false-triggering operations. The most challenging situation arises when the relation between the power of the source and the power load demand is near balanced. The principal protective functions that are involved in these methods are fundamentally: the rate-of-change of frequency protection (ROCOF), the rate-of-change of voltage (ROCOV), under/over voltage (UVP/OVP), under/over frequency (UFP/OFP), the rate-of-change of active and reactive power (ROCOP/ROCOQ), the

vector surge (VS) relay, and the harmonic distortion deviation; these methods have been implemented in the following works [2.62-2.64].

The second group is aimed at detecting IO by injecting signals into the system (e.g. from the DN substation to the target islanded source). This technique has generated successful results; see, for instance, [2.65]. The weakest aspect of these methods falls in the complexity of the required equipment and its impact on the grid PQ.

The third group uses several technologies (e.g., optic-fibre, power line communications, GPRS, etc.) to communicate the substation-feeder CB with the interconnection CB located at the PCC of the target DG. If communications are feasible, it is an excellent option to consider. Moreover, it is widely extended in practical industry applications.

2.4.3 Passive-based methods

This section reviews the main principles of some passive-based ID methods. It is essential to mention that this topic has been the subject of many other research studies; see for instance [2.66-2.67]. In general, the main disadvantage of these methods is observed when the amount of generation and load are close, because the system can remain stable, therefore frequency and do not exceed the acceptable thresholds.

***Under/Over Frequency* (81*U*/81*O*)**

Frequency values are usually captured every cycle, at voltage zero-crossing. The classical frequency thresholds for a 50 Hz system are 50.5 Hz for over-frequency values and 49.75 Hz for under-frequency values. As a rule of thumb, relays generate a trip signal with a delay after any of these thresholds has been exceeded. Both under/over frequency protection can be implemented using either a time curve or a fixed time. The tripping time can be adjusted between 0.16 s for the highest deviation, and 300 s for the minimum deviation [2.68]. For deviations beyond 95% of rated the frequency, a 0.16 s fixed time delay is used. Slight frequency deviations in transmission levels may involve frequency nuisance tripping with this method.

Under/Over Voltage (27/59)

Voltages are measured to obtain the RMS value of the phase-to-ground voltages. Commonly used voltage thresholds are set to 1.2 pu for over-voltages and 0.8 pu for under-voltages. Voltage deviation protection can be set using either a time curve or a fixed time. Typically, the delay is set to 100 ms for both over- and under-voltage protection. Nonetheless, for voltages between 1.1 pu and 1.2 pu, the time delay is set to 500 ms. A succinct assessment concerning voltage curves for ID detection is presented in [2.69].

ROCOF* (*81R*)/*ROCOV

ROCOF and ROCOV are methods based on the derivative with respect to time of respectively frequency and voltage measurements. Usually, *df/dt* is measured over a few cycles, generally between 2 and 50, and its value is sent to a low-pass filter to remove the high-frequency harmonics. A value of 1.2 Hz/s is seen as an inadmissible frequency rate of change. Nevertheless, the value typically ranges from 0.1 to 3.5 Hz/s; see, for instance, [2.70-2.71]. A minimum voltage supervision is also implemented in ROCOF relays, commonly 0.85 pu.

Although measurements are available for a minimum of four cycles, false tripping could occur if only four cycles were selected. Typically, 7-cycle supervision is considered; for a 50 Hz power frequency, this is a time delay of 140 ms, a widely used setting in ROCOF relays. Voltage derivative will be similarly computed as for the ROCOF relay. A typical rate-of-change of 250

V/s is used, with a time delay of 100 ms; however, as for the ROCOF, a 140-ms delay will be used in the present work for this derivative.

***ROCOP/ROCOQ* (32*R*)**

The rate-of-change in both active and reactive powers is a reasonable indicator for islanding detection, considering that, except for a balanced situation, it competes favourably for a quick IO detection.

To sum up, in this subsection, the most common magnitudes used in the passive-based methods have been defined, however, other parameters are also used, see for instance [2.72].

2.4.4 Active-based methods

These methods are based on the injection of a signal at the substation once the main CB has opened, in order to indicate that the CB located at the PCC of the DG has to be tripped. These techniques have high feasibility in detecting islanding operations; nevertheless, these methods jeopardise the power quality of the grid because of the harmonic and sub-harmonic components. A widely known method is the power line communication (PLC), where the signal is transmitted through the power wires. On the other hand, other techniques such as ripple control, waveform shift technique or waveform distortion techniques have been previously used as active methods. Additionally, it has to be highlighted that successful results were achieved by applying these methods in the presence of synchronous-based DGs in [2.73-2.74].

2.4.5 HIDM Overview

Once the currently available methods for ID for DG units have been described, it seems appropriate that a new tool is required to prevent the IO object of study. Since the IO object of study is not caused by DG but due to large induction motors, a comprehensive evaluation regarding which of the parameters mentioned above would be useful to identify such IO. As has been stated above, the passive-based ID methods can lead to missoperations in near balanced islands. Thus, the same situation may occur for the present case if voltage and frequency remain within the thresholds, which evidence that another criterion is required. Therefore, this thesis proposes a hybrid tool which merges some of the previously defined parameters used in passive-based ID with an additional directional criterion to assure absolute efficiency in detecting IO.

Note that some of the passive-based methods cause untimely tripping due to events that are not likely to provoke an islanding operation (e.g., faults in MV neighbour feeders, induction motor starting, capacitors switching, faults at the transmission network or even frequency excursions). The hybrid islanding detection method has been created to prevent both islanding and non-islanding methods. This islanding detection tool will be evaluated in detail in the subsequent Chapter 9.

2.5 Conclusions

To conclude this Chapter, it is worth pointing that the transient behaviour of the motor during these bus transfers, provides a general idea about the transient object of study in this thesis. Nonetheless, this research has gone beyond. Indeed, the islanding operation caused into the DN and its effects have not been evaluated yet. On the other hand, the motor bus transfers techniques

defined in this section establishes a starting point for our research as well as help the reader in understanding the islanding operation explored in this thesis.

2.6 References

[2.1] M. R. Iravani *et al.*, "Modelling and analysis guidelines for slow transients: Parti torsional oscillations; transient torques; turbine blade vibrations; fast bus transfer," *IEEE Trans. Power Deliv.*, 1995.

[2.2] S. S. Mulukutla and E. M. Gulachenski, "A Critical Survey of Considerations in Maintainingprocess Continuity During Voltage Dips While Protecting Motors with Reclosing and Bus-Transfer Practices," *IEEE Trans. Power Syst.*, vol. 7, no. 3, pp. 1299–1305, 1992.

[2.3] T. R. Beckwith and W. G. Hartmann, "Motor bus transfer: Considerations and methods," *IEEE Trans. Ind. Appl.*, vol. 42, no. 2, pp. 602–611, 2006.

[2.4] P. K. Muralimanohar, D. Haas, J. R. McClanahan, R. T. Jagaduri, and S. Singletary, "Implementation of a Microprocessor-Based Motor Bus Transfer Scheme," *IEEE Trans. Ind. Appl.*, vol. 54, no. 4, pp. 4001–4008, 2018.

[2.5] M. V. V. S. Yalla, "Design of a High-Speed Motor Bus Transfer System," *IEEE Trans. Ind. Appl.*, vol. 46, no. 2, pp. 612–619, 2010.

[2.6] J. Bumworth *et al.*, "Motor bus transfer," *IEEE Trasactions Power Deliv.*, vol. 8, no. 4, pp. 1747–1758, 1993.

[2.7] S. Li, K. El-Arroudi, G. Joós, and A. J. Rodolakis, "Islanding protection of multiple distributed resources under adverse islanding conditions," IET Gener. Transm. Distrib., vol. 10, no. 8, pp. 1901–1912, 2016.

[2.8] IEEE Standards Coordinating Committee 21, IEEE Application Guide for IEEE Std 1547™, IEEE Standard for Interconnecting Distributed Resources with Electric Power Systems, no. April. 2009.

[2.9] Y. Chen, Z. Xu, and J. Østergaard, "Security assessment for intentional island operation in modern power system," Electr. Power Syst. Res., vol. 81, no. 9, pp. 1849–1857, 2011.

[2.10] H. H. Zeineldin and J. L. Kirtley, "A simple technique for islanding detection with negligible nondetection zone," IEEE Trans. Power Deliv., vol. 24, no. 2, pp. 779–786, 2009.

[2.11] J. Quiros-Tortos, M. Panteli, V. Terzija, and P. A. Crossley, "On evaluating the performance of intentional controlled islanding schemes," IEEE Power Energy Soc. Gen. Meet., 2013.

[2.12] D. Hill, "Definition and Classification of Power System Stability," IEEE Trans. Power Syst., pp. 1–15, 2004.

[2.13] A. Gómez-Expósito, A. J. Conejo, and C. Cañizares, Electric Energy Systems, vol. 17. 2008.

[2.14] M. H. Oboudi, R. Hooshmand, and A. Karamad, "A feasible method for controlled intentional islanding in microgrids based on PSO algorithm," Swarm Evol. Comput., vol. 35, pp. 14–25, 2017.

[2.15] N. D. Hatziargyriou et al., "Causes of the 2003 Major Grid Blackouts in North America

and Europe , and Recommended Means to Improve System Dynamic Performance Causes of the 2003 Major Grid Blackouts in North America and Europe , and Recommended Means to Improve System Dynamic Perform," vol. 20, no. February 2016, pp. 1922–1928, 2005.

[2.16] L. Ding, F. M. Gonzalez-Longatt, P. Wall, and V. Terzija, "Two-step spectral clustering controlled islanding algorithm," IEEE Trans. Power Syst., vol. 28, no. 1, 2013.

[2.17] J. Quiros-Tortos, P. Demetriou, M. Panteli, E. Kyriakides, and V. Terzija, "Intentional Controlled Islanding and Risk Assessment: A Unified Framework," IEEE Syst. J., no. August 2005, 2017.

[2.18] P. Fuangfoo, W. J. Lee, and M. T. Kuo, "Impact study on intentional islanding of distributed generation connected to a radial subtransmission system in Thailand's electric power system," IEEE Trans. Ind. Appl., vol. 43, no. 6, pp. 1491–1498, 2007.

[2.19] M. H. Oboudi, R. Hooshmand, and A. Karamad, "Feasible method for making controlled intentional islanding of microgrids based on the modified shuffled frog leap algorithm," Int. J. Electr. Power Energy Syst., 2016.

[2.20] P. Kundur et al., "Definition and Classification of Power System Stability IEEE/CIGRE Joint Task Force on Stability Terms and Definitions," IEEE Trans. Power Syst., vol. 19, no. 3, pp. 1387–1401, 2004.

[2.21] S. M. Nesci and J. C. Gómez, "Study of the out-of-phase connection of doubly fed induction generators," 2010 IEEE ANDESCON Conf. Proceedings, ANDESCON 2010, pp. 1–6, 2010.

[2.22] J. S. K. Leung, D. J. Hill, and G. H. Zhang, "Coordinated stability control," IET Gener. Transm. Distrib., vol. 3, no. 1, p. 38, 2009.

[2.23] N. Amjady and S. A. Banihashemi, "Transient stability prediction of power systems by a new synchronism status index and hybrid classifier," IET Gener. Transm. Distrib., vol. 4, no. 4, p. 509, 2010.

[2.24] F. Milano and I. Dassios, "Small-Signal Stability Analysis for Non-Index 1 Hessenberg Form Systems of Delay Differential-Algebraic Equations," IEEE Trans. Circuits Syst. I Regul. Pap., vol. 63, no. 9, pp. 1521–1530, 2016.

[2.25] M. Anghel, F. Milano, and A. Papachristodoulou, "Algorithmic construction of lyapunov functions for power system stability analysis," IEEE Trans. Circuits Syst. I Regul. Pap., vol. 60, no. 9, pp. 2533–2546, 2013.

[2.26] C. A. Cañizares, N. Mithulananthan, and F. Milano, "Linear performance indices to predict oscillatory stability problems in power systems," IEEE Trans. Power Syst., vol. 19, no. 2, pp. 1104–1114, 2004.

[2.27] G. Delille, B. François, and G. Malarange, "Dynamic frequency control support by energy storage to reduce the impact of wind and solar generation on isolated power system's inertia," IEEE Trans. Sustain. Energy, vol. 3, no. 4, pp. 931–939, 2012.

[2.28] "El Sistema Eléctrico Español," *Red Eléctrica España*"https://www.ree.es/es/. [2.29] D. J. Hill, "Nonlinear dynamic load models with recovery for voltage stability studies," IEEE Trans. Power Syst., vol. 8, no. 1, pp. 166–176, 1993.

[2.30] T. Zabaiou, L.-A. Dessaint, and I. Kamwa, "Preventive control approach for voltage stability improvement using voltage stability constrained optimal power flow based on static line voltage stability indices," IET Gener. Transm. Distrib., vol. 8, no. 5, pp. 924–934, 2014.

[2.31] M. Z. El-Sadek, "Voltage Instabilities Subsequent to Short-circuit Recoveries," Electr. Power Syst. Res., vol. 21, no. 1, pp. 9–16, 1991.

[2.32] D. M. Laverty, R. J. Best, and D. J. Morrow, "Loss-of-mains protection system by application of phasor measurement unit technology with experimentally assessed threshold settings," IET Gener. Transm. Distrib., vol. 9, no. January 2014, pp. 146–153, 2015.

[2.33] A. Serrano-Fontova, P. C. Torrens, and R. Bosch, "Power Quality Disturbances Assessment During† Unintentional Islanding Scenarios. A Contribution to Voltage Sag Studies," Energies 2019, Vol. 12, Page 3198, vol. 12, no. 16, p. 3198, Aug. 2019.

[2.34] P. Systems and E. Committee, IEEE 1100:2005 - IEEE Recommended Practice for Powering and Grounding Electronic Equipment, vol. 1999. 2006.

[2.35] IEC 61400-21 - Measurement and assessment of power quality characteristics of grid connected wind turbines, vol. 3, no. 2. 1960.

[2.36] M. H. Bollen, *Understanding Power Quality Problems*. Wiley - IEEE Press, 2000.

[2.37] A. Sendin, I. Berganza, A. Arzuaga, A. Pulkkinen, and I. H. Kim, "Performance results from 100,000+ PRIME smart meters deployment in Spain," in 2012 IEEE 3rd International Conference on Smart Grid Communications, SmartGridComm 2012, 2012, pp. 145–150.

[2.38] A. Broshi, "Monitoring power quality beyond EN 50160 and IEC 61000-4-30," in 2007 9th International Conference on Electrical Power Quality and Utilisation, EPQU, 2007.

[2.39] M. B. I. Reaz, F. Choong, M. S. Sulaiman, F. Mohd-Yasin, and M. Kamada, "Expert system for power quality disturbance classifier," IEEE Trans. Power Deliv., vol. 22, no. 3, pp. 1979–1988, 2007.

[2.40] O. Florencias-Oliveros, A. Aguera-Perez, J. J. Gonzalez-De-La-Rosa, J. C. Palomares-Salas, J. M. Sierra-Fernandez, and A. J. Montero, "Cluster analysis for Power Quality monitoring," in 2017 11th IEEE International Conference on Compatibility, Power Electronics and Power Engineering, CPE-POWERENG 2017, 2017, pp. 626–631.

[2.41] S. Ali, K. Wu, K. Weston, and D. Marinakis, "A Machine Learning Approach to Meter Placement for Power Quality Estimation in Smart Grid," IEEE Trans. Smart Grid, vol. 7, no. 3, pp. 1552–1561, 2016.

[2.42] J. M. Sierra-Fernández, S. Ronnberg, J. J. G. De La Rosa, M. H. J. Bollen, and J. C. Palomares-Salas, "Application of spectral kurtosis to characterize amplitude variability in power systems' harmonics," Energies, vol. 12, no. 1, pp. 1–15, 2019.

[2.43] H. Sha et al., "Online Recognition Method for Voltage Sags Based on a Deep Belief Network," Energies, vol. 12, no. 1, p. 43, 2018.

[2.44] M. S. Manikandan, S. R. Samantaray, and I. Kamwa, "Detection and classification of power quality disturbances using sparse signal decomposition on hybrid dictionaries," IEEE Trans. Instrum. Meas., vol. 64, no. 1, pp. 27–38, 2015.

[2.45] L. Cai, N. F. Thornhill, S. Kuenzel, and B. C. Pal, "Real-Time Detection of Power System Disturbances Based on k-Nearest Neighbor Analysis," IEEE Access, vol. 5, pp. 5631–5639, 2017.

[2.46] M. N. Moschakis and N. D. Hatziargyriou, "Analytical calculation and stochastic assessment of voltage sags," IEEE Trans. Power Deliv., vol. 21, no. 3, pp. 1727–1734, 2006.

[2.47] M. H. J. Bollen and I. Y. H. Gu, Signal Processing of Power Quality Disturbances. 2005.

[2.48] M. H. J. Bollen, "Algorithms for characterizing measured three-phase unbalanced voltage dips," IEEE Trans. Power Deliv., vol. 18, no. 3, pp. 937–944, 2003.

[2.49] J. Bollen, "Method of critical distances for stochastic assessment of voltage sags," vol. 145, no. 1.

[2.50] M. H. J. Bollen et al., "Voltage dip immunity aspects of power-electronics equipment - Recommendations from CIGRE/CIRED/UIE JWG C4.110," in Proceeding of the International Conference on Electrical Power Quality and Utilisation, EPQU, 2011.

[2.51] J. C. Cebrian, N. Kagan, and J. V. Milanovic, "Probabilistic Estimation of Distribution Network Performance with Respect to Voltage Sags and Interruptions Considering Network Protection Setting-Part I: The Methodology," IEEE Trans. Power Deliv., vol. 33, no. 1, pp. 42–51, 2018.

[2.52] D. V. Tien, R. Gono, and Z. Leonowicz, "A multifunctional dynamic voltage restorer for power quality improvement," Energies, vol. 11, no. 6, 2018.

[2.53] G. Yalçinkaya, "Characterization of voltage sags in industrial distribution systems," IEEE Trans. Ind. Appl., vol. 34, no. 4, pp. 682–688, 1998.

[2.54] A. F. Bastos, K. W. Lao, G. Todeschini, and S. Santoso, "Accurate Identification of Point-on-Wave Inception and Recovery Instants of Voltage Sags and Swells," IEEE Trans. Power Deliv., vol. 34, no. 2, pp. 551–560, 2019.

[2.55] R. A. Flores, I. Y. H. Gu, and M. H. J. Bollen, "Positive and negative sequence estimation for unbalanced voltage dips," 2004, pp. 2498–2502.

[2.56] Y. Wang, A. Bagheri, M. H. J. Bollen, and X. Y. Xiao, "Single-Event Characteristics for Voltage Dips in Three-Phase Systems," IEEE Trans. Power Deliv., vol. 32, no. 2, pp. 832–840, 2017.

[2.57] R. A. Cisneros-Maga, A. Medina, and O. Anaya-Lara, "Time-domain voltage sag state estimation based on the unscented kalman filter for power systems with nonlinear components," Energies, vol. 11, no. 6, 2018.

[2.58] E. E. Juárez and A. Hernández, "An analytical approach for stochastic assessment of balanced and unbalanced voltage sags in large systems," IEEE Trans. Power Deliv., vol. 21, no. 3, pp. 1493–1500, 2006.

[2.59] N. Huang, H. Peng, G. Cai, and J. Chen, "Power quality disturbances feature selection and recognition using optimal multi-resolution fast S-transform and CART algorithm," Energies, vol. 9, no. 11, 2016.

[2.60] Y. Wang, M. H. J. Bollen, A. Bagheri, X. Y. Xiao, and M. Olofsson, "A quantitative comparison approach for different voltage dip characterization methods," Electr. Power Syst. Res., 2016.

[2.61] M. H. J. Bollen, "Influence of motor reacceleration on voltage sags," IEEE Trans. Ind. Appl., vol. 31, no. 4, pp. 667–674, 1995.

[2.62] K. El-arroudi, G. Joós, and I. Kamwa, "Intelligent-Based Approach to Islanding Detection in Distributed Generation," IEEE Trans. onPower Deliv., vol. 22, no. 2, pp. 828–835, 2007.

[2.63] S. R. Samantaray, K. El-Arroudi, G. Joós, and I. Kamwa, "A fuzzy rule-based approach for islanding detection in distributed generation," IEEE Trans. Power Deliv., 2010.

[2.64] A. Samui and S. R. Samantaray, "New active islanding detection scheme for constant power and constant current controlled inverter-based distributed generation," IET Gener. Transm. Distrib., vol. 7, no. 7, pp. 779–789, 2013.

[2.65] A. H. Mohammadzadeh Niaki and S. Afsharnia, "A new passive islanding detection method and its performance evaluation for multi-DG systems," Electr. Power Syst. Res., vol. 110, 2014.

[2.66] H. G. Far, A. J. Rodolakis, and G. Joos, "Synchronous distributed generation islanding protection using intelligent relays," IEEE Trans. Smart Grid, vol. 3, no. 4, pp. 1695–1703, 2012.

[2.67] D. Salles, W. Freitas, J. C. M. Vieira, and W. Xu, "Nondetection index of anti-islanding passive protection of synchronous distributed generators," IEEE Trans. Power Deliv., vol. 27, no. 3, pp. 1509–1518, 2012.

[2.67] J. C. M. Vieira, W. Freitas, W. Xu, and A. Morelato, "Performance of frequency relays for distributed generation protection," IEEE Trans. Power Deliv., 2006.

[2.68] J. C. M. Vieira, D. S. Correa, W. Freitas, and W. Xu, "Performance curves of voltage relays for islanding detection of distributed generators," IEEE Trans. Power Syst., vol. 20, no. 3, pp. 1660–1662, 2005.

[2.69] P. Gupta, R. S. Bhatia, and D. K. Jain, "Active ROCOF Relay for Islanding Detection," IEEE Trans. Power Deliv., vol. 32, no. 1, 2017.

[2.70] C. M. Affonso, W. Freitas, W. Xu, and L. C. P. da Silva, "Performance of ROCOF relays for embedded generation applications," IEE Proc. - Gener. Transm. Distrib., vol. 152, no. 1, p. 109, 2005.

[2.71] T. Ghanbari, H. Samet, and F. Hashemi, "Islanding detection method for inverter-based distributed generation with negligible non-detection zone using energy of rate of change of voltage phase angle," IET Gener. Transm. Distrib., vol. 9, no. 15, 2015.

[2.72] W. Wang, J. Kliber, G. Zhang, W. Xu, B. Howell, and T. Palladino, "A power line signaling based scheme for anti-islanding protection of distributed generators - Part II: Field test results," IEEE Trans. Power Deliv., vol. 22, no. 3, pp. 1767–1772, 2007.

[2.73] D. S. Kumar, D. Srinivasan, and T. Reindl, "A Fast and Scalable Protection Scheme for Distribution Networks with Distributed Generation," IEEE Trans. Power Deliv., vol. 31, no. 1, pp. 67–75, 2016.

[2.74] W. Xu, G. Zhang, C. Li, W. Wang, G. Wang, and J. Kliber, "A power line signaling based technique for anti-islanding protection of distributed generators - Part I: Scheme and analysis," IEEE Trans. Power Deliv., vol. 22, no. 3, pp. 1758–1766, 2007.

Chapter 3

Voltage sags review

3.1 Voltage sags with constant magnitude

3.1.1 Voltage sag general classification

Voltage sags with a constant magnitude (i.e., voltage sags originated by short-circuits) have been thoroughly analysed and can be classified as in [3.1]. As a general distinction, voltage sags can be divided into symmetrical (i.e., sag magnitude is equal the three-phases and the angle between them is 120 degrees) or asymmetrical (i.e., the voltage reduction is not equal for all phases and the angle is no longer 120 degrees). Symmetrical sags are usually originated due to three-phase faults (LLL) or three-phase-to-ground faults (LLLG) and the asymmetrical ones, are originated by single-line-to-ground (SLG), two-phase (LL) or two-phase-to-ground faults (LLG). Each type of fault causes a particular voltage sag, however, the voltage sag is propagated along the grid and due to the transformer windings connection, the type of sag changes. Thence, the type of sag expected on a particular bus depends on the type of fault where it is originated as well as on the windings connection of the transformer between the fault and this bus, see Table 3.1.

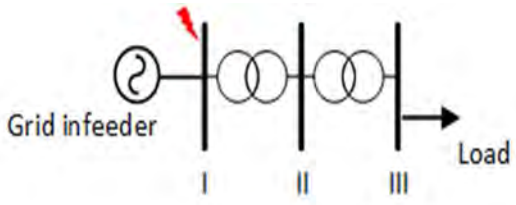

Figure 3.1: Test system with three voltage levels to represent sag types.

The voltage sag classification into seven types is done according to Figure 3.1, where the test system used to define this voltage sag topologies is shown. Furthermore, in Table 3.2, this seven type of voltage sags are summarised where the fault that originated the sag, the temporal expression and the phasor expressions are deduced.

From table 3.2, it should be noted that the angles α_1, α_2, α_3, α_4 depend on the transformer windings connection, and can be computed as follows in Table 3.3.

Table 3.1: Voltage sags general classification

Type of fault	Location of the voltage sag		
	I	**II**	**III**
LLL	A	A	A
LLLG	A	A	A
SLG	B	C	D
LLG	E	F	G
LL	C	D	C

*Table obtained from *M.H.J Bollen* in [3.2].

Table 3.2: Summary of the voltage sags general classification.

Sag Type	**Fault origin**	**Voltage sag temporal expression**	**Phasor expression**
Type A	LLL LLLG	$V_a = \sqrt{2}\cdot V\cdot h\cdot \sin(\omega t + \alpha_a)$ $V_b = \sqrt{2}\cdot V\cdot h\cdot \sin(\omega t + \alpha_{a-120^0})$ $V_c = \sqrt{2}\cdot V\cdot h\cdot \sin(\omega t + \alpha_{a+120^0})$	$V_a = V\cdot h$ $V_b = -\frac{1}{2}\cdot V\cdot h - j\frac{\sqrt{3}}{2}V$ $V_c = -\frac{1}{2}V\cdot h + j\frac{\sqrt{3}}{2}V$
Type B	SLG	$V_a = \sqrt{2}\cdot V\cdot h\cdot \sin(\omega t + \alpha_a)$ $V_b = \sqrt{2}\cdot V\cdot \sin(\omega t + \alpha_{a-120^0})$ $V_c = \sqrt{2}\cdot V\cdot \sin(\omega t + \alpha_{a+120^0})$	$V_a = V\cdot h$ $V_b = -\frac{1}{2}\cdot V - j\frac{\sqrt{3}}{2}V$ $V_c = -\frac{1}{2}\cdot V + j\frac{\sqrt{3}}{2}V$
Type C	LL SLG*	$V_a = \sqrt{2}\cdot V\cdot \sin(\omega t + \alpha_a)$ $V_b = \sqrt{2}\cdot V\frac{\sqrt{1+3\cdot h^2}}{2}\cdot \sin(\omega t + \alpha_{a-120^0-\alpha 1})$ $V_b = \sqrt{2}\cdot V\frac{\sqrt{1+3\cdot h^2}}{2}\cdot \sin(\omega t + \alpha_{a+120^0+\alpha 1})$	$V_a = V$ $V_b = -\frac{1}{2}\cdot V - j\frac{\sqrt{3}}{2}h\cdot V$ $V_c = -\frac{1}{2}V + j\frac{\sqrt{3}}{2}h\cdot V$
Type D	LL* SLG**	$V_a = \sqrt{2}\cdot V\cdot \sin(\omega t + \alpha_a)$ $V_b = \sqrt{2}\cdot V\frac{\sqrt{3+h^2}}{2}\cdot \sin(\omega t + \alpha_{a-120^0-\alpha 2})$ $V_b = \sqrt{2}\cdot V\frac{\sqrt{3+h^2}}{2}\cdot \sin(\omega t + \alpha_{a+120^0+\alpha 2})$	$V_a = V\cdot h$ $V_b = -\frac{1}{2}V\cdot h - j\frac{\sqrt{3}}{2}V\cdot h$ $V_c = -\frac{1}{2}V\cdot h + j\frac{\sqrt{3}}{2}V\cdot h$

Type E LLG	$V_a = \sqrt{2}\cdot V\cdot \sin(\omega t + \alpha_a)$ $V_b = \sqrt{2}\cdot V\cdot h\cdot \sin(\omega t + \alpha_{a-120^0})$ $V_c = \sqrt{2}\cdot V\cdot h\cdot \sin(\omega t + \alpha_{a+120^0})$	$V_a = V$ $V_b = -\frac{1}{2}\cdot V\cdot h - j\frac{\sqrt{3}}{2}h\cdot V$ $V_c = -\frac{1}{2}\cdot V\cdot h + j\frac{\sqrt{3}}{2}h\cdot V$
Type F LLG*	$V_a = \sqrt{2}\cdot V\cdot h\cdot \sin(\omega t + \alpha_a)$ $V_b = \sqrt{2}\cdot\sqrt{\frac{1+h+h^2}{3}}\cdot \sin(\omega t + \alpha_{a-120^0-\alpha_3})$ $V_c = \sqrt{2}\cdot\sqrt{\frac{1+h+h^2}{3}}\cdot \sin(\omega t + \alpha_{a-120^0-\alpha_3})$	$V_a = V\cdot h$ $V_b = -\frac{1}{2}\cdot V\cdot h - j\frac{2+h}{\sqrt{12}}\cdot V$ $V_c = -\frac{1}{2}\cdot V\cdot h + j\frac{2+h}{\sqrt{12}}\cdot V$
Type G LLG**	$V_a = \sqrt{2}\cdot V\cdot\frac{2+h}{3}\cdot \sin(\omega t + \alpha_a)$ $V_b = \sqrt{2}\cdot\frac{\sqrt{1+h+7h^2}}{3}\cdot \sin(\omega t + \alpha_{a-120^0-\alpha_4})$ $V_c = \sqrt{2}\cdot\frac{\sqrt{1+h+7h^2}}{3}\cdot \sin(\omega t + \alpha_{a-120^0-\alpha_4})$	$V_a = \frac{2+h}{3}\cdot V$ $V_b = -\frac{2+h}{6}\cdot V - j\frac{\sqrt{3}}{2}\cdot h\cdot V$ $V_c = --\frac{2+h}{6}\cdot V + j\frac{\sqrt{3}}{2}\cdot h\cdot$

* Sag obtained after one Dy transformer

** Sag obtained after two Dy transformers

Table 3.3: Angles for voltage sags C, D, F and G

Type of Sag	**Angle**
Type C	$\alpha_1 = -\arctan(\sqrt{3}\cdot h) + \frac{\pi}{3}$
Type D	$\alpha_2 = \arctan(\frac{h}{\sqrt{3}}) - \frac{\pi}{6}$
Type F	$\alpha_3 = \arctan(\frac{\sqrt{3}\cdot h}{2+h}) - \frac{\pi}{6}$
Type G	$\alpha_4 = \arctan(\frac{3\sqrt{3}\cdot h}{2+h}) + \frac{\pi}{3}$

*Table obtained from *M.H.J Bollen* in [3.3]

By observing voltage sags Type C and D, one can conclude that both sags can be caused by either a SLG or a LL fault due to the transformer effects (e.g., Dy in this case). The type of transformer and its clock ratio will be assessed in the following subsection. The phasor expressions in Table 3.2 can be also expressed in terms of its symmetrical components. Based on this transformation, Table 3.4 will summarise the direct, inverse and zero components of each type of sag. It must be

Table 3.4: Symmetrical components of the voltage sags.

Sag Type	Fault origin	Symmetrical components		
		Zero sequence	**Direct sequence**	**Inverse sequence**
Type A	LLL or LLLG	$V_0 = 0$	$V_1 = h \cdot V$	$V_2 = 0$
Type B	SLG	$V_0 = -\frac{1-h}{3} \cdot V$	$V_1 = -\frac{2+h}{3} \cdot V$	$V_2 = -\frac{1-h}{3} \cdot V$
Type C	LL or SLG*	$V_0 = 0$	$V_1 = \frac{1+h}{2} \cdot V$	$V_2 = \frac{1-h}{2} \cdot V$
Type D	LL* or SLG**	$V_0 = 0$	$V_1 = \frac{1+h}{2} \cdot V$	$V_2 = -\frac{1-h}{2} \cdot V$
Type E	LLG	$V_0 = \frac{1-h}{3} \cdot V$	$V_1 = \frac{1+2h}{3} \cdot V$	$V_2 = \frac{1-h}{3} \cdot V$
Type F	LLG*	$V_0 = 0$	$V_1 = \frac{1+2 \cdot h}{3} \cdot V$	$V_2 = -\frac{1-h}{3} \cdot V$
Type G	LLG**	$V_0 = 0$	$V_1 = \frac{1+2 \cdot h}{3} \cdot V$	$V_2 = \frac{1-h}{3} \cdot V$

* Sag obtained after one Dy transformer

** Sag obtained after two Dy transformers

noted that these expressions are crucial to understand how these voltage sags are propagated along the grid.

Following the previous general classification which has considered the type of fault and the influence of the transformers winding connection, the voltage sag recovery has to be evaluated. Since the short-circuit currents originate a voltage sag during a fault and these currents are cleared by a protective device following a certain period (i.e., the clearing time), the recovery has to take into consideration the shift between currents and voltages. The instant when the fault current zero-crossing takes place will dictate the beginning of the recovery process, and the grid thévenin angle will play a significant role in this recovery. Indeed, this angle indicates the shift between voltage and current (i.e., it can be considered as the grid cos φ). Depending on the type fault as well as on

the Thévenin angle of the grid where the fault occurs, the voltage sag recovery will take place in one, two or three stages. Thévenin angle depends on the X/R ratio of the grid, for example, if the grid is purely inductive this would mean that fault current lags 90º the pre-fault voltage, meanwhile if resistance increases (i.e., as occur in DNs) this angle will vary. The point on wave of the voltage recovery after a voltage dip due to a fault is ψ or ψ +180º. Since the CB clears the fault at the current zero-crossing, the recovery can occur either at t = 0 s plus the angle or half-cycle after this, plus the angle. Besides, depending on where the fault occurs (i.e., at the transmission system or DN), this angle will inevitably vary; for distribution networks, this value is typically between 40º and 60º whereas in transmission networks, it is between 70º and 80º.

If the voltage sag recovers at the same instant, this would mean that the sag is abrupt, on the contrary, if the recovery takes place with different stages, the voltage sag is considered discrete. To observe the differences between these two types of recovery, see Figure 3.2**.** In that figure, the CB clearing times are showed, tcl_1 belongs to the first zero-crossing, tcl_2 to the zero-crossing of the second fault current and lastly, tcl_3 is the clearing time of the last fault current. Particularly, the recovery shown in Figure 3.2, belongs the voltage recovery due to a three-phase-to-ground fault. Note that depending on ψ, these instants correspond to a specific moment on the voltage waveform, for example, if the grid is mainly inductive, the zero-crossing corresponds to voltage maximum value. Each fault has a different thévenin angle, and therefore, the type of voltage sag recovery is obtained by considering the angles difference between faults. Crucially, a useful summary of the voltage sags recovery is done by A. Rolan *et al.* in [3.4-3.5].

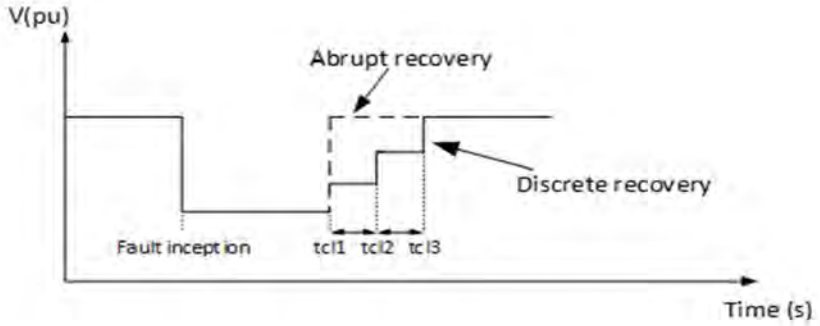

Figure 3.2: Types of voltage recovery. Abrupt (Dashed line), Discrete (Solid line).

According to the previous explanation, in this section, the stages and the total recovery time will be shown separately for each type of fault for a solidly grounded system. Nonetheless, it has to be underlined that the DN object of study in this thesis is a resistance-grounded network. The particularities of such grounding will be evaluated in the next subsections.

3.1.2 Voltage sags with abrupt recovery

As has been previously introduced, the abrupt voltage sags are those where all faulted phases recover at the same instant. In this category, the voltage sags originated by either SLG faults or LL faults are included.

SLG and LL faults

Voltage sags type B are due to SLG faults and the voltage recovery process is abrupt with the point-on-wave in the faulted phase equal to the angle of the fault current (ψ_1). Equation (3.1) shows the temporal expresions of the voltage recovery.

$$\begin{aligned} V_a &= \sin(\omega t + \psi_1) \\ V_b &= \sin(\omega t + \psi_{1-120^0}) \\ V_c &= \sin(\omega t + \psi_{1+120^0}) \end{aligned} \tag{3.1}$$

Voltage sags type C are due to LL faults or SLG faults after a Dy transformer, and the recovery takes place at the same instant, see eq. (3.2). If the voltage sag type C has been caused by an SLG after a Dy transformer, equation (3.1) has to be rewritten as (3.3).

$$\begin{aligned} V_a &= \sin(\omega t + \psi_{2+90^0}) \\ V_b &= \sin(\omega t + \psi_{2-30^0}) \\ V_c &= \sin(\omega t + \psi_{1-150^0}) \end{aligned} \tag{3.2}$$

$$\begin{aligned} V_a &= \sin(\omega t + \psi_{1+90^0}) \\ V_b &= \sin(\omega t + \psi_{1-30^0}) \\ V_c &= \sin(\omega t + \psi_{2-150^0}) \end{aligned} \tag{3.3}$$

where ω is the synchronous speed of the grid, ψ_1 the Thevenin angle for an SLG fault and ψ_2 the Thevenin angle for a LL fault. Since a voltage sag type D is produced by either a LL fault after one Dy transformer or an SLG after two Dy transformers, the termporal equations for the voltage sag recovery are defined in (3.4).

$$\begin{aligned} V_a &= \sin(\omega t + \psi_k) \\ V_b &= \sin(\omega t + \psi_{k-120^0}) \\ V_c &= \sin(\omega t + \psi_{k+120^0}) \end{aligned} \tag{3.4}$$

where k = 1 for an SLG fault and k = 2 for a LL fault.

Table 3.5 summarises the point-on-wave angle of the recovery process for both SLG and LL faults.

Table 3.5: Voltage recovery for SLG and LL faults.

Sag Type	**Point-on-wave of voltage recovery**
Type B	$\theta_A = \psi_1$ $\theta_B = \psi_1$-120º $\theta_C = \psi_1$+120º
Type C	$\theta_A = \psi_2$+90º $\theta_B = \psi_2$-30º $\theta_C = \psi_2$-150º
Type D	$\theta_A = \psi_k$ $\theta_B = \psi_k$-120º $\theta_C = \psi_k$+120º

In this subsection, the voltage sag types B, C and D have been characterised. As can be deduced from Table 3.5, the recovery takes place at the same instant for all phases. Therefore, these voltage

recovery of these voltage sags is considered abrupt. The voltage waveforms of these voltage sags will be depicted in Figure 3.3. The first plot of this Figure shows the sag at location I (Type B) the second plot shows the sag at location II (Type C) and the third plot the sag at location III (Type D). It can be seen that these types of sags recover abruptly at t = 0.404 s.

Figure 3.4 shows the phasor representation of the originated voltage sags at the different locations depicted in Figure 3.1 due to a SLG fault at location I. Thus, 3.4(a) represents voltage sag type B at location I, 3.4(b) represents voltage sag type C and, 3.4(c) depicts the voltage sag type D at location III. In this figure, phase-voltages are plotted as follows: V_a (blue-solid line), V_b (Yellow-solid line) and V_c (solid-purple line).

For this particular case, location I is the HV system at 120 kV, location II belongs to the MV grid at 25 kV and location III is the LV grid at 0.4 kV.

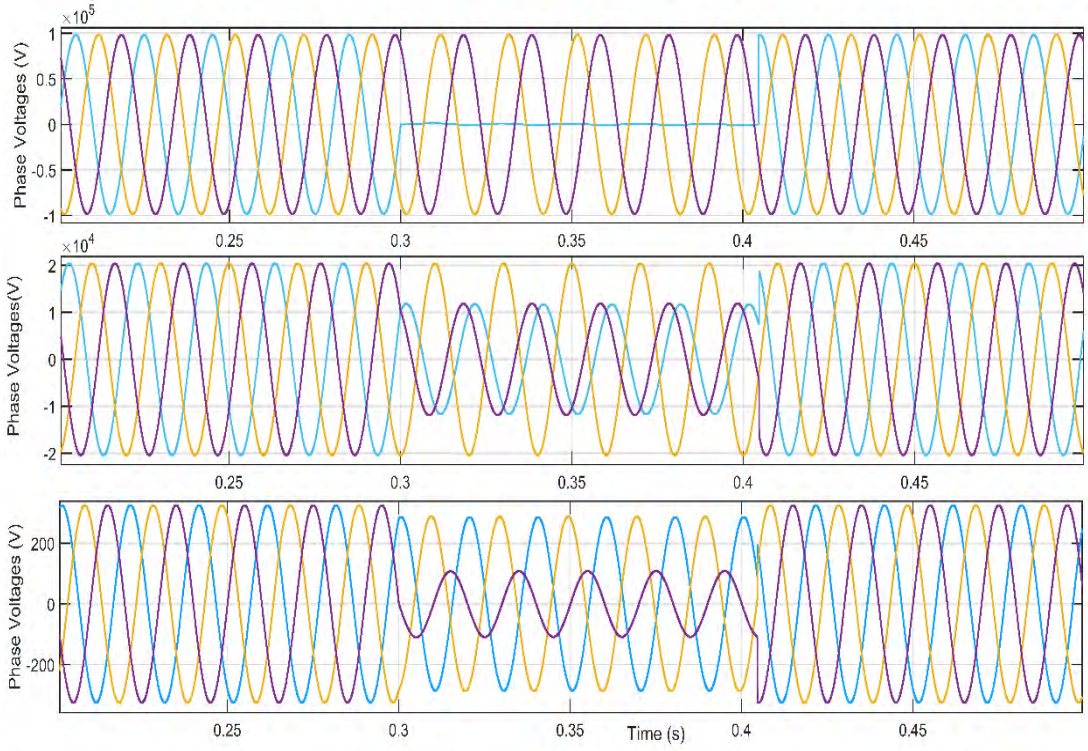

Figure 3.3: Voltage waveform of sags type B, C and D.

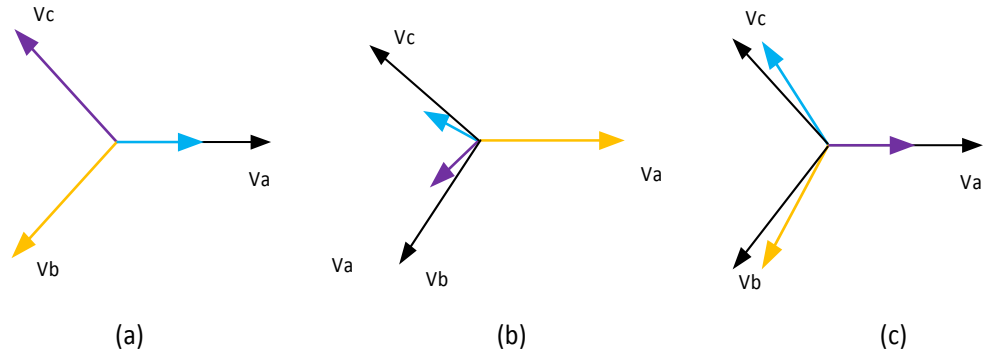

Figure 3.4: Phasor representation of sags type B, C and D.

3.1.3 Voltage sags with discrete recovery

LLG faults

To clear a two-phase-to-ground fault, two steps will be needed, and therefore, the voltage recovery will take place in two stages. Once the first fault current is cleared, this fault evolves to a SLG fault. If we consider a LLG fault between phases b and c to the ground and let's assume 0^o as a reference, the CB has four possible clearance sequences during a cycle. Firstly, fault in phase b is cleared at 0^o and phase c at 120^o. The second likely sequence clears the fault current in phase c at 120^o and phase b is cleared half cycle after, that is, 180^o. The third possible sequence clears phase b at 180^o and phase c 120^o after (300^o). Lastly, the fourth option can occur at phase c at 300^o and phase b at the end of the cycle (360^o). Even though the current angle between the LLG and SLG has been neglected, this difference should be considered to obtain an accurate time recovery. If we consider this difference, the main consequence is that more degrees will be added to the second clearing (i.e., the time between the first clearing and the full recovery will be extended few degrees). Table 3.6 presents the recovery cases that may occur for a LLG, considering the test system defined in Figure 3.1.

Table 3.6: Voltage recovery for LLG faults.

Sag Type	**Point-on-wave of voltage first recovery**	**Intermediate stage and duration**	**Point-on-wave of Voltage second recovery**
Type E_1	$\theta_A = \psi_1+120^o$ $\theta_B = \psi_3$ $\theta_C = \psi_3-120^o$	B_c $120^o+\psi_1-\psi_3$	$\theta_A = \psi_1-120^o$ $\theta_B = \psi_1+120^o$ $\theta_C = \psi_1$
Type E_2	$\theta_A = \psi_3-120^o$ $\theta_B = \psi_3+120^o$ $\theta_C = \psi_3$	B_b $60^o+\psi_1-\psi_3$	$\theta_A = \psi_1-60^o$ $\theta_B = \psi_1+180^o$ $\theta_C = \psi_1+60^o$
Type F_1	$\theta_A = \psi_3-150^o$ $\theta_B = \psi_3+90^o$ $\theta_C = \psi_3-30^o$	C_c $120^o+\psi_1-\psi_3$	$\theta_A = \psi_1-30^o$ $\theta_B = \psi_1-150^o$ $\theta_C = \psi_1+90^o$
Type F_2	$\theta_A = \psi_3+150^o$ $\theta_B = \psi_3+30^o$ $\theta_C = \psi_3-90^o$	C_b $60^o+\psi_1-\psi_3$	$\theta_A = \psi_1-150^o$ $\theta_B = \psi_1+90^o$ $\theta_C = \psi_1-30^o$
Type G_1	$\theta_A = \psi_3+120^o$ $\theta_B = \psi_3$ $\theta_C = \psi_3-120^o$	D_c $120^o+\psi_1-\psi_3$	$\theta_A = \psi_1-120^o$ $\theta_B = \psi_1+120^o$ $\theta_C = \psi_1$
Type G_2	$\theta_A = \psi_3-120^o$ $\theta_B = \psi_3+120^o$ $\theta_C = \psi_3$	D_b $60^o+\psi_1-\psi_3$	$\theta_A = \psi_1-60^o$ $\theta_B = \psi_1+180^o$ $\theta_C = \psi_1+60^o$

It is relevant to mention that the recovery instants that appear in Table 3.6 have considered the fact that the CB clears the second fault current (i.e., the SLG fault current) at the first chance after the first clearance. This might not be the case if the CB clears the fault half-cycle later; therefore, in such case, 180° will be added in both intermediate stages and the final recovery will be prolonged. In the intermediate stage, ψ_1 and ψ_3 belong the fault current angles of the SLG and LLG fault current respectively and subindexs b and c indicate that the voltage sag due to the SLG that occurs in the intermediate stage is symmetrical with respect to phase b or c. The phasor representation will clearly see this last consideration in the next subsection.

Thus, if phase b is cleared first, the intermediate stage involves phase c-to-ground fault, therefore, a voltage sag type E_1 is obtained in bus I (E_A- B_C), a voltage sag F_1 occur in bus II (F_A- C_C) and, a voltage sag G_1 in bus III (G_A- D_C). On the other hand, if phase c is cleared first, this causes phase b-to-ground fault and, as a consequence, voltage sag type E_2 is obtained in bus I (E_A- B_B), a voltage sag F_2 in bus II (F_A- C_B) and, a voltage sag G_2 in bus III (G_A- D_B).

The phasor representation for the discrete recovery for voltage sags originated by LLG faults is showed in the following figures 3.5, 3.6 and 3.7. In this figures, the intermediate stage between the first clearing and the full recovery is described. Accordingly, Figure 3.5(a) shows the phasor representation of sag E_1 and Figure 3.5(b) sag E_2. Figure 3.6(a) shows the phasor representation of sag F_1 and Figure 3.6(b) sag F_2 and lastly, Figure 3.7(a) shows the phasor representation of sag G_1 and Figure 3.7(b) sag G_2.

The waveform of the previously mentioned voltage sags, which are originated due to LLG faults are plotted in figure 3.8. In this figure, it can be seen that, as stated before, the recovery of this sags takes place in two stages (the first recovery at t = 0.401 s and the second at t = 0.407 s). For this particular voltage sag, the second cleared phase after phase b is c; therefore these sags are E_2 (the first plot), F_2 (the second plot) and, G_2 (the third plot) respectively. The plotted voltages in Figure 3.6 have the same colours as in Figure 3.1 of the previous subsection.

To sum up, in this subsection the following types of sags have been obtained: E_1, E_2, F_1, F_2, G_1 and G_2.

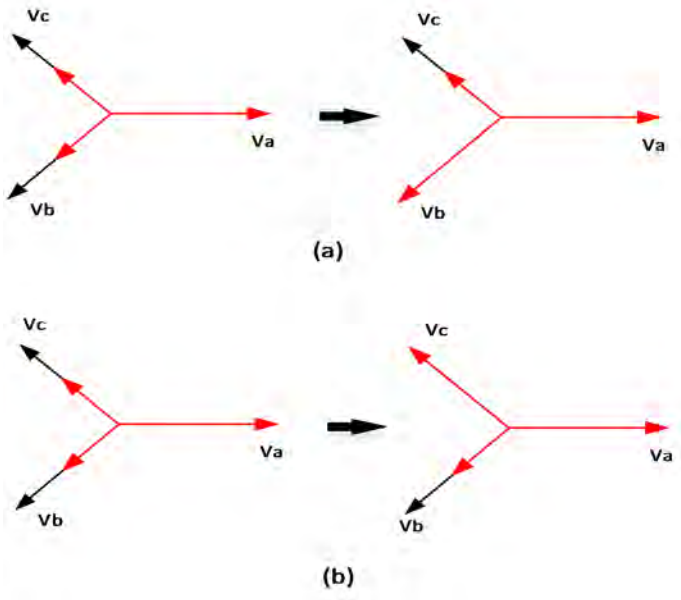

Figure 3.5: Phasor representation of sags type E_1-E_2.

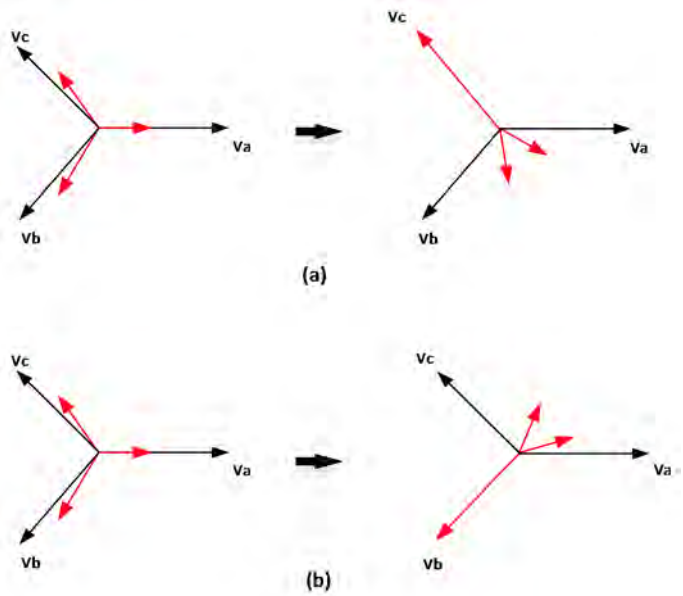

Figure 3.6: Phasor representation of sags type F_1-F_2.

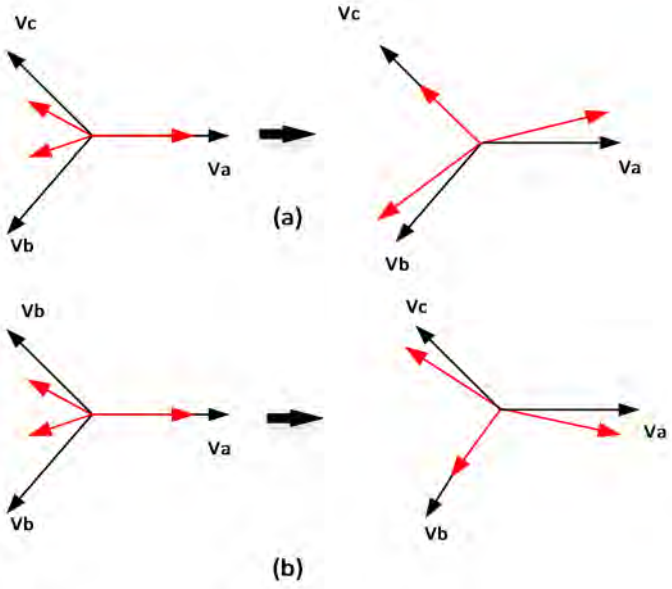

Figure 3.7: Phasor representation of sags type G_1-G_2.

LLL and LLLG faults

These types of faults are balanced faults since the current magnitude and its originated voltage sag magnitude is equal for the three phases and angles between phases are 120^0.

Both LLL and LLLG faults cause voltage sags type A. However, LLL three involves three fault currents, whereas LLLG four current faults, and as a consequence, the voltage sag recovery will be different. The voltage recovery of each type of fault is described down below.

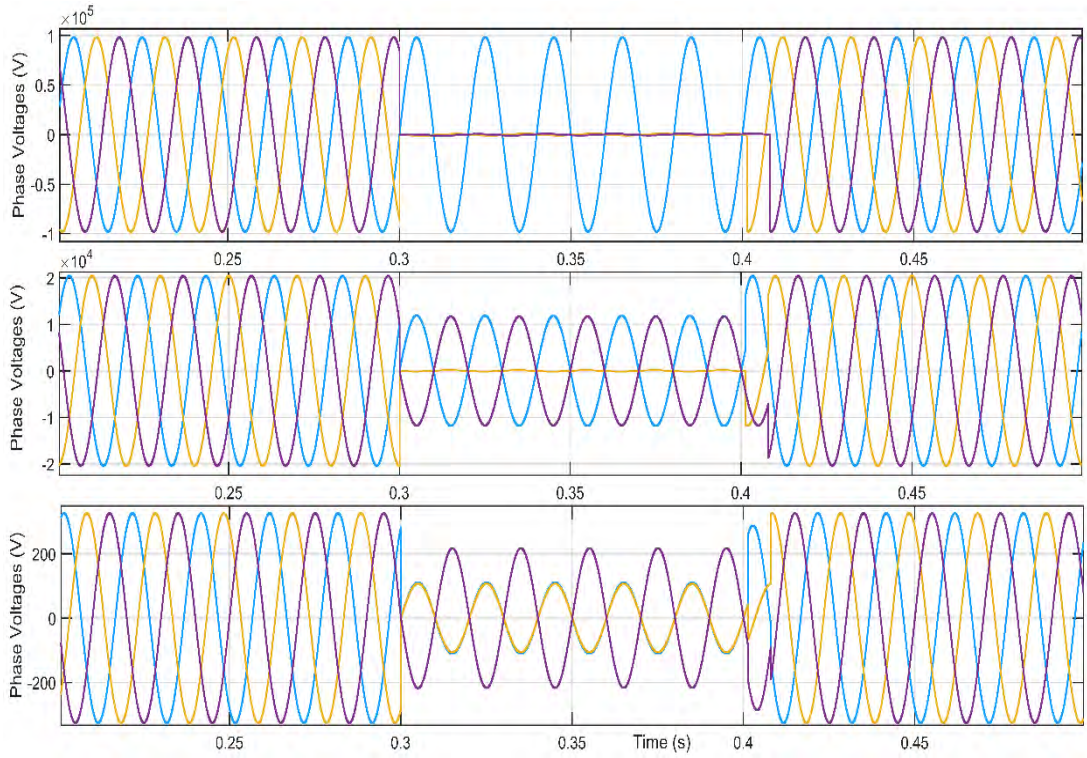

Figure 3.8: Voltage waveform for a LLG fault at location I.

- *Three-phase fault*

Once the first current of a LLL fault has been cleared, this fault evolves to a LL fault which, as has been described in the previous subsection, will be cleared at the same instant. Hence, LLL faults will be cleared in two steps. If the first clearing is in phase a (i.e., the first chance of the CB), the remaining LL fault between phases b and c is cleared in one step. At location I the voltage sag will evolve to a sag type C after the first clearing, whereas, at location II the voltage sag will evolve to a sag type D and thus, two voltage sags named A_1 and A_2 are obtained. The first plot of figure 3.9 depicts the voltage waveform of sag A_1 which occurs at location I, and the second plot shows sag A_2 which occurs at location II. From 3.9 it has been demonstrated that the voltage sag recovery is discrete and it takes place with two steps (the first at t = 0.401s and the second at t = 0.406 s).

- *Three-phase-to-ground*

Once the first current of an LLLG fault is cleared, this fault evolves to an LLG fault which, as has been described in the previous subsection, will be cleared in two stages due to the remaining SLG after the latter clearing. As a consequence, LLLG faults will be cleared in three steps. If phase a is the first cleared phase (the first chance of the CB), the remaining LLG fault between phases b and c and ground is cleared in two steps. The duration of each intermediate stage between clearing instants is 60^0, therefore, three voltage sags are obtained, named A_3, A_4 and A_5**.** These three topologies are detected at different locations; the first type results in A-E-B (location I at Figure 3.1), the second A-F-C (location II at Figure 3.1) and A-G-D (location III at Figure 3.1).

The first plot of figure 3.10 depicts the voltage waveform of sag A_3 which occurs at location I, the second plot shows sag A_4 which is observed at location II, and the third plot shows A_5 which is observed at location III.

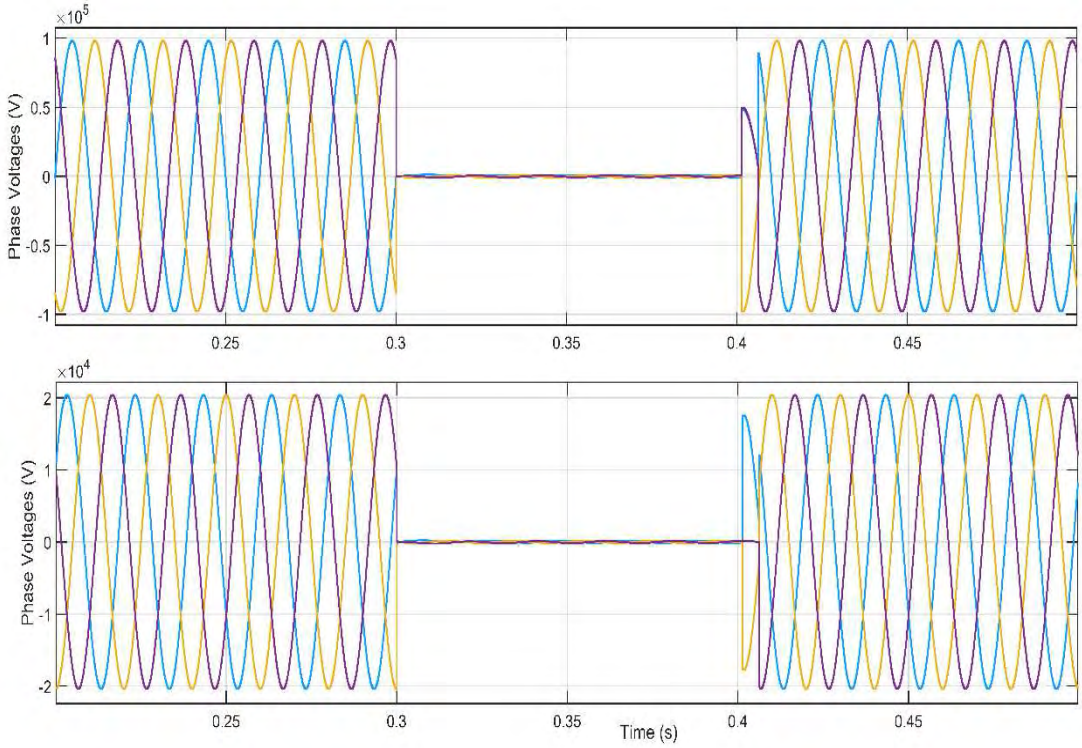

Figure 3.9: Phase voltage waveform for sags type $A_1$and A_2.

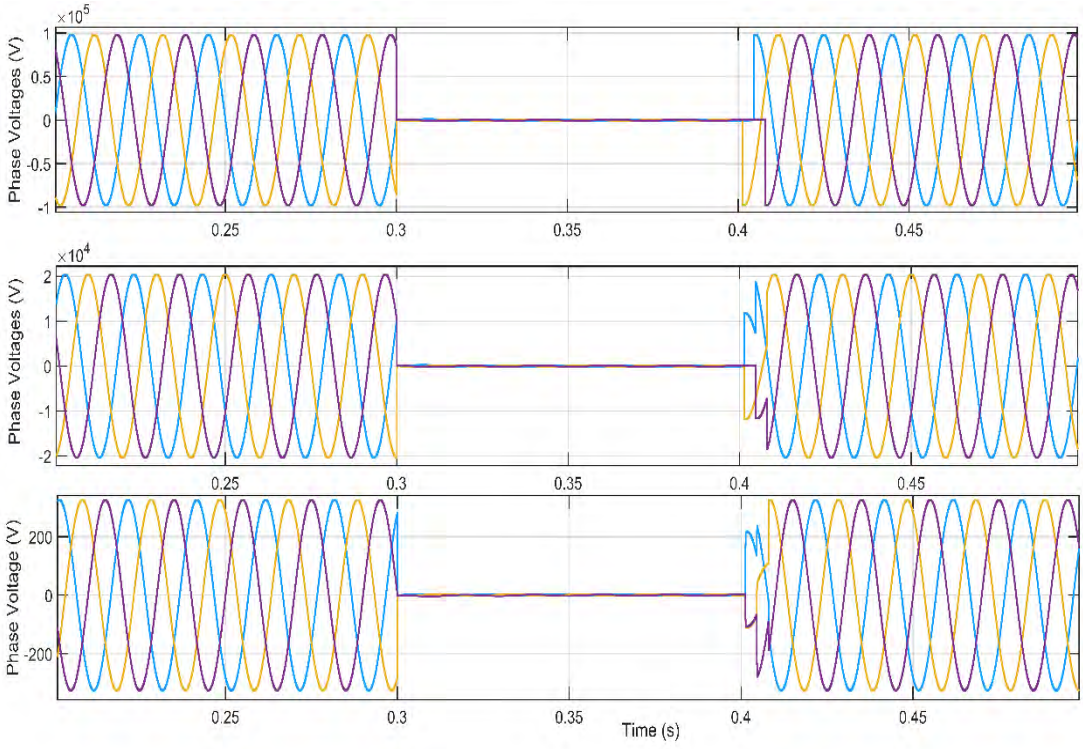

Figure 3.10: Phase voltage waveform for sags type A_3, A_4 and A_5.

The first recovery takes place at t = 0.401 s, the second at t = 0.404 and the third at t = 0.408 s, as expected, this means that there are two intermediate stages and three steps to full recovery.

Table 3.7: Voltage recovery for LLL and LLLG faults.

Sag Type	First recovery	Intermediate stage 1	Second recovery	Intermediate stage 2	Third recovery
Type A_1	$\theta_A = \psi_4$ $\theta_B = \psi_4 - 120^o$ $\theta_C = \psi_4 + 120^o$	C_a $60^o + \psi_2 - \psi_4$	$\theta_A = \psi_2 + 90^o$ $\theta_B = \psi_2 - 30^o$ $\theta_C = \psi_2 - 150^o$		
Type A_2	$\theta_A = \psi_4 + 90^o$ $\theta_B = \psi_4 - 30^o$ $\theta_C = \psi_4 - 150^o$	D_a $60^o + \psi_2 - \psi_4$	$\theta_A = \psi_2 + 180^o$ $\theta_B = \psi_2 + 60^o$ $\theta_C = \psi_2 - 60^o$		
Type A_3	$\theta_A = \psi_4$ $\theta_B = \psi_4 - 120^o$ $\theta_C = \psi_4 + 120^o$	E_a $60^o + \psi_3 - \psi_4$	$\theta_A = \psi_3 + 60^o$ $\theta_B = \psi_3 - 60^o$ $\theta_C = \psi_3 + 180^o$	B_b $60^o + \psi_1 - \psi_3$	$\theta_A = \psi_1 + 120^o$ $\theta_B = \psi_1$ $\theta_C = \psi_1 - 120^o$
Type A_4	$\theta_A = \psi_4 + 90^o$ $\theta_B = \psi_4 - 30^o$ $\theta_C = \psi_4 - 150^o$	F_a $60^o + \psi_3 - \psi_4$	$\theta_A = \psi_3 + 150^o$ $\theta_B = \psi_3 + 30^o$ $\theta_C = \psi_3 - 90^o$	C_b $60^o + \psi_1 - \psi_3$	$\theta_A = \psi_1 - 150^o$ $\theta_B = \psi_1 + 90^o$ $\theta_C = \psi_1 - 30^o$
Type A_5	$\theta_A = \psi_4$ $\theta_B = \psi_4 - 120^o$ $\theta_C = \psi_4 + 120^o$	G_a $60^o + \psi_3 - \psi_4$	$\theta_A = \psi_3 + 60^o$ $\theta_B = \psi_3 - 60^o$ $\theta_C = \psi_3 + 180^o$	D_c $60^o + \psi_1 - \psi_3$	$\theta_A = \psi_1 + 120^o$ $\theta_B = \psi_1$ $\theta_C = \psi_1 - 120^o$

Figure 3.10 depicts the discrete voltage sags that are originated due to LLLG faults. Thus, the first plot shows the originated sag at location I (type A_3), the second plot the sag at location II (type A_3) and the third plot the sag at location III (type A_5).

The evolution of this voltage sags during the recovery has been detailed in table 3.7. Nevertheless, the phasor representation for all stages will be shown in the following figure 3.11. In this Figure (a) represents the evolution A_3-E_2-B, (b) A_4-F_2-C and, (c) A_5-G_2-D.

As a main accomplishment of this subsection, the voltage sags A_1, A_2, A_3, A_4 and A_5 have been obtained.

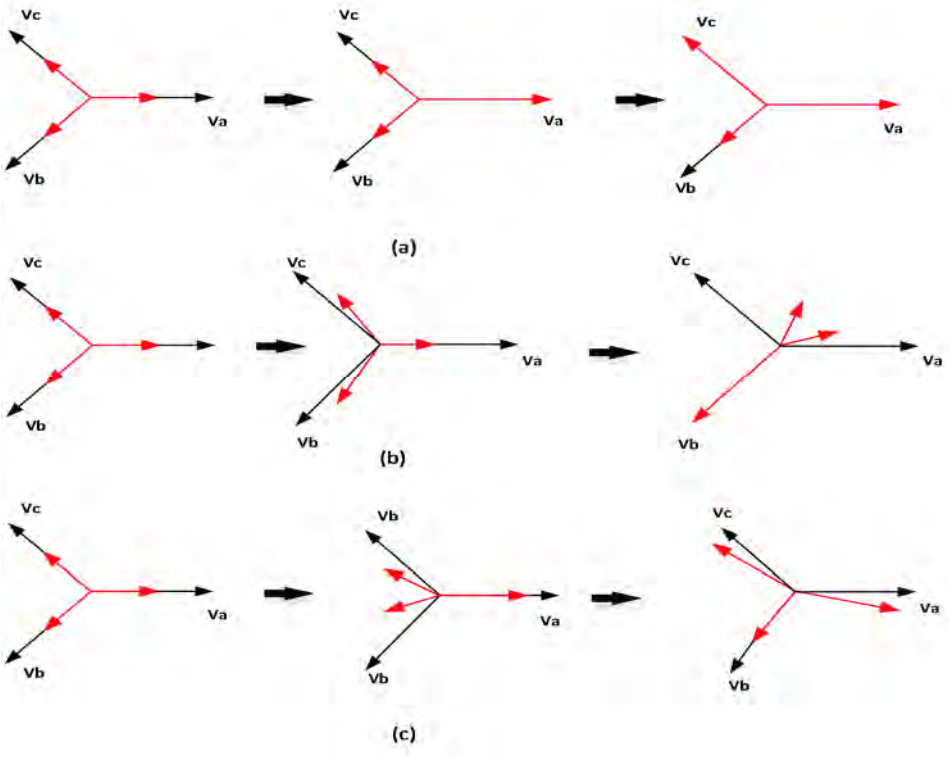

Figure 3.11: Voltage sag phasor representation for a LLLG fault. (a) Sag A_1, (b) Sag A_2 and (c) Sag A_3.

3.1.4 Transformers influence on voltage sags

When performing a voltage sag assessment to study the behaviour of electrical devices due to such disturbances, one can either consider the transformer influence or dismiss its one. If this effect is taken into consideration, two factors such as transformer windings connection and the shift between primary and secondary windings (i.e., the clock ratio) are of interest. Since several transformer configurations remove the voltage zero sequence component, the type of sag also changes. To observe the effects of the windings connection, Table 3.8 will show the changes in the voltage sag type due to transformer windings connection. By observing that table, the wye/wye (grounded at both sides) transformer connection is the only configuration that has no change in voltage sag type. Since the zero-sequence is removed by transformers with a winding connected in delta or zig-zag, the voltage sags that have a zero-sequence component (i.e., sag type B and sag type E) evolves to other types of sags after a Dy transformer. On the contrary, voltage sags with no zero-sequence components (Type C, D, F and G) only change with Dy transformers.

Table 3.8: Influence of transformers winding connection.

Transformer	**Sag at the primary side**						
connection	**Type A**	**Type B**	**Type C**	**Type D**	**Type E**	**Type F**	**Type G**
YNyn	A	B	C	D	E	F	G
Yy, Dd, Dz	A	D	C	D	G	F	G
Yd, Dy, Yz	A	C	D	C	F	G	F

*Table obtained from *M.H.J Bollen* in [3.1].

On the other hand, regardless of the type of windings connection, the shift introduced by the transformer between the primary and secondary voltages influences the voltage angle taken as a reference. By observing the temporal expression defined in the second column of Table 3.2, it can be seen that all cases consider the phase a as a reference and if this angle is shifted, this reference will change as well. Table 3.9 summarises, for a Dy transformer, the most commonly used shift ratios and its effects in voltage sag characterisation. This shift between windings is expressed in degrees and is defined as the product by the shift index (known for electrical engineers as clock ratio) multiplied by 30^0. This shifting between angles has been considered in the present subsection for an SLG fault at location I of Fig. 3.1. However, this reasoning can be similarly applied to other types of faults.

To clearly observe what has been deduced in Table 3.9, Fig. 3.12 shows the transformer shifting effects for three types of faults (SLG, LLG and LLL). The test used to define the voltage sag topologies (i.e., Fig. 3.1) is also used here with two Dy transformers with different shift ratios, the first is a Dy11 and the second is a Dy1.

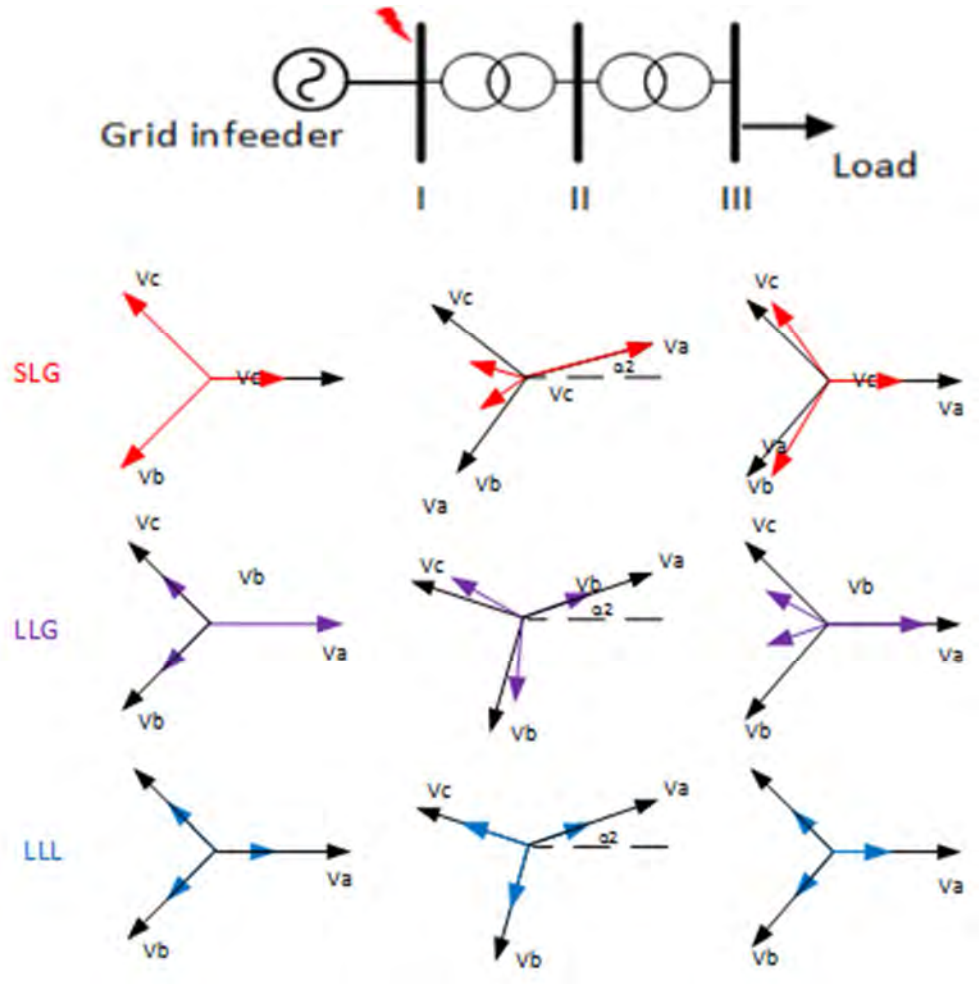

Figure 3.12: Phasor representation of the voltage sags considering transformer shifting.

Table 3.9: Transformers shift influence.

Location I **Sag type/α_{a1}**	**Shift index**	**Location II** **Sag type/ α_{a2}**	**Shift index**	**Location III** **Sag type/ α_{a3}**
Type B/ α_a	1	Type C/ α_{a1}-30^0	11	Type C/ $\alpha_{a1} = \alpha_2+30^0$
Type B/ α_a	3	Type C/ α_{a1}-90^0	9	Type C/ $\alpha_{a1} = \alpha_2+90^0$
Type B/ α_a	5	Type C/ α_{a1}-150^0	7	Type C/ $\alpha_{a1} = \alpha_2+150^0$
Type B/ α_a	7	Type C/ α_{a1}-$210^0 = \alpha_{a1}+150^0$	5	Type C/ $\alpha_{a1} = \alpha_2-150^0$
Type B/ α_a	9	Type C/ α_{a1}-$270^0 = \alpha_{a1}+90^0$	3	Type C/ $\alpha_{a1} = \alpha_2-90^0$
Type B/ α_a	11	Type C/ α_{a1}-$330^0 = \alpha_{a1}+30^0$	1	Type C/ $\alpha_{a1} = \alpha_2-30^0$

3.1.5 Effects of the type of grounding

Conceptually, the system grounding is the process of establishing a connection from one wire of the system to earth. Typically, in electrical power systems, the grounding is carried out through power transformers. Depending on the transformer type of windings connection, the system can be connected to ground in either one way or another and, the resulting fault currents will be different. Therefore, since voltage sags are caused by faults, the type of grounding will also affect.

The most common types of power systems grounding can be: (i) solidly grounded, (ii) impedance-based grounding, which can be either a pure resistance, a reactor (e.g., the Petersen coil), or a combination of both [3.6] and, (iii) ungrounded [3.7-3.8]. In the latter case, the system is uniquely connected to earth thought the capacitance of the cable. It is important to note that the voltage sags detailed in the previous subsections have been simulated in a solidly grounded system. Considering the fact that the electrical network under investigation in this thesis is grounded with a derived neutral via a zig-zag transformer with a series resistance, the influence of the resistance-based grounding in voltage sags will be further discussed. It should be noted that a thorough explanation regarding reactance-grounding and other configurations is done in the following studies [3.8-3.9].

Crucially, the ratio between the zero-sequence reactance and the direct-sequence reactance X_0/X_1 and the ratio between the zero-sequence resistance and direct-sequence reactance R_0/X_1, depend on the type of grounding. Thereby, these ratios will influence the phase-voltages during the fault.

Resistance-grounded systems

This type of grounding is typically used to limit the earth fault current to a particular value. The wye connection of a transformer or an artificial derived neutral from a zig-zag transformer, generally are used to add an impedance. This impedance can be purely resistive, a reactor or a mixed combination impedance. Depending on the voltage level, the type of grounding can change, and consequently, its fault currents.

The voltage sag magnitude expected at the point of common coupling (PCC) between the source (or its equivalent infeeder) and the impedance to the fault, can be expressed as a voltage divider such that:

$$V_{sag} = \frac{Z_{feeder}}{Z_{feeder} + Z_{source}} * V_{source} \tag{3.5}$$

where Z_{feeder} represents the impedance between PCC and the fault and has this notation in order not to confuse it with the impedance fault (i.e., resistance fault). In (1) it is assumed that the pre-fault voltage is 1 pu, there are no pre-fault currents before the event, and the three-phase fault is solid. To show the influence of the grounding in the voltages during an earth-fault, the symmetrical components for the unbalanced faults such as SLG and LLG faults will be detailed down below. Since LLLG fault is balanced and only has direct-sequence component, voltages during the fault are not affected by the grounding connection of generators or transformers.

- SLG

During an SLG fault, the three-phase system can be decoupled into the direct, inverse and zero sequence components, see the Fortescue transform in [3.3]. Considering the voltage divider expressed in (1), now it can be rewritten for the three sequences. Thus, the direct, inverse and zero sequence voltages at the point of common coupling (PCC) are as follows:

$$\begin{aligned} V_{(1)} &= \frac{Z_{feeder(0)} + Z_{feeder(1)} + Z_{feeder(2)} + Z_{source(0)} + Z_{source(2)}}{(Z_{feeder(0)} + Z_{feeder(1)} + Z_{feeder(2)} + Z_{source(0)} + Z_{source(2)}) + Z_{source(1)}} \\ V_{(2)} &= \frac{Z_{source(2)}}{(Z_{feeder(0)} + Z_{feeder(1)} + Z_{feeder(2)} + Z_{source(1)} + Z_{source(0)}) + Z_{source(2)}} \\ V_{(0)} &= \frac{Z_{source(0)}}{(Z_{feeder(0)} + Z_{feeder(1)} + Z_{feeder(2)} + Z_{source(1)} + Z_{source(2)}) + Z_{source(0)}} \end{aligned} \tag{3.6}$$

Taking advantage of the Fortescue transform, the phase-to-neutral voltages during the fault can be expressed as (3.7):

$$\begin{aligned} V_a &= 1 - \frac{Z_{source(1)} + Z_{source(2)}Z_{source(0)}}{Z_{feeder(1)} + Z_{feeder(2)} + Z_{feeder(0)} + Z_{source(0)} + Z_{source(1)} + Z_{source(2)}Z_{source(0)}} \\ V_b &= a^2 - \frac{a^2 Z_{source(1)} + aZ_{source(2)}Z_{source(0)}}{Z_{feeder(1)} + Z_{feeder(2)} + Z_{feeder(0)} + Z_{source(0)} + Z_{source(1)} + Z_{source(2)}Z_{source(0)}} \\ V_c &= a - \frac{aZ_{source(1)} + a^2 Z_{source(2)} + Z_{source(0)}}{Z_{feeder(1)} + Z_{feeder(2)} + Z_{feeder(0)} + Z_{source(0)} + Z_{source(1)} + Z_{source(2)}Z_{source(0)}} \end{aligned} \tag{3.7}$$

In a solidly-grounded network, the three-sequence source impedances and variables in the numerator are canceled, therefore, these voltages can be rewritten as in (3.8):

$$\begin{aligned} V_a &= -\frac{3Z_{source(1)}}{\frac{(Z_{feeder(1)} + Z_{feeder(2)} + Z_{feeder(0)})}{3} + 3Z_{source(1)}} \\ V_b &= a^2 \\ V_c &= a \end{aligned} \tag{3.8}$$

Nonetheless, in an impedance-based system, Z_0 is no longer equal to Z_1 and Z_2, (the two latter can be considered equal for both source and feeder) and the numerator is not cancelled. Therefore, the voltages during the voltage sag are expressed as in (3.9):

$$V_a = 1 - \frac{Z_{source(0)} + 2Z_{source(1)}}{(2Z_{feeder(1)} + Z_{feeder(0)}) + (2Z_{source(1)} + Z_{source(0)})}$$
$$V_b = a^2 - \frac{Z_{source(0)} - 2Z_{source(1)}}{(2Z_{feeder(1)} + Z_{feeder(0)}) + (2Z_{source(1)} + Z_{source(0)})} \quad (3.9)$$
$$V_c = a - \frac{Z_{source(0)} - 2Z_{source(1)}}{(2Z_{feeder(1)} + Z_{feeder(0)}) + (2Z_{source(1)} + Z_{source(0)})}$$

It can be seen that during a fault, between the first phase and ground, the voltage sag for the faulted phase is the same as in (3.8). However, the voltage for the non-faulted phases changes because the numerator is no longer cancelled. This voltage drop can be related to the difference between direct and zero impedances. Since in a resistance-grounded system $Z_0 \geq Z_1$, the non-faulted phases will experience, as commented before, a voltage swell. This over-voltage for the phase-to-ground voltages that is produced during the fault has to be at most the rated RMS value of the line voltage, see references [3.7-3.9].

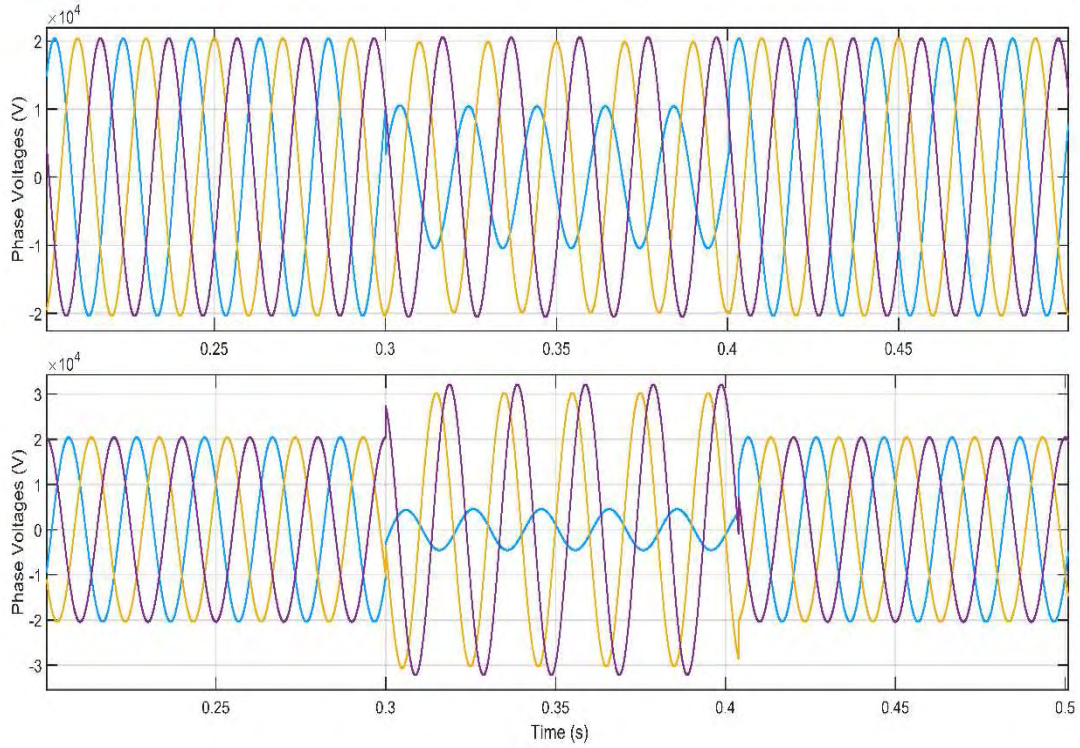

Figure 3.13: Comparison between solid and resistance-grounded networks for a SLG.

The second plot of Figure 3.13 shows an SLG in a resistance-based MV network, where both voltage sag and swells can be observed. On the other hand, the first plot shows that for an SLG in a solidly-grounded system, no swells occur. Besides, the more significant is the difference between these two impedances, the lower is the voltage drop during the sag, even for a zero-resistance fault.

- LLG

Similarly, as calculated for the SLG fault, the voltages during this type of fault can be decoupled into direct, inverse and zero sequences. Voltages at the PCC during the fault are computed as the

voltage divider of (1), but applied to the LLG fault (for a solidly-grounded system) are expressed as (3.10):

$$V_{(1)} = 1 - \frac{(Z_{feeder(0)} + Z_{feeder(2)} + Z_{source(0)} + Z_{source(2)}) \cdot Z_{source(1)}}{(Z_{feeder(0)} + Z_{source(0)}) \cdot (Z_{feeder(1)} + Z_{source(1)} + Z_{feeder(2)} + Z_{source(2)}) + (Z_{feeder(1)} + Z_{source(1)}) \cdot (Z_{feeder(2)} + Z_{source(2)})}$$

$$V_{(2)} = \frac{(Z_{feeder(0)} + Z_{source(0)}) \cdot Z_{source(2)}}{(Z_{feeder(0)} + Z_{source(0)}) \cdot (Z_{feeder(1)} + Z_{source(1)} + Z_{feeder(2)} + Z_{source(2)}) + (Z_{feeder(1)} + Z_{source(1)}) \cdot (Z_{feeder(2)} + Z_{source(2)})} \quad (3.10)$$

$$V_{(0)} = \frac{(Z_{feeder(2)} + Z_{source(2)}) \cdot Z_{source(0)}}{(Z_{feeder(0)} + Z_{source(0)}) \cdot (Z_{feeder(1)} + Z_{source(1)} + Z_{feeder(2)} + Z_{source(2)}) + (Z_{feeder(1)} + Z_{source(1)}) \cdot (Z_{feeder(2)} + Z_{source(2)})}$$

Now, symmetrical voltage components can be converted into phase-to-neutral voltages through the Fortescue transform. During an LLG fault, the phase-voltage of the faulted phases is the same and the non-faulted phase remains equal for a solid grounded system, nevertheless, as for the SLG, as the $Z_0 \geq Z_1$, the non-faulted phase experience a voltage swell.

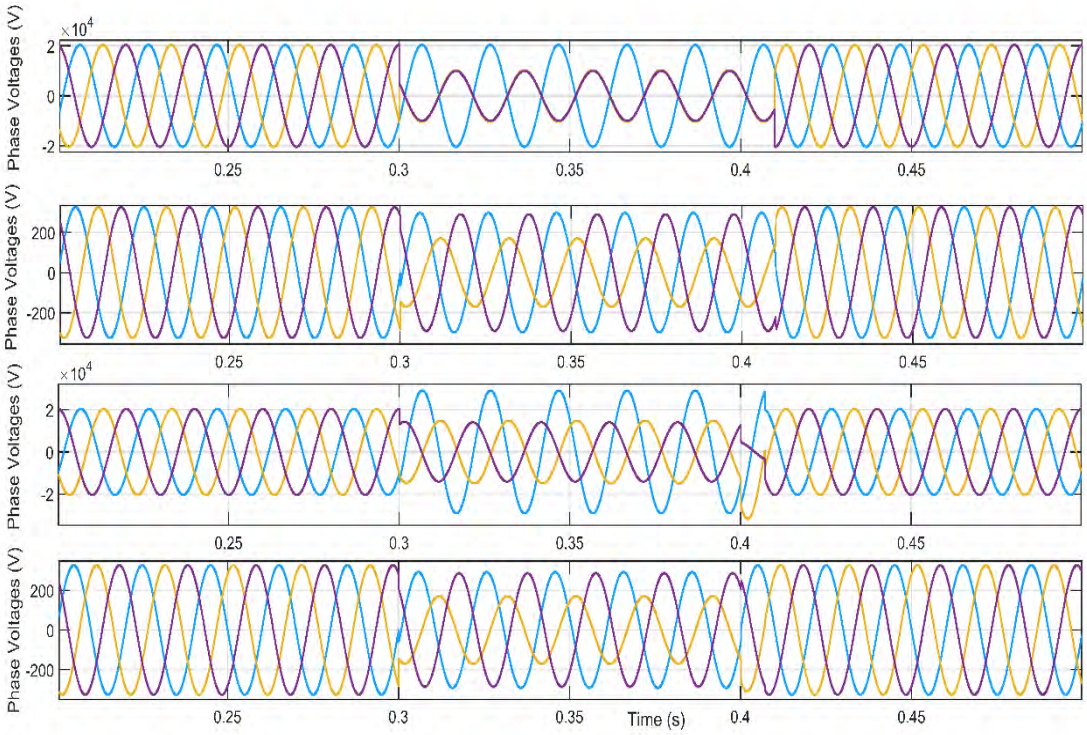

Figure 3.14: Comparison between LL and LLG faults in resistance-based grounding grids.

It has to be underlined that the effects of either a LL or LLG faults in a resistance-based grounded system produce the same voltage sag, therefore, after a Dy transformer, the voltage sag will be also the same. To observe such effect, Figure 3.14 shows the three-phase voltages for both LL and LLG faults in a resistance-grounded system like the one object of study (see the test system under investigation in Figure 4.1 of the next Chapter 4). In the first plot of Figure 3.14, the resulting phase voltages for a LL fault at the MV network are depicted, and the second plot shows the voltage sag at the LV level (i.e, after a Dy transformer). The third plot of this Figure shows the voltage sag originated due to an LLG at the MV network, while the four shows the voltage sag at the LV side (after a Dy transformer). By comparing the second and fourth plots of Fig.

3.14, it can be seen that in a resistance-grounded network, both LL and LLG produce the same sag after a Dy transformer (Sag type D).

To observe such effect, Figure 3.15 shows the three-phase voltages at the LV network for both LLG (Solid lines) and LL (dashed lines) at the MV network. It is worth mentioning that the only difference between sags is observable in the recovery because as mentioned earlier, the LLG recovery differs from the LL.

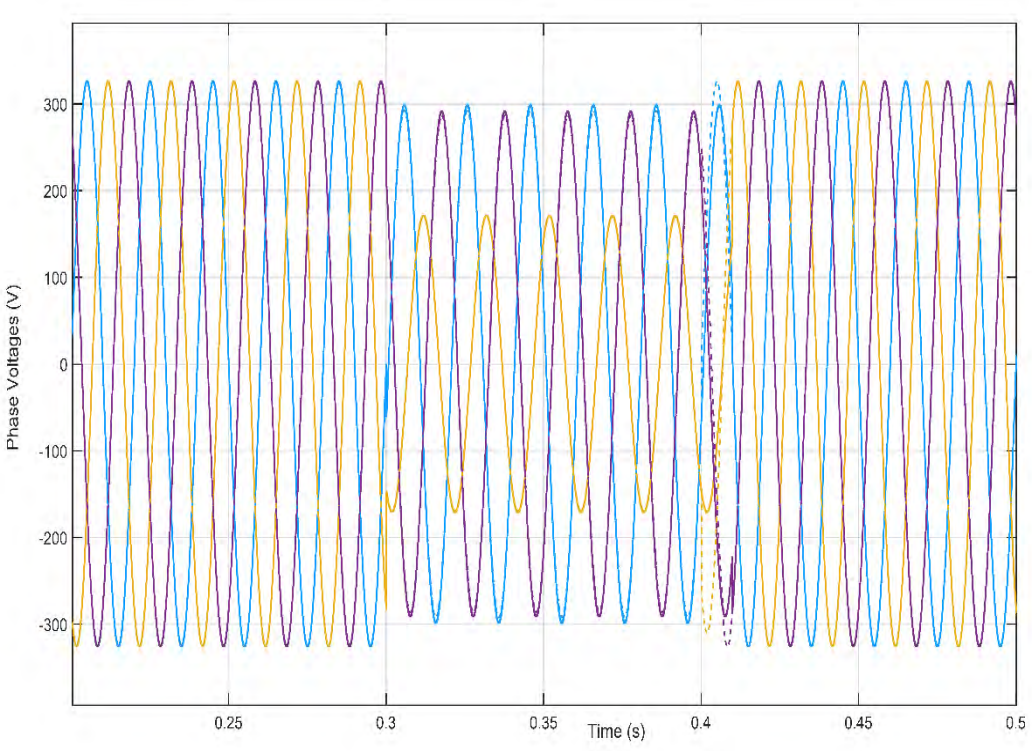

Figure 3.15: Detailed comparison between the sags produced by LL and LLG faults.

3.1.6 Phase-angle jump

During a fault, the involved phases experience an angle shift, and this angle depends on the Thévenin angle of the grid. It has to be noted that, depending on the ratio between X/R, which can be seen as the power factor of the fault, this angle jump will vary. Typically, the angle jump is not considered in HV networks because the grid is mainly inductive and X/R is between 7 and 10, however, in distribution networks, where this ratio is higher, this shift has to be taken into consideration. As a matter of fact, this angle has been used to compute the voltage sag recovery in the previous section. Whereas in DNs it is roughly between 45^0 and 60^0 (or even lower for high-resistance faults), in transmission networks, it is close to the 80^0.

Figure 3.13 shows the phase angle jump for faults at different locations, where the effects of the different impedance on the phase-angle-jump can be seen. The purple line represents a fault at the beginning of an MV feeder (i.e., at the HV/MV substation) meanwhile, the red line belongs to a fault at a midpoint in the MV feeder. By comparing purple and red lines, the change in the phase-angle jump due to change in the thévenin impedance can be noticed. On the other hand, if the resistance of the Thévenin impedance is increased, the angle jump is also affected, see for instance blue and green lines. In fact, blue and green lines are the obtained phase-angle jumps for faults at MV lateral branches where the cross-section of the wires is small and consequently, the relation X/R is low.

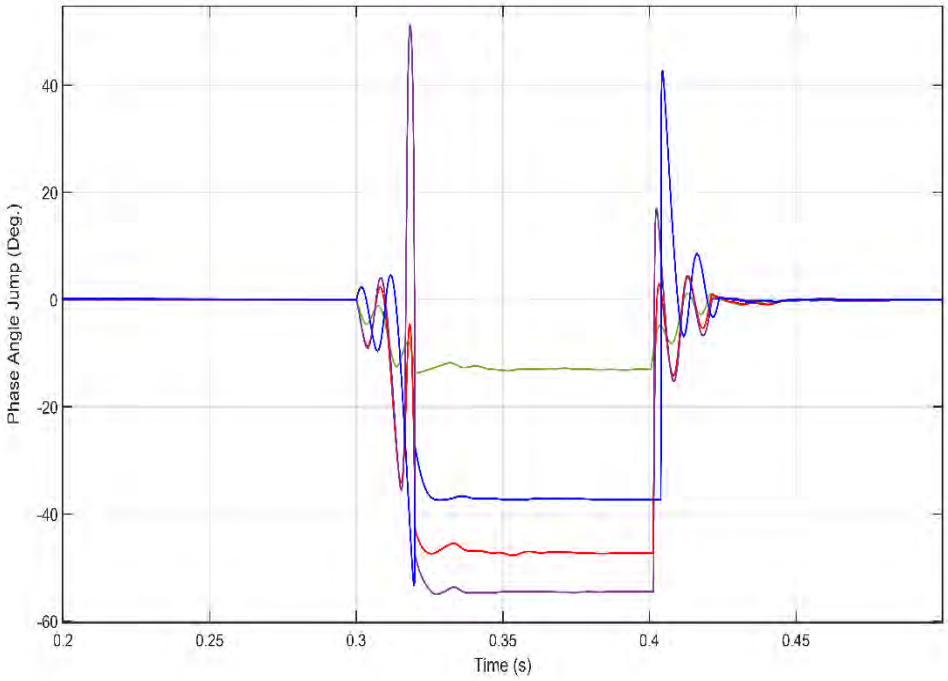

Figure 3.16: Phase-angle jump comparison for different fault locations.

3.2 Voltage sags with a non-constant magnitude

The previous subsection has reviewed the voltage sags caused by faults, which show a constant magnitude during the whole event. Nonetheless, this subsection focuses on analysing those sags where the voltage is not constant during the event (i.e., voltage recovers or decreases during the event). The latter type of sags, are not caused by faults but due to transients such as induction machine starting, transformer energisation, or sudden load connections. Additionally, a particular type of sag with a non-constant magnitude can be observed when an induction motors fault contribution is considered. This effect is discussed M.H.J Bollen in [3.10]. To illustrate such effect, Figure 3.17a shows an example of the voltage sag produced when an IM contributes to a three-phase fault. In that Figure, the symmetrical voltage sag (Type A) is plotted.

Nevertheless, to properly observe the voltage variation due to the contribution of the motor, in Figure 3.17b, the voltage sag is enlarged. In this figure, the decrease in the voltage magnitude during the event can be observed. This voltage reduction during the voltage sag is due to the brief IM contribution towards the fault, which starts at t = 1.62 s, and in 2 cycles, the current starts to decrease. In this case, the voltage variation due to this effect is $\Delta V = 125$ V.

Figure 3.18 depicts the voltage sag produced when a transformer is energized. Due to the current drawn by the transformer, transiently, the voltage drops to 0.94 pu. As can be seen, the voltage magnitude is not constant; it reaches a minimum value at t = 0.82 and starts to increase until t = 1s when the voltage sag is absolutely recovered. This voltage sag is unbalanced due to the current unbalance during this energisation. By observing the third plot of Figure 4, the high content of harmonics of the current waveform can be seen; these harmonics are a direct consequence of the transformer core saturation [3.11].

Figure 3.19 shows the voltage sag produced by IMs starting; in this case, a group of 4 IMs of 160 kW have been simulated. It can be seen that the duration of the event is 500 ms, the voltage depth is 0.96 pu, and the voltage sag is balanced. Nevertheless, it is easy to observe that its magnitude is not constant during the event. The first plot depicts the RMS phase voltage; the second represents the RMS current, while the third shows the current waveform.

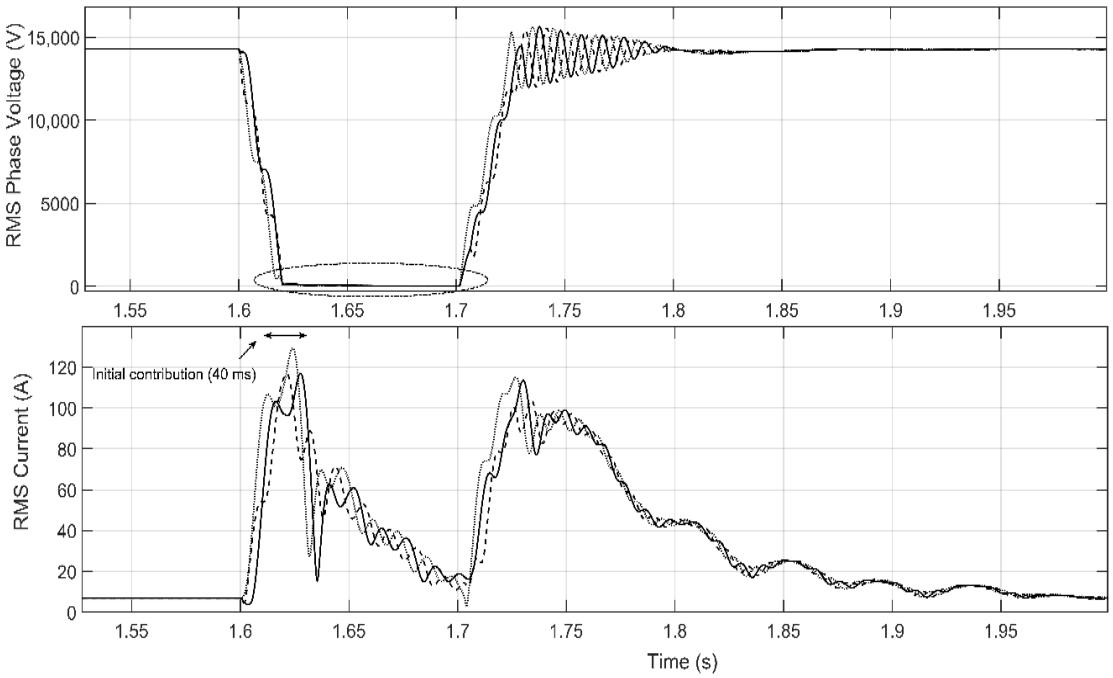

(**a**)

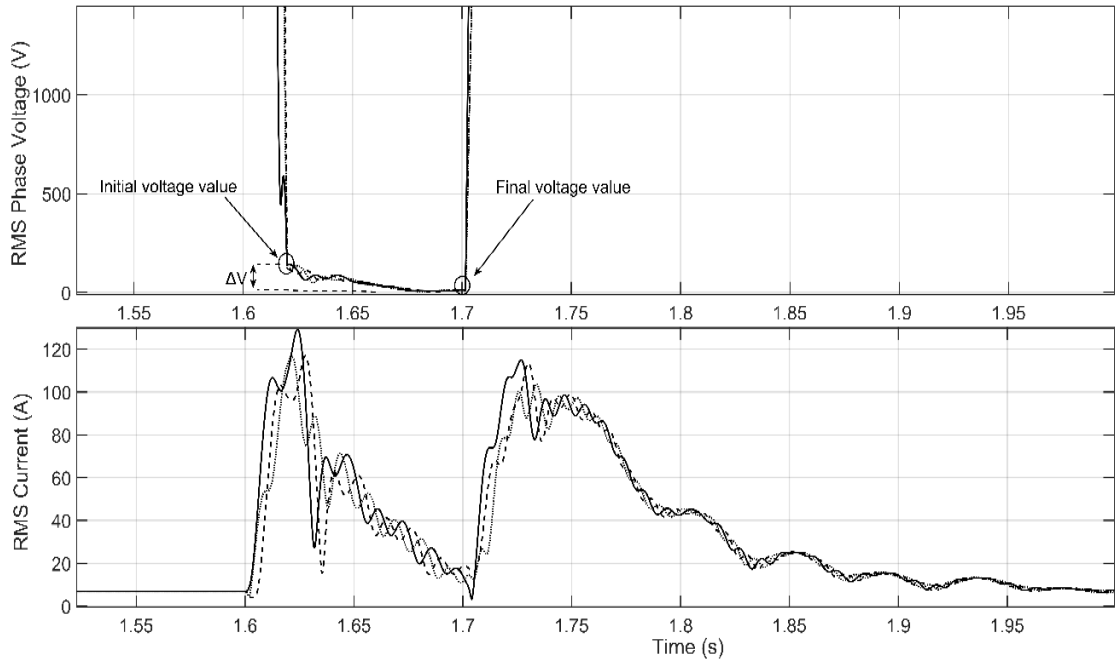

(**b**)

Figure 3.17: Voltage sag for a three-phase fault considering induction motors contribution.

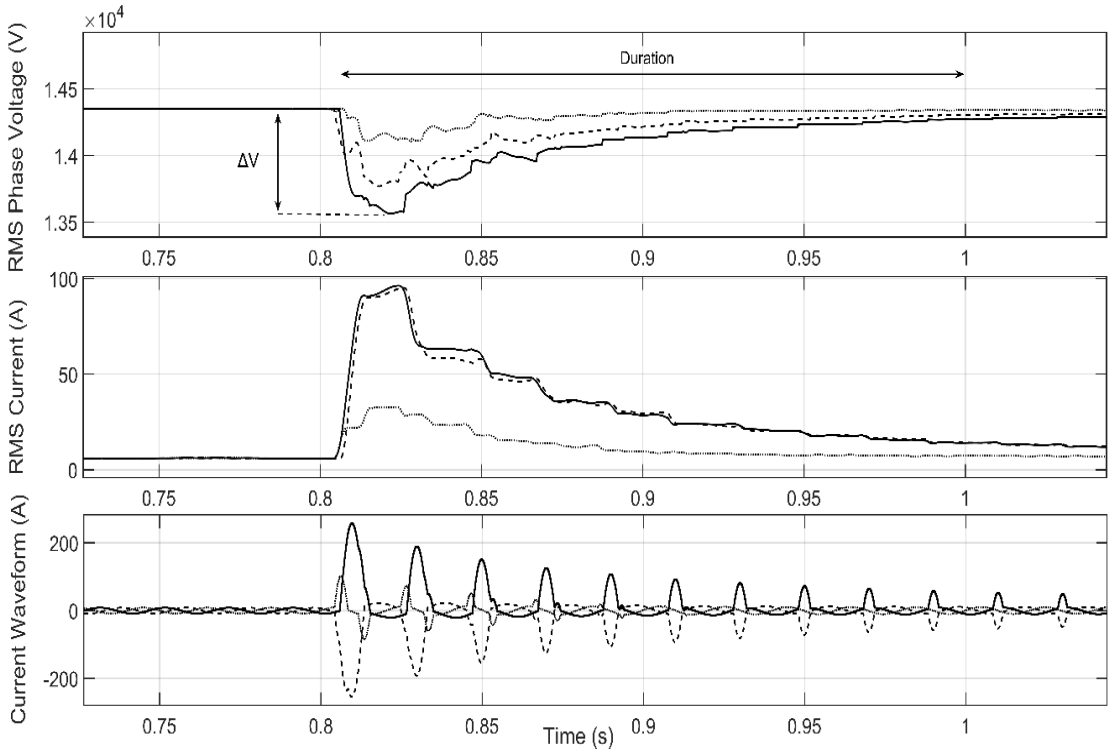

Figure 3.18: Voltage sag due to transformer energisation.

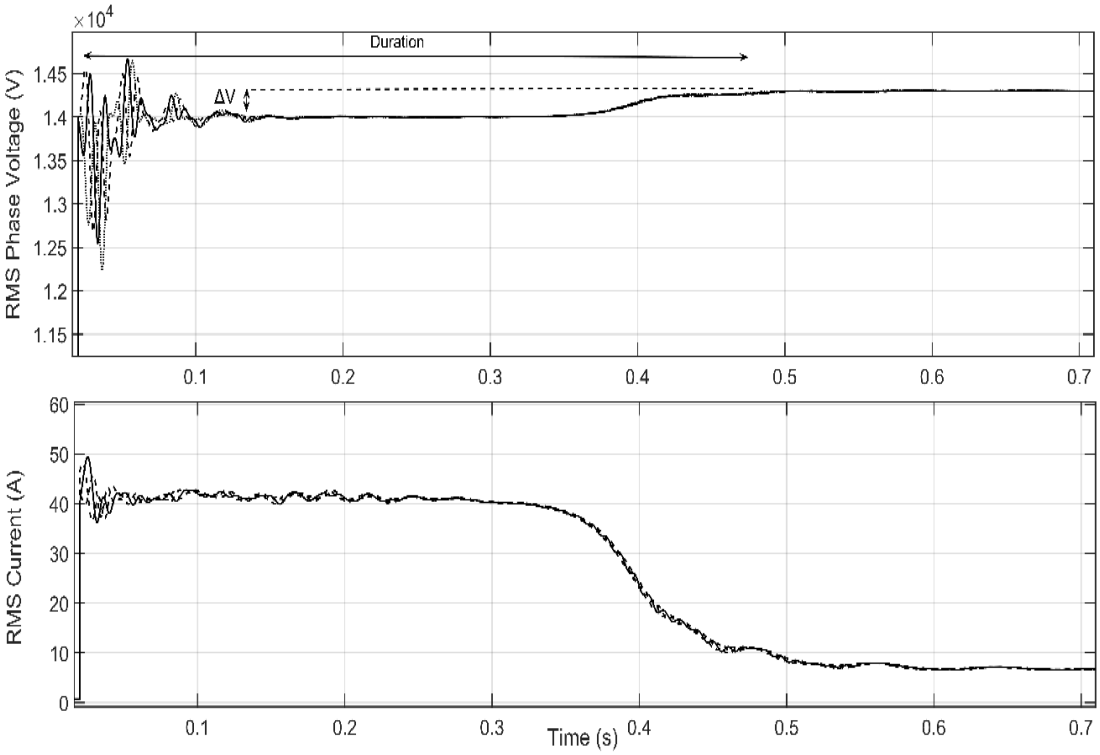

Figure 3.19: Voltage sag due to induction motor starting.

3.3 Conclusions

This Chapter has made a general review regarding the main features of the voltage sags. Thus, voltage sags have been divided into two major groups; the ones with a constant magnitude (i.e., the ones caused by faults), and the ones with a non-constant magnitude. After this principal classification, the next distinction is done regarding its symmetry (i.e., symmetrical and non-symmetrical voltage sags). The subsequent distinction considers its recovery; on the one hand, we have the ones which recover in one stage (abrupt sags) whereas the others, recover with several steps (discrete sags). Each type of fault has been detailed separately to observe the originated voltage sags for each event.

Secondly, the effects of the transformer in voltage sags have been considered in subsection 3.1.4, where it has been observed that considering the shift introduced becomes crucial to determine the type of sag transmitted along the grid.

Thirdly, the influence of the type of grounding has also been assessed in subsection 3.1.5. Many studies considered the voltage sags are originated in transmission networks where the connection is commonly solidly-grounded. However, in this section, other topologies such as the resistance-based grounding and its effects into voltage sags have been studied. Crucially, it has been demonstrated that while in a solidly-grounded system LL and LLG faults cause a different sag (Sag type C or E), in resistance-grounded systems both LLG and LL faults cause the same voltage sag (E).

Additionally, the phase-angle-jump is discussed for several fault locations, and the effects of this shift have been evidenced, especially, in distribution networks where X/R is weak.

To summarise, in this section the following 14 topologies of voltage sags have been obtained: A_1, A_2, A_3, A_4, A_5, B, C, D, E_1, E_2, F_1, F_2, G_1 and, G_2. This classification is essential to assess the during-fault behaviour of the IM in the subsequent Chapter 4. Additionally, in this section, sags with constant and non-constant magnitude have been evaluated, which allows the reader to understand the new voltage sag topology presented in the subsequent Chapter 9.

3.4 References

[3.1] M. H. J. Bollen, IEEE Power Engineering Society., IEEE Power Electronics Society., and IEEE Industry Applications Society., Understanding power quality problems : voltage sags and interruptions. 2000.

[3.2] M. H. J. Bollen, “Voltage recovery after unbalanced and balanced voltage dips in three-phase systems,” *IEEE Trans. Power Deliv.*, vol. 18, no. 4, pp. 1376–1381, 2003.

[3.3] Lidong Zhang and M. H. J. Bollen, “A method for characterisation of three-phase unbalanced dips (sags) from recorded voltage waveshapes,” 21st Int. Telecommun. Energy Conf. INTELEC ’99 (Cat. No.99CH37007), p. 188, 1999.

[3.4] A. Rolán, F. Córcoles, J. Pedra, L. Monjo, and S. Bogarra, “Testing of three-phase equipment under voltage sags,” *IET Electr. Power Appl.*, vol. 9, no. 4, pp. 287–296, 2015.

[3.5] A. Rolán, F. Córcoles, and J. Pedra, “Doubly fed induction generator subject to symmetrical voltage sags,” *IEEE Trans. Energy Convers.*, vol. 26, no. 4, pp. 1219–1229, 2011.

[3.6] I. P. E. Society, "IEEE Guide for the Application of Neutral Grounding in Electrical Utility Systems," Group, vol. 2000, 2000.

[3.7] J. C. Das, Transients in Electrical Systems. McGraw-Hill, 2010.

[3.8] D. Patynowski et al., "Fault Locator approach for high-impedance grounded or ungrounded distribution systems using synchrophasors," in 2015 68th Annual Conference for Protective Relay Engineers, CPRE 2015, 2015.

[3.9] X. Lin, J. Huang, and S. Ke, "Faulty feeder detection and fault self-extinguishing by adaptive petersen coil control," *IEEE Trans. Power Deliv.*, vol. 26, no. 2, pp. 1290–1291, 2011.

[3.10] M. H. J. Bollen, "Influence of motor reacceleration on voltage sags," *IEEE Trans. Ind. Appl.*, vol. 31, no. 4, pp. 667–674, 1995.

[3.11] F. de León and J. A. Martinez, "Dual three-winding transformer equivalent circuit matching leakage measurements," *IEEE Trans. Power Deliv.*, vol. 24, no. 1, pp. 160–168, 2009.

Chapter 4

Islanding operation: Theoretical analysis

4.1 Introduction

The central pillar of this thesis is the assessment of the IO that occurs in a DN. Conceptually, IO can be defined as an abnormal operation that occurs when a portion of the grid is isolated from the main grid due to a protective device operation but, even so, this grid portion remains energised. In this chapter, an in-depth analysis of the IO operation that occurs following a CB operation in the presence of large induction motors will be carried out**.** In this Chapter, the modelling guidelines used to assess the IO are provided. The mathematical equations of each element of the model are analysed and a broad discussion is done to evaluate the feasibility of each selected element. Indeed, the model defined in this Chapter is a crucial means in order to achieve a successful validation of the transient under study.

In consideration of the above, the main goals of this Chapter can be summarised as follows:

1. Describe the main features of each test system component used in the model. This description can be found in ***section 4.2*** and ***section 4.3***.
2. The stages of the whole event are detailed separately.
   - Firstly, the pre-fault conditions are evaluated (i.e., steady-state analysis of the system) in ***section 4.3.*** The obtained pre-fault results are required to initialise the transient behaviour of the subsequent section.
   - Secondly, the induction motors behaviour during the fault before the CB operation are analysed in ***section 4.4***. The results obtained in this section will be used to initialise the islanding operation evaluated in the next section.
   - The IO is explored in ***section 4.5***.

Lastly, to conclude this Chapter, the main conclusions are summarised in ***section 4.6***.

4.2 Electrical network under investigation

The system where measurements have been recorded is a real DN, which is operating radially with an infeeder from a transmission system at 120 kV, 50 Hz. The single-line diagram of the system is depicted in Figure 4.1. As shown in the figure, the substation wye/delta transformer

supplies three medium voltage (MV) feeders; Feeder 2 and sub-feeders A and B form the system analysed in this work. Feeders 1 and 3 are not detailed, because they are not relevant to the task due to its radial configuration and also because feeder 1 is the one where the unintentional IO object of study occurs. The end-users are supplied at a low voltage (LV) of 0.4 kV through their MV/LV Dyn 11 transformers. The MV system is grounded via a zig-zag transformer with a resistance of 23 Ω that limits the fault current to 630 A. The short circuit capacity at the 120 kV busbar is 1000 MVA. The main system parameters and the IMs data, are detailed in Table 4.1.

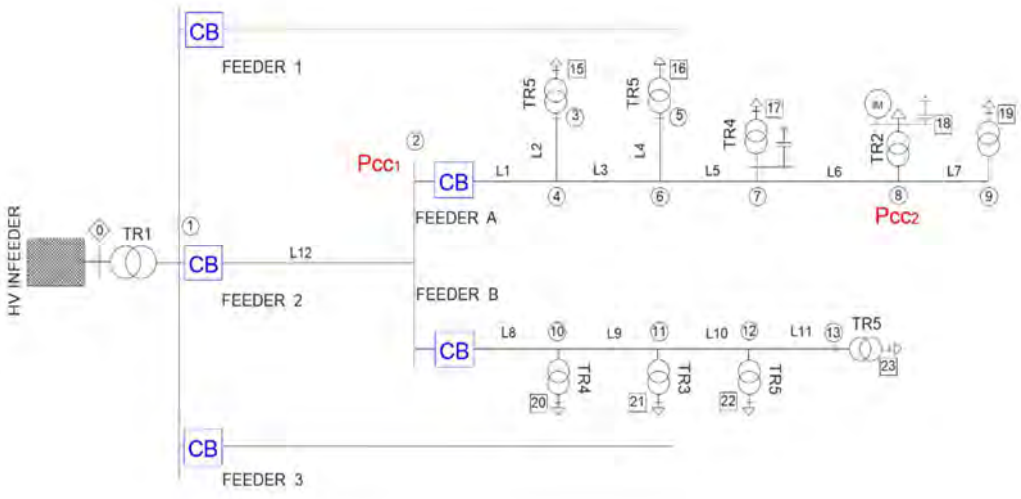

Figure 4.1: One-line diagram of the test system under study.

Table 4.0.1: Test system parameters.

Transformers					
		V_p/V_s (kV)	S (MVA)	ε (%)	L_m/R_m (H/kΩ)
Substation transformer	TR1	120/25 kV	10	10.4	78 ; 313
Distribution transformers	TR2	25/0.4 kV	1	6	180 ; 370
	TR3	25/0.4 kV	0.63	5.1	350 ; 480
	TR4	25/0.4 kV	0.4	4.3	404 ; 694
	TR5	25/0.4 kV	0.25	4.1	811 ; 1666

Distribution Lines				
Lines	Nodes	Length (km)	Parameters: Z_1 /Z_0 (Ω/km) ; C_0 (μF/km)	Loadbility (A)
L1	2 – 4	5	0.306+j0.405/0.38+j1.62	300
L2	4 – 3	3.3	1.07+j0.441/1.3+j1.76,	120
L3	4 – 6	4.3	0.306+j0.405/0.38+j1.62	300
L4	6 – 5	4	1.07+j0.441/1.3+j1.76	120
L5	6 – 7	2.5	0.306+j0.405/0.38+j1.62	300
L6	7 – 8	2	0.306+j0.405/0.38+j1.62	300
L7	8 – 9	7	0.687+j0.416/0.8+j1.66	200
L8	2 – 10	3.8	0.127+j0.114/0.17+j0.45 ; 0.229	389
L9	10 -11	4.43	0.208+j0.123/0.278+j0.492 ; 0.192	320
L10	11 -12	4	0.687+j0.416/0.8+j1.66	200
L11	12 -13	3.3	0.687+j0.416/0.8+j1.66	200
L12	1-2	0.28	0.306+j0.405/0.38+j1.62	300

4.3 System components modelling

4.3.1 Introduction to modelling guidelines

This section aims to discuss how to model the main test system elements: lines, transformers, loads, IMs, and protective devices. A crucial aspect to consider in order to accurately assessing the transient behaviour of the test system is the range of frequencies with which transients are generated. Other factors that may significantly affect the simulation results are the load profiles, the voltage/frequency-dependence of loads, or protective device settings. The guidelines followed when implementing the test system model are summarized hereunder:

- The saturation effect is considered in transformers for modelling purposes, so as to fulfil the maximum accuracy.
- Transmission line impedance, for each particular section, is assumed to be equal for the three phases.
- Very low load unbalances are assumed. Accordingly, a single line diagram power flow would be precise enough to establish the initial conditions of the transient.
- IM is modelled as saturable because of the stator current increase, following circuit breaker (CB) disconnection.
- Widely known IEC-IEEE curves of protective devices are considered.

4.3.2 Distribution lines

Transmission and distribution lines representation can be based on distributed or lumped parameters. A precise way to model a transmission line is with distributed parameters at a specific range of frequency. An extensive literature about transmission lines is available; particularly this matter was deeply discussed in [4.1]. In the particular case of insulated cables, the shunt capacitance has to be considered. Hence, any transmission line can be represented by a four-terminal ABCD network. The initial and final buses are named *r* and *s* respectively. Accordingly, the equation is defined:

$$\begin{bmatrix} V_s \\ I_s \end{bmatrix} = \begin{bmatrix} A & B \\ C & D \end{bmatrix} \begin{bmatrix} V_r \\ I_r \end{bmatrix} \tag{4.1}$$

where *V* is the bus voltage, *I* the line current, subscripts *r* and *s* are referred to the buses *r* and *s* respectively. For transient studies, a detailed representation of transmission lines has been extensively studied in [4.2]. The frequency dependence in transmission line modelling is discussed in [4.3, 4.4]. In the case of over-head distribution lines where the admittance values can be neglected, the term *B* corresponds to the series impedance. However, despite this, in the present study to achieve higher precision, the pi section will be used. Although the central part of the system under study is composed of overhead lines, a non-negligible portion is formed of underground cables; a thorough evaluation regarding cables is done in [4.5]. Thereby, modelling overhead lines as pi section line at a 50 Hz will suffice in our study. Due to the underground cables, the zero sequence component of the shunt capacitance has to be taken into consideration. Direct and inverse sequence values of the series impedance will be assumed equal. The line parameters of the test system have been previously summarised in Table 4.1.

4.3.3 Transformers

Transformers are one of the most critical elements of an electrical system and are used to adjust the voltage level to the desired value; thus, it can be used to increase or decrease (i.e., step-up and step-down transformers) the voltage level through its electromagnetic fields between windings. They transfer power through its windings without changing the frequency. Transformers can be categorised by the number of windings and its connection, the number of phases (e.g., three-limb core, five-limb core or three single-phase transformer), the transformation ratio, the power rating, its clock ratio between windings, and the type of cooling. Furthermore, depending on its use, several transformers can be used, for instance, power distribution transformers, grounding transformers, measurement transformers; either potential or current transformers, phase-shifting transformers or even shell transformers. ANSI/IEEE-Std. C57.12 provides useful data regarding transformers characteristics and tests [4.6].

The magnetic field in the air gap is considered as nonlinear and depending on the transient object of study, take into account the saturation effects is crucial [4.7]. Therefore, in the present study, transformers will be modelled as saturable. Even though taking into consideration the frequency-dependence is required in transformer transients, and this dependence will not be considered in the present modelling due to the low-frequency range of the transient object of study.

Thus, the saturation effect curve that has been used in our model for a three-limb three-phase transformer belongs to the power systems toolbox library of Matlab/Simulink, and describes the following generic polynomial curve:

$$I_m = A_0 + A_1\lambda + A_2\lambda^2 + A_3\lambda^3 + \ldots + A_n\lambda^n \tag{4.2}$$

where the generic coefficients expressed in (4.2) are different depending on each transformer power rating as well as depending on its configuration. In-depth research regarding transformer modelling for low and mid-frequencies are detailed in [4.8-4.10]. In [4.11] a practical saturation estimation from recorded inrush currents waveform is developed.

In this study, the transformer tap changer will not be considered under the assumption that the transformer ratio between primary and secondary will remain constant during the whole transient. Particularly, in our model there are three types of transformers; (i) HV/LV transformer which is wye/delta winding connection (Substation transformer), (ii) MV/LV transformers which are delta/wye winding connection and (iii) grounding zig-zag transformer via artificially derived neutral, which allows the system to be resistance grounded. Transformers direct and inverse impedances will be assumed to be equal; the zero sequence impedances will be considered in (iii) and neglected in (i) and (ii) transformers regarding its winding connection. Transformer parameters are provided in Table 4.1.

4.3.4 Induction motors mathematical model

Introduction to modelling

The induction machine (IM) modelling will depend on the level of accuracy required as well as on the type of study that is going to be carried out. As a general classification, there are two types of models to evaluate the induction machines, the fifth-order model which is composed by four electrical equations plus the mechanical equation and the reduced third-order model composed by two electrical equations plus the mechanical one. The latter is derived from the fifth-order model, considering stator fluxes derivative to zero. It should be noted that both models are derived

from the seventh-order induction model composed by six electrical equations (i.e., model in the abc reference frame), plus one mechanical. The selected model depends on the purpose of the study, for instance, in wide-area power systems stability studies, the third-order model due to the fact that it considers negligible the dynamics stator transients, see [4.12, 4.13]. By considering the third-order model, the complexity of the system is notably reduced, nonetheless, to study the behaviour of the induction motor during transients, the fifth-order is more appropriate.

The necessity of transforming these set of equations is due to the angle between the magnetic axes of the stator phase *a*, and rotor winding phase *a*, which constitutes a time-varying set of differential equations. To overcome such drawback, the induction equations are converted through a transformation into time-invariant differential equations, and the equations are transformed from the three-axis system into a two-axis system. The most used transform is the one developed by Park. Nevertheless, other important transformations are available like KU transform or αβ transform, for a detailed explanation of the possible transformations, take a look at [4.14-4.16].

Prior to machine modelling, the following assumptions have been considered:

- The machine is considered symmetrical (i.e., both windings are equals, and its magnetic axes are shifted 120^0).
- The distribution of the magnetic field is considered senoidal.
- The air gap between the rotor and stator is smooth.
- The machine model considers magnetic saturation.
- The connection of the motor is connected through an isolated wye, it has no neutral connector and consequently, zero-sequence components can be neglected.
- The machine is single-cage and rotor windings are short-circuited.

Transient state model of the IM

In Figure 4.2 the representation of the induction machine is depicted, in this figure, it can be seen that the currents have a positive sign, thus indicating the motor mode. Once the motor becomes generator following the CB, the sign of these currents will be negative. Indeed, acting as a motor, currents are entering to the windings.

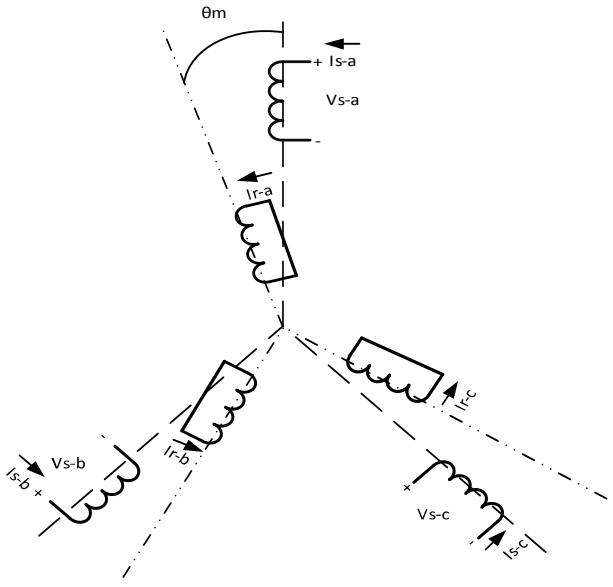

Figure 4.2: Induction machine model in the abc-reference frame.

The induction motor model is given by (4.3):

$$V = Ri + \frac{d\phi}{dt} \tag{4.3}$$

The set of electrical equations of the single-cage induction machine which define its transient behaviour (expressed in the *abc* reference frame) are detailed down below:

$$\begin{aligned}
V_{sa} &= R_s \cdot i_{sa} + \frac{d\phi_{sa}}{dt} \\
V_{sb} &= R_s \cdot i_{sb} + \frac{d\phi_{sb}}{dt} \\
V_{sc} &= R_s \cdot i_{sc} + \frac{d\phi_{sc}}{dt} \\
V_{ra} &= R_r \cdot i_{ra} + \frac{d\phi_{ra}}{dt} \\
V_{rb} &= R_r \cdot i_{rb} + \frac{d\phi_{rb}}{dt} \\
V_{rc} &= R_r \cdot i_{rc} + \frac{d\phi_{rc}}{dt}
\end{aligned} \tag{4.4}$$

where V is voltage, i current, R is resistance, ϕ flux linkage, and subindexes r and s are referred to stator and rotor respectively. The set of Eqs. (4.4), can now be expressed in matrix form as (4.5):

$$\begin{bmatrix} V_s \\ 0 \end{bmatrix} = \begin{bmatrix} R_s & 0 \\ 0 & R_r \end{bmatrix} \cdot \begin{bmatrix} i_s \\ i_r \end{bmatrix} + \frac{d}{dt} \begin{bmatrix} \phi_s & 0 \\ 0 & \phi_r \end{bmatrix} \tag{4.5}$$

where stator voltages (rotor voltage is set to zero due to the rotor winding is short-circuited) and currents vector are expressed as a three-dimension vector, resistances are expressed as a six-dimension matrix. The flux linkages can be expressed with the matrix form of (4.6):

$$\phi = M(\theta_m) \cdot i = \begin{bmatrix} M_{ss} & M_{sr} \\ M_{rs} & M_{rr} \end{bmatrix} \cdot \begin{bmatrix} i_s \\ i_r \end{bmatrix} \tag{4.6}$$

The inductances of the linkages matrix for stator and rotor can be expressed as in (4.7):

$$M_{ss} = \begin{bmatrix} l_s & -\frac{1}{2}m_s & -\frac{1}{2}m_s \\ -\frac{1}{2}m_s & l_s & -\frac{1}{2}m_s \\ -\frac{1}{2}m_s & -\frac{1}{2}m_s & l_s \end{bmatrix}; M_{rr} = \begin{bmatrix} l_r & -\frac{1}{2}m_r & -\frac{1}{2}m_r \\ -\frac{1}{2}m_r & l_r & -\frac{1}{2}m_r \\ -\frac{1}{2}m_r & -\frac{1}{2}m_r & l_r \end{bmatrix} \tag{4.7}$$

where ls and lr are the self-inductances of both stator and rotor, m_s and m_r are the mutual inductances between stator windings and rotor windings respectively. The mutual inductance between stator and rotor windings is expressed as m.

The mutual inductance (magnetizing) matrix is expressed as in (4.8):

Note that the term M_{RS} is the transposed of matrix M_{RS}.

$$M_{sr} = \begin{bmatrix} m\cos\theta_m & m\cos(\theta_m - \frac{4\pi}{3}) & m\cos(\theta_m - \frac{2\pi}{3}) \\ m\cos(\theta_m - \frac{2\pi}{3}) & m\cos\theta_m & m\cos(\theta_m - \frac{4\pi}{3}) \\ m\cos(\theta_m - \frac{4\pi}{3}) & m\cos(\theta_m - \frac{2\pi}{3}) & m\cos\theta_m \end{bmatrix} \tag{4.8}$$

The six-dimension flux linkages vector is related to the six-dimension currents vector as:

$$\begin{bmatrix} \phi_{sa} \\ \phi_{sb} \\ \phi_{sc} \\ \phi_{ra} \\ \phi_{rb} \\ \phi_{rc} \end{bmatrix} = \begin{bmatrix} l_s & -\frac{1}{2}m_s & -\frac{1}{2}m_s & m\cos\theta_m & m\cos(\theta_m + \frac{2\pi}{3}) & m\cos(\theta_m + \frac{4\pi}{3}) \\ -\frac{1}{2}m_s & l_s & -\frac{1}{2}m_s & m\cos(\theta_m + \frac{4\pi}{3}) & m\cos\theta_m & m\cos(\theta_m + \frac{2\pi}{3}) \\ -\frac{1}{2}m_s & -\frac{1}{2}m_s & l_s & m\cos(\theta_m + \frac{2\pi}{3}) & m\cos(\theta_m + \frac{4\pi}{3}) & m\cos\theta_m \\ m\cos\theta_m & m\cos(\theta_m + \frac{4\pi}{3}) & m\cos(\theta_m + \frac{2\pi}{3}) & l_r & -\frac{1}{2}m_r & -\frac{1}{2}m_r \\ m\cos(\theta_m + \frac{2\pi}{3}) & m\cos\theta_m & m\cos(\theta_m + \frac{4\pi}{3}) & -\frac{1}{2}m_r & l_r & -\frac{1}{2}m_r \\ m\cos(\theta_m + \frac{4\pi}{3}) & m\cos(\theta_m + \frac{2\pi}{3}) & m\cos\theta_m & -\frac{1}{2}m_r & -\frac{1}{2}m_r & l_r \end{bmatrix} \begin{bmatrix} i_{sa} \\ i_{sb} \\ i_{sc} \\ i_{ra} \\ i_{rb} \\ i_{rc} \end{bmatrix} \tag{4.9}$$

A non-dimensional factor k factor is used to compute inductances between stator and rotor windings (m), magnetising inductance between stator windings (m_s) and the magnetising inductance between rotor windings (m_r). This factor has been analysed in electric machinery research and can be computed as:

$$k = \frac{\mu_0 \cdot \pi \cdot r \cdot l}{4\delta} \tag{4.10}$$

where r is the equivalent radius of the air gap, is the μ_0 vacuum permeability, l is the length of the air gap and δ is the thickness of the air gap.

The electromagnetic torque developed by the machine can be expressed in terms of the magnetic energy as (4.11):

$$\Gamma_{em} = \frac{\partial W_{mag}}{\partial \theta_m} = i_s^{\,T} \cdot \frac{\partial M_{sr}}{\partial \theta_m} \cdot i_r \tag{4.11}$$

The equations of the induction machine can be summarised as in (4.12):

$$\begin{aligned} V &= R \cdot i + \frac{dM}{dt} \cdot \omega_m \cdot i + M \cdot \frac{di}{dt} \\ \Gamma_{em} - \Gamma_{load} &= J_t \frac{d\omega_m}{dt} \\ \omega_m &= \frac{d\theta_m}{dt} \end{aligned} \tag{4.12}$$

where Γ_{load} is the mechanical load coupled with the rotor shaft and J_t is the total moment of inertia composed by the inertia of the load and the motor. The rotor output power can be expressed in terms of the space vectors of rotor voltage and current as follows:

$$P_r = -\mathrm{Re}\left\{V_r i_r^*\right\} = -\mathrm{Re}\left\{R_r i_r i_r^* + \frac{d\phi_r}{dt} i_r^* + j(\omega_s - \omega_m)\phi_r i_r^*\right\} \tag{4.13}$$

where ω_s is the synchronous angular speed, ω_s is the mechanical angular speed. The first term of (4.13) represents the rotor losses, the second is the magnetic energy variation and the third is the electromagnetic power developed by the machine.

Park's transformation

By applying the Park's transformation to the abc-reference equations of (4.14), the fifth-order model plus two mechanical equations can be obtained in (4.14):

$$\begin{aligned}
V_{sd} &= (R_s + L_s \frac{d}{dt}) i_{sd} + M \frac{d\, i_{rd}}{dt} - L_s \omega_\psi i_{sq} - M\ \omega_\psi\ i_{rq} \\
0 &= (R_r + L_r \frac{d}{dt}) i_{rd} + M \frac{d\, i_{sd}}{dt} - L_r(\omega_\psi - \wp\, \omega_m)\, i_{rq} - M\ (\omega_\psi - \wp\, \omega_m)\ i_{sq} \\
V_{sq} &= (R_s + L_s \frac{d}{dt}) i_{sq} + M \frac{d\, i_{rq}}{dt} + L_s \omega_\psi i_{sd} + M\ \omega_\psi\ i_{rd} \\
0 &= (R_r + L_r \frac{d}{dt}) i_{rq} + M \frac{d\, i_{rd}}{dt} + L_r(\omega_\psi - \wp\, \omega_m)\, i_{rd} + M\ (\omega_\psi - \wp\, \omega_m)\ i_{sd} \\
\Gamma_{em} - \Gamma_{load} &= J \frac{d\omega_m}{dt} \\
\omega_m &= \frac{d\theta_m}{dt}
\end{aligned} \tag{4.14}$$

Considering eq. (4.11), the electromagnetic torque developed by the IM can be obtained in *dq* components as (4.15):

$$\Gamma_{em}(t) = \wp\, i_s^T \cdot \begin{bmatrix} 0 & 0 & 0 \\ 0 & 0 & -M \\ 0 & M & 0 \end{bmatrix} \cdot i_r = \wp\, M\, (i_{rd} i_{sq} - i_{rq} i_{sd}) \tag{4.15}$$

Figure 4.3 shows the representation of the induction motor in two electrical circuits (i.e., direct and quadrature). The inductances L_s-M and L_r-M depicted in Figure 4.3 can be computed as in (4.16):

$$\begin{aligned}
L_s - M &= (l_s + \frac{1}{2} m_s) - \frac{3}{2} m \\
L_r - M &= (l_r + \frac{1}{2} m_r) - \frac{3}{2} m
\end{aligned} \tag{4.16}$$

Considering that the rotor windings is electrically reduced into the stator winding ($m_s = mr = m$), it can be seen that the stator and rotor leakage inductances are as follows:

$$L_s - M = (l_s + \frac{1}{2} m_s) - \frac{3}{2} m = l_s - m = L_{sd}$$
$$L_r - M = (l_r + \frac{1}{2} m_r) - \frac{3}{2} m = l_r - m = L_{rd} \quad (4.17)$$

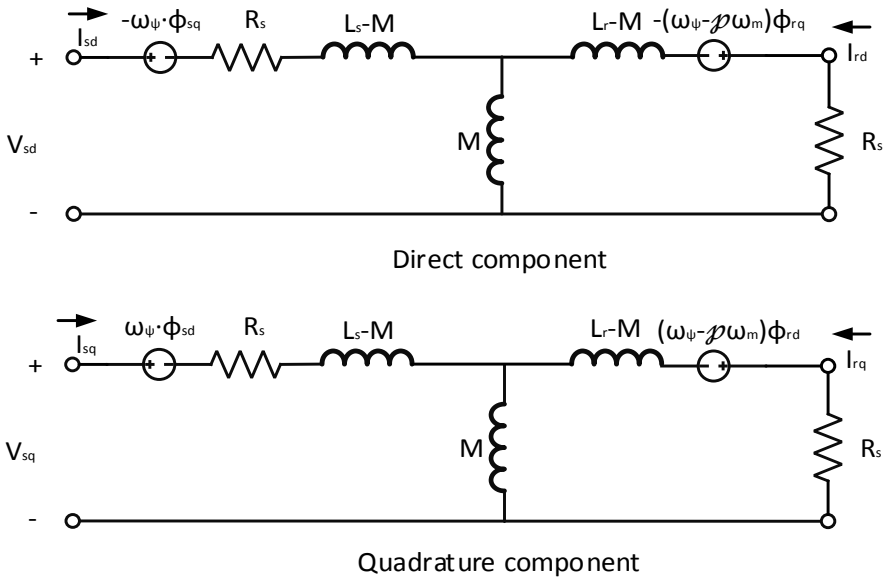

Figure 4.3: Electrical model of the induction machine in dq components.

Note that in this representation, the rotor mechanical speed has been multiplied by the IM pole pairs ($\wp$) and ω_ψ depends on the selected reference. The most commonly used references are: (i) synchronous reference, (ii) stator reference and (iii) rotor reference. These references are expressed down below in (4.18):

$$\begin{aligned} &Synchronous\ ref. \longrightarrow \psi_s = \int \omega_s(t)\, dt \\ &Stator\ ref. \longrightarrow \psi_s = 0 \\ &Rotor\ ref. \longrightarrow \psi_s = \wp\, \theta_m \end{aligned} \quad (4.18)$$

The synchronous reference is used in case ω_s is constant, this expression depends on the synchronous speed ($2\pi f$) where f is the system frequency (which is assumed constant in steady-state). In the present thesis, given the natural tendency of the IM to decelerate following the CB opening, and given the fact that the frequency of the island decreases with time, the stator reference will be used. Consequently, the set of Eqs. (4.14) is now converted, thus obtaining (4.19):

$$
\begin{aligned}
V_{sd} &= (R_s + l_s\frac{d}{dt})i_{sd} + M\frac{d\,i_{rd}}{dt} \\
0 &= (R_r + l_r\frac{d}{dt})i_{rd} + M\frac{d\,i_{sd}}{dt} + l_r(\wp\,\omega_m)\,i_{rq} + M\,(\wp\,\omega_m)\,i_{sq} \\
V_{sq} &= (R_s + l_s\frac{d}{dt})i_{sq} + M\frac{d\,i_{rq}}{dt} \\
0 &= (R_r + l_r\frac{d}{dt})i_{rq} + M\frac{d\,i_{sq}}{dt} - l_r(\wp\,\omega_m)\,i_{rd} - M\,(\wp\,\omega_m)\,i_{sd} \\
\Gamma_{em} - \Gamma_{load} &= J\frac{d\omega_m}{dt} \\
\omega_m &= \frac{d\theta_m}{dt}
\end{aligned}
\tag{4.19}
$$

Considering stator reference, Figure 4.3 is now converted into Figure 4.4.

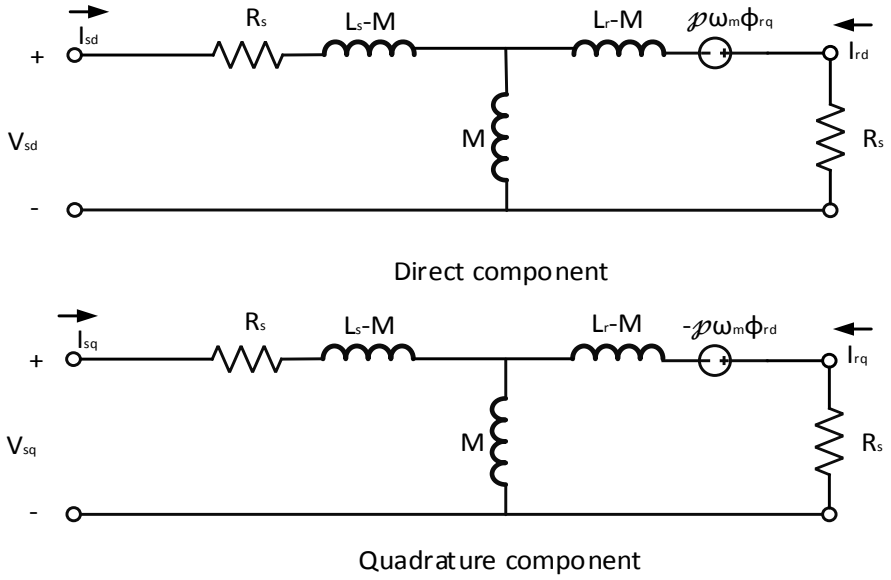

Figure 4.4: Electrical model of the induction machine in dq components in stator reference.

Lastly, the transformed stator voltages, rotor currents and stator currents from *dq* components into *abc* components with fixed stator reference are obtained applying the Park's anti-transformation:

$$
\begin{aligned}
V_{sa} &= \sqrt{\frac{2}{3}}V_{sd} & i_{sa} &= \sqrt{\frac{2}{3}}i_{sd} & i_{ra} &= \sqrt{\frac{2}{3}}i_{rd} \\
V_{sb} &= \sqrt{\frac{2}{3}}\cdot(-\frac{1}{2}\cdot V_{sd} + \frac{\sqrt{3}}{2}V_{sq}) & i_{sb} &= \sqrt{\frac{2}{3}}\cdot(-\frac{1}{2}i_{sd} + \frac{\sqrt{3}}{2}i_{sq}) & i_{rb} &= \sqrt{\frac{2}{3}}\cdot(-\frac{1}{2}i_{rd} + \frac{\sqrt{3}}{2}i_{rq}) \\
V_{sc} &= \sqrt{\frac{2}{3}}\cdot(-\frac{1}{2}\cdot V_{sd} - \frac{\sqrt{3}}{2}V_{sq}) & i_{sc} &= \sqrt{\frac{2}{3}}\cdot(-\frac{1}{2}i_{sd} - \frac{\sqrt{3}}{2}i_{sq}) & i_{rc} &= \sqrt{\frac{2}{3}}\cdot(-\frac{1}{2}i_{rd} - \frac{\sqrt{3}}{2}i_{rq})
\end{aligned}
\tag{4.20}
$$

Steady-state model of the IM

Obtain the model equations in steady-state becomes crucial to initialise a transient behaviour. Since a steady-state model considers the derivatives zero, the equations of the transient behaviour in the previous subsection will be used to obtain the steady-state model. If the machine is fed through a symmetric system of voltages (only the direct-sequence component of the voltage is considered), phase-voltages take this form:

$$\begin{aligned} V_{sa} &= \sqrt{2}V\sin(\omega_s t + \varphi) \\ V_{sb} &= \sqrt{2}V\sin(\omega_s t + \varphi_{-120^0}) \\ V_{sc} &= \sqrt{2}V\sin(\omega_s t + \varphi_{+120^0}) \end{aligned} \tag{4.21}$$

If the machine is considered under steady-state (i.e., derivatives are set to zero), the set of equations expressed in *dq* components of (4.19), are now expressed as in (4.22):

$$\begin{aligned} V_{sd} &= R_s i_{sd} \\ 0 &= R_r i_{rd} + l_r(\wp\,\omega_m)\, i_{rq} + l_m(\wp\,\omega_m)\, i_{sq} \\ V_{sq} &= R_s i_{sq} \\ 0 &= R_r i_{rq} - l_r(\wp\,\omega_m)\, i_{rd} - l_m(\wp\,\omega_m)\, i_{sd} \end{aligned} \tag{4.22}$$

The active and reactive-power drawn by the machine acting as a motor in *dq* components are defined in (4.23):

$$\begin{aligned} P &= v_{sd}\cdot i_{sd} + v_{sq}\cdot i_{sq} \\ Q &= v_{sq}\cdot i_{sd} - v_{sd}\cdot i_{sq} \end{aligned} \tag{4.23}$$

The equations to compute both active and reactive powers in steady-state and considering *abc* reference frame are expressed in (4.24):

$$\begin{aligned} P &= \mathrm{Re}\left\{V_{sa}\cdot I_{sa}^{*} + V_{sb}\cdot I_{sb}^{*} + V_{sc}\cdot I_{sc}^{*}\right\} = 3\,\mathrm{Re}\left\{V_s\cdot I_s^{*}\right\} \Leftrightarrow (V_{S(2)} = 0 \,\&\, I_{s(2)}^{*} = 0) \\ Q &= \mathrm{Im}\left\{V_{sa}\cdot I_{sa}^{*} + V_{sb}\cdot I_{sb}^{*} + V_{sc}\cdot I_{sc}^{*}\right\} = 3\,\mathrm{Im}\left\{V_s\cdot I_s^{*}\right\} \Leftrightarrow (V_{S(2)} = 0 \,\&\, I_{s(2)}^{*} = 0) \\ S &= V_{sa}\cdot I_{sa}^{*} + V_{sb}\cdot I_{sb}^{*} + V_{sc}\cdot I_{sc}^{*} = 3\left\{V_s\cdot I_s^{*}\right\} \Leftrightarrow (V_{S(2)} = 0 \,\&\, I_{s(2)}^{*} = 0) \end{aligned} \tag{4.24}$$

In (4.24) subindex (2) is referred to inverse-sequence component, therefore, if there is only direct sequence component for stator voltages and currents, the active and reactive powers drawn by the induction machine can be computed as $3VI^{*}$. The single-line diagram of the IM electrical model is depicted in the following Figure 4.5.

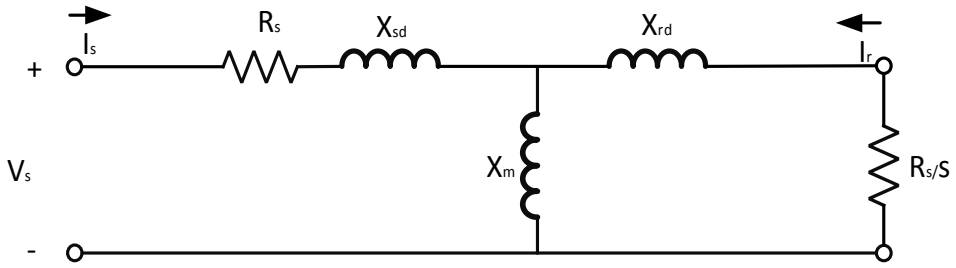

Figure 4.5: Electrical model of the induction machine for steady-state analysis.

where X_{sd} is the stator leakage reactance, X_{rd} is the rotor leakage reactance, X_M is the magnetizing reactance, and S is the slip between the synchronous speed and the rotor mechanical speed. These reactances are computed as (4.25):

$$M = \frac{X_m}{\omega}; L_s = \frac{X_{sd} + X_m}{\omega}; L_r = \frac{X_{rd} + X_m}{\omega} \tag{4.25}$$

In this subsection, the fifth-order mathematical model of the IM to study the transient behaviour as well as the simplified model to assess steady-state have been obtained. The mathematical model of the IM for transients will be used in stator reference and considering the *dq* components of the Park's transform as in (4.19) and represented by Figure 4.4. Secondly, the IM model in steady state is given by (4.22) and represented by Figure 4.5.

The initial point of operation of an IM can be defined utilizing the torque-speed curve provided by the manufacturer. As stated above, the initial values in steady-state will be of interest to evaluate the transient behaviour of the IM during the voltage sag originated by the fault.

The data of the IMs used in the simulations is summarised in Table 4.2.

Table 4.2: Induction motor data.

Internal parameters	**Values**	**Rated parameters**	**Values**
L_s	0.0078 H	P	160 kW
L_r	0.0078 H	$\wp$	1
R_r	0.0077 Ω	f	50 Hz
R_s	0.0137 Ω	V	400 V
L_m	0.0076 H	J	2.9 kgm^2

4.3.5 Protective devices

Protective devices can have a significant impact on IO. Certainly, the protection devices settings affect the duration of this IO. This section characterises the protective devices implemented in the model. Relay settings and its characteristic curves are critical factors to consider when designing the protective coordination between devices. Overcurrent protection is commonly used in radial DNs because of its simplicity for selectivity purposes. Therefore, the protections accounted here are 50/51 (phase-overcurrent) and 50/51N (neutral overcurrent), respectively. Note that the clearing time depends upon these curves and its settings.

Although a source working in parallel with the grid misscoordinates the protective equipment due to the change in the short-circuit current sensed by the main relays [4.17] which can cause serious issues, the main concern for DSOs is still being the IOs. A general overview of protections in distribution networks in the presence of DG sources has been analysed in [4.18]. As mentioned several times in the document, in this model, there are not DG but large IMs. As a consequence, we will only consider the main characteristics of overcurrent relays, its features are detailed down below. In case a curve is selected, its input is the line current of the three phases, and for the neutral calculation, it is computed as the vector sum of each one. On the other hand, the output is the clearing time composed of the operation time and pick up time. The most common used curves are; standard inverse (SI), very inverse (VI) or extremely inverse (EI) as can be seen in Figure 4.6. The operation time T of phase overcurrent is defined by equation (4.26):

$$T(I) = \frac{t \cdot K}{\left(\frac{I}{I_n \cdot I >}\right)^n - 1} \tag{4.26}$$

The operation time T_0 for earth overcurrent is then calculated as follows;

$$T_0(I) = \frac{t \cdot K_0}{\left(\frac{I_0}{I_n \cdot I_0 >}\right)^n - 1} \tag{4.27}$$

where factors K and K_0 are adjustable and typically ranged between 0.05 and 1.6, I is the picked up current by the relay, I_n is the rated current controlled by the relay, that is, the load current during regular operation, $I>$ is an acceptable overload factor, and n a factor to distinguish between relay curves. Particularly, n is 0.02 for SI, 1 for VI and 2 for EI, t is a factor which also depends on the curve, for SI is 0.14, for VI is 13.5 and for EI is 80. For ground faults, I_0 is the sum vector of the three picked up currents sensed by the relay, $I_0>$ is the factor between 0.1 and 0.8. Selectivity tasks define the time constraint. CB modelling is not unique because of some physical factors are involved (e.g., SF_6, oil or air insulation), a thorough study of CB characterisation can be found in [4.19]. Lastly, several preset reclosing operations are implemented into the relay, which are aimed at restoring the electrical supply after its tripping. Commonly, between three and four reclosing are used, where the first reclosing is typically fast, between 0.5 and 1 s. This fast reclosing plays a pivotal role because it defines the IO duration. The implemented settings in the relay located at the PCC_1 are summarised in Table 4.3.

Table 4.3: Over-current relay parameters.

ANSI code	k	n	t	$I_{threshold}$ (A)	I_{of}	ANSI Curve
50	0.05	0.02	0.14	100	1.25	Standard inverse
50n	0.05	2	80	20	-	Extremely inverse

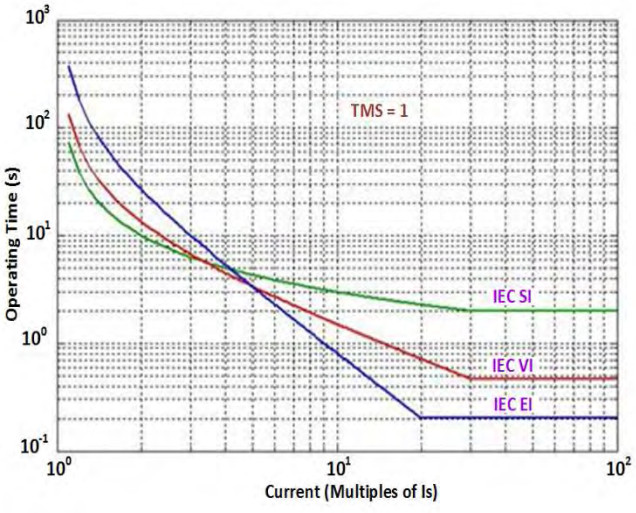

Figure 4.6: Time-current curves of overcurrent relays.

4.3.6 Load models

Load modelling has been evaluated for stability studies, for instance, see [4.20-4.22]. Other studies, such as [4.23], developed a method to estimate different load models from measurements.

In [4.24], the composite load models voltage and frequency dependence are evaluated, thereby, from this analysis, the equations for both active (4.28) and reactive (4.29) powers are derived:

$$\frac{P}{P_n} = \left(\frac{V}{V_n}\right)^{kpv} \cdot (1 + kpf \cdot \Delta f) \tag{4.28}$$

$$\frac{Q}{Q_n} = \left(\frac{V}{V_n}\right)^{kpv} \cdot (1 + kpf \cdot \Delta f) \tag{4.29}$$

where P_n and Q_n are the initial active and reactive powers, V is the initial value of voltage, V_n is the adjusted voltage, P and Q the active and reactive power with the adjusted voltage, Δf is the difference between the rated frequency (50 Hz) and the adjusted frequency, *kpv* is the exponential factor that varies from 0 to 2 depending on the load type, and *kpf* is the frequency sensitivity factor. It is relevant to point out the fact that in (4.28- 4.29), not only the voltage dependence is considered, but also the frequency dependence. Since a deviation in the supply frequency affects the power drawn by loads, this dependence has to be considered as a frequency sensitivity [4.25, 4.26]. Even though in this study frequency deviations occur during islanding, the loads are considered mainly resistive; therefore, they are not affected by this frequency deviation. Although there is not sufficient evidence (or field measurements) to select a given model, the model selected for each load provides a close enough simulation result to that obtained from measurements. Crucially, the appropriateness of the selected load models is evidenced in section 3 if one takes a look into the pre-fault values in column 9 and 10 of Table 4.4, feeder loads power is mainly active. Therefore, in the current implemented model, loads are only considered voltage dependents. Thence, the available three-phase dynamic load model of the specialised power systems toolbox library of Matlab is used [4.27]. Both active and reactive powers are defined by the following equations (4.30 - 4.31):

$$P(s) = P_o\left(\frac{V}{V_o}\right)^{np} \frac{1 + tp_{1s}}{1 + tp_{2s}} \tag{4.30}$$

$$Q(s) = Q_o\left(\frac{V}{V_o}\right)^{nq} \frac{1 + tq_{1s}}{1 + tq_{2s}} \tag{4.31}$$

where P_0 and Q_0 are the active and reactive powers at the initial voltage V_o, $P(s)$ and $Q(s)$ are the active and reactive powers a the adjusted voltage V, n_p and n_q are constants to model the three type of loads (i.e., if $n = 0$ the load is modelled as constant power if $n = 1$ the load is modelled as constant current and if $n = 1$ the load is modelled as constant impedance) and t_p and t_q are time constants. The rated power and the load models for each LV feeder loads are summarised in Table 4.3. Note, however, that the active and reactive at the time the fault occurs, does not have to meet this value due to the random pattern of costumers. In such a way, Figure 4.7 shows the real load profile for a half month in order to observe its effect on the survivability of the islanding events. During the period of the load profile depicted in this figure (between 15-01-16 and 30-01-16), four events were recorded. These events are highlighted in red circles.

Table 4.4: Feeder A loads rated value

Load Node	**Rated Voltage (V)**	**Rated P/Q (kW/kVAr)**	**Load model***
Node 15	400	30/4	Constant power
Node 16	400	100/20	Constant impedance

Node 17	400	300/45	Constant impedance
Node 18	400	600/-157	Induction motors
Node 19	400	100/10	Constant impedance
Node 20	400	30/4	Constant current
Node 21	400	25/10	Constant impedance
Node 22	400	200/80	Constant impedance
Node 23	400	40/18	Constant impedance

***** The load model type listed in the table is model type implemented in Matlab/Simulink. Although there is not sufficient evidence (or field measurements) to select a given model, the model selected for each load provides a close enough simulation result to that obtained from measurements.

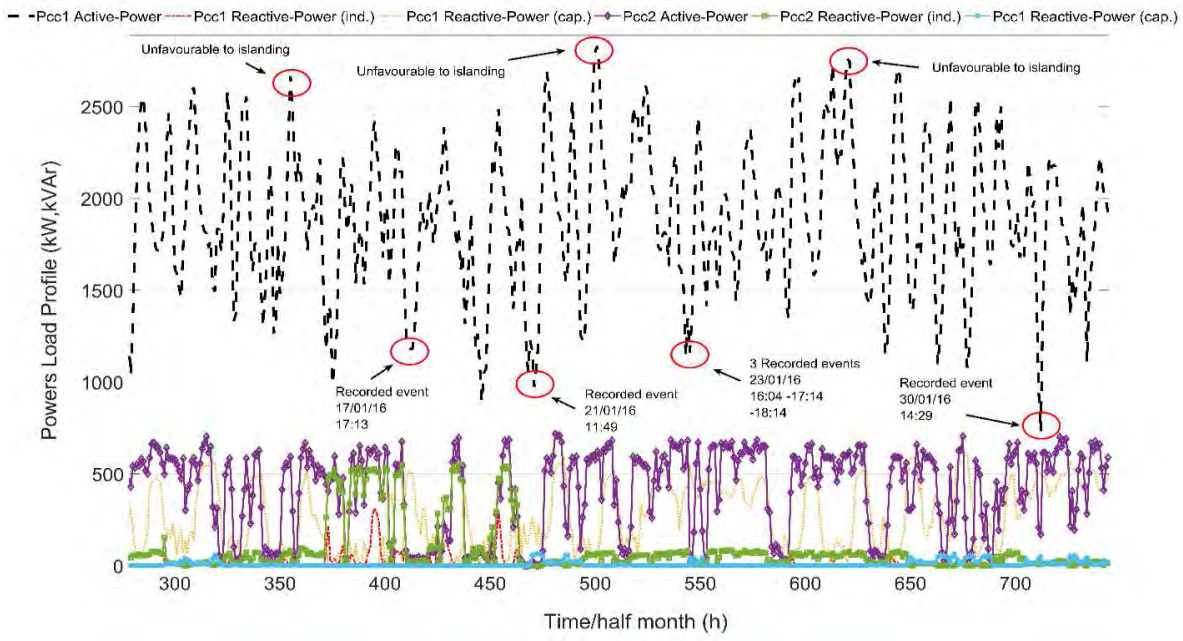

Figure 4.7: Load profile at PCC_1 with the time of occurrence of some events.

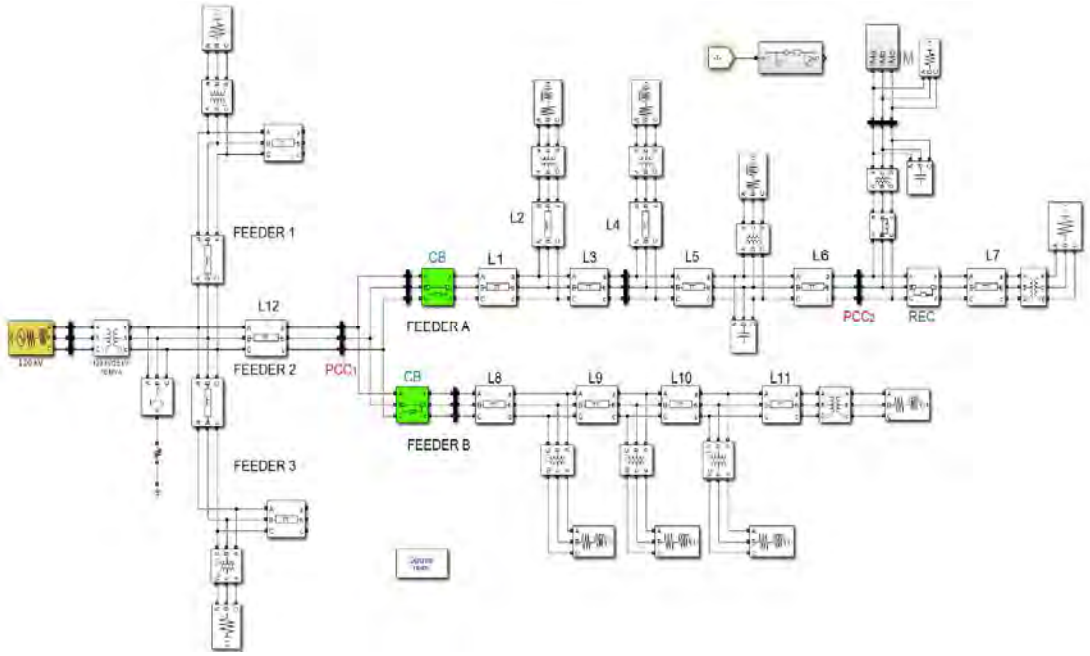

Figure 4.8: Three-phase Matlab/Simulink implementation of the test system.

4.3.7 Three-phase Model adopted

The test system model has been implemented in the MATLAB/Simulink environment using the specialised power systems toolbox library [4.28]. The three-phase model shown in Fig. 4.8 has been implemented in a computer with a processor of 3.6 GHz 8-core Intel i7 and 8 GB of RAM. The simulation has been conducted in a discrete mode with a fixed sample time of 50·µs, a solver based on the Dormand-Prince eight-order (RK8) method and a simulation time for all scenarios of 2.5 s.

4.4 IM behaviour during the fault

4.4.1 Introduction

The grid is feeding the induction machine when it is acting as a motor and its mechanical speed and torque define its point of operation. This point of operation is of utmost importance to determine the IM behaviour in steady stated and consequently, to initialise the transient state. In the previous Chapter 3, the general expression for all type voltage sags was obtained, resulting in a classification of 14 types of sags. In that chapter, it was demonstrated that depending on the type of network, some particularities have to be considered when assessing voltage sags. The procedure of this subsection is as follows:

- Define the initial conditions to initialise the transient state and provide the set of equations which dictate the behaviour of the IM during the fault, see ***subsection 4.4.2***.
- Given the particular type of DN and the IM windings connection, the voltage sags that can occur at IM terminals can be reduced from the 14 sag types obtained in Chapter 3. The main aim is to reduce the number of voltage sags to be studied. This discussion is done in ***subsection 4.4.3***.
- Assess the influence of the clearing time in this process. (***see subsection 4.4.4***)

It is worth highlighting that the results of this transient state will influence the next stage (i.e., the island). Thus, the initial conditions for the IO will be given by the results obtained in this transient state.

4.4.2 Transient behaviour during the fault

Initial variables

To obtain the values of the IM variables during the voltage sag (i.e., stator and rotor currents, mechanical speed and torque), the point of operation of the IM before the disturbance occurs is of paramount importance. Thus, in Figure 4.17, the procedure to obtain such point is described. It is worth mentioning that, although L. Guasch in [4.29] assessed the influence of voltage sags towards the IMs, it did not consider the IM as a bus in the electrical network. Instead, in the present study, the IM is viewed as a bus of the electrical grid, where the impedance seen by the IM is represented by its Thévenin equivalent (considering the main source, feeder impedances and feeder loads). The single-line diagram of this system is depicted in Figure 4.9, where Feeder 1 and 3 are not represented because the islanding process only occurs in Feeder 2. Note that by considering this Thévenin equivalent, the voltage across the IM stator before the fault and its point of operation, can be accurately determined.

As can be seen in 4.13, the first stage of the flowchart has two groups of inputs; the first is the IM data, including the type of torque and its value. Secondly, the grid parameters are introduced. From the first group of data, the IM internal parameters (i.e., R_r, R_s, L_{RD}, L_{SD}, M, $\mathscr{P}$) can be obtained. On the other hand, taking advantage of the second group of data, the Thévenin equivalent of the grid seen by the IM terminals (i.e., V_{th}, Z_{th}) can be determined. In Figure 4.9, the electrical loads are represented as shunt admittances framed in colours (e.g., green, yellow and purple), the step-down transformer is blue framed and, the IM is red framed.

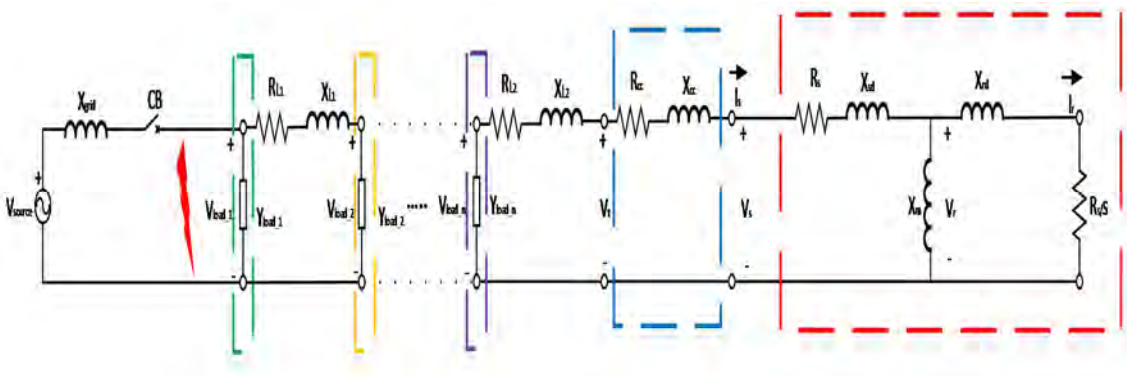

Figure 4.9: Single-line representation of the test system under study.

where X_{grid} is the grid reactance (this term includes the reactance of the grid and the reactance of the HV/MV transformer), Z_{cc} is the short-circuit impedance of the step-down transformer through which the IM is connected to the MV grid, Z_{L1} and Z_{L2} are the impedances of two MV lines, and Y_{load} represents the shunt admittance of loads.

Assuming negligible the voltage drop in the MV lines due to its short length, electrical loads can be grouped into one bus. Thus, this approximation will contain all feeder loads that remain within the island aggregated at the same bus. Considering this assumption, the scheme of 4.9 can be expressed as in Figure 4.10.

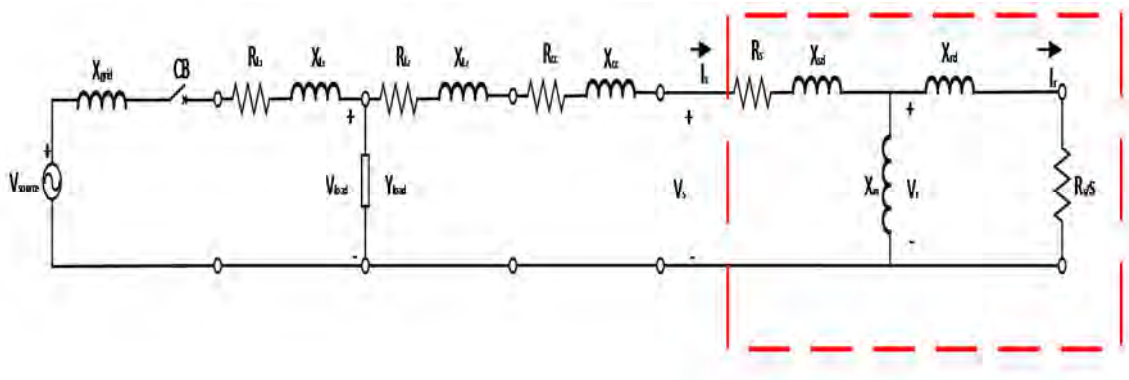

Figure 4.10: Equivalent circuit of the test system.

The thévenin equivalent seen by the stator windings is depicted in the following Figure 4.11.

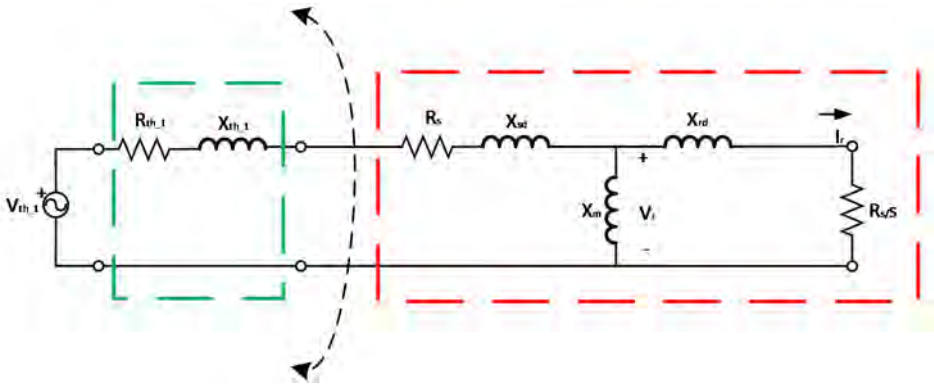

Figure 4.11: Thévenin equivalent seen by the IM stator.

The expression of the Thévenin equivalent seen by the IM is computed as follows:

$$Z_{th1} = \frac{(Z_{grid} + Z_{Line1}) \cdot Z_{load}}{(Z_{grid} + Z_{Line1}) \cdot Z_{load}} + Z_{Line2} + Z_{Transformer}$$

$$V_{th1} = \frac{Z_s}{Z_{stator} + (Z_{Line2} + Z_{Transformer}) + \frac{(Z_{grid} + Z_{Line1}) \cdot Z_{load}}{(Z_{grid} + Z_{Line1}) \cdot Z_{load}}} \cdot V_{source} \tag{4.32}$$

This Thévenin equivalent is designed as th_1.

Another Thévenin is now represented, this one is the equivalent seen by the IM magnetisation branch, expressed as th_2 and showed in Figure 4.12.

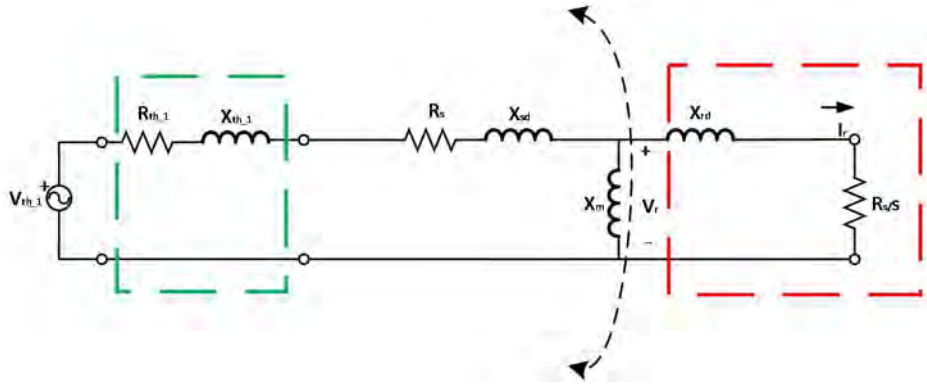

Figure 4.12: Thévenin equivalent seen by the IM magnetisation branch.

The expression of this second Thévenin equivalent seen by the IM magnetisation branch is depicted in Fig. 4.12 and computed as in (4.33):

$$Z_{th2} = \frac{(Z_{th1} + Z_{stator}) \cdot Z_M}{(Z_{th1} + Z_{stator} + Z_M)}$$
$$V_{th2} = \frac{Z_M}{Z_{stator} + Z_M + Z_{th1}} \cdot V_{source} \tag{4.33}$$

The second stage of the flowchart in 4.13 uses the parameters obtained in the first stage to obtain the IM in steady-state (i.e., i_{rd}, i_{rq}, i_{sd}, i_{sq}, Γ_{em}, ω_m) and the Thévenin equivalent and is obtained by applying equations (4.22-4.23). The subindex (0) is referred to as initial values.

The IM point of operation to initialise the transient state (i.e., initial conditions) has been obtained in the previously described stages. Therefore, the next step focuses on obtaining the voltages across the IM during the fault. By using the voltage divider of Eq. (4.34), the voltage sag across the IM stator is obtained. Afterwards, the stator voltages in the abc reference frame variables are converted into *dq* components as in (4.35).

Lastly, the transient state of the IM during the voltage sag is obtained by introducing these stator voltages into the set of differential equations in stator reference of (4.36). Note that the *dq* components of the stator voltage will depend on the type of fault and its location.

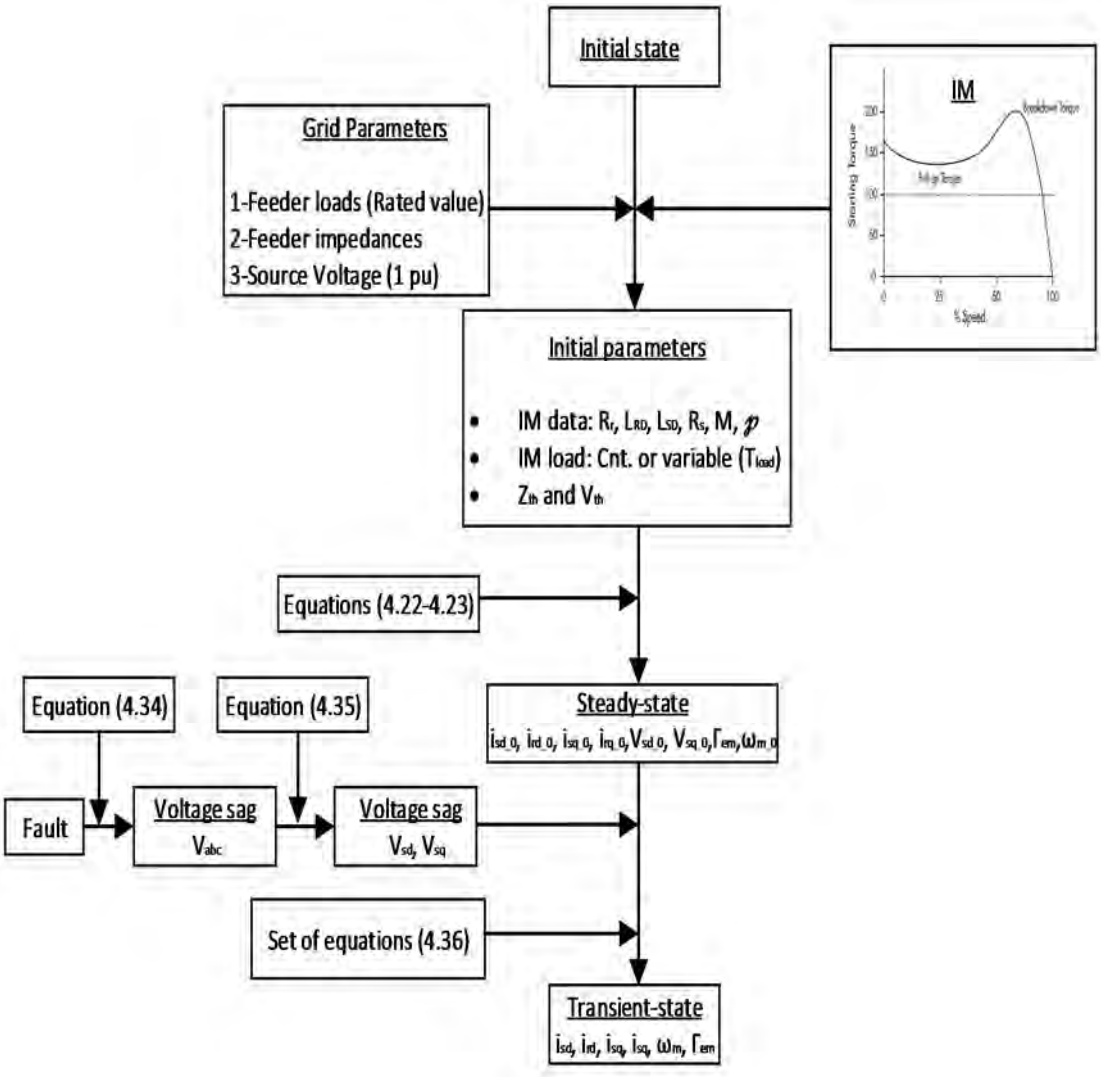

Figure 4.13: Flowchart to obtain the transient behaviour of the IM during the voltage sag.

The dynamic model to study the IM transient state is described by the following set of equations, where the input are the stator voltages (V_{sd} and V_{sq}) and the output, the stator and rotor currents, the rotor speed and rotor angle (i_{sd}, i_{sq}, i_{rq},, i_{rq}, ω_m, and θ_m). The voltage sag across the IM stator terminals (in *abc* components) is obtained from the voltage divider as in (4.34):

$$V_{s\_abc} = \frac{Z_{feeder}}{Z_{feeder} + Z_{source}} V_{source\_abc} \tag{4.34}$$

Since *abc* components can be converted into symmetrical components (with the Fortescue transform), similarly, the voltage sag at the IM stator terminals in *abc* components can be converted into the *dq* voltage components as follows:

$$\begin{aligned} V_{sa} &= \sqrt{\frac{2}{3}} V_{sd} \\ V_{sb} &= \sqrt{\frac{2}{3}} \cdot \left(-\frac{1}{2} \cdot V_{sd} + \frac{\sqrt{3}}{2} \cdot V_{sq}\right) \\ V_{sc} &= \sqrt{\frac{2}{3}} \cdot \left(-\frac{1}{2} V_{sd\_} - \frac{\sqrt{3}}{2} \cdot V_{sq}\right) \end{aligned} \tag{4.35}$$

Given the stator voltages as an input, by solving the set of equations in (4.36), the transient behaviour during the voltage sag is obtained.

$$
\begin{aligned}
V_{sd} &= (R_s + l_s\frac{d}{dt})i_{sd} + M\frac{d\,i_{rd}}{dt} \\
0 &= (R_r + l_r\frac{d}{dt})i_{rd} + M\frac{d\,i_{sd}}{dt} + l_r(\wp\,\omega_m)\,i_{rq} + M\,(\wp\,\omega_m)\,i_{sq} \\
V_{sq} &= (R_s + l_s\frac{d}{dt})i_{sq} + M\frac{d\,i_{rq}}{dt} \\
0 &= (R_r + l_r\frac{d}{dt})i_{rq} + M\frac{d\,i_{rd}}{dt} - l_r(\wp\,\omega_m)\,i_{rd} - M\,(\wp\,\omega_m)\,i_{sd} \\
\Gamma_{em} - \Gamma_{load} &= J\frac{d\omega_m}{dt} \\
\omega_m &= \frac{d\theta_m}{dt}
\end{aligned}
\tag{4.36}
$$

The set of differential equations of (4.36) with six equations and six unknown variables can be solved with numerical methods such as the Runge-Kutta-Fehlberg method, see [4.30]. As mentioned earlier, the initial values to start the iterative process are the ones obtained in the steady-state model, see parameters and Eqs. (4.22-4.23).

4.4.3 Influence of the fault-type

Introduction

In Chapter 3, a list of 14 types of voltage sags have been defined. However, some of them can be caused for faults upstream the CB of Feeder A (located at PCC_1) which cannot cause an IO. Thereby, in this section, only the voltage sags originated by faults which imply the opening of the CB in Feeder A (i.e., faults located downstream of this CB) will be considered. Since this thesis is evaluating the IO that occurs in Feeder A, either faults at neighbour MV feeders or the HV system do not cause an IO. Hence, the following assumptions are summarised down below:

1. Voltage sags originated at the HV transmission system are not considered.
2. Since the LV grids are typically protected with fuses, there are no reclosing operations
3. The type of network under study is resistance-grounded via a zig-zag transformer.
4. Only the effects of one transformer will be considered (i.e., the step-down MV/LV transformer).
5. Other voltage sags due to IM starting or transformer energisation are dismissed because they do not imply the operation of the CB located at PCC_1.

Voltage sags grouping

Considering the above assumptions, the following casuistry is taken into consideration:

- A SLG fault at the MV grid causes a voltage sag type B, and given the step-down transformer windings connection, a voltage sag type C is expected at the LV side. The voltage sag type B will not be considered at the IM terminals because faults at the LV grid are not considered.
- Either a LL or LLG fault at the MV grid causes a voltage sag Type D (see Figs. 3.14 and 3.15 of Chapter 3). Even though the voltage sag produced is the same, the recovery is slightly different. Therefore, these two types of faults will be considered.
- A LLL fault at the MV grid cause a voltage sag type A_2 at the LV grid.

- An LLLG fault at the MV grid cause a voltage sag type A_4 at the LV grid.

Table 4.5 shows a summary of the faults originated at the MV grid which have been considered. The third column of this Table shows the voltage sag at the LV network after a Dy transformer.

Table 4.5: Voltage sags grouping.

Fault	Location of the voltage sag	
	I (MV)	II (LV)
SLG	B	C
LLG	E	D
LL	E	D
LLL	A_1	A_2
LLLG	A_3	A_4

4.4.4 Clearing time influence

As stated in the modelling section 4.3.5, the clearing time is dictated by the relay settings. The process that takes place when a fault occurs is described further on. The first cycles (typically between 4 and 6) after the fault occurrence, the IMs contribute towards the fault. Along with this contribution, it experiences a deceleration which is prolonged during the sag. After that, once the voltage sag recovers, the machine reaccelerate [4.31], and return to the initial point of operation. However, for large clearing times, the voltage sags will force the IM to stall. In [4.32], an analytical expression is provided to compute the critical voltage sag clearing time.

The influence of voltage sags into induction motors have been the object of study in several studies, among them, L. Guasch *et at.* in [4.33]. On the other hand, the behaviour of the double-fed-induction machine during voltage sags (both symmetrical and non-symmetrical) in wind power applications has been investigated by A. Rolan in [4.35]. On the other hand, interesting research is carried out by F. Córcoles *et al.* in [4.36-4.37] where the voltage sags are assessed. In these three works, the IM deceleration during the voltage sag has been considered negligible (below 1%) due to the brief duration of the sag (e.g., around 60 ms). Nonetheless, in distribution networks, the clearing times can be longer (e.g., see [4.38]). Frequently, faults at the MV grid exceed this duration (e.g., an average value may be around 200 ms). As a consequence, the speed derivative during the voltage sag cannot be assumed zero in the present thesis.

4.5 Islanding operation

4.5.1 Overview

The current section is divided into two parts; the first gives a brief overview of the islanding process and presents the mathematical model of the IM during the island. The second one is aimed at describing the principal influential factors into the IO.

To emphasise the importance of this phenomenon, as an example, Fig. 4.14 shows the simulated three-phase voltages of two scenarios; one scenario with IMs (solid lines) and another one replacing the IMs (dashed lines) with a static load of the same rated power. By carefully observing

this Figure between the fault clearing (t = 0.9 s) and the CB reclosing (t = 1.4 s), one can notive that the IMs are energising the isolated feeder A once its CB has opened. On the other hand, when the IMs are replaced with static loads, as expected, an interruption occurs.

Furthermore, to provide more evidence that following the CB the IM is energising the DN and acting as a generator, Figure 4.15 plots the active-power recorded at the PCC_2 where IMs are connected. In this figure, it can be seen that before the fault appears (t = 0.8 s) the induction machine is acting as a motor (i.e., the measured active power is positive), but once the fault is cleared, the power becomes negative. This fact undeniably demonstrates that the IMs are transiently acting as generators.

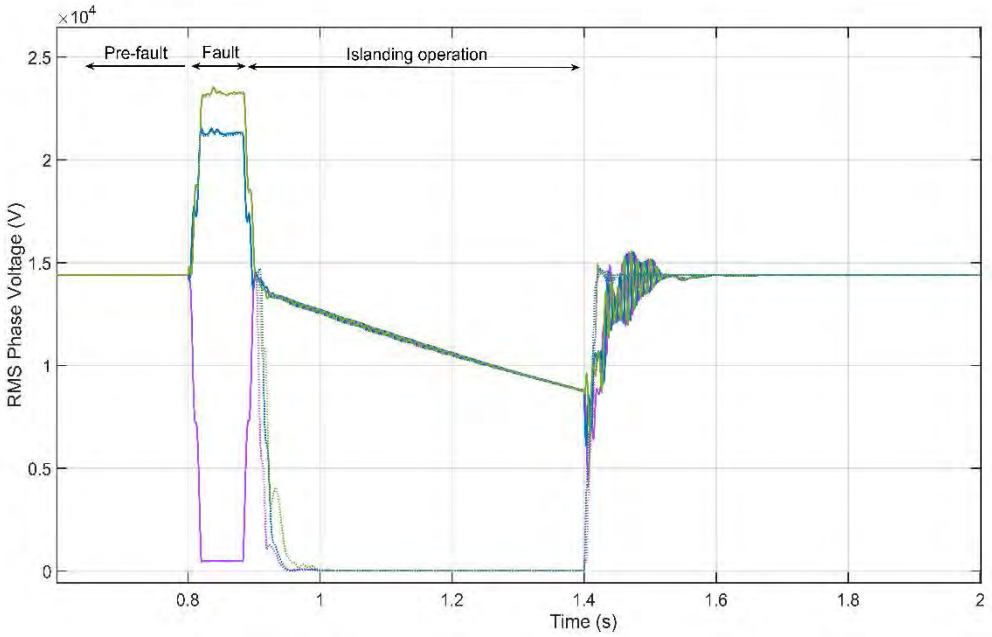

Figure 4.14: Phase-voltage comparison scenarios with and without IMs.

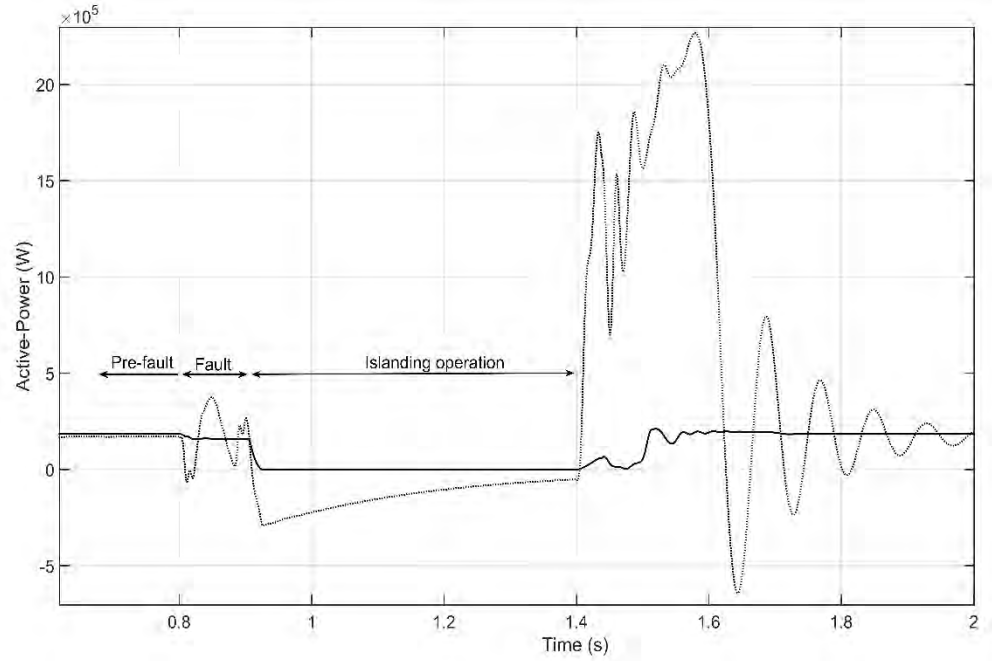

Figure 4.15: Phase voltage comparison scenarios with and without IMs.

4.5.2 IM Mathematical model during the island

As seen in the previous subsections 4.4.2 to 4.4.4, during the fault, the IM tend to decelerate. This deceleration depends on the severity of the originated voltage sag (i.e., magnitude and duration). Once the CB clears the fault, the motor is disconnected from the grid, and due to its inertia, transiently act as a generator. The initial kinetic energy before the IO begins (i.e., the speed once the voltage sag has recovered) is as follows:

$$E_{Kin\_initial} = \frac{1}{2} J_T \omega_{pre\_islanding}{}^2 \tag{4.37}$$

where $E_{Kin\_initial}$ is the initial kinetic energy before the CB opening, J_T the total moment of inertia (considering the rotor inertia and mechanical load), and $\omega_{pre\_islanding}$ is the mechanical speed before the island is formed. Following the CB opening, due to the lack of supply, the equilibrium between torques is broken, the IM speed derivative becomes negative and, thereby, only the dynamic torque (i.e. the torque due to the non-zero derivative of the rotor speed) drives the machine. Hence, the mechanical equation in (4.36) can now be rewritten as (4.38):

$$-\left(\Gamma_{load}\right) = J_T \frac{d\omega_m}{dt} \tag{4.38}$$

Before the fault, the electromagnetic torque of the IM acting as a motor is by convention positive. This fact can be observed before the fault occurs (before t = 0.8 s) in Figure 4.16. During the voltage sag, the torque is oscillatory (between t = 0.8 s and t= 0.9 s). Once the main CB has opened (at t = 0.9 s), the dynamic torque drives the machine; its speed derivative and electromagnetic torque are both negative when acting as a generator (between t = 0.9 s and t = 1.4 s). Note that the high torque that occurs once the CB recloses (t = 1.4 s) is due to the out-of-phase reclosing. This reclosing transient can be more or less severe depending on the voltage amplitude and frequency difference between sources (i.e., the main grid and the island).

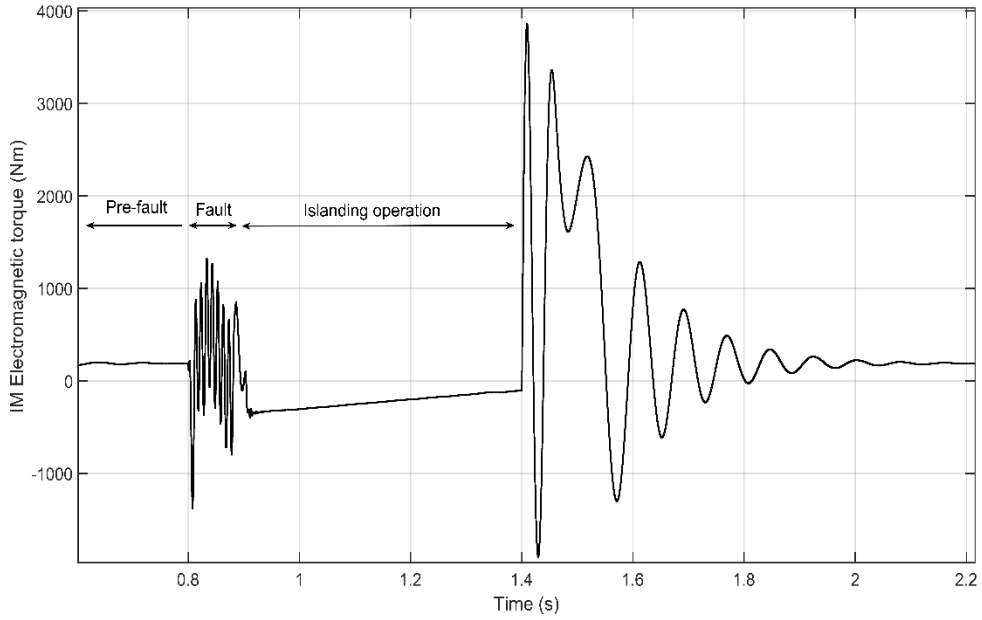

Figure 4.16: Electromagnetic torque developed by the IM.

The procedure to obtain the transient behaviour of the IM during the IO is detailed in Figure 4.17. The first stage provides the initial values for the IO, which are obtained from the previous section where the transient state during the voltage sag has been evaluated.

To assess the IO, the reduced grid scheme of Figure 4.10 will be used, where all feeder loads have been grouped in one bus.

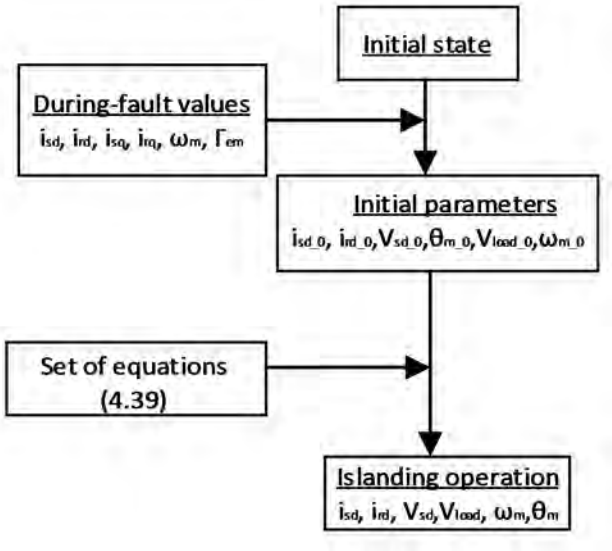

Figure 4.17: Flowchart to obtain the transient behaviour of the IM during islanding.

As can be seen in Fig. 4.10, the variables of interest for the IO are (i_{sd}, i_{rd}, V_{sd}, ω_m, θ_m, V_{load}). Since there is no noticeable load unbalance during the islanding, only d-component is considered, and the q-component of stator voltages, rotor currents and stator currents is set to zero. By solving the set of six differential equations with six unknown variables in (4.39), the transient state of the IM during the island is obtained.

$$
\begin{aligned}
V_{sd} &= (R_s + l_s \frac{d}{dt}) i_{sd} + M \frac{d\, i_{rd}}{dt} \\
0 &= (R_r + l_r \frac{d}{dt}) i_{rd} + M \frac{d\, i_{sd}}{dt} \\
0 &= M \frac{d\, i_{rd}}{dt} - l_r (\wp\, \omega_m)\, i_{rd} - M\ (\wp\, \omega_m)\, i_{sd} \\
0 - \Gamma_{load} &= J \frac{d\, \omega_m}{dt} \\
\omega_m &= \frac{d\, \theta_m}{dt} \\
V_{sd} &= i_{sd} \cdot (Z_{line} + Z_{load})
\end{aligned}
\tag{4.39}
$$

As mentioned earlier in subsection 4.3.6, if a voltage-dependence load model is considered, three types of load models can be used. Therefore, the term Z_{load} of (4.39), can be computed as a mix of the aforementioned three load models:

$$
Z_{load} = (\frac{|V_{load}{}^2|}{P_{load} + jQ_{load}}) + (R_{load} + jX_{load}) + (\frac{V_{load}}{I_{cnt\,load}}) \tag{4.40}
$$

The voltages and currents are now rewritten by separating stator and rotor components:

$$\begin{aligned} V_s &= R_s \cdot i_s + \frac{d\phi_s}{dt} + j\omega\cdot\phi_s = R_s \cdot i_s + \frac{di_s}{dt}M + \frac{dM}{dt}\omega\cdot i_s \\ 0 &= R_r \cdot i_r + \frac{d\phi_r}{dt} + j(\omega-\omega_r)\cdot\phi_r = R_r \cdot i_r + \frac{di_r}{dt}M + \frac{dM}{dt}(\omega-\omega_r)\cdot i_r \end{aligned} \tag{4.41}$$

where ω can be computed as $2\pi f$, being f the frequency of the system and, ω_r the rotor speed. If the rotor resistance is neglected, the time derivative of the rotor flux linkage with respect to time can be obtained as follows:

$$\begin{aligned} 0 &= \frac{d\phi_r}{dt} + j(\omega-\omega_r)\cdot\phi_r = \frac{di_r}{dt}M + \frac{dM}{dt}j(\omega-\omega_r)\cdot i_r \\ 0 &= \frac{d\phi_r}{dt} + j(\omega-\omega_r)\cdot\phi_r \rightarrow \phi_r = \int_{ti}^{tf} -(\omega-\omega_r)\cdot\phi_r\, dt \rightarrow \phi_r = \phi_{r\_0}\cdot e^{-j(\omega-\omega_r)t} \end{aligned} \tag{4.42}$$

Once the CB has opened, the remnant magnetic flux at the rotor forces the IM to behave as a generator, see [4.39]. Therefore, the rotor flux derivative with respect to time is deduced from (4.42), which depends on the rotor initial magnetic flux (ϕ_{r_0}) as well as on the rotor mechanical speed ω_r. The relationship between current and magnetic fluxes are expressed with the following matrix equation:

$$\begin{bmatrix} \phi_s \\ \phi_r \end{bmatrix} = \begin{bmatrix} M_{ss} & M_{sr} \\ M_{rs} & M_{rr} \end{bmatrix} \cdot \begin{bmatrix} i_s \\ i_r \end{bmatrix} \tag{4.43}$$

If the stator flux is set to zero due to the lack of external supply, the remnant magnetic rotor flux can be computed as:

$$\begin{aligned} 0 &= M_{ss}\cdot i_s + M_{sr}\cdot i_r \\ \phi_r &= M_{rs}\cdot i_s + M_{rr}\cdot i_r \rightarrow \phi_{r\_0}\cdot e^{-j(\omega-\omega_r)t} = M_{rs}\cdot i_s + M_{rr}\cdot i_r \end{aligned} \tag{4.44}$$

Indeed, the induced voltage across the IM magnetisation branch is due to this remnant magnetic flux available at the rotor winding at the time the fault occurs, which in turn, is maintained by the rotor speed while the rotor it is driven by the transient dynamic torque. When the motor is acting as a generator, this voltage can be represented as a voltage behind a transient reactance. If the IM stator resistance is neglected, this voltage can be computed with the following equation:

$$E_r = \left(j\omega_r \cdot \frac{M_{sr}}{M_{rr}} \cdot \phi_r\right) \cdot e^{-j(\omega-\omega_r)t} \tag{4.45}$$

The voltage behind the transient reactance ($E_{r\angle\delta_{im}}$) can be defined as a sinusoidal and balanced, and the frequency of this voltage is determined by the IM rotor speed (ω_r). Thereby, a slip can be defined between the frequency of the island and the frequency of the main grid. To observe the relationship between the IM rotor angle, its mechanical speed and the frequency of the island, see Eq. (4.50). The voltage at the IM terminals during the island (V_{sd}) is obtained by solving the set of differential equations (4.39-4.40). However, it can alternatively be computed as the voltage behind the transient reactance plus the voltage drop across the stator winding, see equation (4.46).

$$V_s = jX_s\cdot i_s + E_r \tag{4.46}$$

where X_s is the stator leakage reactance.

The reduced test system shown in Figure 4.10, was used to represent the system before and during the fault. However, once the CB has opened, the system is represented by Figure 4.18. In this Figure, the rotor winding plus the magnetisation branch are being replaced by the equivalent source behind the transient reactance (if stator and rotor resistances are both neglected). In case no load is connected with the stator, the voltage at the IM main terminals is the same as the one obtained across the magnetisation branch, however, if the load is connected to the IM terminals, a certain voltage drop takes place across the stator inductance.

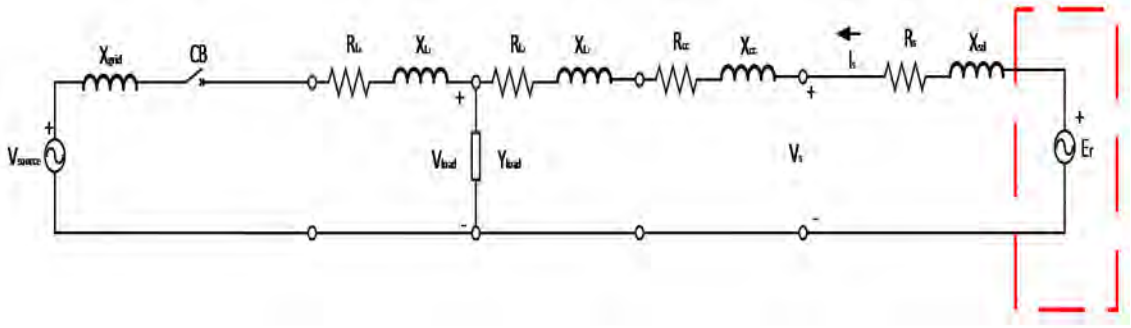

Figure 4.18: Single-line diagram of reduced test system before islanding.

Once the CB has opened the circuit, the impedance of the line Z_{L1} can be neglected because no current is flowing through this impedance, and therefore, the single-line diagram of the system during the island is depicted in Figure 4.19. As mentioned earlier, the amount of feeder loads in the island are grouped into one bus and expressed with the term Z_{load}.

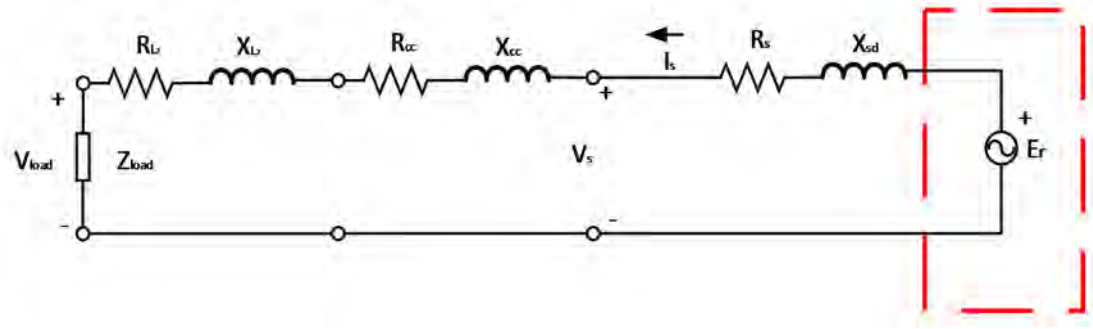

Figure 4.19: Single-line diagram of the reduced scheme of the system during islanding.

where X_{sd} is the stator leakage reactance, Z_{cc} is the short-circuit impedance of the MV/HV transformer, Z_{L1} is the line impedance and Z_{load} represents load impedance (i.e., the sum of all feeder loads grouped in one bus).

Alternatively, the IM speed derivative during the islanding can be computed by using the classical stability equation. Thus, if it is assumed that the IM is under no-load torque at the time the fault occurs (i.e., that there is no mechanical load coupled to the rotor shaft) and considering that there is no damping effect while acting as generator, the balance during the island is given by:

$$\frac{d\omega_{im}}{dt} = \frac{1}{2H_{im}}[Pm - Pe_{load}] \tag{4.47}$$

$$\frac{d\delta_{im}}{dt} = \omega_{im} - \omega_{im0} \tag{4.48}$$

where ω_{im} is the IM angular speed, ω_{im0} is IM initial angular speed, δ_{im} is the IM rotor angle, P_m is the mechanical power developed by the IM when acting as a generator, P_{eload} is the power drawn by the feeder loads, and H_{im} is the inertia constant of the IM expressed in seconds.

The variation over time of the IM rotor angle during the island (i.e., between t_i and t_f) is related to the frequency during islanding as follows:

$$\Delta\delta_{im} = \int_{ti}^{tf} \Delta\omega_m \; dt = \frac{1}{2\pi}\int_{ti}^{tf} \Delta f_{island} \; dt \tag{4.50}$$

where f_{island} is the frequency during the island and δ_{im} is the IM rotor angle.

As for the impedance load calculation (i.e., the term Z_{load} of (4.40)), if we consider voltage-dependence load models, the term P_{eload} has to be also divided into three different terms. The power drawn by the loads in the island are divided into term P_1 which is assumed to be the sum of all constant impedance loads, P_2 represents the sum of all constant current loads and, P_3 is the sum of all constant power loads. Whereby, the term P_{eload} has the following expression:

$$Pe_{load} = \frac{P_1}{|\Delta V|^2} + \frac{P_2}{|\Delta V|} + P_3 \tag{4.51}$$

where ΔV represents the voltage variation, P_1, P_2, P_3 are the sum of all constant impedance, constant current and constant power, which individually are computed as follows:

$$P_1 = \sum_{i=0}^{n} P_i \;\; ; P_2 = \sum_{j=0}^{n} P_j \;\; ; P_3 = \sum_{k=0}^{n} P_k \tag{4.52}$$

Note that in equation (4.47), the active-power losses term has been neglected due to the short MV line lenghts.

4.5.3 Islanding influential factors

As can be appreciated from the previous equations in subsection 4.5.2, the rotor magnetic flux at the precise moment when the island is initiated (i.e., remnant magnetic flux), is of utmost importance to assess the IO. Based on the mathematical evaluation of the previous subsections, the influential factors of this IO are listed down below:

- The type and value of the load torque coupled with the IM rotor shaft.
- The IM inertia.
- The IM point of operation in steady-state.
- The type of fault that originated the IO.
- The duration of the IO.

4.6 Conclusions

In general terms, this chapter has described the theoretical analysis of the IO and the main influential factors have been identified.

Firstly, the single-line diagram of the test system under investigation have been defined in subsection 4.2. In it, the data of the network such as the type of grounding, the number of transformers and its rated capacity and line impedances are provided. After that, the description of the model is done in section 4.3. Particularly, each element of the model is detailed in a separate subsection (e.g., transformers, transmission lines, CBs, IMs and load models). The three-phase implemented model in Matlab/Simulink is shown in 4.3.7.

Secondly, once the system components have been described, the mathematical model of the IM before the island can be established. Thus, the IM modelling is analysed in both steady-state (i.e., non-linear set of equations (4.22-4.23) to obtain pre-fault point of operation) and transient state (i.e., the set of differential equations in (4.36)). Hence, subsection 4.4 analyses the transient behaviour of the IM during the fault, which proved to be crucial for the islanding evaluation. To successfully perform this analysis, the pre-fault IM point of operation and grid parameters are of utmost importance.

The procedure to obtain the transient behaviour of the IM during the fault is depicted in Figure 4.13. Besides, in this subsection, a reduced group of sags is proposed in order to reduce the number of scenarios to be evaluated. Thus, only the faults that occur in the MV network are of interest, and as a consequence, the voltage sags originated by events that do not imply a CB operation are dismissed**.** Among these events, we can find voltage sags due to faults at HV transmission system, voltage sags due to IM starting in the same feeder or faults in neighbour MV feeders. Accordingly, in this section, only five voltage sag types are analysed instead of the full list of fourteen types defined in Chapter 3.

Thirdly, the IO is assessed in subsection 4.5. The procedure to obtain the variables during the IO is shown in Figure 4.17. The main variables of the system during the island are obtained by solving the set of differential equations (4.39-4.40), where the initial conditions are the ones obtained after the voltage sag recovery (i.e., the end of the voltages sag, see the previous section 4.4).

To sum up, this Chapter has defined the model used to represent the IO and has provided the mathematical equations of each element individually. The dependability of the analytical expressions detailed in this Chapter will be demonstrated in the subsequent Chapters 5, 6 and 7 (i.e., simulations, Field measurements and Model validation). Furthermore, to support the feasibility of the analytical analysis of this Chapter, three Figures have been provided (4.14-4.16). In these Figures, the feasibility of this IO is demonstrated by making a comparison between one scenario with IMs and another one without them.

4.7 References

[4.1] J. A. Martinez, *Power System Transients: Parameter Determination, Book Review*, vol. 8, no. 6. 2010.

[4.2] J. A. Martinez, B. Johnson, and C. Grande-Moran, "Parameter determination for modeling system transients-Part IV: Rotating Machines," *IEEE Trans. Power Deliv.*, vol. 20, no. 3, pp. 2063–2072, 2005.

[4.3] J. A. Martinez, B. Gustavsen, and D. Durbak, "Parameter determination for modeling system transients- Part I: Overhead lines," *IEEE Trans. Power Deliv.*, vol. 20, no. 3, pp. 2038–2044, Jul. 2005.

[4.4] G. K. Papagiannis, T. A. Papadopoulos, and A. I. Chrysochos, "Rigorous calculation method for resonance frequencies in transmission line responses," *IET Gener. Transm. Distrib.*, vol. 9, no. 8, pp. 767–778, 2015.

[4.5] T. A. Papadopoulos, A. I. Chrysochos, and G. K. Papagiannis, "Analytical study of the frequency-dependent earth conduction effects on underground power cables," *IET Gener. Transm. Distrib.*, vol. 7, no. 3, pp. 276–287, 2013.

[4.6] T. A. Papadopoulos, D. A. Tsiamitros, and G. K. Papagiannis, "Impedances and admittances of underground cables for the homogeneous earth case," *IEEE Trans. Power Deliv.*, vol. 25, no. 2, pp. 961–969, Apr. 2010.

[4.7] IEEE, *IEEE Standard for General Requirements for Liquid-Immersed Distribution, Power, and Regulating Transformers*. 2016.

[4.8] W. L. A. Neves and H. W. Dommel, "Saturation Curves of Delta-Connected Transformers from Measurements," *IEEE Trans. Power Deliv.*, vol. 10, no. 3, pp. 1432–1437, Jul. 1995.

[4.9] J. A. Martinez, R. Walling, B. A. Mork, J. Martin-Arnedo, and D. Durbak, "Parameter determination for modeling system transients-Part III: Transformers," *IEEE Trans. Power Deliv.*, vol. 20, no. 3, pp. 2051–2062, Jul. 2005.

[4.10] F. de León and J. A. Martinez, "Dual three-winding transformer equivalent circuit matching leakage measurements," IEEE Trans. Power Deliv., vol. 24, no. 1, pp. 160–168, Jan. 2009.

[4.11] A. Rezaei-Zare, "Enhanced transformer model for low- and mid-frequency transients-part II: Validation and simulation results," *IEEE Trans. Power Deliv.*, vol. 30, no. 1, pp. 316–325, Jul. 2015.

[4.12] A. Gómez-Expósito, A. J. Conejo, and C. Cañizares, *Electric Energy Systems*, vol. 17. 2008.

[4.13] J. C. Das, Transients in Electrical Systems. McGraw-Hill, 2010.

[4.14] F. Corcoles, J. Pedra, M. Salichs, and L. Sainz, "Analysis of the induction machine parameter identification," *IEEE Trans. Energy Convers.*, vol. 17, no. 2, pp. 183–190, Jun. 2002.

[4.15] J. Pedra, "Estimation of typical squirrel-cage induction motor parameters for dynamic performance simulation," *IEE Proc. Gener. Transm. Distrib.*, vol. 153, no. 2, pp. 137–146, 2006.

[4.16] L. Monjo, H. Kojooyan-Jafari, F. Corcoles, and J. Pedra, "Squirrel-cage induction motor parameter estimation using a variable frequency test," *IEEE Trans. Energy Convers.*, vol. 30, no. 2, pp. 550–557, 2015.

[4.17] V. A. Papaspiliotopoulos, G. N. Korres, V. A. Kleftakis, and N. D. Hatziargyriou, "Hardware-In-the-Loop Design and Optimal Setting of Adaptive Protection Schemes for Distribution Systems with Distributed Generation," *IEEE Trans. Power Deliv.*, vol. 32, no. 1, pp. 393–400, Feb. 2017.

[4.18] K. Jia, H. Wei, T. Bi, D. W. P. Thomas, and M. Sumner, "An Islanding Detection Method for Multi-DG Systems Based on High-Frequency Impedance Estimation," *IEEE Trans. Sustain. Energy,* vol. 8, no. 1, Jan. 2017.

[4.19] J. A. Martinez, J. Mahseredjian, and B. Khodabakhchian, "Parameter Determination for modeling system transients-Part VI: Circuit Breakers," *IEEE Trans. Power Deliv.*, vol. 20, no. 3, pp. 2079–2085, Jul. 2005.

[4.20] F. Corcoles, J. Pedra, M. Salichs, and L. Sainz, "Analysis of the induction machine parameter identification," *IEEE Trans. Energy Convers.*, vol. 17, no. 2, pp. 183–190, Jun. 2002.

[4.21] K. P. Schneider, J. C. Fuller, and D. P. Chassin, "Multi-state load models for distribution system analysis," *IEEE Trans. Power Syst.*, vol. 26, no. 4, pp. 2425–2433, 2011.

[4.22] M. C. Alexiadis, G. K. Papagiannis, and I. P. Panapakidis, "Enhancing the clustering process in the category model load profiling," *IET Gener. Transm. Distrib.*, vol. 9, no. 7, pp. 655–665, 2015.

[4.23] D. J. Hill, "Nonlinear dynamic load models with recovery for voltage stability studies," *IEEE Trans. Power Syst.*, vol. 8, no. 1, pp. 166–176, Feb. 1993.

[4.24] H. Li, Q. Chen, C. Fu, Z. Yu, D. Shi, and Z. Wang, "Bayesian Estimation on Load Model Coefficients of ZIP and Induction Motor Model," *Energies,* vol. 12, no. 3, p. 547, 2019.

[4.25] IEEE Task Force on Load Representation for Dynamic Performance, "Load representation for dynamic performance analysis (of power systems)," *IEEE Trans.*

Power Syst., vol. 8, no. 2, May. 1993.

[4.26] Z. Zhang, H. Yang, X. Yin, J. Han, Y. Wang, and G. Chen, *"*A load-shedding model based on sensitivity analysis in on-line power system operation risk assessment,*" Energies,* vol. 11, no. 4, 2018.

[4.27] M. Farrokhabadi, C. A. Cañizares, and K. Bhattacharya, "Frequency control in isolated/islanded microgrids through voltage regulation," *IEEE Trans. Smart Grid,* vol.8, no. 3, May. 2017.

[4.28] Simulink Power Systems library. "MATLAB 2015-MathWorks Doc.," *www.mathworks.com/products/matlab*, 2016.

[4.29] L. Guasch (2006). "*Efectos de los huecos de tensión en las máquinas de inducción y en los transformadores trifásicos"* (PhD Thesis dissertation). UPC, Barcelona, 2006.

[4.30] L. Guasch, F. Córcoles, and J. Pedra, "Effects of symmetrical and unsymmetrical voltage sags on induction machines," IEEE Trans. Power Deliv., vol. 19, no. 2, pp. 774–782, 2004.

[4.31] J. H. Mathews and K. D. Fink, "Runge-Kutta-Fehlberg Method (RKF45)," Numer. Methods Using Matlab, pp. 497–499, 2004.

[4.32] M. H. J. Bollen, "Influence of motor reacceleration on voltage sags," IEEE Trans. Ind. Appl., vol. 31, no. 4, pp. 667–674, Jul./Aug. 1995.

[4.34] Z. Wang, X. Wang, and C. Y. Chung, "An analytical method for calculating critical voltage sag clearance time of induction motors," IEEE Trans. Power Deliv., vol. 27, no. 4, pp. 2412–2414, Oct. 2012.

[4.35] G. Yalçinkaya, "Characterization of voltage sags in industrial distribution systems," IEEE Trans. Ind. Appl., vol. 34, no. 4, pp. 682–688, 1998.

[4.36] F. Córcoles and J. Pedra, "Algorithm for the study of voltage sags on induction machines," IEEE Trans. Energy Convers., vol. 14, no. 4, pp. 959–966, Dec. 1999.

[4.37] F. Córcoles, S. Bogarra, J. Pedra, and A. Luna, "Discrete fault-clearing instant influence on the simulation of voltage-source-inverter-fed adjustable-speed drives subjected to voltage sags," IET Electr. Power Appl., vol. 5, no. 5, pp. 465–477, 2011.

[4.38] M. H. Bollen, Understanding Power Quality Problems. 1999.

[4.39] N. Fischer, B. K. Johnson, A. G. Miles, and J. D. Law, "Induction motor modeling for development of a secure in-phase motor bus transfer scheme," in *IEEE Transactions on Industry Applications*, 2019, vol. 55, no. 1, pp. 203–212.

Chapter 5

Simulations

5.1 Introduction

The main goal of this section is to perform simulations considering a wide range of scenarios to test the impact of the previously mentioned factors into the IO. To this end, the three-phase Matlab/Simulink model described in Subsection 4.3.7 will be used. It should be stated that some additional hypothesis have been assumed during the simulations, see the details in ***section 5.2***. For the sake of clarity, each subsection shows and discusses the simulation results for every influential factor.

The main parts of this chapter can be listed as follows:

- The first section is aimed at analysing the influence of the feeder loads into the IO. Besides, the impact of the type of load models into the IO is also investigated. All the results, as well as its discussion, can be found in ***section 5.3***.
- Secondly, the impact of the type of fault that originated the IO and its clearing time is analysed. Given the fact that in the previous subsection only SLG faults have been considered, this subsection explores the effects of the rest of faults into the IO. The simulation results and a thorough discussion can be found in ***section 5.4***.
- Different reclosing times are investigated in ***section 5.5***.
- In ***section 5.6,*** the simulations results for different load torques are provided.
- ***Section 5.7*** analyses the islanding operations in case of permanent faults. The previous sections considered that faults were cleared together with the CB operation (i.e., temporary faults), instead, this section will study the permanent ones. This fact means that even with the CB opening, the fault remains applied, and therefore, the IM continues feeding the fault during the island.

Finally, the main conclusions obtained from the simulations results will be summarised in ***section 5.8***.

5.2 Hypothesis and considerations

Since the simulations are analysed for each influential factor separately, the considered hypothesis will also be provided separately. Hence, the assumptions are detailed down below:

- *Hypothesis for simulations of* ***section 5.3***.
  1. The reclosing time is set to 0.5 s for all simulated scenarios.
  2. A SLG fault at node 7 with a fault resistance of 1 Ω is simulated for all scenarios. Consequently, for this resistance fault and location, the obtained fault current is 466 A (RMS current value). The fault is cleared within 100 ms, due to the fixed time implemented in the relay. This clearing time includes the sensing time (one-cycle), plus the CB mechanical time (40 ms).
  3. The IM is under no-load torque at the time the fault occurs.
  4. The CB clears the fault satisfactorily.
- *Hypothesis for simulations of* ***section 5.4***.
  1. The IM is under no-load torque at the time the fault occurs.
  2. Reclosing time is set to 0.5 s.
  3. The CB clears the fault satisfactorily.
  4. The total feeder loads are set to 80 kW(constant impedance).
- *Hypothesis for simulations of* ***section 5.5***.
  1. A SLG fault at node 7 with a fault resistance of 1 Ω is simulated for all scenarios. Consequently, for this resistance fault and location, the obtained fault current is 466 A (RMS current value). The fault is cleared within 100 ms, due to the fixed time implemented in the relay. This clearing time includes the sensing time (one-cycle), plus the CB mechanical time (40 ms).
  2. The IM is under no-load torque at the time the fault occurs.
  3. The total amount of feeder loads is set to 500 kW(400 cnt. impedance, 50 cnt. current and 50 cnt. power).
- *Hypothesis for simulations of* ***section 5.6***.
  1. The reclosing time is set to 0.5 s for all simulated scenarios.
  2. A SLG fault at node 7 with a fault resistance of 1 Ω is simulated for all scenarios. Consequently, for this resistance fault and location, the obtained fault current is 466 A. The fault is cleared within 100 ms, due to the fixed time implemented in the relay. This clearing time includes the sensing time (one-cycle), plus the CB mechanical time (40 ms).
  3. The CB clears the fault satisfactorily.
  4. A constant torque model is considered.
  5. The reclosing is set to 0.5 s.
  6. The total amount of feeder loads is set to 100 kW(80 cnt. impedance and 20 cnt. current).
- *Hypothesis for simulations of* ***section 5.7***.
  1. The reclosing time is set to 0.5 s for all simulated scenarios.
  2. Feeder loads are set to 80 kW(constant impedance).
  3. The IM is under no-load torque at the time the fault occurs.

5.3 Effects of feeder loads and its load model

5.3.1 Simulations for different load scenarios

In this section, seven simulated scenarios will be analysed and discussed. Each particular scenario considers one value of active-power, which in turn, is the sum of all loads connected to the LV buses. Besides, this value corresponds at a given instant of the daily load profile (e.g., see the half month load profile obtained from the grid under study in Figure 4.7 of subsection 4.3.6). The

power values used for such simulation have been selected in order to represent the influence of the feeder loads on the IO considering a realistic load profile. Although faults have a random occurrence and the power drawn by loads at that time may vary, the simulated scenarios provide a sufficient casuistry to accurately evaluate its effect into the IO.

As underlined in the previous section 5.2, the fault conditions (i.e., the type of fault, its location and resistance fault value) that originated the CB opening are the same. Therefore, voltage and current measurements at PCC_1 will be only shown ones. Particularly, the first plot of Fig. 5.1 displays the phase voltage, meanwhile the second plot shows the current. Note that, the voltage measurement is done upstream the CB. Each scenario is analysed separately, where the voltage at PCC_2 and the frequency of the island are shown in separate plots for each Figure.

Lastly, Table 5.1 summarises the main features of the simulated scenarios. These results are graphically plotted in Figure 5.8, where the first plot shows the voltages and the frequency is shown in the second plot.

Since in the previous events only voltage and frequency have been shown, additionally, a selection of events is made to show the IM mechanical variables during the island. This selection of scenarios is aimed at reducing the number of plots to show in this Chapter. Thus, from the seven simulated events, the mechanical parameters are only shown for scenarios (II, III, IV and V). In Figures 5.9 to 5.11, the IM parameters such as the mechanical rotor speed (ω_m), the electromagnetic torque (T_e) and the active-power (P_e) are displayed respectively.

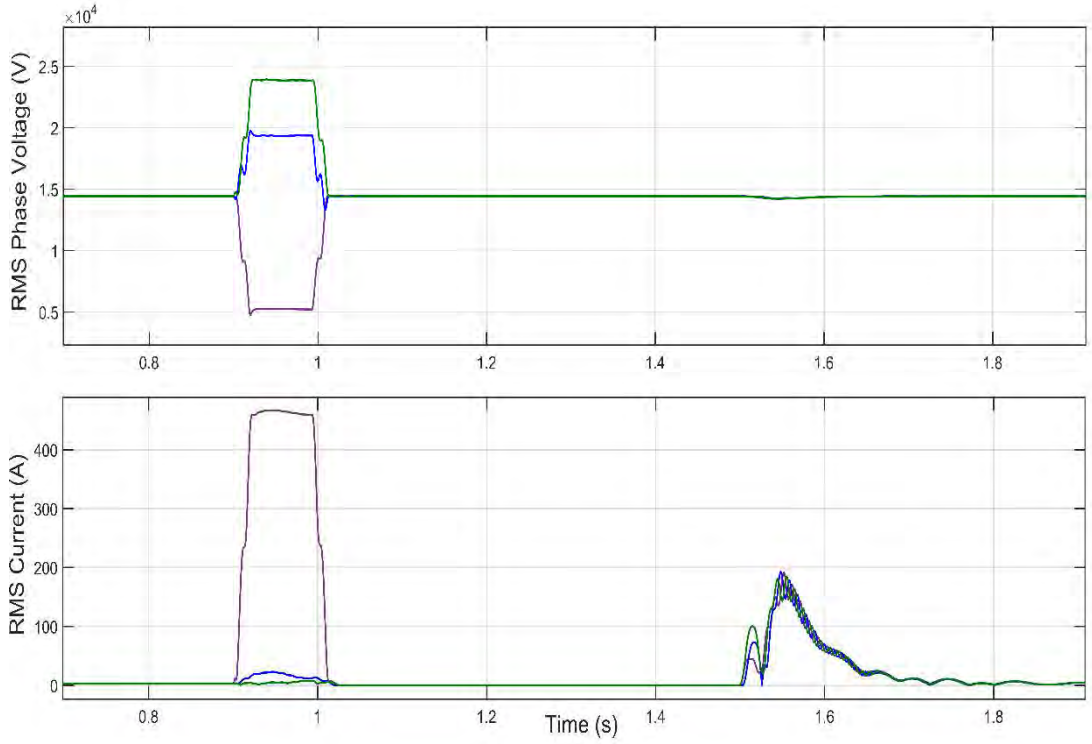

Figure 5.1: Voltage and current measured at PCC_1.

Scenario I

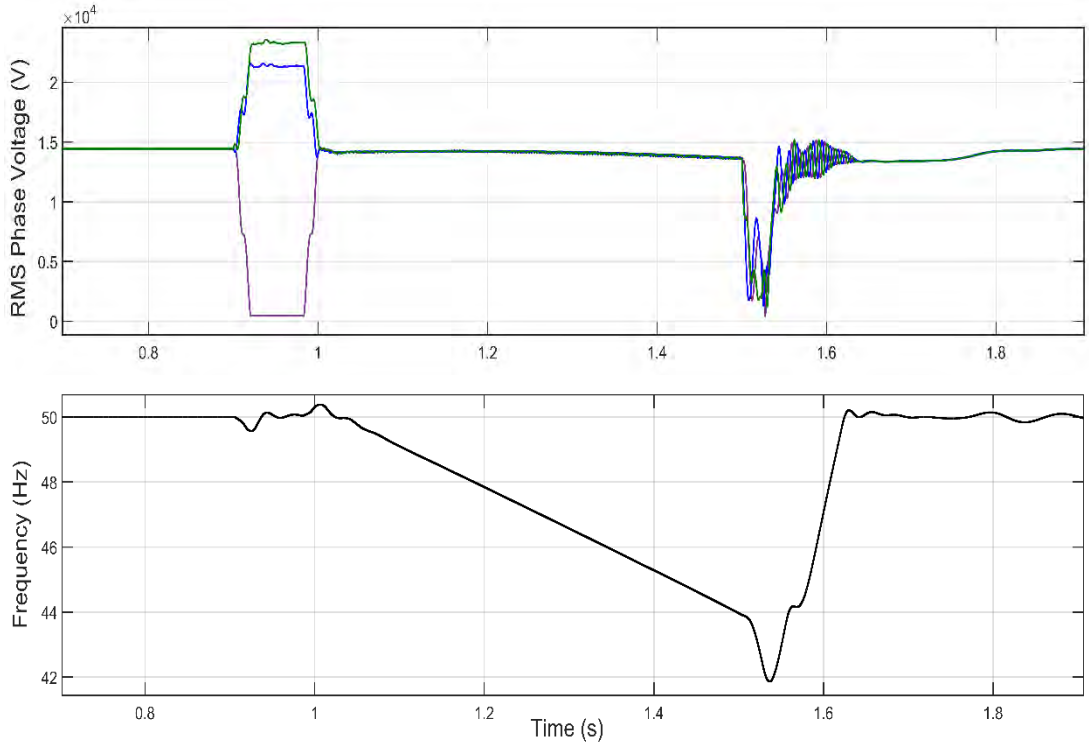

Figure 5.2: Voltage and frequency measurements obtained from scenario I.

Scenario II

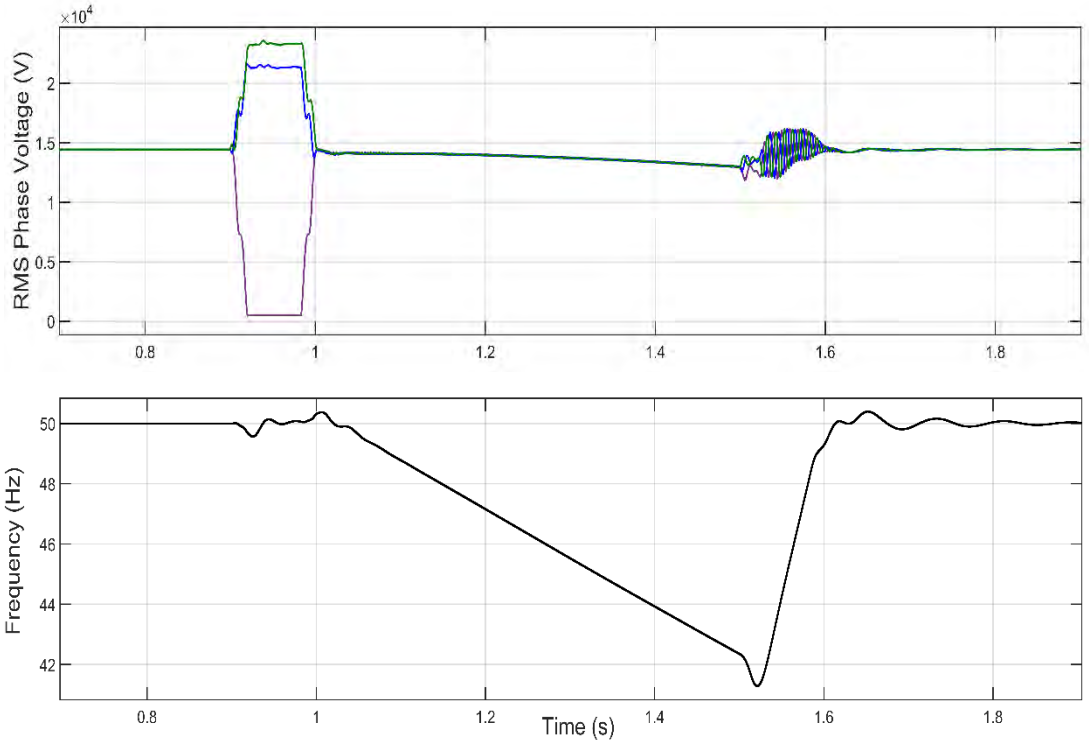

Figure 5.3: Voltage and frequency measurements obtained from scenario II.

Scenario III

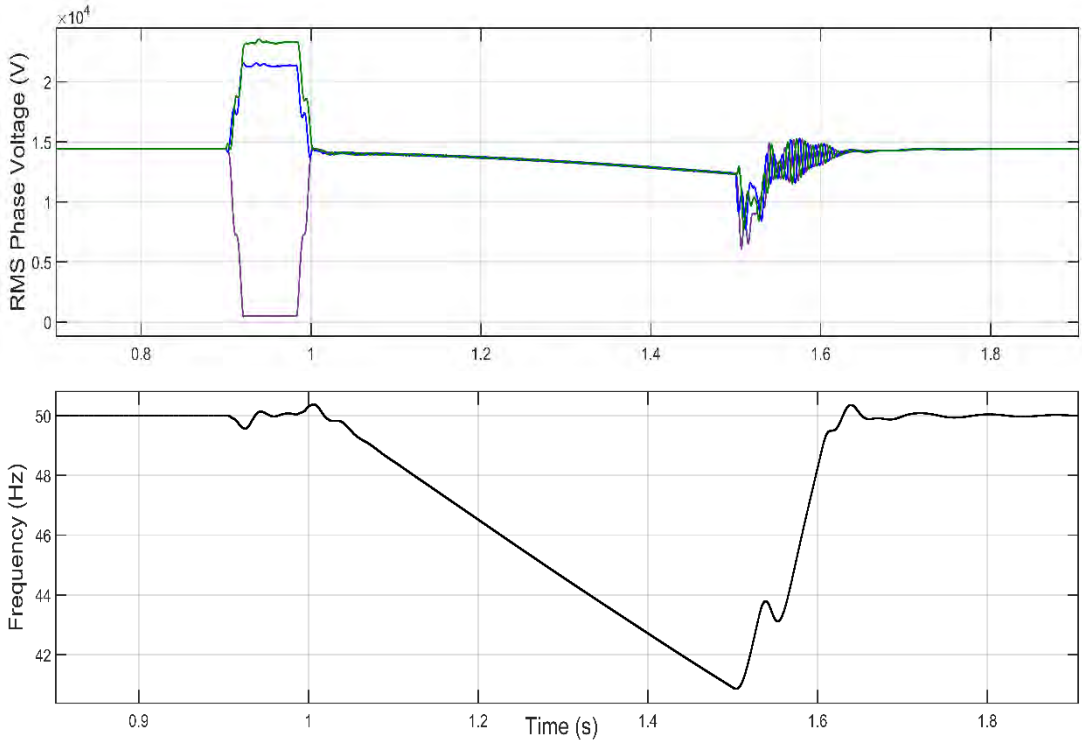

Figure 5.4: Voltage and frequency measurements obtained from scenario III.

Scenario IV

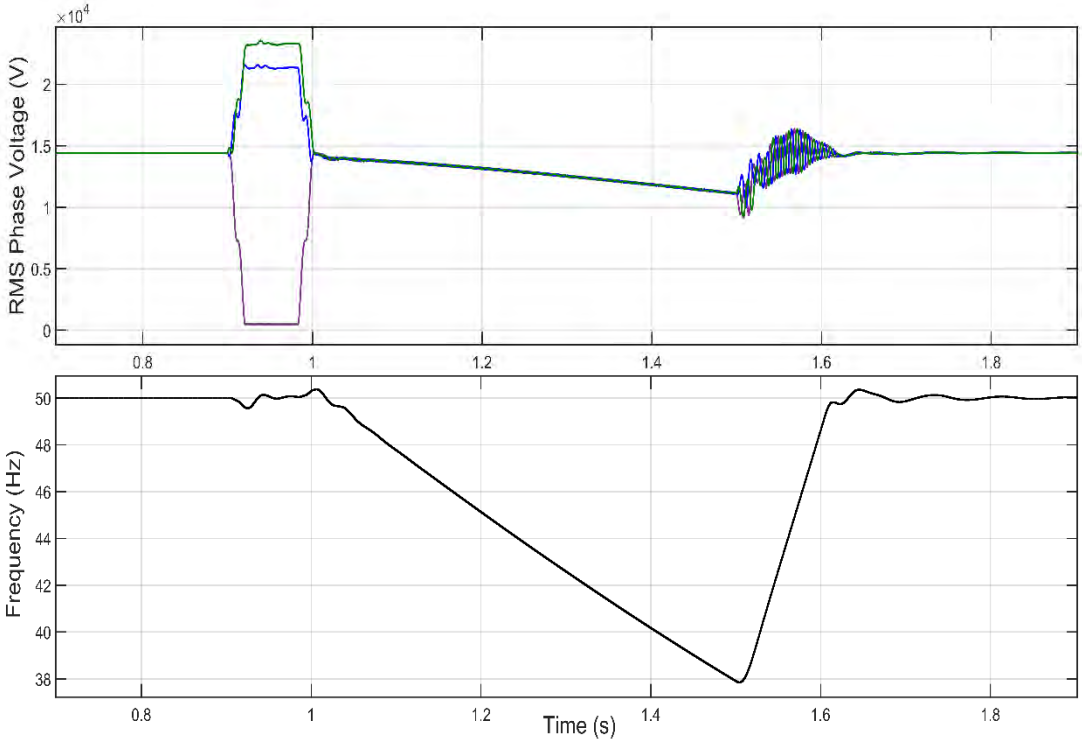

Figure 5.5: Voltage and frequency measurements obtained from scenario IV.

Scenario V

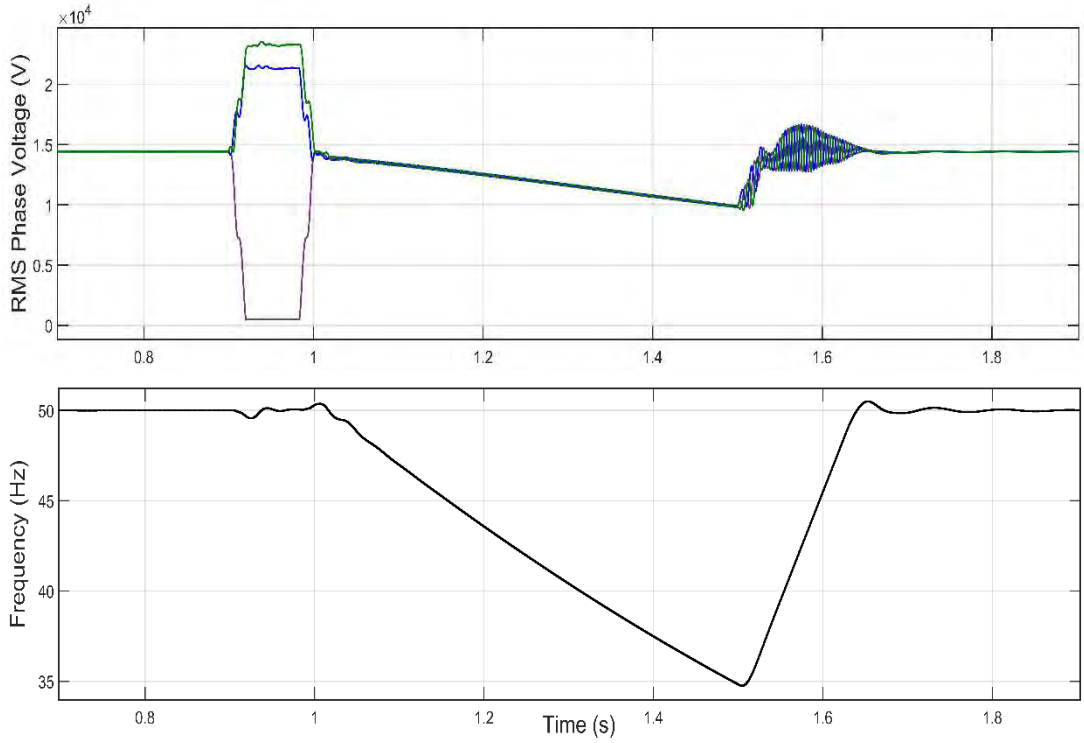

Figure 5.6: Voltage and frequency measurements obtained from scenario V.

Scenario VI

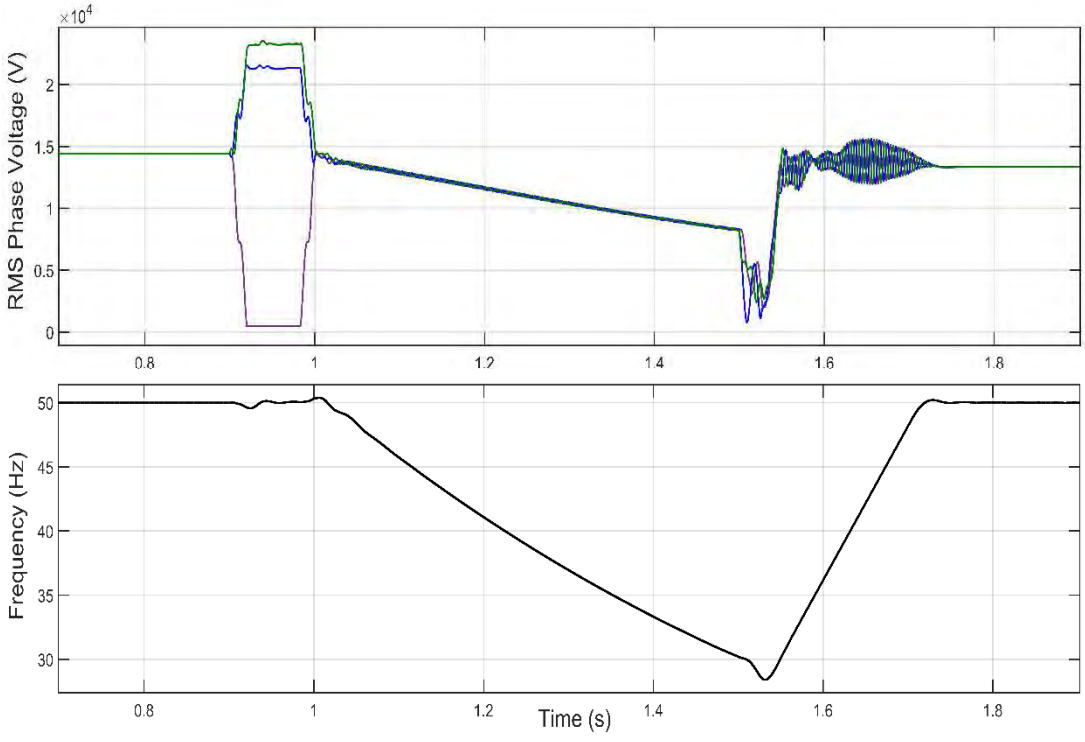

Figure 5.7: Voltage and frequency measurements obtained from scenario VI.

Scenario VII

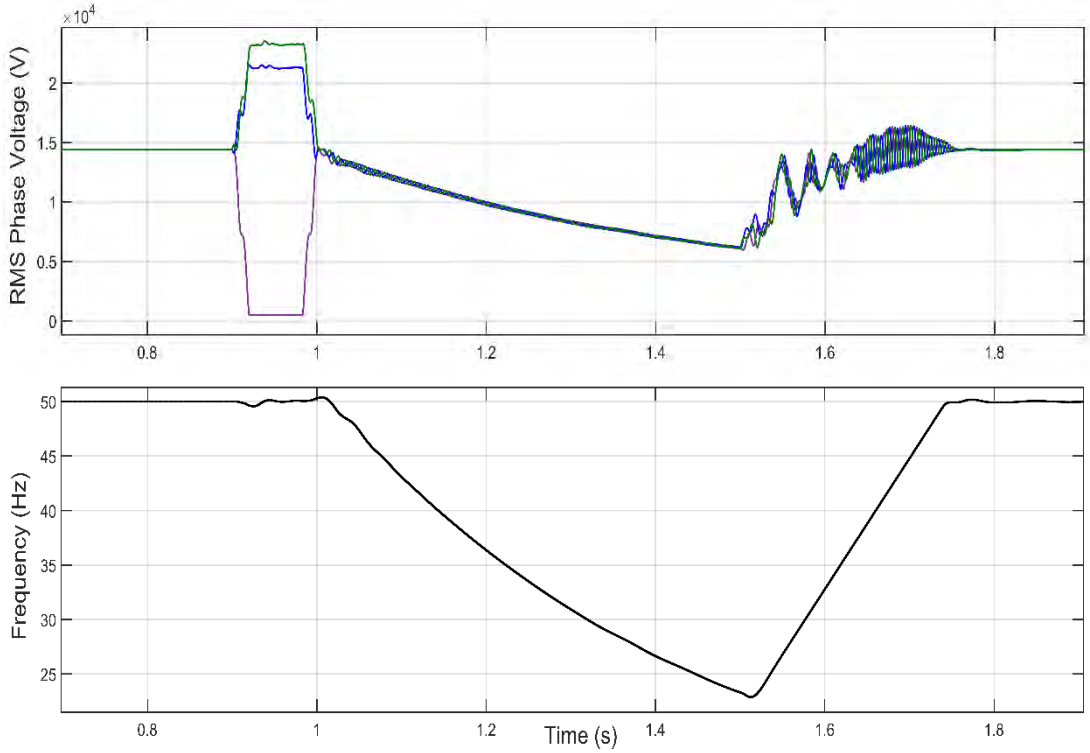

Figure 5.8: Voltage and frequency measurements obtained from scenario VII.

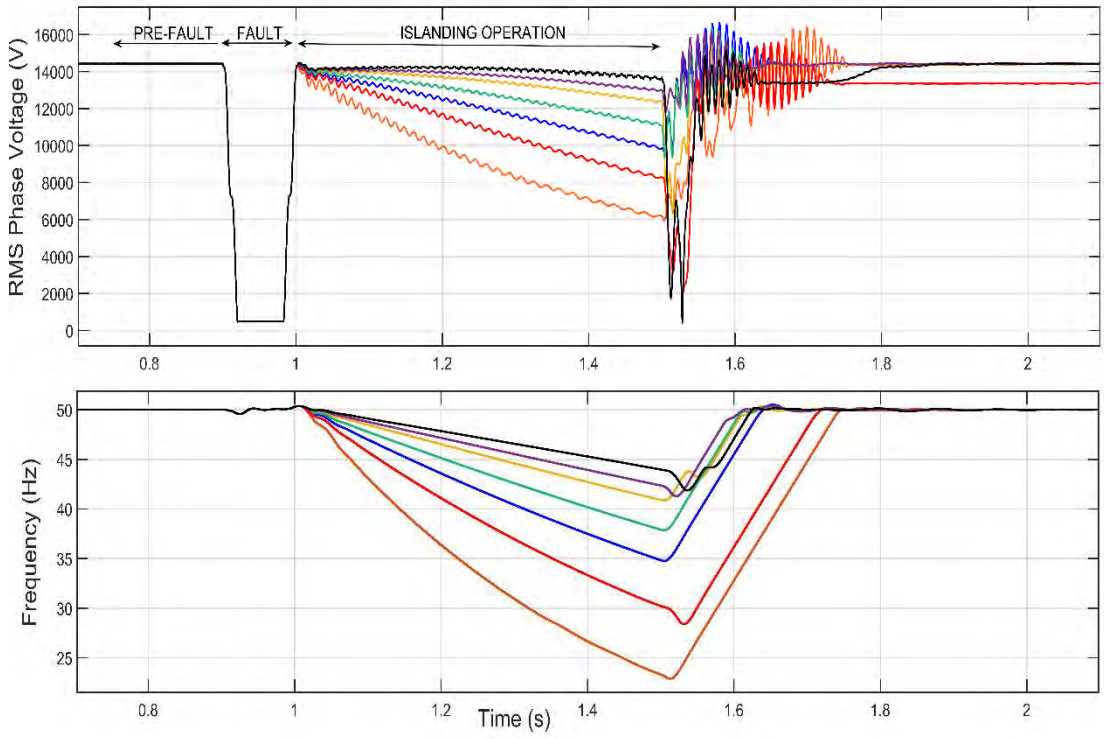

Figure 5.9: Voltage and frequency during the island for all simulated scenarios.

Summary of scenarios

Figure 5.8 compares the voltages and frequency results obtained from simulations. In it, the voltage measured at PCC_2 (only one phase) and the frequency of the island are depicted. By observing this Figure, the effect of the active-power loads that remain within the island is remarkable. From these simulations it can be also highlighted that in case the power drawn by the loads in the island is low at the instant the fault occurs, voltages remain stable meanwhile the frequency shows a slight drop.

On the contrary, a large amount of power drawn by loads forces the machine to a more significant deceleration and consequently, it causes a substantial decrease in voltage and frequency.

Besides, this selection has been done to perform a better analysis of the mechanical parameters in one plot. From Figure 5.10, it can be seen that, as expected, the rotor speed decreases during the IO. On the other hand, Figures 5.11 and 5.12 highlight that both active power and torque are positive before the fault and becomes negative during islanding. The pre-fault power measured at PCC_2 belongs to the load placed at bus 18 plus the IM losses.

Lastly, Table 5.1 summarises the parameters obtained from the performed simulations.

Table 5.1: Summary of the simulated scenarios for different feeder loads value.

Scenario	**P (kW)**	**V* (kV)**	**f* (Hz)**	**ω_m* (rpm)**	**Colour (Figure 5.8)**
I	60	13.7	44	1315	Black
II	80	13	42.4	1268.3	Purple
III	100	12.4	40.9	1224.4	Yellow
IV	150	11.1	37.9	1134.5	Green
V	200	9.8	34.9	1041.8	Blue
VI	300	8.31	30.3	903	Red
VII	500	6.19	23.4	696	Orange

* Values obtained one cycle before CB reclosing

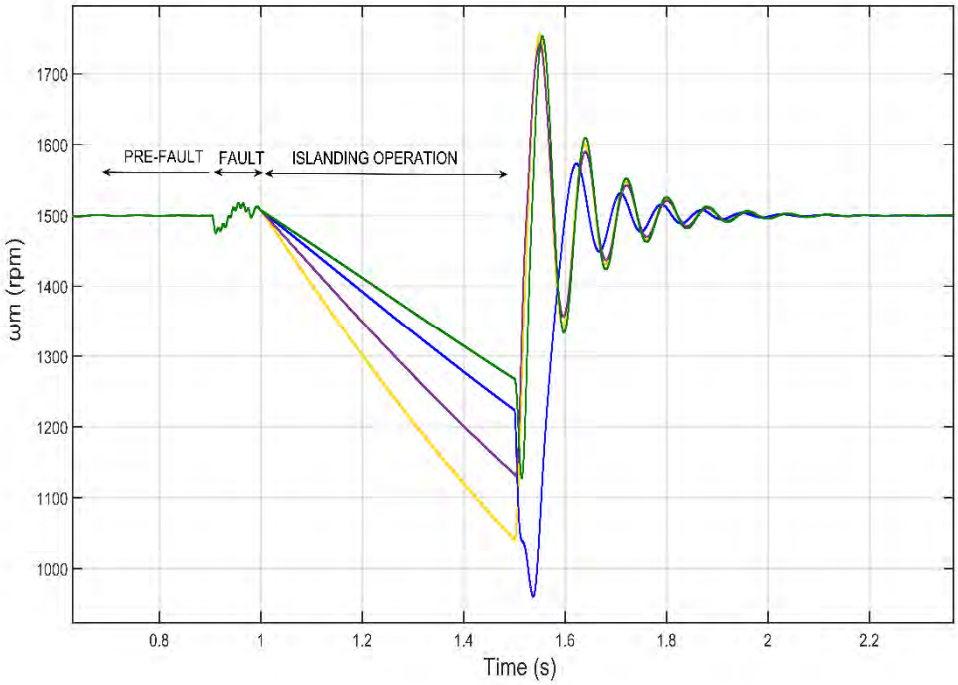

Figure 5.10: IM mechanical speed comparison between scenarios II, III, IV and V.

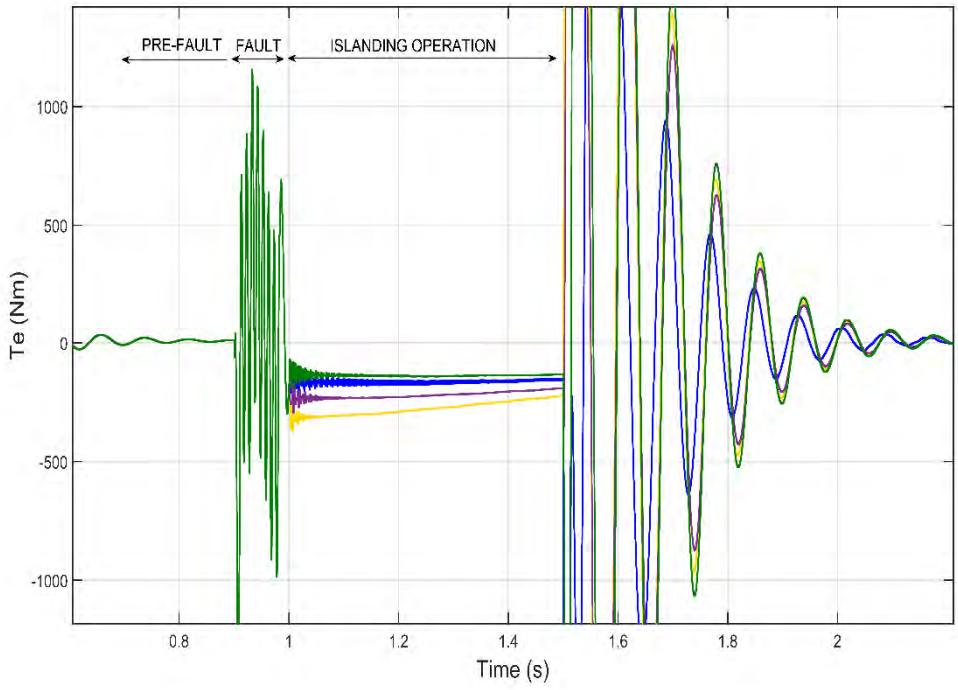

Figure 5.11: Comparison between torques in scenarios II, III, IV and V.

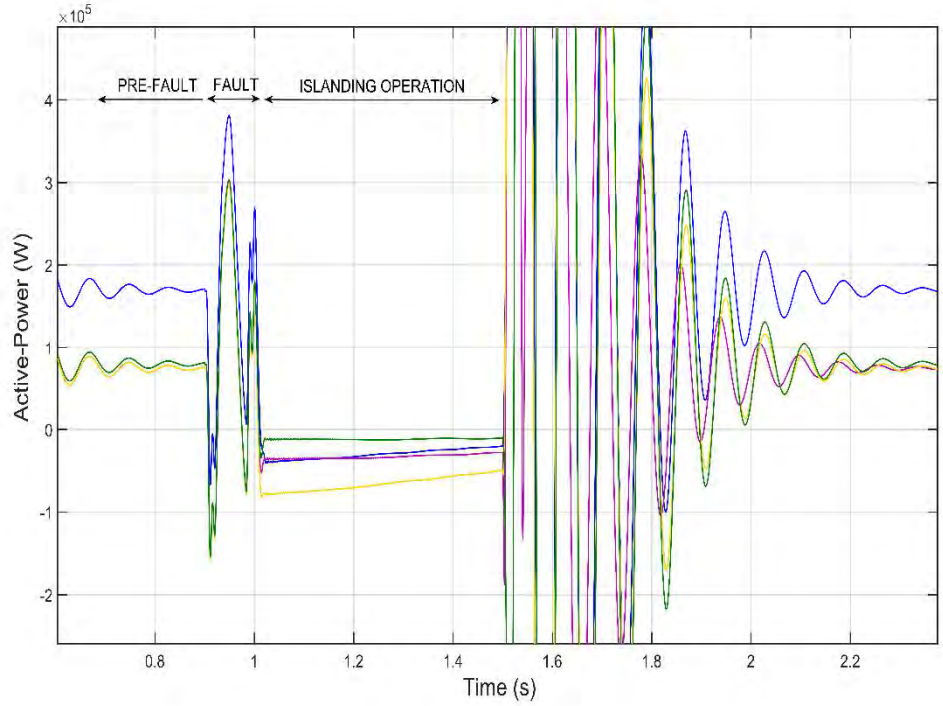

Figure 5.12: Active-power comparison between scenarios II, III, IV and V.

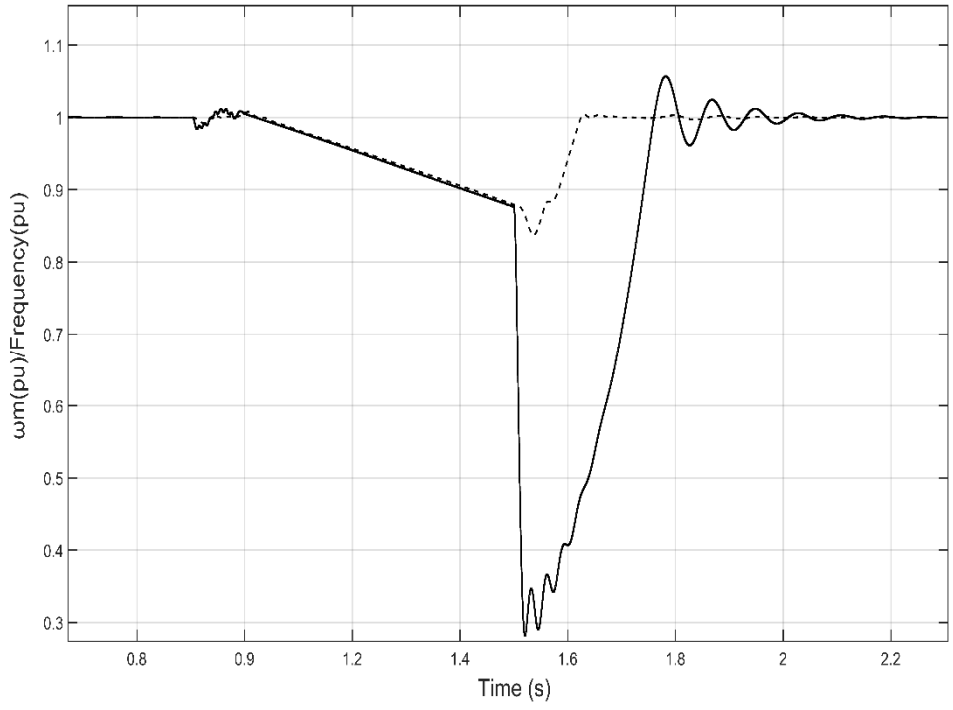

Figure 5.13: Frequency and IM rotor speed in per unit comparison.

To provide more evidence that following the CB disconnection the IM is acting as a generator and also demonstrate that the IM rotor speed dictates the frequency during the IO, Figure 5.13 shows the comparison between the frequency and mechanical speed in per unit. By observing that Figure, before the fault occurs, as expected, the IM rotor speed is slightly below the synchronous due to the low slip when the motor is under no-load torque (before t = 0.8s). Once the fault takes

place, due to the voltage sag, the speed is slightly reduced (between t = 0.8 s and t = 0.9 s), and during the island (between t = 0.9 s and t = 1.4 s), the mechanical speed matches the synchronous one.

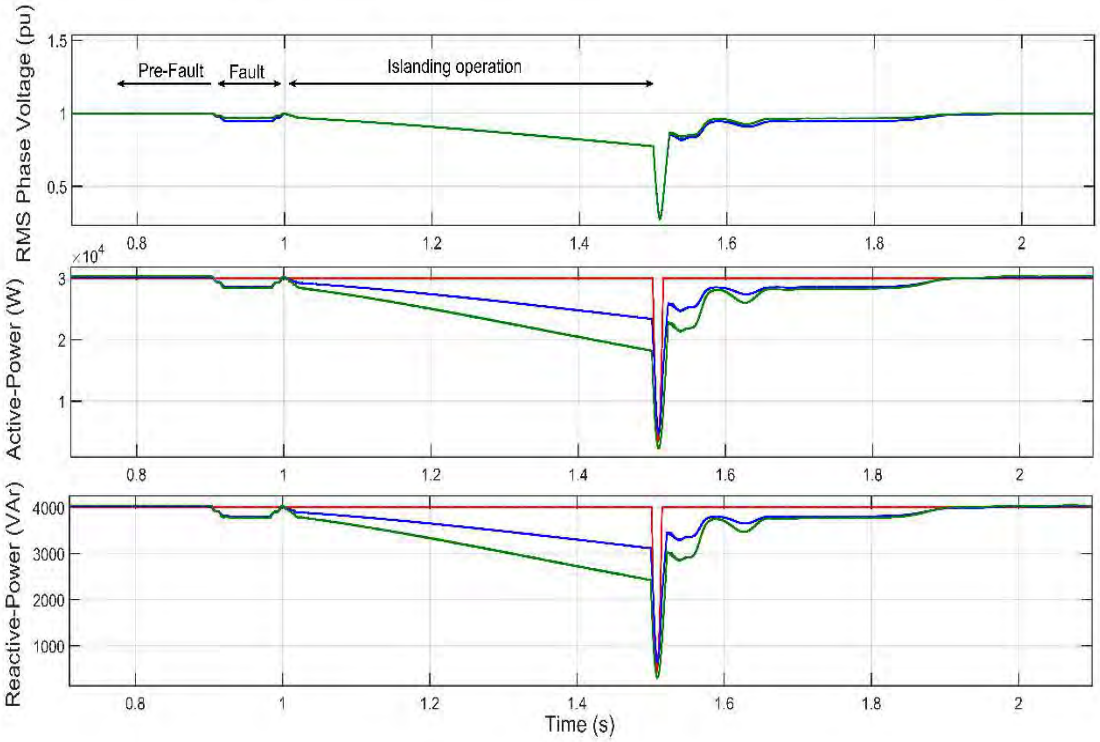

Figure 5.14: Voltage, active-power and reactive-power for the three type of load models.

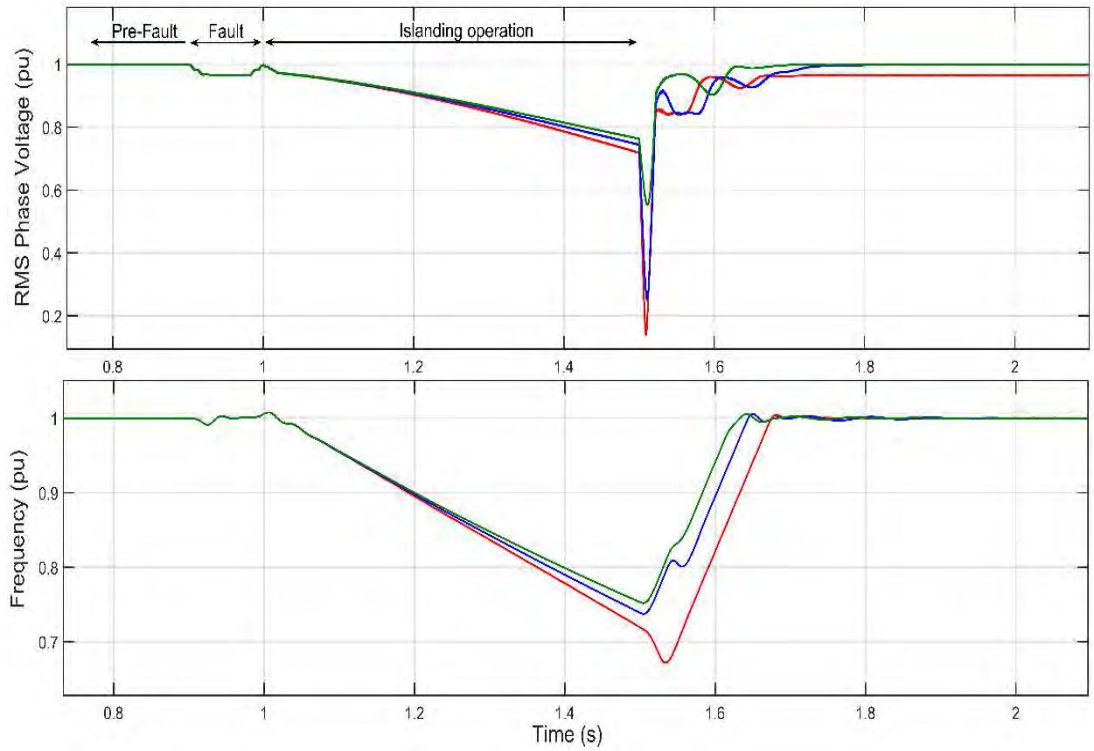

Figure 5.15: Voltage and frequency for the three types of load models.

5.3.2 Load models impact

As has been seen in the previous subsection, the number of loads within the island plays a pivotal role in this study. Furthermore, this subsection will demonstrate that depending on the selected type of load model (i.e., consider the voltage-dependence in load models), frequency and voltage during islanding will vary. Thus, Figure 5.14 show voltage (first plot), active-power (second plot) and reactive-power (third plot) in per unit measured at node 15 for the three types of load models when considering voltage-dependence (i.e., cnt. impedance, cnt. current and cnt. power). Theoretically, a constant power load model is the one that has to cause a high deceleration in the IM since the power delivered by the IM decreases with time. On the contrary, constant impedance and constant current load models, due to a decrease in power with the voltage drop, may cause less deceleration. By taking a look at Figure 5.15, this fact has been demonstrated. The highest voltage and frequency drop during the island occurs for a constant power load model, and the lesser drop occurs for constant impedance load model.

5.4 Type of fault and clearing time influence

Since the IO object of study is originated by a fault and the subsequent CB clearing, the main aim of this section is to study the effects of this type of fault into it. Depending on the type of fault and the clearing time, the IM behaviour during the fault will be different, and as a consequence, the islanding initial conditions will also change. Accordingly, this subsection will show eight scenarios. These scenarios will test all types of faults at different locations and different clearing times. Scenarios I, II, III and IV belong to a fixed clearing time, however, scenarios V, VI, VII, VIII belong to simulations where the clearing time depends on the fault current and the selected curves.The reason why some scenarios have a fixed clearing time (100 ms) is that a fixed time is implemented in the relay, which trips in case fault current exceeds a certain threshold. The phase voltages and the frequency of the island are both measured at PCC_2. The simulated scenarios are plotted in Figure 5.16. The first column shows the phase voltage while the second the frequency value. To make a clear comparison between the simulated scenarios, Figure 5.17 merges the obtained voltages and frequencies of 5.16 into two plots.

Table 5.2: Parameters of the simulated faults.

Scenario	Fault location	Type fault	R_f (Ω)	Fault current* (A)	Clearing time (ms)
I	Node 7	SLG	1	460	100
II	Node 7	LL	1	1560	100
III	Node 7	LLLG	1	1890	100
IV	Node 7	LLLG	10	967	100
V	Node 5	LLL	5	1021	175
VI	Node 5	LLG	5	899	197
VII	Node 9	LL	5	624	240
VIII	Node 9	LLLG	5	726	216

* RMS Current measured in PCC_1

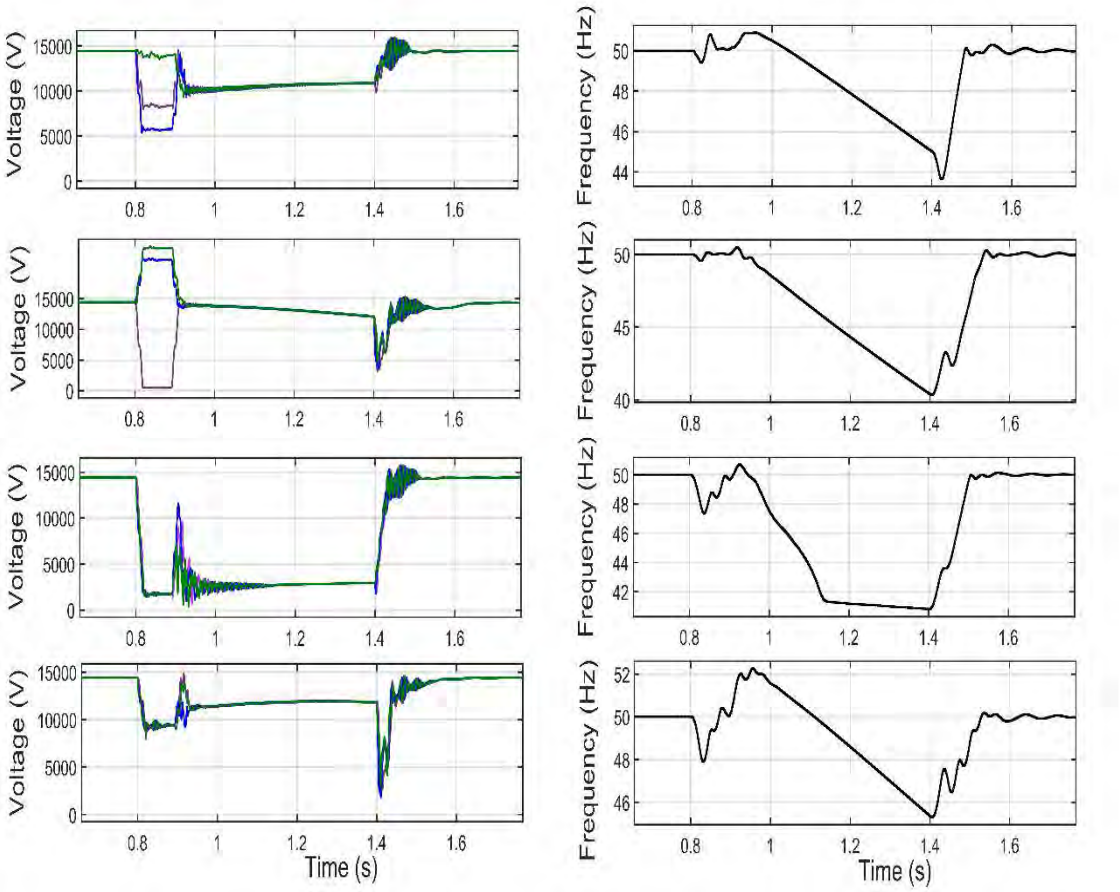

Figure 5.16: Simulated scenarios with fixed clearing time.

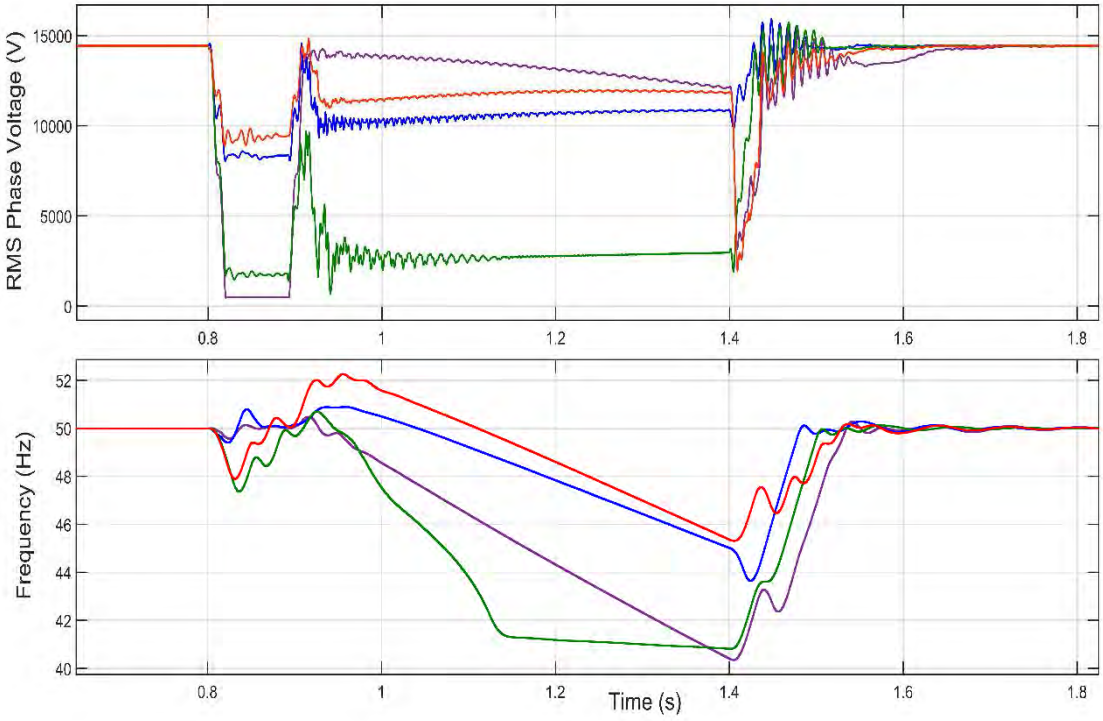

Figure 5.17: Voltage and frequency comparison between scenarios with fixed clearing time.

From both 5.16 and 5.17, it can be seen that, undeniably, the type of fault have a noticeable impact in the IO. On the one hand, in scenario III, for a LLLG fault with a R_f of 1 Ω, the motor stalls and cannot recover after the CB clearing, meanwhile in scenario IV, at the same fault location but increasing R_f to 10 Ω, the motor decelerates during the fault and reaccelerates once the fault is cleared. By observing scenario III, it can be seen that depending on the type of fault and its severity, voltage and frequency will collapse.

Crucially, the larger post-fault reacceleration in scenario IV causes a frequency increasing above 50 Hz at the beginning of the island and also makes that during the island this value is slightly higher in comparison with scenarios I and II.

On the other hand, it is observed that for SLG faults, the voltage during the island is higher in comparison with the rest of faults (see scenarios II and IV). It is seen that the faults which cause the higher deceleration during the fault are the LLL or LLLG faults with large clearing times. From these results, the conclusion that can be drawn is clear, the higher is the speed drop during the fault (i.e., during the voltage sag) the higher is the reacceleration once the CB clears the fault (i.e., the beginning of the island). Therefore, this fact will be traduced in a frequency increasing during the island.

The results for the simulated scenarios V, VI, VII and VIII (Figures 5.19 to 5.21) where the clearing time is not fixed, are showed down below. In these Figures, the phase voltage measured at PCC_2 and the frequency island is showed.

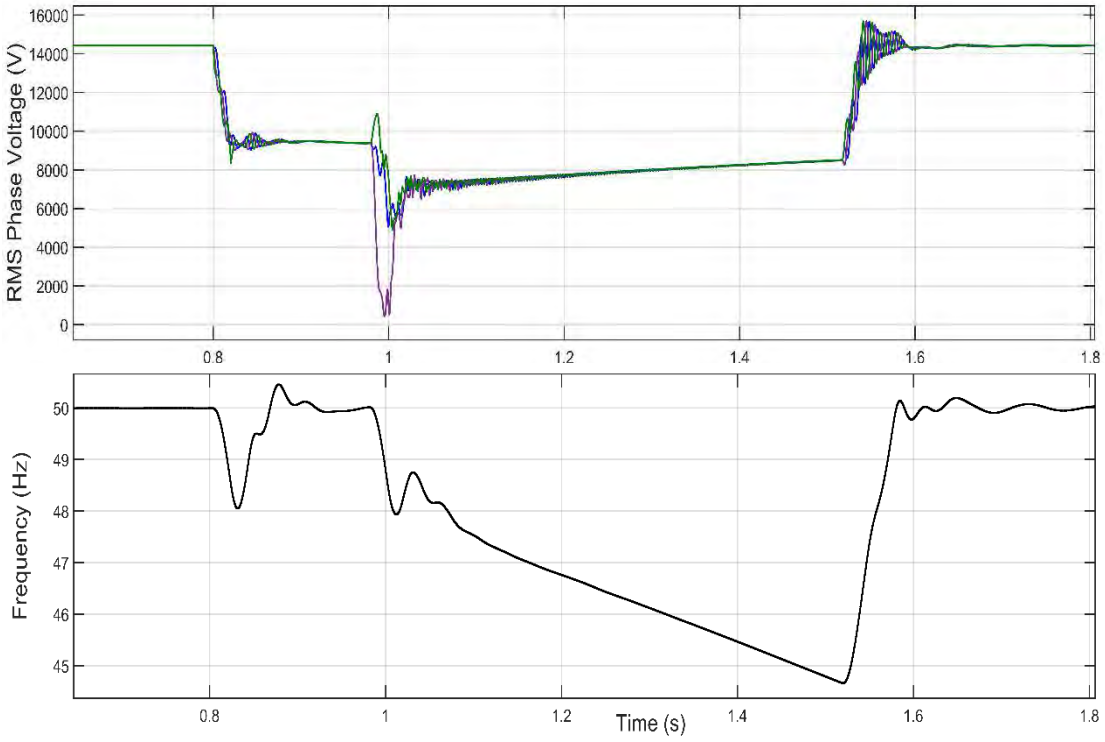

Figure 5.18: Voltage and frequency of scenario V.

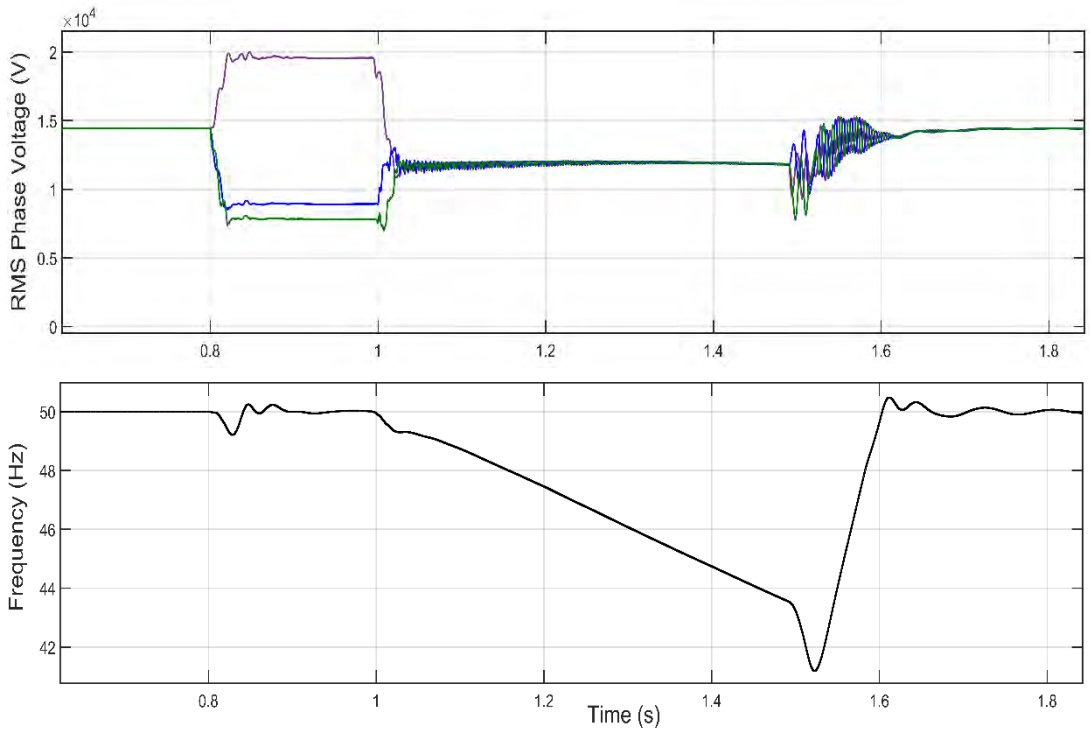

Figure 5.19: Voltage and frequency of scenario VI.

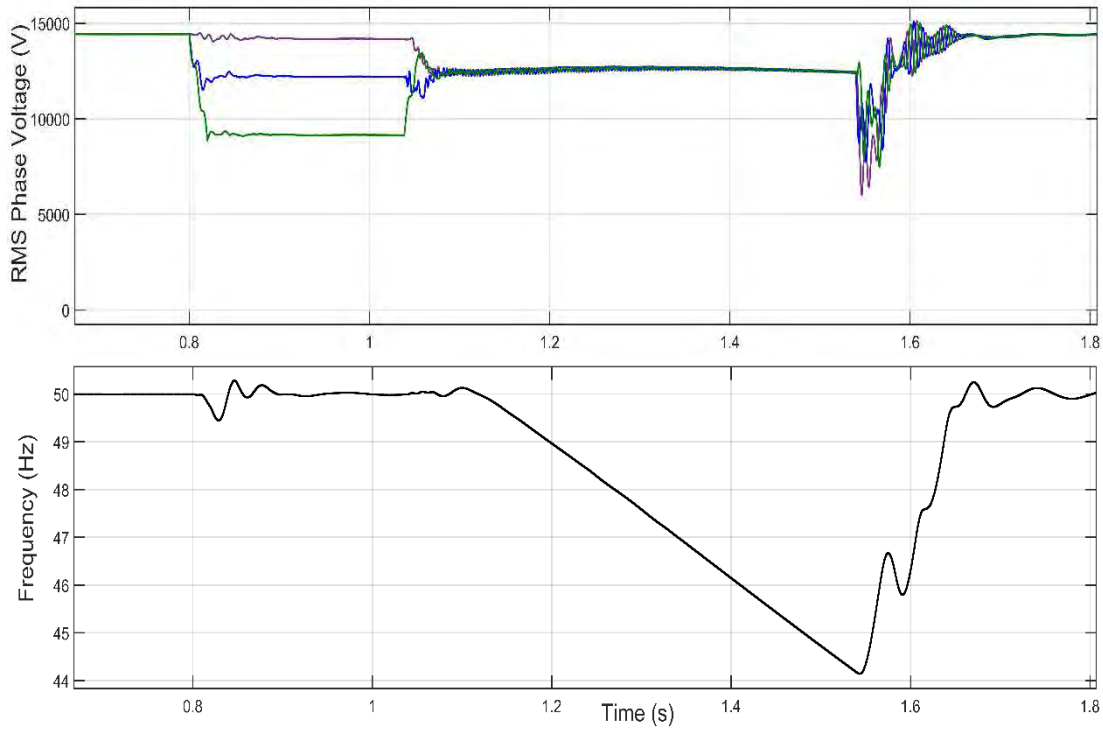

Figure 5.20: Voltage and frequency of scenario VII.

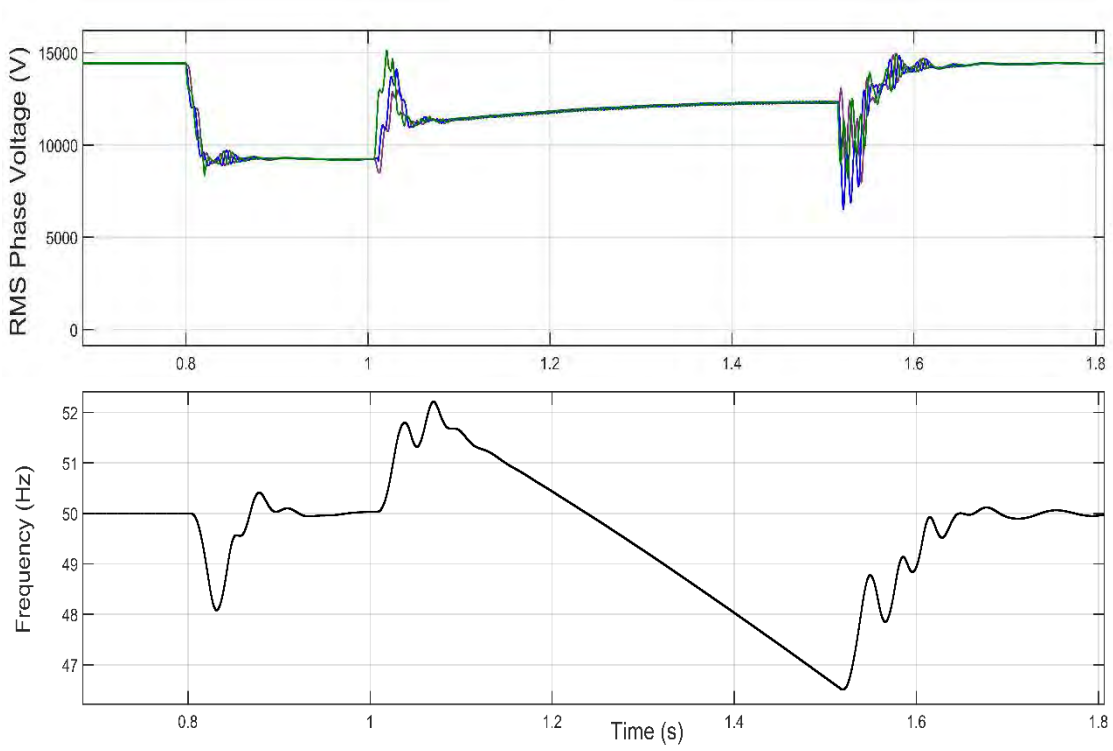

Figure 5.21: Voltage and frequency of scenario VIII.

Table 5.3: Summary of the simulation results to evaluate the fault influence.

Scenario	P (kW)	V* (kV)	f* (Hz)	ω_m* (rpm)	Clearing time (ms)
I	80	10.9	45.1	1349	100
II	80	12.1	40.5	1210	100
III	80	-	-	-	100
IV	80	11.8	45.4	1359	100
V	80	8.49	44.7	1341	175
VI	80	11.8	43.6	1307	197
VII	80	12.5	44.2	1324	240
VIII	80	12.3	46.6	1394	216

* Values obtained one cycle before CB reclosing.

Summary of scenarios

This subsection has shown the influence of the type of fault and the clearing time into the IO. A summary of the discrete values of the islanding (i.e., voltage, frequency and mechanical speed) one-cycle before the CB reclosing takes place are listed in Table 5.3. From that table, it has been demonstrated that the larger is the fault duration, the larger is frequency during the island due to the IM reacceleration. This phenomenon is especially significant for LLL and LLLG faults provided that the motor does not stall, which only takes place for the severest faults. The proof that the rotor of the IM dictates the frequency during the island is evidenced by comparing both

values in per unit. As an example, by observing Table 5.3 values, for scenario VIII the frequency before the CB reclosing in per unit (46.6/50 Hz) is 0.932 pu and the mechanical speed (1394/1500 rpm) is 0.93 pu. In the same way, this comparison can be made for all simulated scenarios.

5.5 Reclosing time influence

The simulations for different reclosing times have been performed according to the previously described hypothesis in section 5.2. The main parameters obtained for the five simulated times are displayed in Figure 5.22. From this Figure, it can be extracted that, as expected, the larger the reclosing time, the more significant is the voltage and frequency drop during the island. Moreover, the discrete values from figure 5.22 and the principal data of the simulations is summarized in table 5.4.

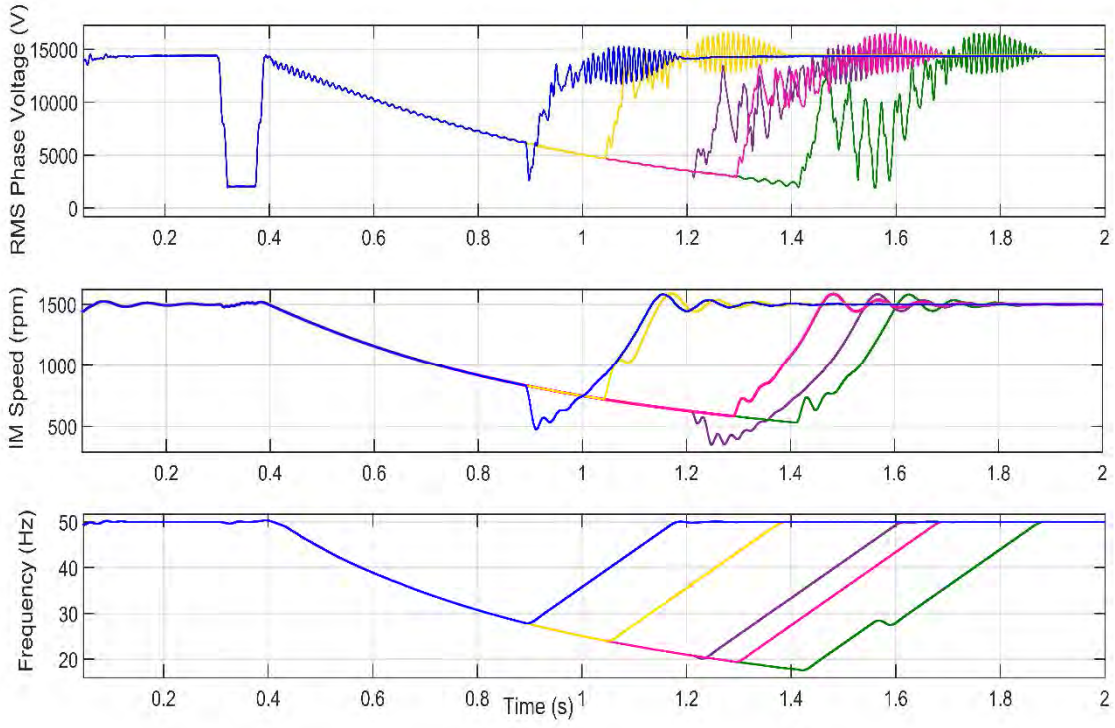

Figure 5.22: Voltage, IM speed and frequency during the IO for several reclosing times.

Table 5.4: Summary of values for different reclosing times.

Scenario	P (kW)	V* (kV)	f* (Hz)	ω_m* (rpm)	Clearing time (ms)	Colour (in Figure 5.21)
I	500	6.1	27.8	834	100	Blue
II	500	4.9	24.1	720	100	Yellow
III	500	3.4	20.6	623	100	Purple
IV	500	3	19.5	596	100	Pink
IV	500	2.3	17.6	534	100	Green

* Values obtained one cycle before CB reclosing.

5.6 Impact of the load torque

The main objective of this section is to analyse the extent to which the load torque coupled with the IM rotor shaft the can influence the IO. Thus, this section will show several scenarios that have been simulated with different torque values. Note that the speed-dependence torque model has not been considered here. Instead, the value of the torque is kept fixed during the whole simulation scenario. The simulated scenarios can be ordered by size from no load to the full-load torque. Table 5.5 shows the discrete values obtained from the simulations measurements.

Table 5.5: Summary of the measurements obtained from simulations.

Scenario	Load torque (Nm)	V* (kV)	f* (Hz)	ω_m* (rpm)	Colour (In Figure 5.22)
I	0	13	42.6	1275.8	Purple
II	150	10.3	35.6	1064	Blue
III	200	9.4	33.2	987	Green
IV	300	7.66	28.4	841.6	Yellow

* Values obtained one cycle before CB reclosing.

In addition to these discrete values (obtained one-cycle before the reclosing), the results of the simulation are plotted in Figures 5.23 and 5.24. In 5.23, the RMS phase voltage measured at PCC_2 and frequency of the island are shown. From these measurements, one can observe the effect of the induction motor deceleration in case the load torque value increases. Therefore, the larger is the motor deceleration, the larger is the voltage and frequency decreasing during the island. Meanwhile, for no-load torque (scenario I) the voltage and frequency drop is not that significant, in case full-load torque (scenario IV), the voltage and frequency drop is noticeable.

On the other hand, Figure 5.23 provides more evidence of the frequency and voltage oscillations showed in 5.22. Undeniable proof of the frequency drop that occurs during the island is given in the first plot where the rotor mechanical speed is shown. Hence, it is demonstrated that as has been stated in the previous subsection, the frequency during the island can be compared with the IM rotor speed in pu. As an example, for scenario II (150 Nm torque) frequency expressed in per unit (35.6/50 Hz) is 0.712 pu, whereas the mechanical speed (1064/1500 rpm) is 0.71 pu, therefore, this result is in accord with the comparison obtained in section 5.4.

Besides that, the second plot of 5.23 shows the load torques, and as expected, before the fault are all positive and, after the fault the torques became negative. To a better detail, the third plot enlarges the second.

From these two plots, it is seen that in case a large torque is applied (e.g., the full-load torque), once the CB recloses the circuit, the recovery process to reach the pre-island point operation is prolonged 1.4 s. However, in case low load torque is applied (e.g., no load), the motor recovers faster, it takes 0.2 s.

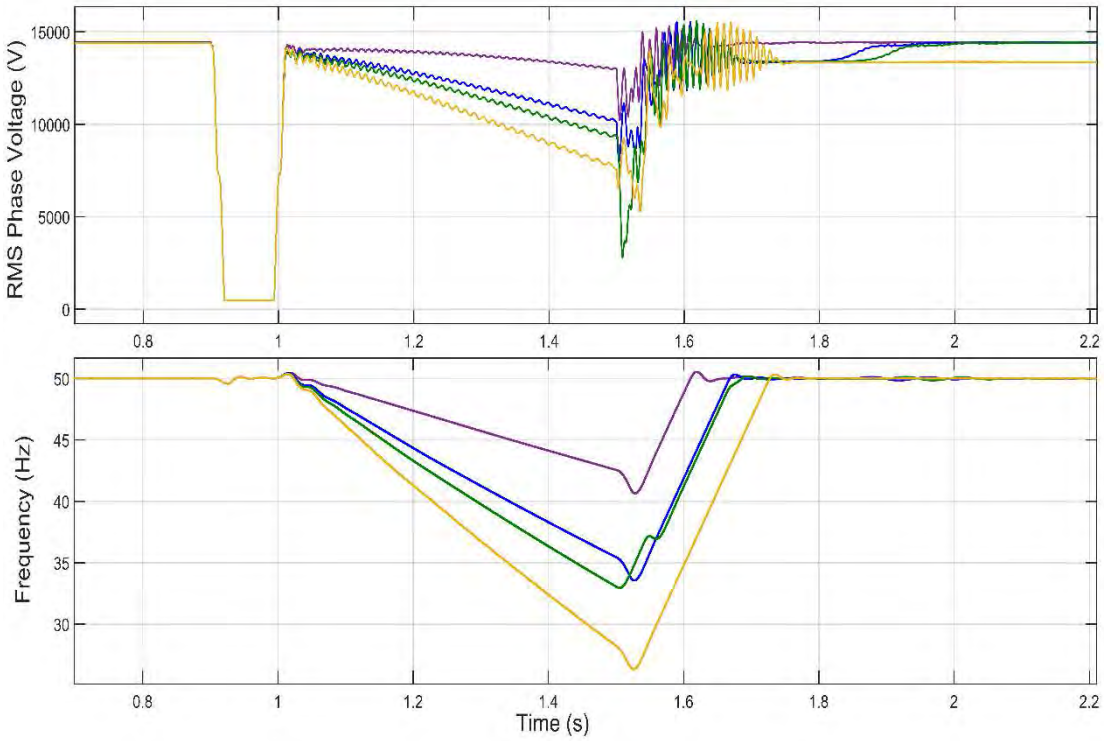

Figure 5.23: Voltage and frequency comparison between scenarios with different load torque values.

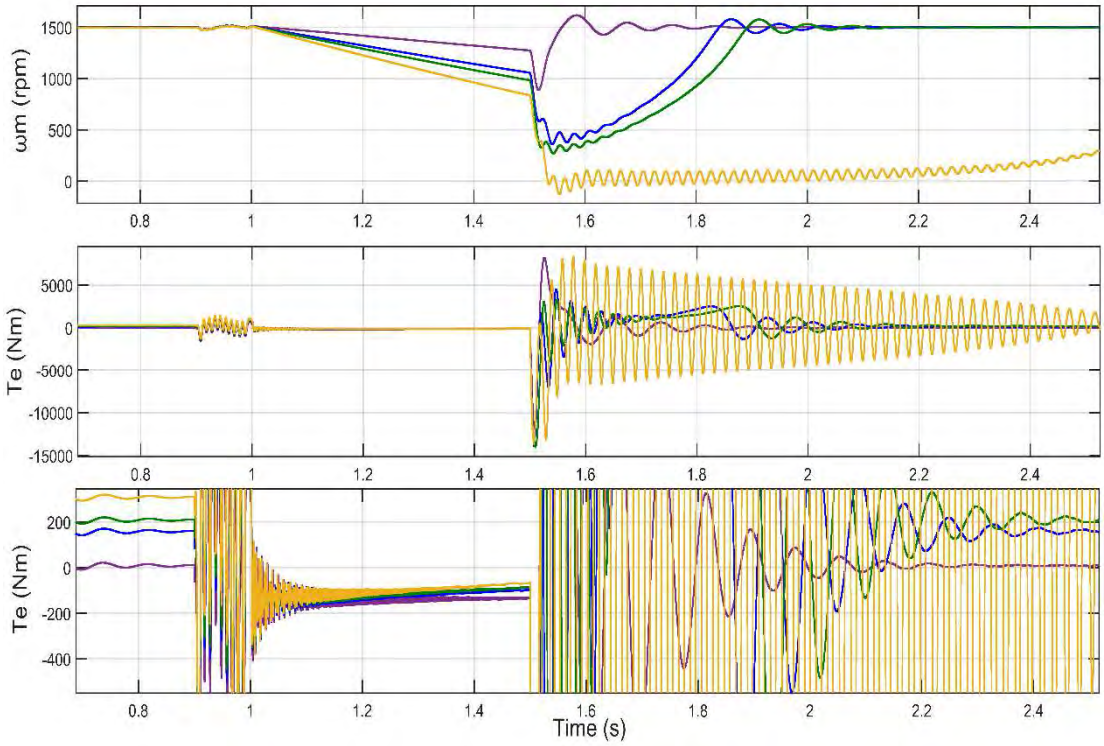

Figure 5.24: Speed and torque comparison between scenarios with different load torques.

5.7 Permanent-faults

As has been mentioned above in the document, the origin of the island object of study is produced due to a CB operation, which is preceded by a fault that occurs in the distribution network. The previous subsections have considered that the CB satisfactorily clears the fault and the beginning of the island coincides with the arc extinction. However, this might not be the case if the fault persists following the CB operation. Conceptually, in this thesis, a permanent fault will mean that the IM is feeding the fault following the CB operation. Consequently, the main aim of this section is to observe the effects of the IM when it is feeding a fault during the island. As a matter of fact, this situation frequently occurs in DNs where, following the CB operation, due to the random nature of the fault, it remains applied for a short period until it is dispelled (e.g., elements colliding in the electrical towers such as tree branches as well as other random items) or even for prolonged faults (e.g., a wire to the ground). Consequently, if the CB operates and the fault continues applied, the IM will feed the fault during the IO.

From this point on, as explained, two options may occur following the non-satisfactorily CB clearing operation; after feeding the fault for a period of time (i.e., it can be a matter of few ms or even hundreds of ms), the fault is extinguished. Or alternatively, if the fault is permanently applied, the IM feeds the fault until voltage and frequency collapse. Indeed, from the protective point of view, this situation causes a protective misscoordination, as well as causes a high risk from the safety perspective.

Having said that, this section shows and discusses five scenarios where several types of faults and locations have been simulated. The main data of the simulated scenarios is detailed in Table 5.6, whereas the simulation results are displayed in the following Figures 5.25 to 5.29.

Table 5.6: Data of the simulated faults.

Scenario	Fault location	Type fault	R_f (Ω)	Fault current[*1] (A)	CB Clearing time[*2] (ms)	Fault extinction[*3] (ms)
I	Node 3	SLG	0.1	473	210	540
II	Node 3	LL	0.1	1742	140	530
III	Node 3	LLLG	10	1272	160	190
IV	Node 7	SLG	5	414	340	1100
V	Node 3	LLG	20	485	280	680

*1 RMS value measured at PCC_1. *2 Time period between the beginning of the fault and CB opening.

*3 Time period between the beginning of the fault and the extinction.

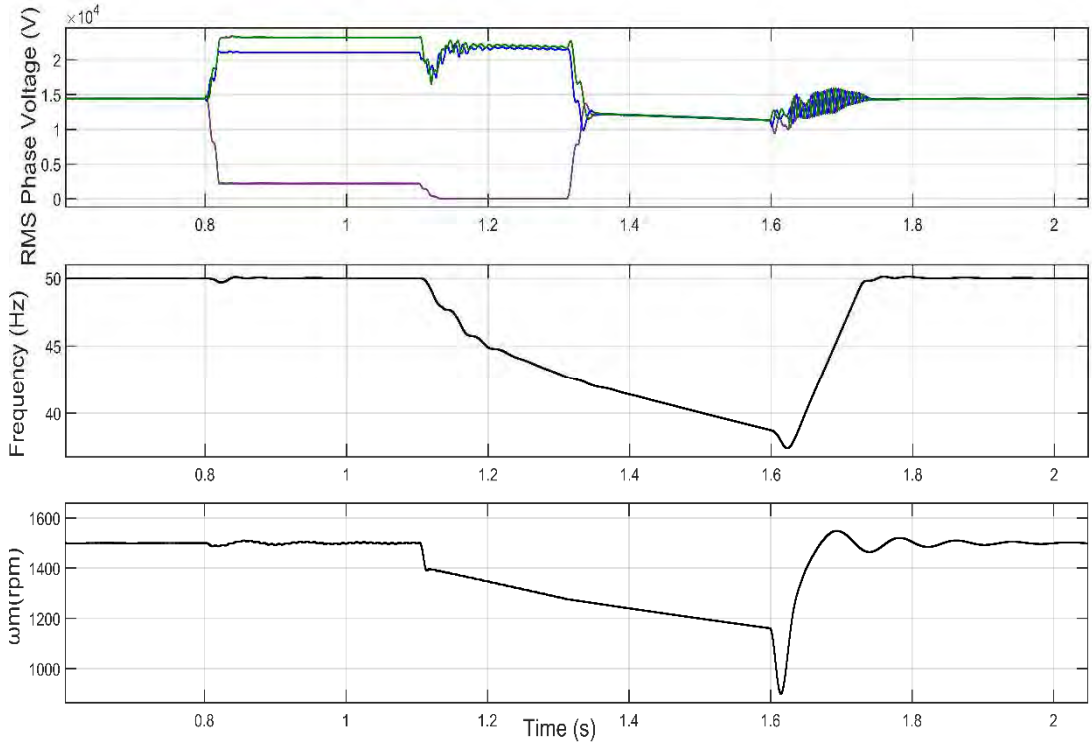

Figure 5.25: Voltage, frequency and IM mechanical speed of permanent fault-scenario I.

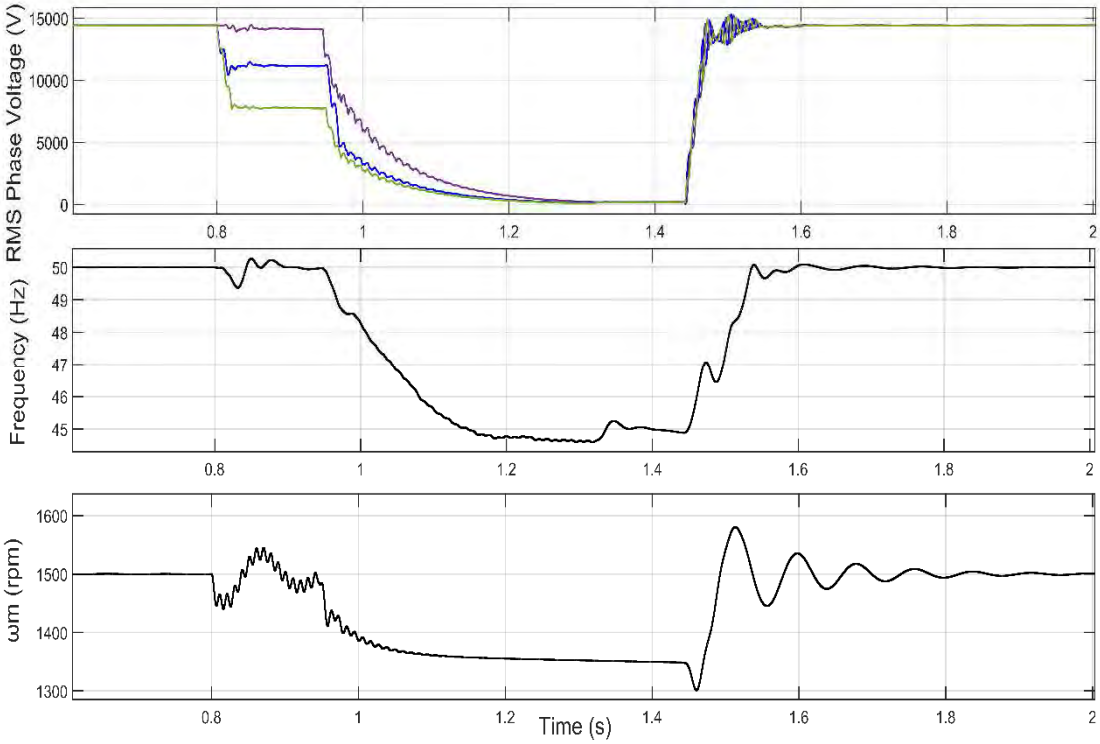

Figure 5.26: Voltage, frequency and IM mechanical speed of permanent fault-scenario II.

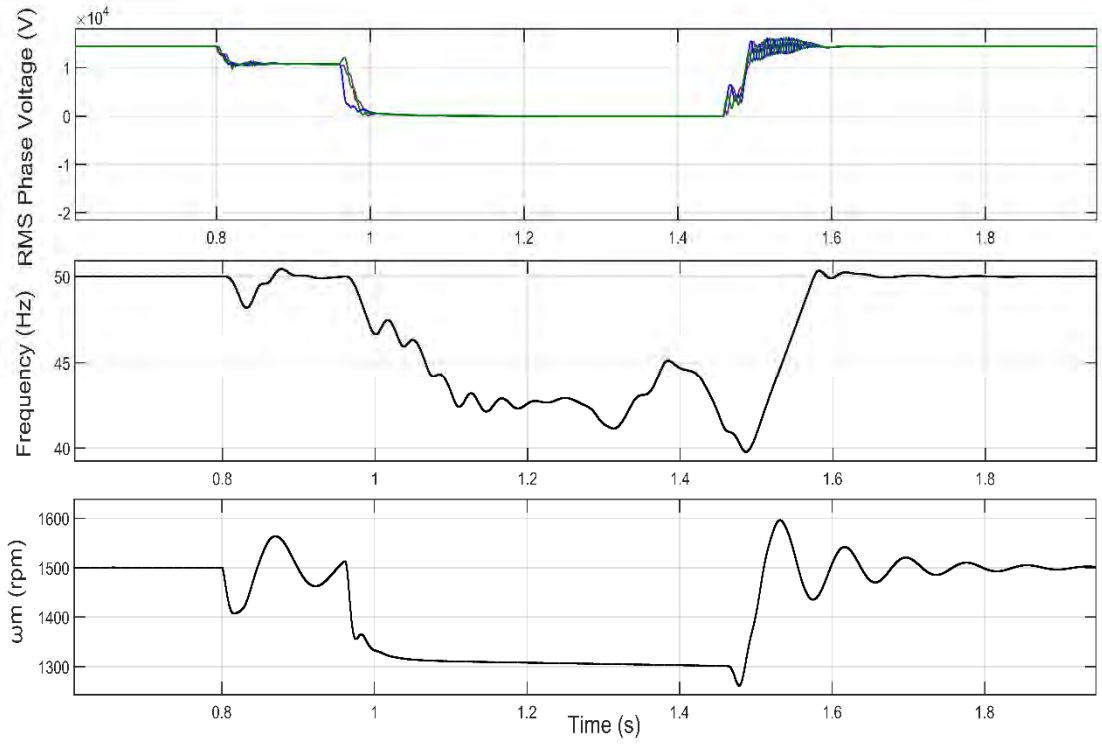

Figure 5.27: Voltage, frequency and IM mechanical speed of permanent fault-scenario III.

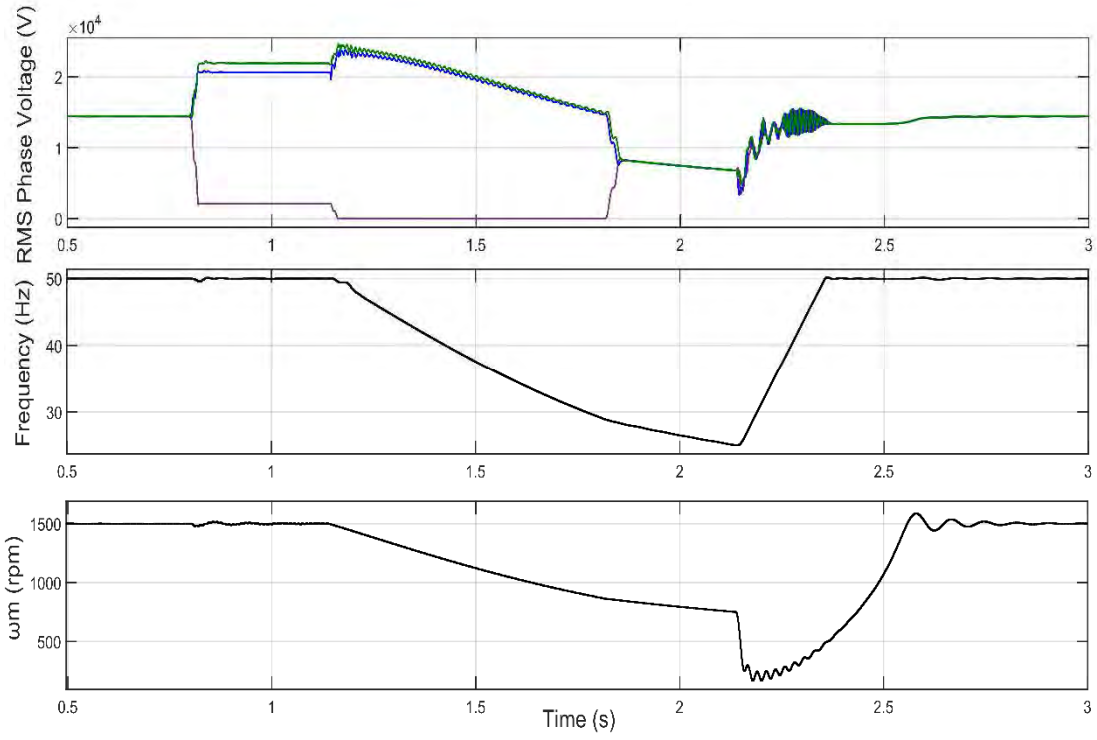

Figure 5.28: Voltage, frequency and IM mechanical speed of permanent fault-scenario IV.

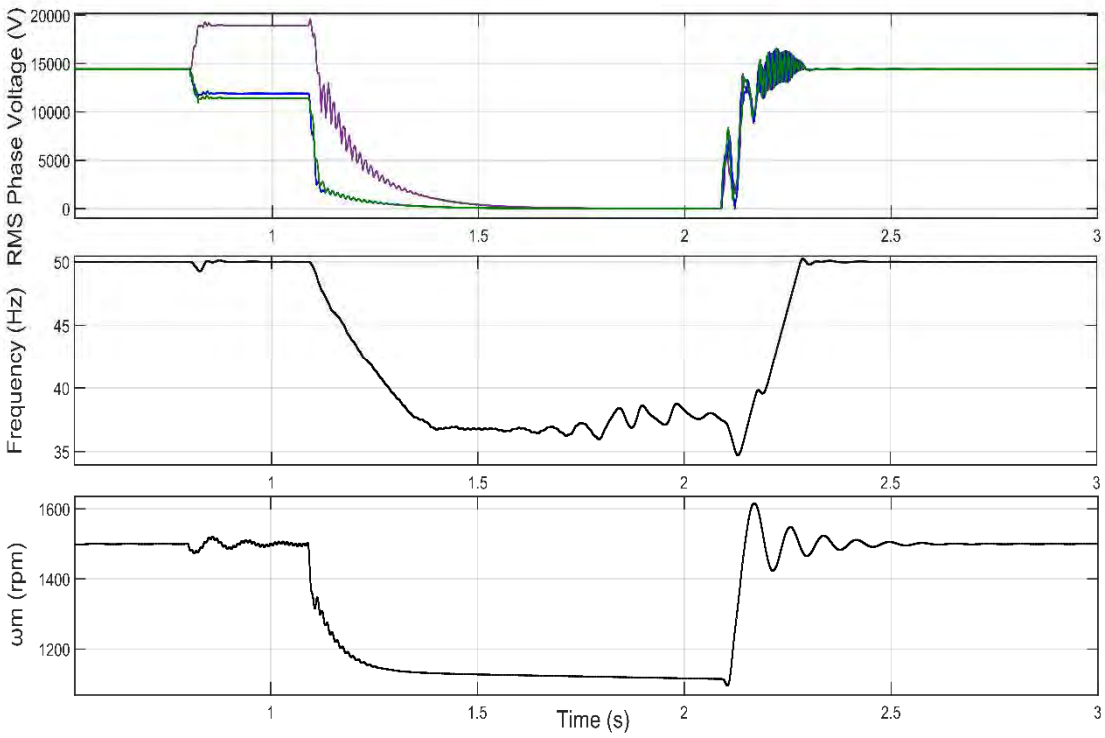

Figure 5.29: Voltage, frequency and IM mechanical speed of permanent fault-scenario V.

From the previous results, the following points can be underscored:

- The lower deceleration occurs for SLG faults. Thus, for these faults, the IM may be capable of feeding the fault for a large period after the CB operation (e.g., roughly between 300 ms and 1 s).
- The large deceleration occurs, as expected, for LLL faults where the contribution following the CB operation is negligible (e.g., roughly one or two cycles).
- In case a SLG fault with high impedance fault occurs, the machine will be feeding the fault until the CB reclosing takes place.
- By analysing the obtained simulations results, more evidence is provided to support that during the island, the frequency is imposed by the IM rotor speed. However, it is also demonstrated that depending on the severity of the fault, the voltage decreases rapidly to zero, and therefore, the frequency goes also to zero even when the machine is running at a certain speed. By observing Figure 5.27 (scenario III), voltage collapses at t = 1 s, where the machine is still at 1330 rpm speed at that time.

5.8 Conclusions

This Chapter has shown the simulation results obtained from the implemented three-phase Matlab/Simulink model defined in the previous Chapter 4. The simulations have been divided into several sections, where each section seeks to address the influence of a particular factor into the IO. Thus, the impact of the following factors have been explored:

- The electrical loads of the island and its load model.
- The type of fault and its clearing time.
- The reclosing time.
- The load torque.
- Permanent-faults.

Firstly, it is crucial to underline that according to the term P_{eload} in equation (4.46) of Chapter 4, the largest is this value, the largest may be the mechanical speed deceleration during the island when acting as a generator. The obtained results from these seven load scenarios substantiate this fact. On the other hand, the lower is this term, the lower voltage drops and smaller frequency deviations occur during the island. Besides, the load models defined in 4.3.6 (i.e., by equations 4.30 and 4.31) proved to be crucial. Mainly, it is seen that type of load model that causes the IM higher deceleration is constant power; nevertheless, the one that causes less deceleration is constant impedance.

Secondly, it has been demonstrated that the larger is the IM deceleration during the fault, the larger is the reacceleration once the fault is cleared. Given the relationship between the frequency during the island and the IM mechanical speed, it has been found that this post-fault reacceleration results in a frequency increasing during the island. To observe such effect, see the measurements in Figure 5.21 for a three-phase fault. On the other hand, it is seen that in case severe faults occur (i.e., three-phase faults close to the IM with a low resistance fault), once the CB has cleared the fault, voltage and frequency show a noticeable decrease in comparison with those which are less severe (faults with high resistance value). This can be appreciated by comparing third and fourth plots of Figure 5.16, where given the same type of fault and clearing time, by varying the resistance fault and location, results are slightly different.

Unlike the faults simulated in 5.4, subsection 5.7 focused on permanent faults. In fact, this casuistry is an extended case of the fault type influence that has been analysed before. The main difference is that while in subsection 5.4 the fault has been considered satisfactorily cleared, in 5.7, the IM feds the fault following CB operation. By observing the obtained results in 5.7, it can be concluded that following the CB operation, the IM is capable of feeding a fault during the island only if it is a SLG. For the rest of faults, it is observed that voltage collapses few ms after the CB operation and so does the frequency and this fact should not go unnoticed. Crucially, the voltage collapse occurs due to the IM rotor demagnetisation, and therefore, even with the IM running at a particular speed, it will no longer act as a generator. This effect is especially remarkable for severe three-phase faults.

In third place, it has been demonstrated that the reclosing time plays a significant role and determines the duration of the island. By observing Figure 5.22, it can be said that the larger the reclosing time, the larger is the decrease in frequency and voltage.

Fourthly, considering the measurements obtained from the simulated scenarios, the impact that has the term Γ_{load} in the islanding proved undeniable. This term belongs to the mechanical equation contained in the set of differential equations (4.39) defined in the previous Chapter 4. It can be concluded that the larger is this value, the larger is the deceleration of the IM during the

island. As a consequence, the higher is the decrease in voltage and frequency during the island and the larger is the time recovery after the CB reclosing. Particularly, Figure 5.23 (scenario IV of section 5.6) show the measurements for a full-load torque scenario, where the IM recovery takes 1.4 s to recover to a pre-fault point of operation.

It is essential to underscore that a common feature observed for all simulated scenarios, is the fact that the larger is the IM deceleration, the larger is the voltage and frequency drop during the island. Furthermore, there has been more than sufficient proof of the relationship between IM rotor mechanical speed and the frequency during the island, which supports the analytical expressions of Chapter 4.

In conclusion, some of the parameters analysed in this chapter have proven to be crucial to assess this IO. Note that some of these simulated scenarios will be used to validate the model in the subsequent Chapter 7, where the comparison between simulations results and the field measurements is presented.

Chapter 6

Field measurements

6.1 Introduction

This section provides a summary of the field measurements and a discussion about the main conclusions derived from the recorded events. Two locations were selected for recording system variables (see Figure 4.1 in Chapter 4, section 4.2): node PCC_1 (node 2), located at the beginning of feeder A, and node PCC_2 (node 8), from which a large IMs are supplied. Although a high number of real events have been recorded, to not excessively extend the document, only seven events are analysed in this Chapter. A representative sample of these events is listed in Table 6.1.The equipment used to record the events are the protective relays installed at both PCC_1 and PCC_2. The fault recorders register voltage and current signals with 32 samples per cycle. The over-current relays are equipped with an oscillography function; in PCC_1 the relay registration is set to 400 ms, whilst in PCC_2, this value is set to 600 ms.

The main reason why each event is displayed in different figures is the memory limitation of the digital fault recorder; therefore, in each relay and for every event, two files are generated. Note, however, that for brevity purposes, the recordings from the relay located at (PCC_1) will not be showed for all events. Measurements at PCC_1, are plotted to display the type of fault that caused CB operation that precedes the IO. Thus, each Figure shows the measurements for each event at one location, which in turn, it is separated into two subfigures, named; (**a**) and (**b**). The first subfigure (**a**), shows the beginning of the event, whereas, (**b**), show the end of the event when the CB recloses the circuit. All recorded events were caused by faults located in Feeder A, at either a system node or a distribution line midpoint (e.g., events 4, 7 and 9 of Table 6.1). An opening operation of the circuit breaker CB, see Figure 6.2, will always cause an island in which the large IM can continue operating after CB operation.

Figure 4.7 in subsection 4.3.6, depicts the load profile measured at PCC_1 during half month and the time of occurrence of some recorded events; namely events 1, 4, 5, 7, 8 and 9, as numbered in Table 6.1. For the sake of brevity, from the 9 listed events in Table 6.1, only seven will be displayed and discussed because, considering that they provide an acceptable sample to represent the phenomenon object of study. In fact, with the events discussed in this section, the required casuistry to achieve further validations will suffice.

Table 6.1: A selected list of the real occurred events.

Event	Beginning	Ending	Fault type	Fault current (A)	Fault location	t_{cl} (ms)	P (MW)	V* (kV)
1	17:01:09.776	17:01:10.636	SLG	218	Node 8	90	0.52	8.58
2	07:44:39.544	07:44:40.354	SLG	224	Node 5	90	0.45	9
3	04:10:35.580	04:10:36.880	LLG/SLG	707	Node 8	90	0.8	0
4	18:14:54.263	18:14:55.128	SLG	240	Line 5	95	0.77	6
5	17:13:58.281	17:13:59.096	SLG	350	Node 7	90	0.85	5
6	09:52:38.440	09:52:39.395	SLG	300	Node 7	100	1.3	3.5
7	11:49:04.702	11:49:05.456	SLG	367	Line 5	95	0.87	4.75
8	16:04:15.667	16:04:16.607	LLG/SLG	360	Node 7	100	1.21	-
9	12:24:19.550	12:24:20.469	SLG	264	Line 6	95	0.7	6.2

* Values measured one-cycle before the CB reclosing.

Fault current RMS current value sensed by the over-current relay at PCC_1

t_{cl} The clearing time of the CB at PCC_1

P Active-power of feeder loads at the time the event occurs

V RMS phase-A voltage value one-cycle before the reclosing takes place.

6.2 Event I

This event is caused by a single line-to-ground (SLG) fault at node 8 with a high-resistance fault of roughly 31.5 Ω. It is event 1 in Table 6.1, and is cleared by the circuit breaker CB installed at the head of feeder A. According to the voltages measured in both PCC_1 and PCC_2, the effect of line impedance from node 2 to 8 (11 Ω) is observable, thus, the voltage sag of 7.1 kV at node 8 becomes 8.89 kV at the PCC_1. The sequence is as follows: (i) SLG fault occurs at node 8; (ii) CB opens; (iii) CB recloses after a prefixed period (810 ms). Figures 6.1 and 6.2 show measurements recorded respectively at PCC_1 and PCC_2, and corresponding to the beginning and the end of Event I. Thus, Figure 6.1 depicts some recordings measured at the source side of PCC_1. The two plots show frequency, voltage and current variations during a period that covers pre-fault, during-fault, and post-fault scenarios, including also the post-reclosing period. The beginning of the full event is depicted in Figure 6.1a; the upper arrows indicate the three parts of the transient process**.** One can observe voltage and current variations due to CB operation: the measured currents correspond to those flowing through feeder B; the frequency is that of the transmission system and remains constant; voltages are affected by substation grounding, and they exhibit a sag and two swells. Take into consideration that this can also affect the unfaulted feeder loads. Figure 6.1b plots the transient response caused by the reclosing operation: the current due to the re-energization, the effect of the current drawn due to the IM reacceleration and the effect of the out-of-phase reconnection are observable. On the other hand, Figure 6.2 depicts the measurements recorded at the MV side of the transformer at the load-side of PCC_2 during the same period that Figure 6.2. After CB operation, the IM continues connected to the feeder, which does not longer supply active power. Consequently, the frequency in this part of the system steadily decreases until the reclosing

instant. Figure 6.2b also shows that, according to the recorded measurements, after the CB reclosing the IM reaccelerates until it recovers its rate speed, although, initially, the frequency (and the IM speed) decreases even more as a consequence of the reclosing transient. Take into account that frequency and voltage mismatches between the two CB terminals at the reclosing time will cause a transient torque that could seriously affect the machine.

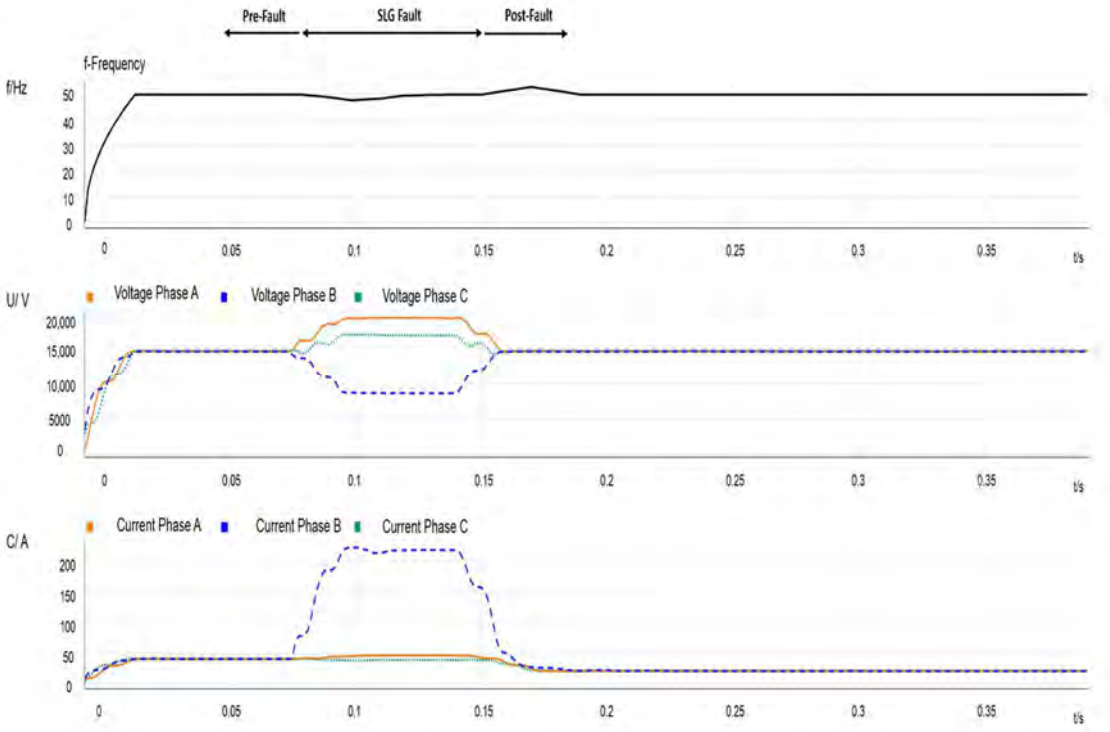

(**a**)

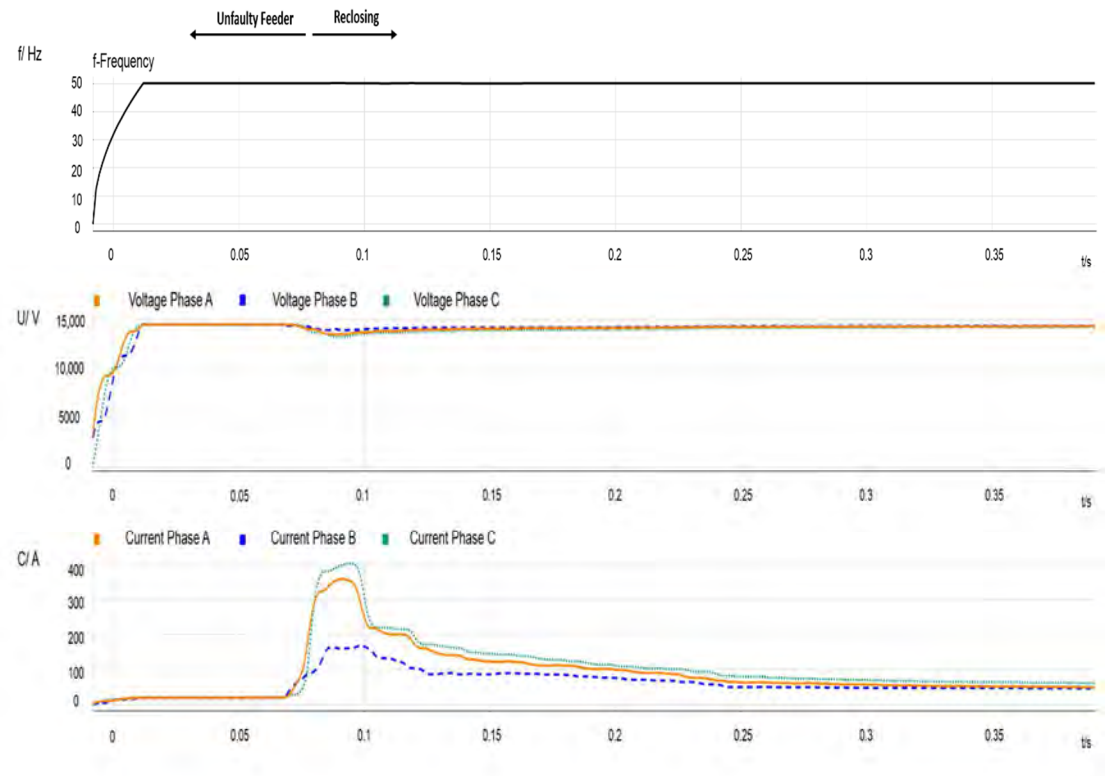

(**b**)

Figure 6.1: Event I – Measurements at PCC_1 for a SLG fault at node 8.

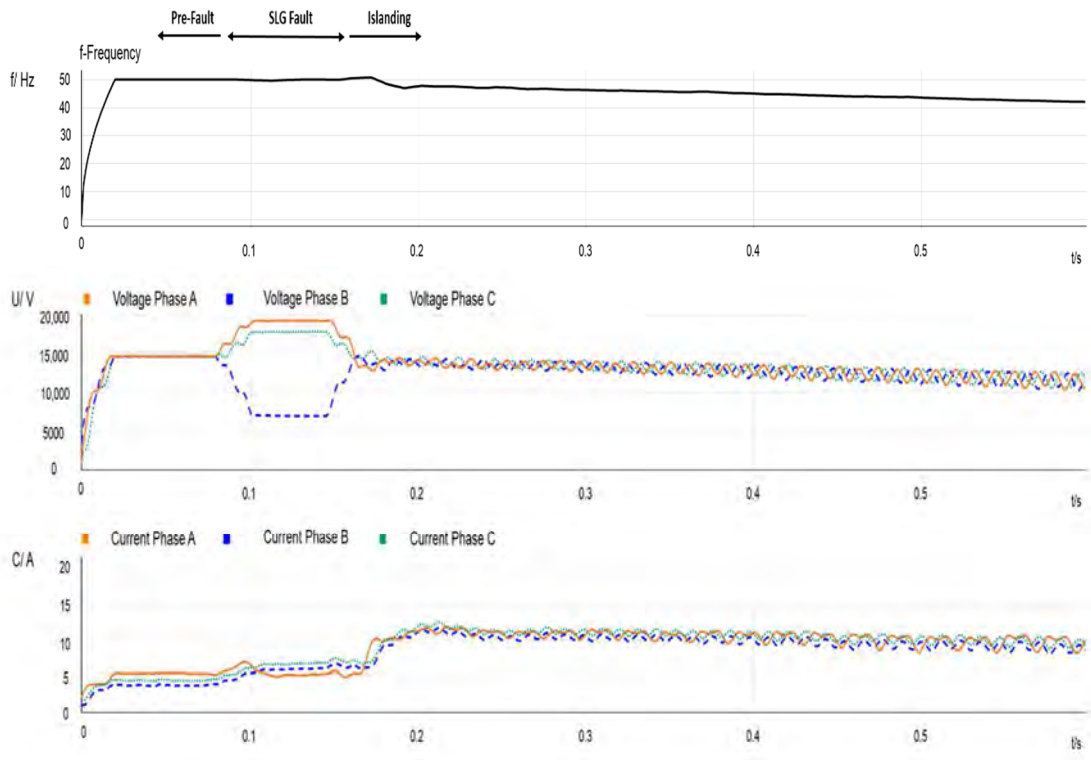

(**a**)

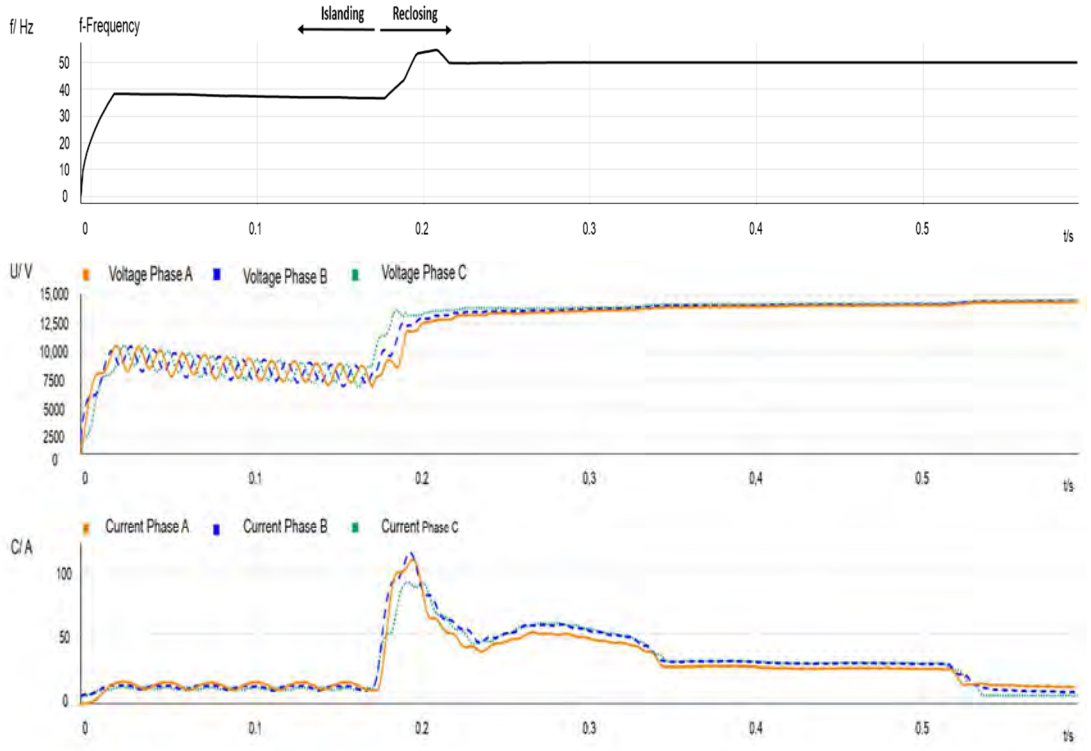

(**b**)

Figure 6.2: Event I - Measurements at PCC_2 for a SLG fault at node 8.

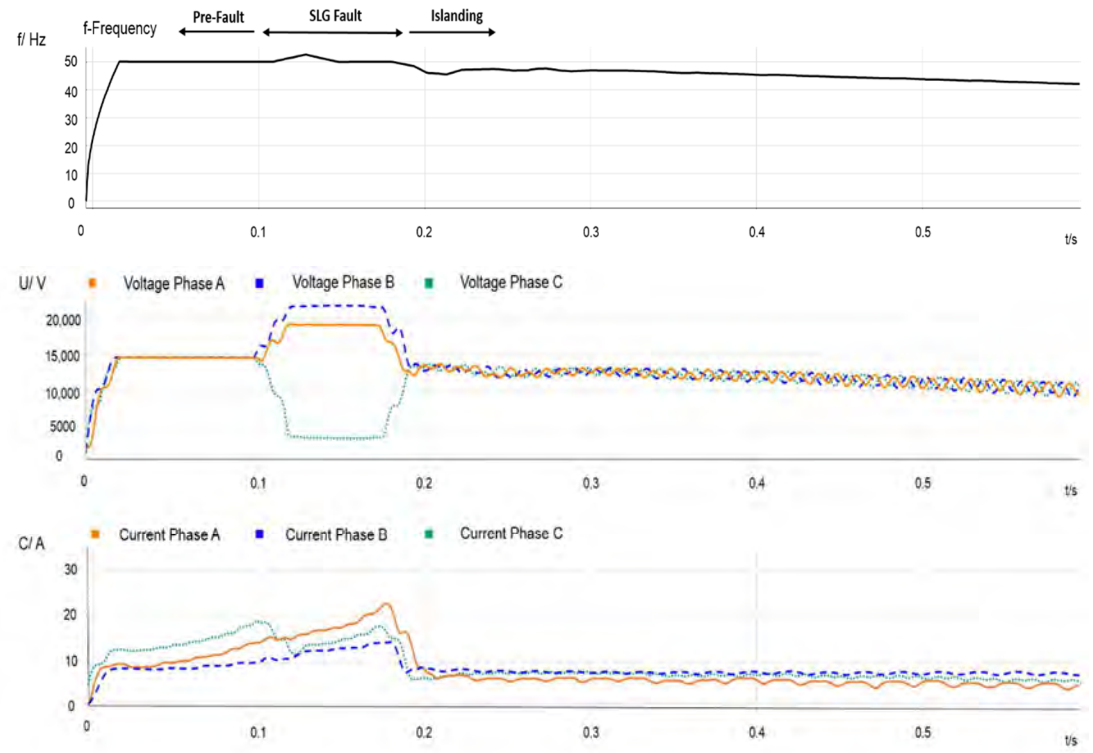

(**a**)

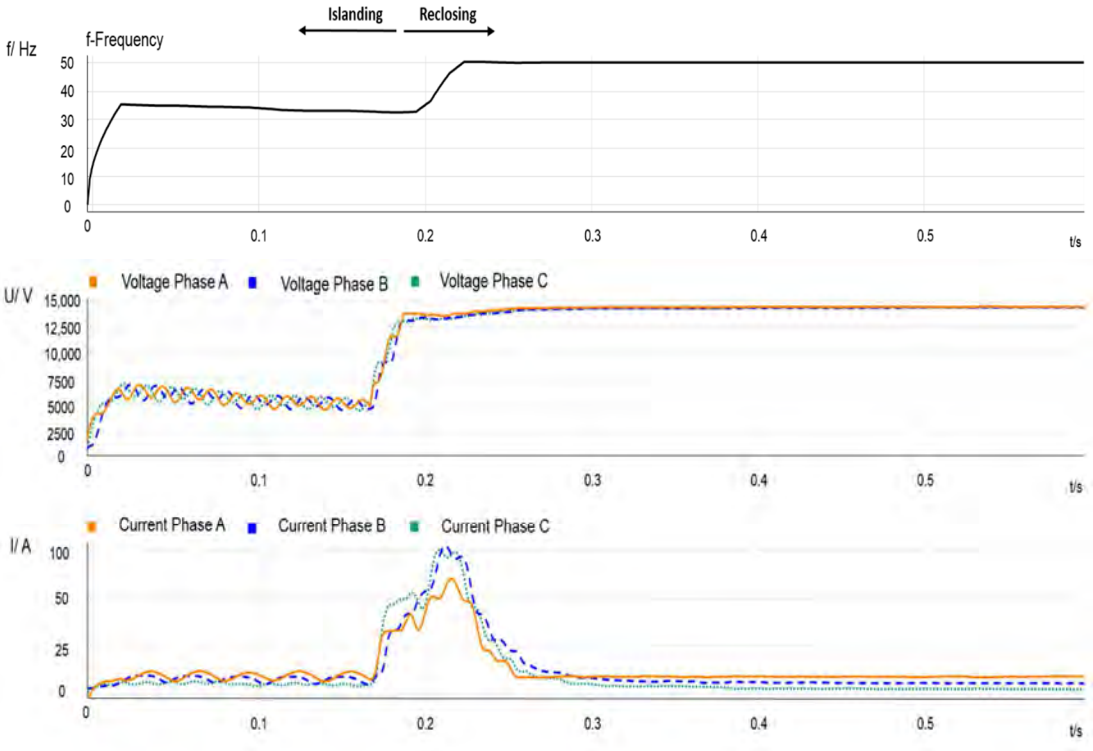

(**b**)

Figure 6.3: Event II - Measurements at PCC_2 for a SLG between nodes 6 and 7.

6.3 Event II

This event corresponds to a SLG fault (phase c is the faulted one) that occurs at a midpoint of the line between nodes 6 and 7 (i.e., Line L5) with low resistance fault; it is event 4 in Table 6.1. Measurements obtained during the fault at PCC_2 are V_a = 18.92 kV, V_b = 21.6 kV and, V_c =3.8 kV, whereas the fault current is 240 A. Figure 6.3 shows measurements recorded at PCC_2. It is clear from Figure 6.3b that the IM is acting as a generator after the circuit breaker CB clears the fault. It is also noticeable that the values when the CB recloses are lower when compared with the previous Event I, due to the higher loads connected into the affected feeder at that instant. At the time occurs, the feeder loads value where 770 kW, which explains this accentuated drop in voltage and frequency during the island. Particularly, the voltage value one-cycle before the CB reclosing is 5.45 kV whereas frequency is 32 Hz.

6.4 Event III

Event III describes the particular case of a permanent fault. Therefore, it presents a different scenario in which the fault is prolonged due to the IM. It must be emphasized that, as stated before, this fact constitutes a high risk for the grid. Figure 6.4 shows measurements recorded at both PCC_1 and PCC_2 corresponding to a permanent SLG fault that occurs at node 8, clearly observable by taking a look at the voltage sag magnitude for the faulty phase at the PCC_2; see Figure 6.4 and event 3 in Table 6.1. Moreover, it is worth mentioning that the SLG in Feeder A appears simultaneously with a two-phase-to-ground (LLG) in an MV neighbor feeder. After the CB opening operation, the fault is fed by the IM. Figure 6.4b shows the measurements of the PCC_2 and evidences the untimely tripping operations by the head-CB. For this event, the fault was prolonged 800 ms after the CB aperture. The transient represented in Figure 6.4b can be divided into parts: the top arrows in this figure indicate the pre-fault situation, the SLG fed by the main grid, and the fault fed by the IM. Thus, the period of time when the fault is feed by the utility represents the clearing time of the CB at PCC_1, and following this period, the IM is feeding the fault during the island.

6.5 Event IV

Event IV belongs to the event 7 in table 6.1 and the islanding operation is preceded by a SLG fault that occurred in a midpoint in line 5 which was cleared in 90 ms. By comparing voltages measured at PCC_2 during the fault (i.e., the voltage sag and both voltage swells) for this event with those measured during Event II, it can be seen that the current values are noticeably larger. This fact underscores that the impedance seen by the fault point is higher. In particular, this event occurred on 21 November 2016 at 11:49, where the power drawn at that time was 0.87 MW. Figures 6.5a and 6.5b show the measurements recorded at PCC_2, corresponding to the beginning and the end of Event IV respectively. Note, that the voltage (voltage phase a) and frequency values measured one-cycle before the CB reclosing are 4.75 kV and 32 Hz. In the previous events, a 100 ms of pre-fault have been displayed. Unfortunately, in this event due to a missoperation of the relay fault recorder in PCC_2 when recording the event, no pre-fault has been recorded.

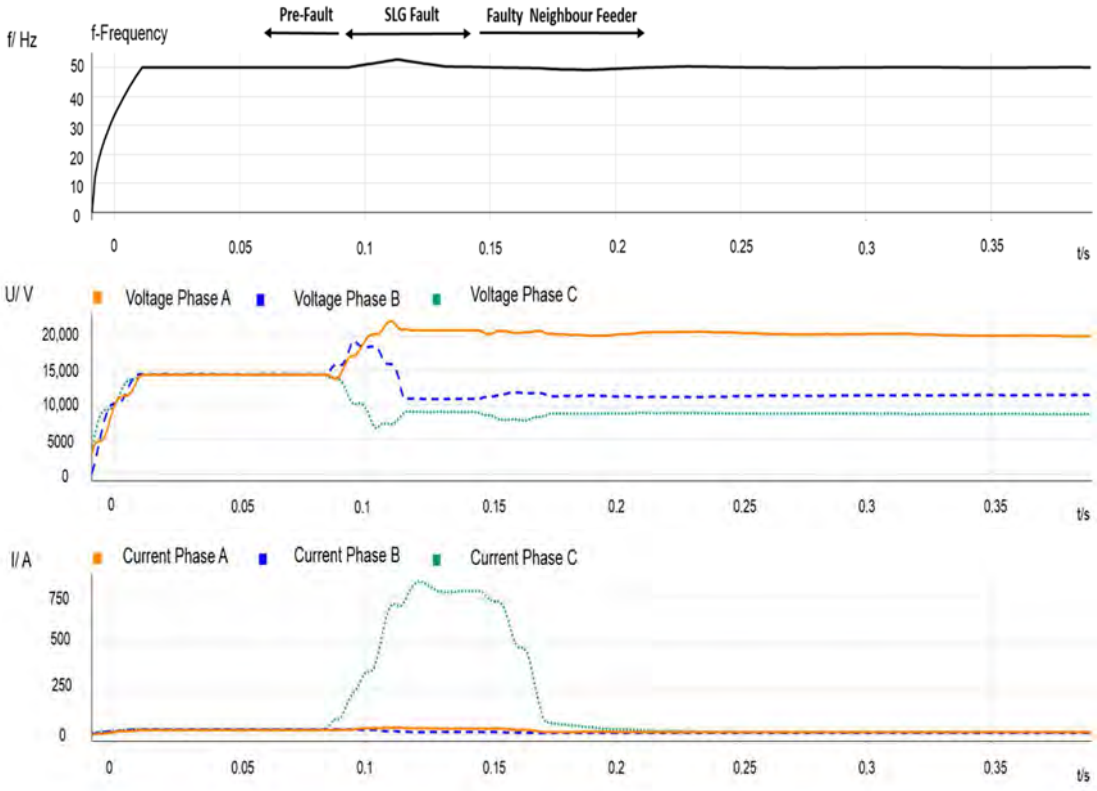

(**a**)

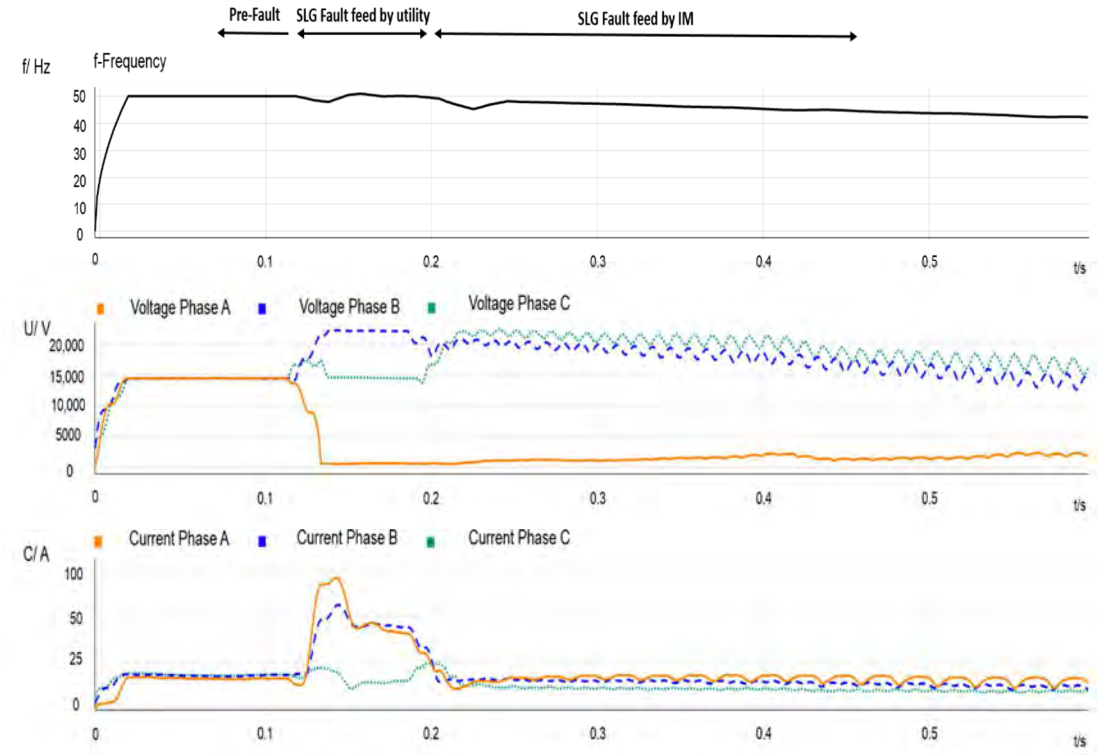

(**b**)

Figure 6.4: Event III – Measurements at PCC_2 for a Permanent fault at node 8.

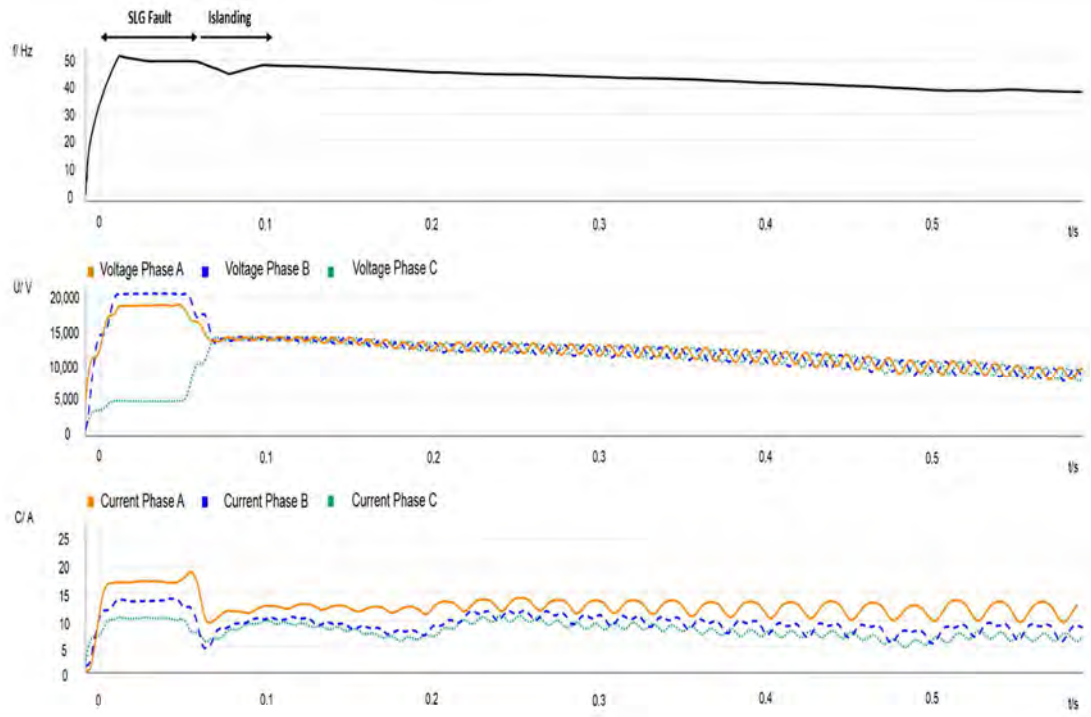

(**a**)

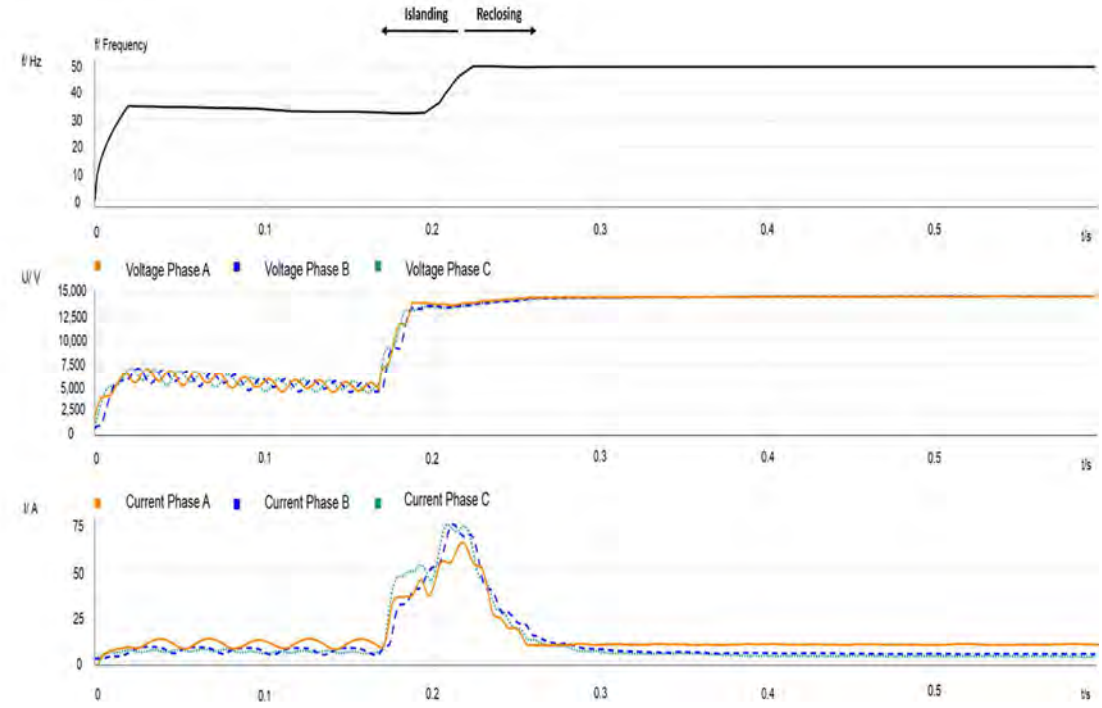

(**b**)

Figure 6.5: Event IV – Measurements at PCC_2 for a SLG in a midpoint in Line 5.

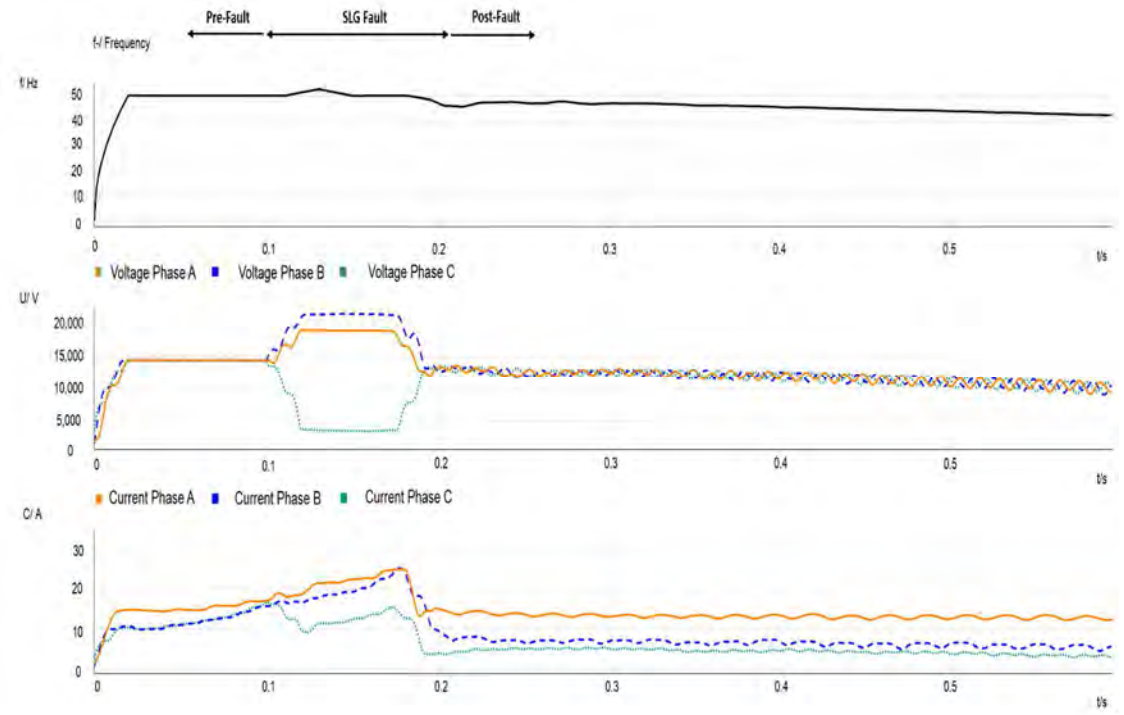

(**a**)

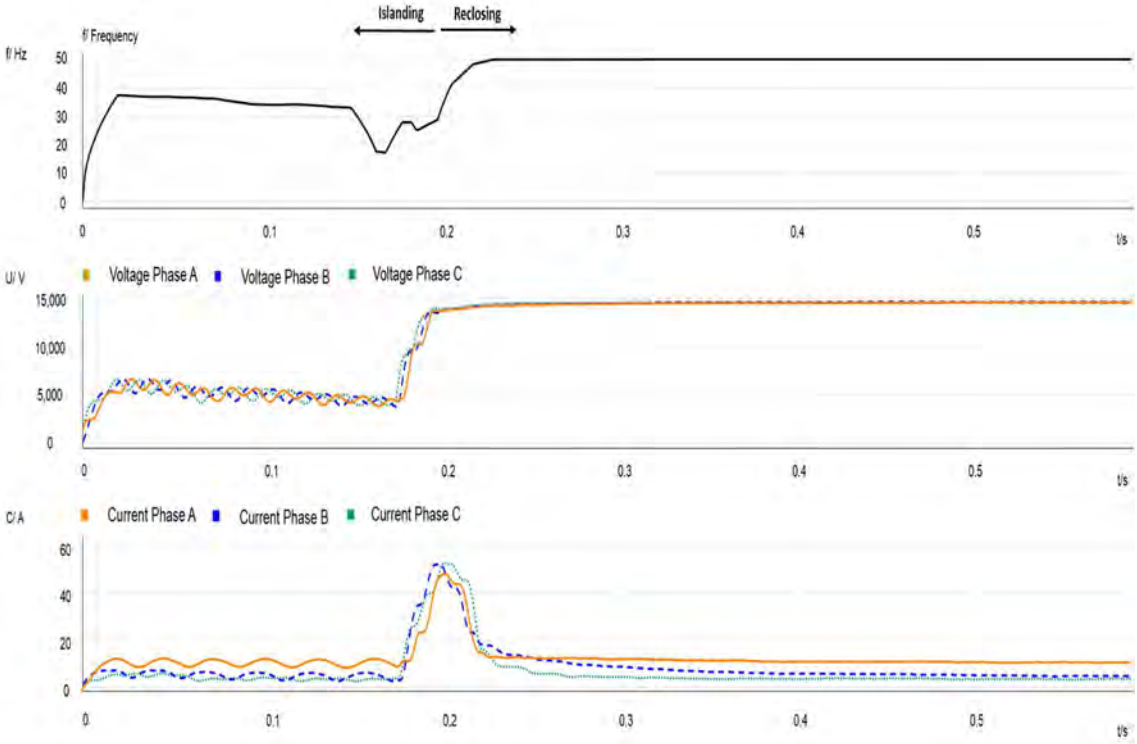

(**b**)

Figure 6.6: Event V – Measurements at PCC_2 for a SLG at node 7.

6.6 Event V

Event V belongs to the event 5 in table 6.1 and the islanding operation is preceded by a SLG fault that occurs at node 7 which is cleared in 90 ms. By analysing voltage and current measurements at PCC_1 as well as taking a look at the voltage sag magnitude in both PCC_1 and PCC_2, it can be seen that the fault is close to PCC_2. In fact, if the voltage sag measured in PCC_2 of event IV is compared with the one measured in event V, the voltage difference belongs to the impedance between buses. In this case, the resistance fault proved to be roughly 5 Ω. As for other events, the sequence is as follows: (i) SLG fault occurs; (ii) CB opens; (iii) CB recloses after 815 ms. Figures 6.6a and 6.6b show the measurements recorded at PCC_2, corresponding to the beginning and the end of event V. The power drawn by the feeder loads at that time the fault occurs, was 0.85 MW. Voltage (Phase a) and frequency measured one-cycle before the CB reclosing are 5 kV and 33 Hz. Although in Figure 6.6b the frequency seems to be below this value, this frequency value contains a measurement error. Proof of this error, is the fact that the time period between the two voltage-zero-crossings have been computed before the CB reclosing, and proved to be 30.3 ms.

6.7 Event VI

Event VI belongs to the event 9 in table 6.1 and the islanding operation is preceded by a SLG fault that occurs at line L5, which is cleared in 95 ms. In this case, an additional measurement is available. The protective relay provisionally located at node 9 recorded an event on November 30 at 12:24, which is compared with the other measurements at both PCC_1 and PCC_2. Figure 6.7 shows depicts the recordings at PCC_1 for the event beginning where the pre-fault, the SLG and the post-fault process can be identified. The fault current is 260 A, the voltage of the faulty phase measured at PCC_1 is 7.55 kV, whereas the phase voltage measured at PCC_2 is 5.5 kV due to the impedance between both nodes. Since the fault is originated upstream of the node 8, due to the low current flowing through impedance between nodes 8 and 9, the measured voltages at PCC_2 and at node 9 are very similar. The power drawn by the total amount of loads at the time the fault occurs proved to be 0.7 MW. As for other events, the sequence is as follows: (i) SLG fault occurs; (ii) CB opens; (iii) CB recloses after 810 ms. Figures 6.7a and 6.7b show the measurements recorded at PCC_1, corresponding to the beginning and the end of event VI respectively. By observing the third plot of Figure 6.7b, the magnetizing current due to transformers energization is observed following the CB reclosing at t = 0.07 s.

Voltage and frequency measurements before, during and after the island are showed in the first and second plot of both Figures 6.8 and Figure 6.9 respectively. On the other hand, current measurements are showed in the third plot of Figures 6.8 and 6.9. The current measurements at PCC_2 corresponds to the IMs and are displayed in Figure 6.9, whilst, the current measurements plotted in Figure 6.8 corresponds to the LV loads of node 19. Note that both current measurements are sensed at the MV side of the transformer. It should be underlined that currents at the beginning of Figure 6.9b are zero due to the operation of an under-voltage relay at that node. In Figure 6.7b the inrush current due to the energisation of the sum of MV/LV transformers in Feeder A is observed, similarly, in Figure 6.8b the inrush current drawn by the MV/LV transformer at node 9 can be observed. One-cycle before the CB reclosing, voltage (for phase a) and frequency values are 6.2 kV and 34.1 Hz respectively.

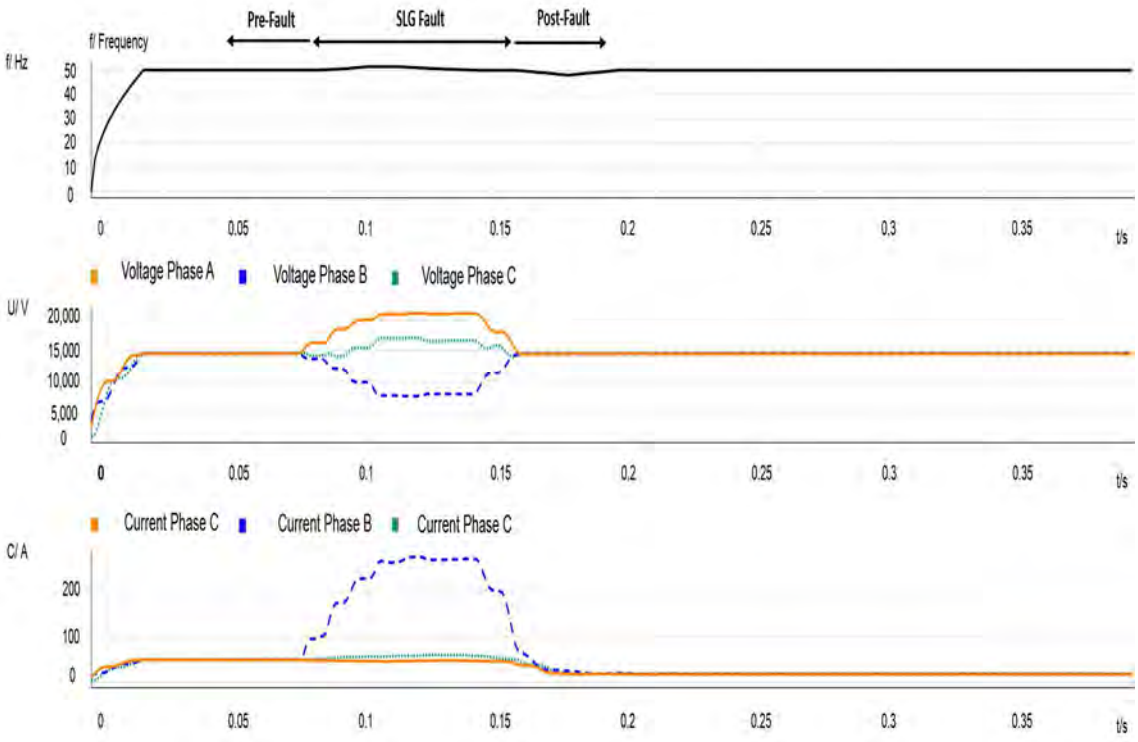

(**a**)

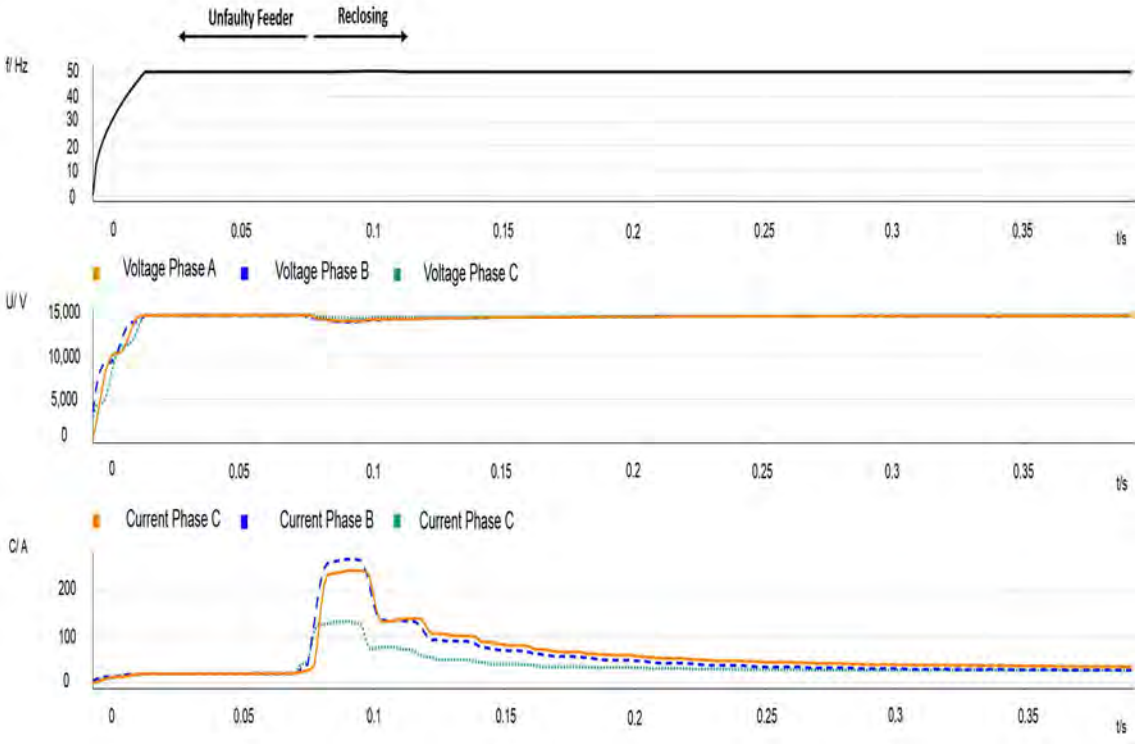

(**b**)

Figure 6.7: Event VI – Measurements at PCC_1 for a SLG at Line L6.

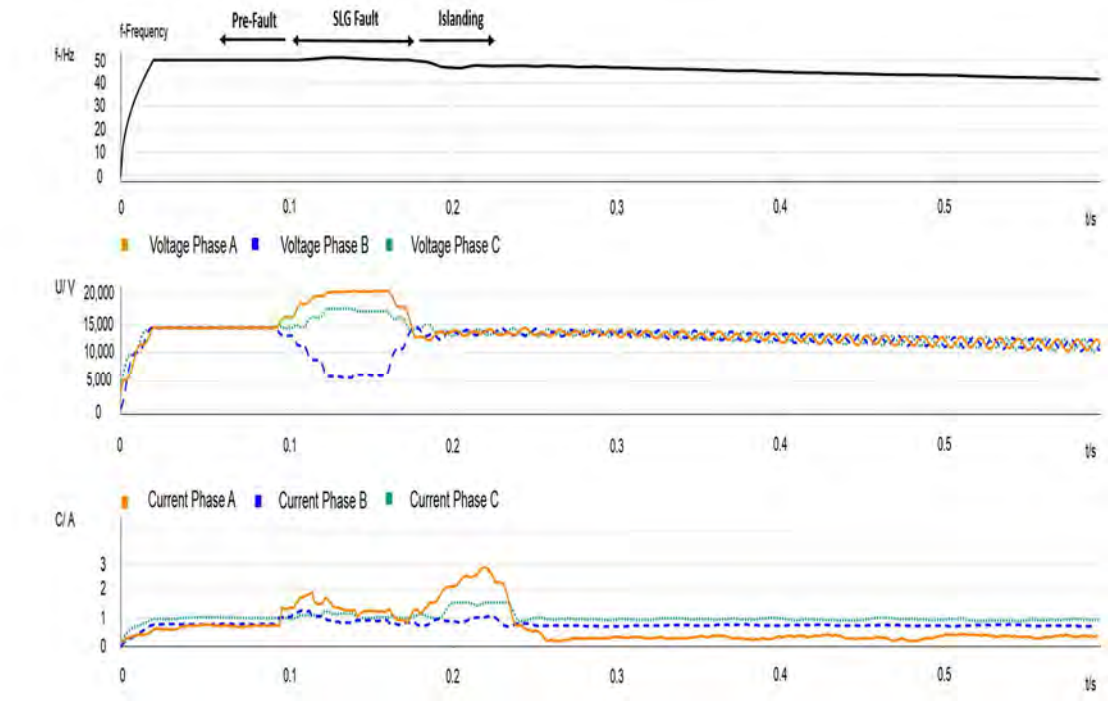

(a)

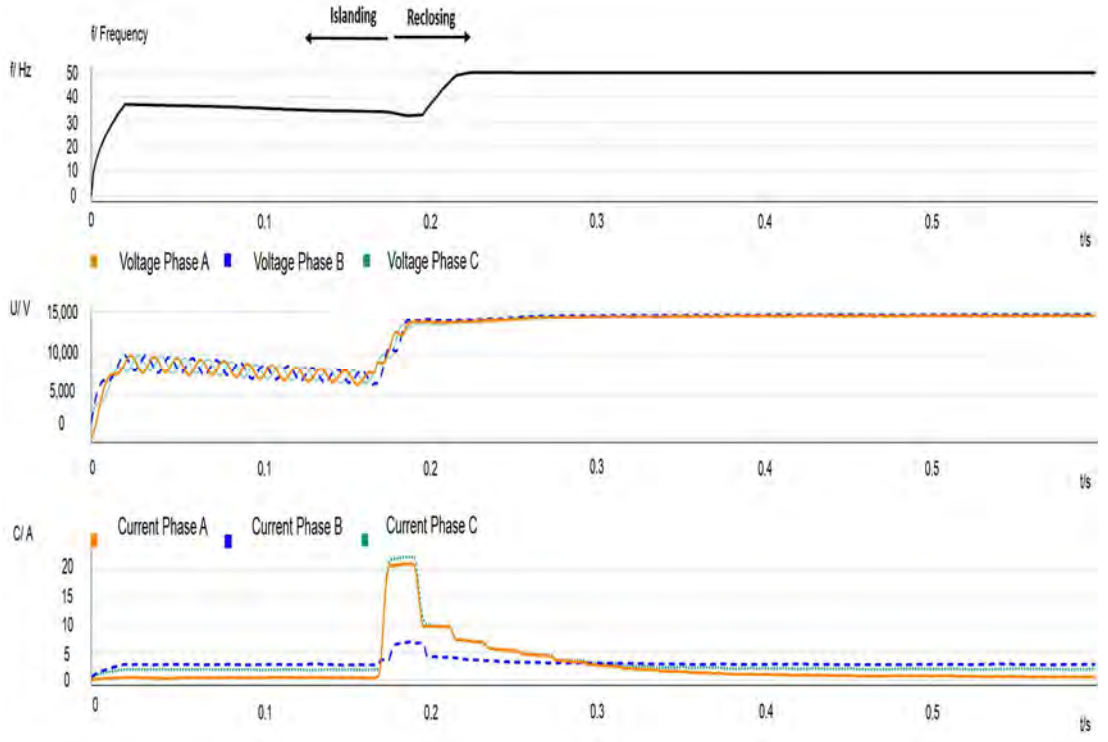

(b)

Figure 6.8: Event VI – Measurements at node 9 for a SLG at Line L6.

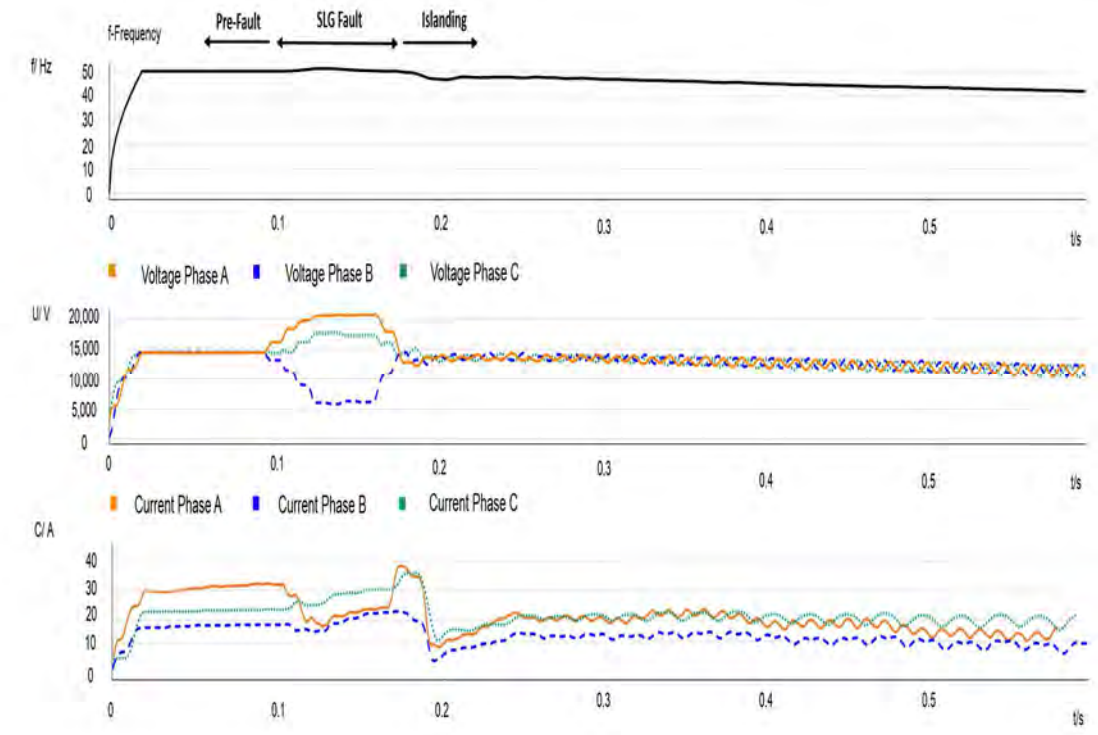

(a)

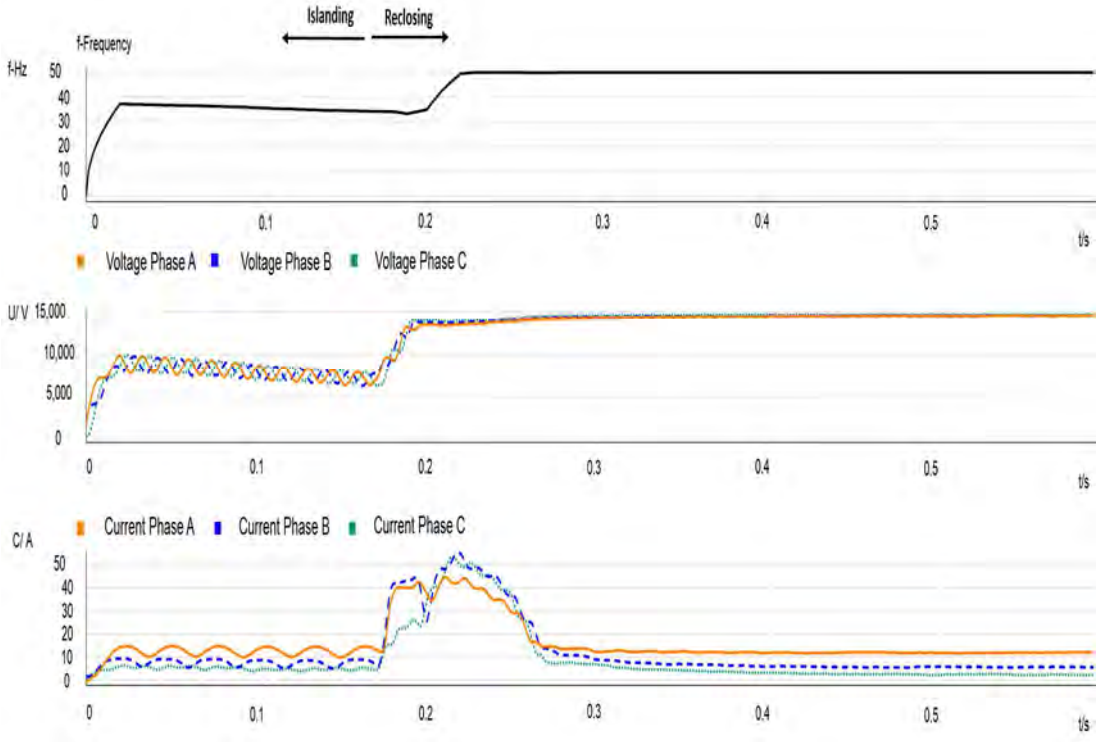

(b)

Figure 6.9: Event VI – Measurements at PCC_2 for a SLG at node at line L6.

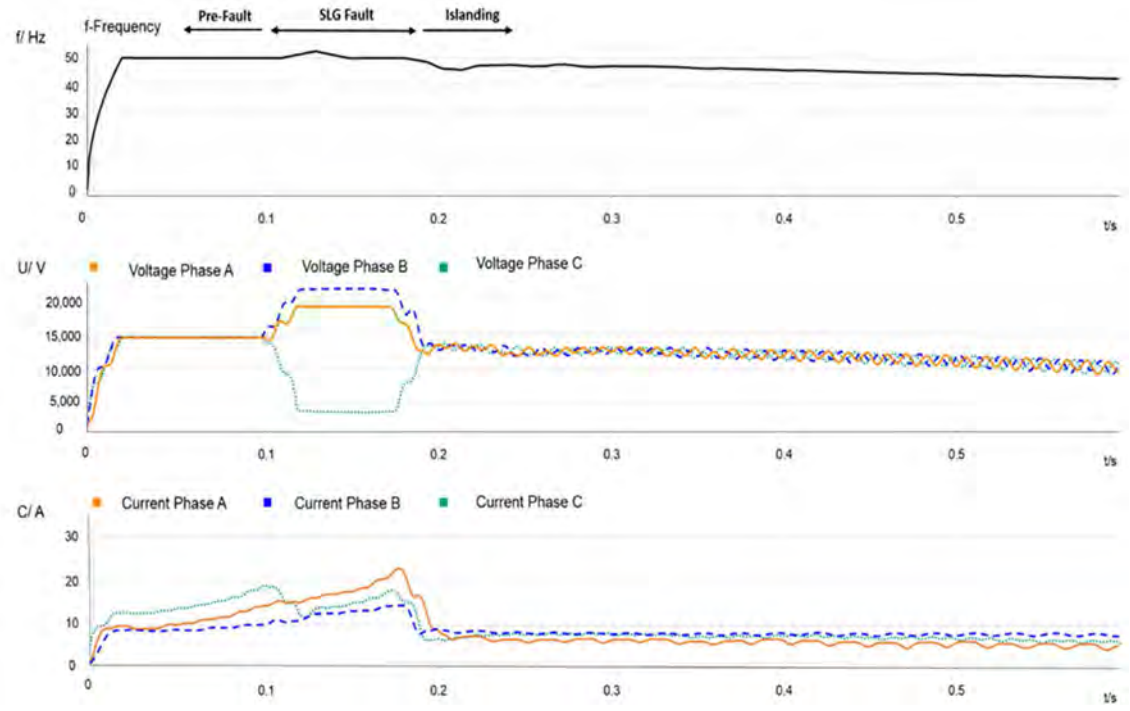

(a)

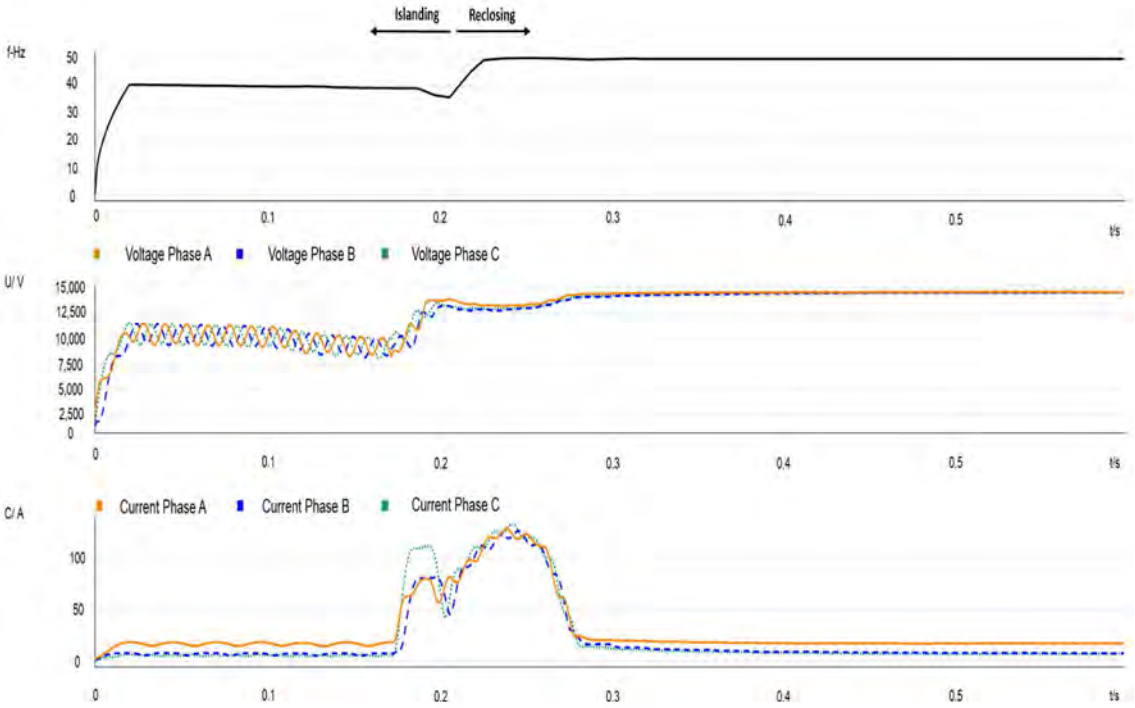

(b)

Figure 6.10: Event VII – Measurements at PCC_2 for a SLG at node at Node 5.

6.8 Event VII

Event VII belongs to the event 2 in table 6.1 and the islanding operation is preceded by a SLG fault that occurs really close to node 5 which is cleared in 90 ms. Voltages measured at PCC_2 are slightly above when compared with those obtained in event II; Va = 4,86 kV, Vb =18.3, kV, Vc = 20.3 kV. Even though the fault occurred closely PCC_1, the large resistance in line L4 due to the lower cross section, increases the fault impedance. Thence, voltage difference is attributed to this larger impedance, which can be proved by observing the fault currents. Thus, in event VII fault current is 240 A whereas in this event, is 224 A. As for all events, the sequence is as follows: (i) SLG fault occurs; (ii) CB opens; (iii) CB recloses after 810 ms. Figures 6.10a and 6.10b show the measurements recorded at PCC_2, corresponding to the beginning and the end of event respectively. This event occurred on August 25 of 2017 at 07:44 h, where the power drawn by the feeder loads at that time was 0.45 MW. Voltage (Phase a) and frequency measured one-cycle before the CB reclosing are 9 kV and 41 Hz.

6.9 Summary of events

This chapter has shown a selection of events occurred in the real distribution network. From these measurements, the following points can be highlighted:

- The discussed events give a realistic idea about the importance of the feeder loads which remain within the island at the time the fault occurs. Therefore, the occurred events with random load scenarios at different hours during the day, provide more evidence of this fact.
- The discrete values obtained one-cycle before the CB reclosing for the seven analysed events are summarised in Table 6.2. By observing this table, it can be seen that the lowest drop in voltage and frequency before the CB reclosing coincides with an instant of the daily profile with low power demand (i.e., early in the morning). On the contrary, the larger voltage drops and frequency excursions, belong to the high power demand scenarios.
- Since the only available data for the distribution operator are measurements at the MV side of the transformer which supplies the industry, the IM measurements such as speed or torque are unknown. However, given the pre-fault measured power, it can be deduced if the motors are operating with full-load torque or with low load torque. Hence, in some events where the power proved to be high, the voltage after CB drop to zero rapidly, meanwhile, when the power is low (i.e., motors with low load torque) voltage is prolonged during the island as can be seen from the previously discussed events.
- As seen above, the faults have been cleared with a short period of time, roughly in 8 cycles. The relay located at the substation (i.e., beginning of the MV feeder 1) is equipped with a VI curve for ground-faults, and given the importance of the protective coordination between devices, the relay located at PCC_1 has to clear the fault in the minimum time possible. Therefore, an instantaneous neutral setting is implemented in that relay.
- As can be seen, SLG faults are the most common type of fault. Nonetheless, other faults such as LLLG or LLG faults had also been recorded during the period of analysis, but unfortunately, the motors were out of service at the time these faults occurred.
- The reclosing times are those obtained from the fault recorder. Initially, the first reclosing was set to 0.8 s, however, as can be seen in event III, later on, the DSO prolonged to 1.3 s.

Table 6.2: Summary of the main values of the recorded events.

Event	V* (kV)	f* (Hz)
I	8.58	40
II	6	36.5
III	-	-
IV	4.75	32
V	5	33
VI	6.2	34.1
VII	9	41

* Values obtained one-cycle before the CB reclosing.

To summarise, this Chapter has showed a selection of real occurred events, which provides enough measurements to perform the model validation.

Chapter 7

Model validation

7.1 General criteria

This Chapter is aimed at validating the model defined in Chapter 4 by comparing the results of the simulations displayed in Chapter 5 with the field measurements showed in Chapter 6. In this chapter, a thorough discussion about the accuracy obtained in the model validation is provided. Besides, the dependability of the equations defined in Chapter 4 is also analysed.

Firstly, the validation will be discussed for each event separately, where the phase-voltages and the frequency are compared in separated plots. It is worth pointing that according to the previous Chapters, for voltage measurements, the RMS value is plotted instead of its waveform. In section 7.6, an explanation about why the RMS value is used instead of the waveform is provided. In addition, the appropriateness of the measurement tools used during simulations is also discussed.

Secondly, even though seven events have been studied in the previous Chapter, considering that the results of some events are very similar, only five events will be validated. From the results provided in Chapter 6, it can be seen that events IV and V are very similar (i.e., voltages and frequencies during the event are not significantly different) and the same happens for events I and VII, where frequency and voltage are almost equal.

As mentioned earlier, field measurements are recorded at the MV side of the transformer (i.e., node 8); therefore, these are the only available measures for the distribution operator. That is the reason why the validation of the mechanical parameters obtained during the simulations such as IM rotor speed or torque cannot be made. However, from the analytical equations defined in Chapter 5, it is seen that the mechanical parameters of the IM are directly linked with the voltage and frequency during the island, thereby, with the available three-phase voltages and frequency measured during the occurred events, the model can be correctly validated.

It is relevant to say that sampling frequency of the relay oscillography function is 32 samples per cycle, thereby, the discrete values obtained from the COMTRADE file downloaded from the relay, are extracted every half cycle. These values are compared with those obtained from the simulations for the same window of time, and therefore, regardless of the simulation time, only the period of time registered by the relay is compared. To fulfil a proper model validation, the comparison between simulated and measured signals has to be performed in the same plot. As mentioned above, the relay has a memory limitation and two files are generated for each event. Hence, in order to appropriately define the event, a collation is done every 10 ms between the end

of the first file and the beginning of the second. In fact, the relay triggers a 100 ms pre-fault and 300 ms post-fault, thereby, the last values of the first file coincide with the initial values of the second file. The validation is separated into two subfigures, named (a) and, (b). The first subfigure (a), shows the frequency validation where measurements are plotted in a dashed-black line, whereas, simulations results are represented with a solid black line. On the other hand, the voltage validation is depicted in subfigures (b), where the solid lines represent the RMS phase voltages obtained from simulation, and dashed-lines represent measurements. Each phase voltage is displayed in a different colour; orange (Phase A), blue (Phase B) and green (Phase C).

7.2 Validation of Event I

Frequency: Figure 7.1a displays the frequency value; its oscillation demonstrates that the adopted model approaches the field measurement satisfactorily. At the reclosing time, the frequency is 40 Hz. The pre-fault active-power of the Feeder A loads is 520 kW.

Voltage: Figure 7.1b compares the three-phase voltages: simulation results are depicted in solid lines whilst field measurements are in dashed lines. The event starts in pre-fault conditions until the single line-to-ground (SLG) fault occurs in phase b at 0.1 s and it is cleared within 95 ms. Afterwards, the islanding operation takes place during 810 ms while the voltage (phase a) at the end of the event reaches 8.58 kV in both simulation and measurements. Moreover, as can be seen in Figure 7.1b, the simulated voltages at PCC_2 during the fault (i.e., the voltage sag and both voltage swells) approach the field measurements with high accuracy, which not only demonstrates the model dependability but the feasibility of the fault location predicted in the previous section. Thus, phase voltages for both simulation and field measurements during the fault are as follows; $V_a = 17.3$ kV, $V_b = 22.1$ kV and, $V_c = 7.1$ kV.

7.3 Validation of Event II

Frequency: Figure 7.2a displays the frequency; its variation demonstrates that the adopted model approaches the recorded event satisfactorily. At the reclosing time, the frequency is 36.5 Hz. The pre-fault active-power of the Feeder A loads is 770 kW when the fault occurs.

Voltage: Figure 7.2b compares the three-phase voltages. The event starts at 0.1 s, the SLG that occurs in phase c is cleared within 95 ms, and the CB reclosing takes place at 1 s (i.e., 800 ms after the fault is cleared) with a voltage of 6 kV; such value is lower than in Event I due to the higher amount of feeder loads connected when the fault occurs. Moreover, as can be seen in Figure 7.4b, the simulated voltages at PCC_2 during the fault (i.e., the voltage sag and both voltage swells) approach the field measurements with high accuracy. Voltages during the fault are as follows; $V_a = 18.92$, kV, $V_b = 21.6$ kV and, $V_c = 3.8$ kV.

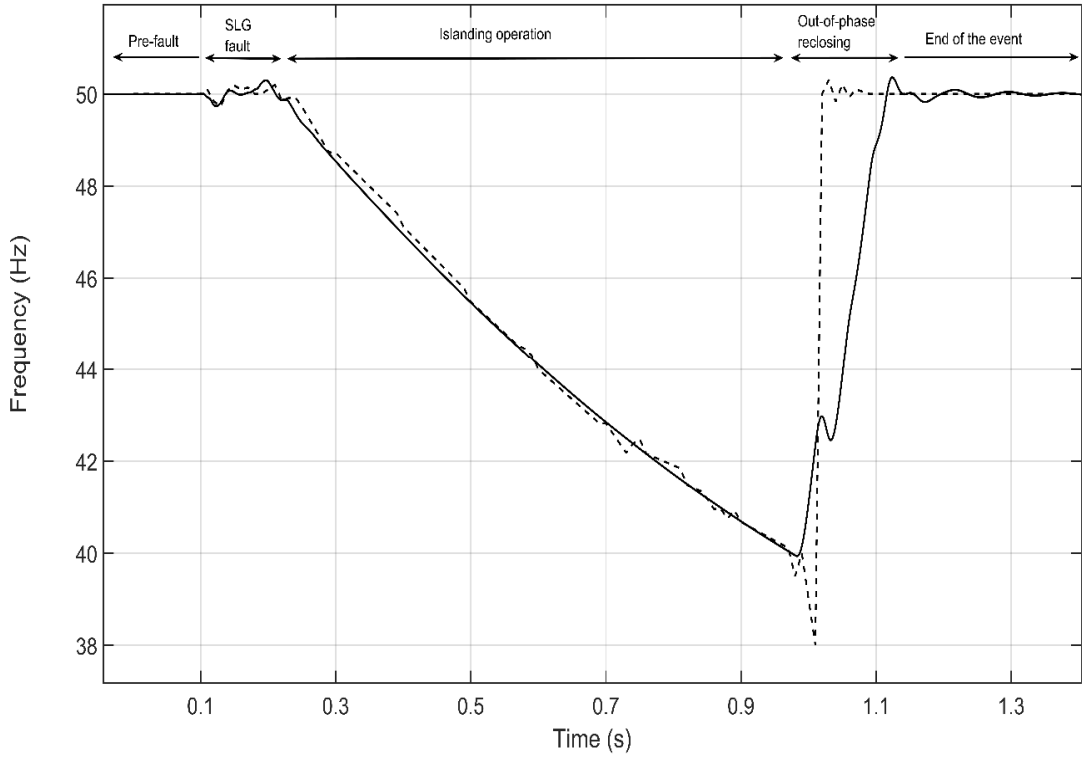

(**a**)

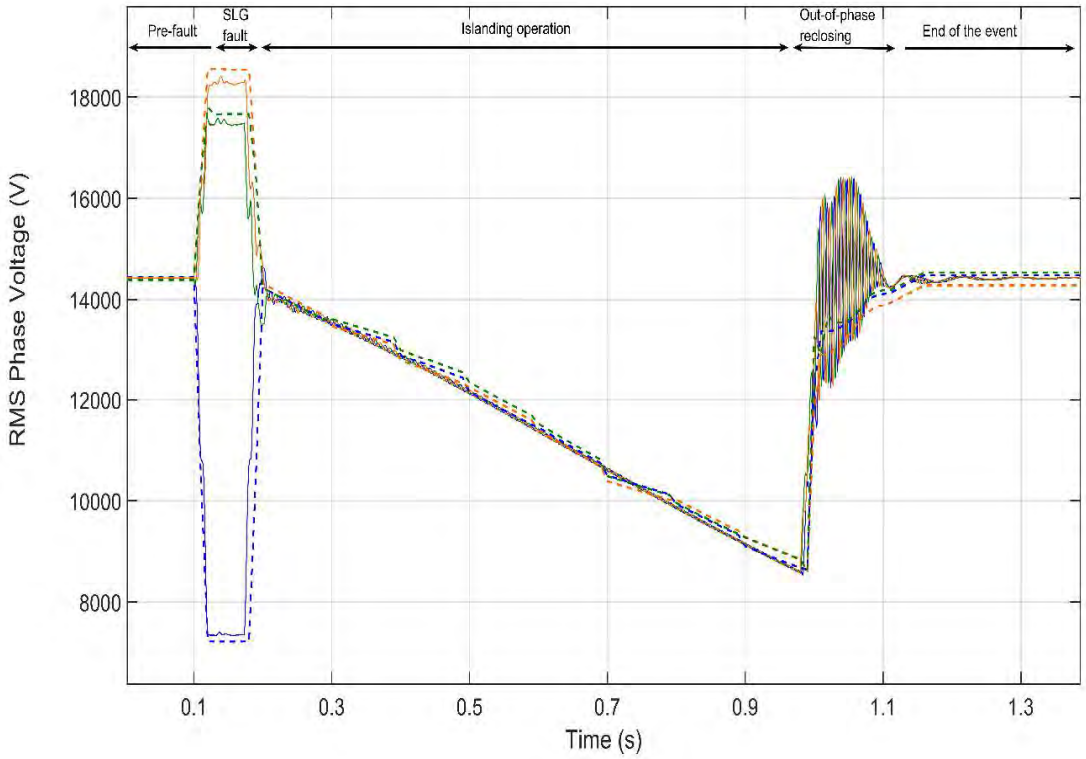

(**b**)

Figure 7.1: Validation of Event I.

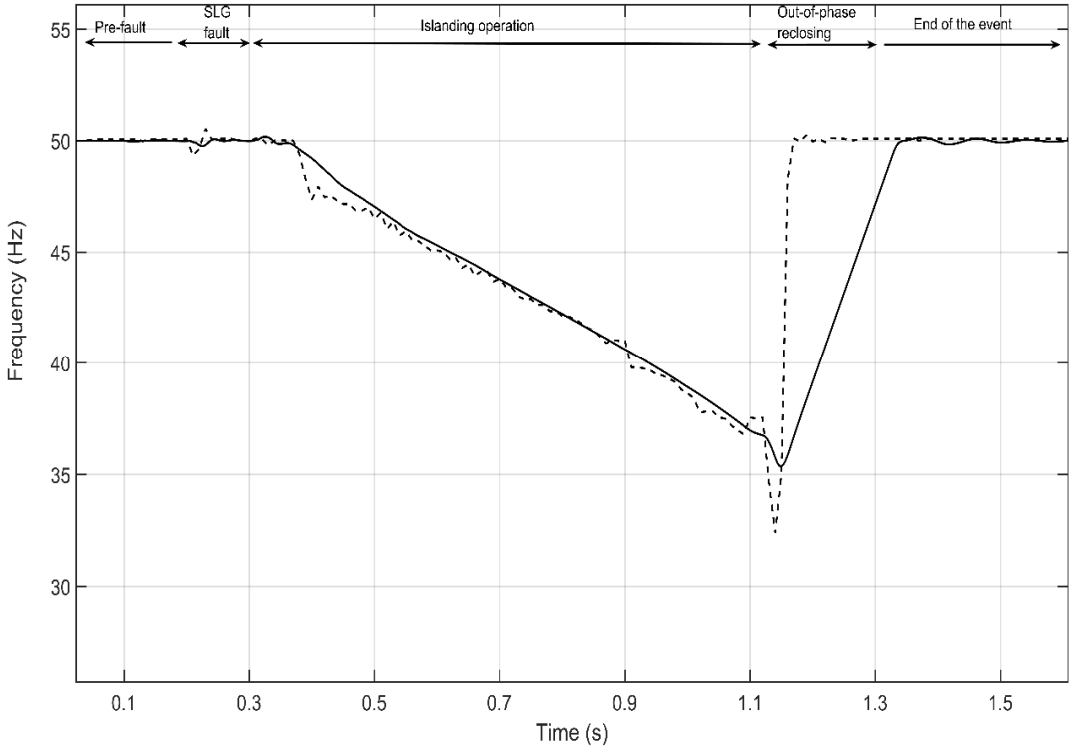

(**a**)

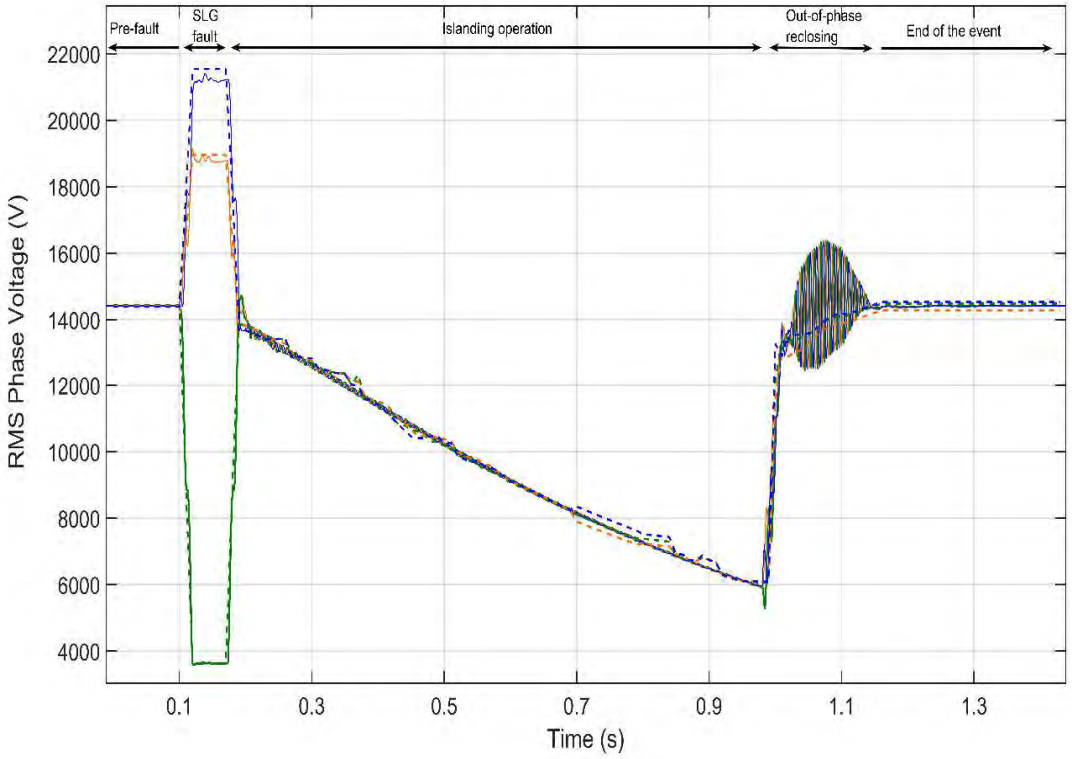

(**b**)

Figure 7.2: Validation of Event II.

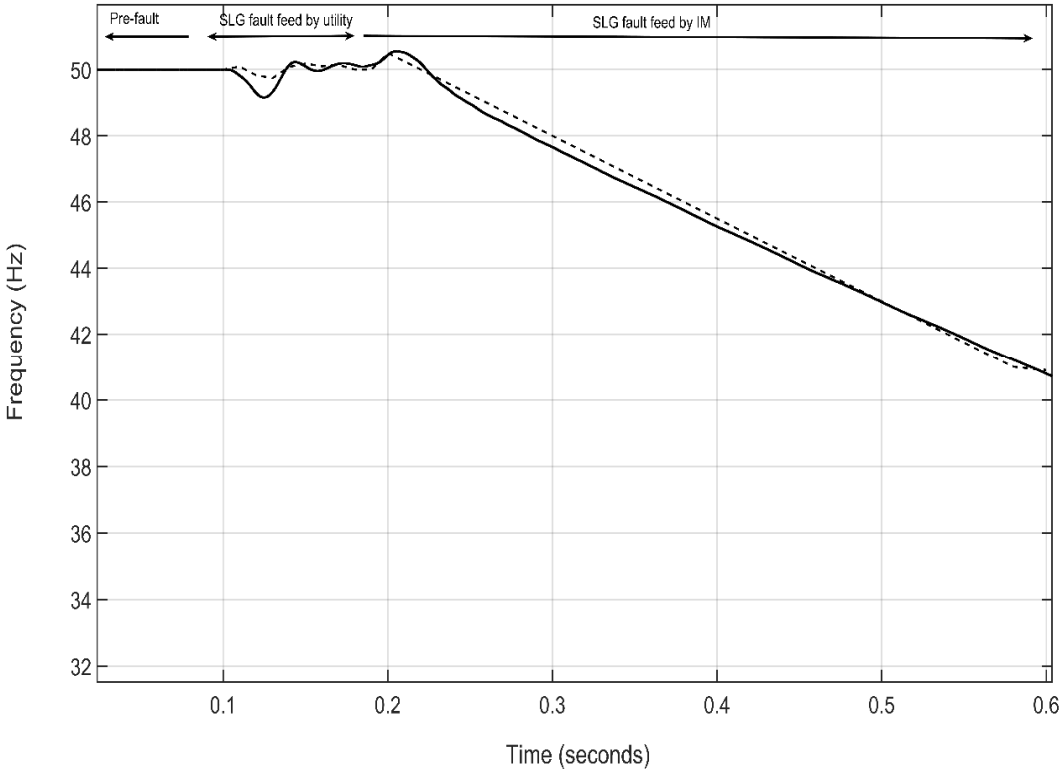

(**a**)

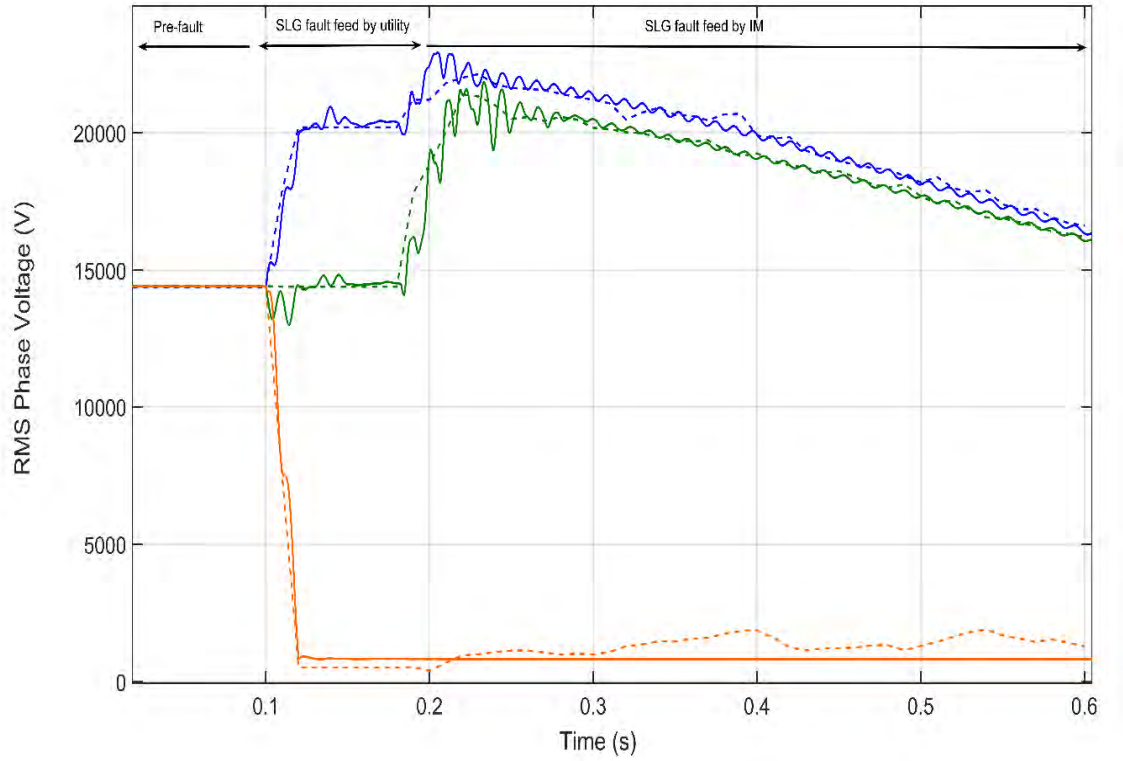

(**b**)

Figure 7.3: Validation of Event III.

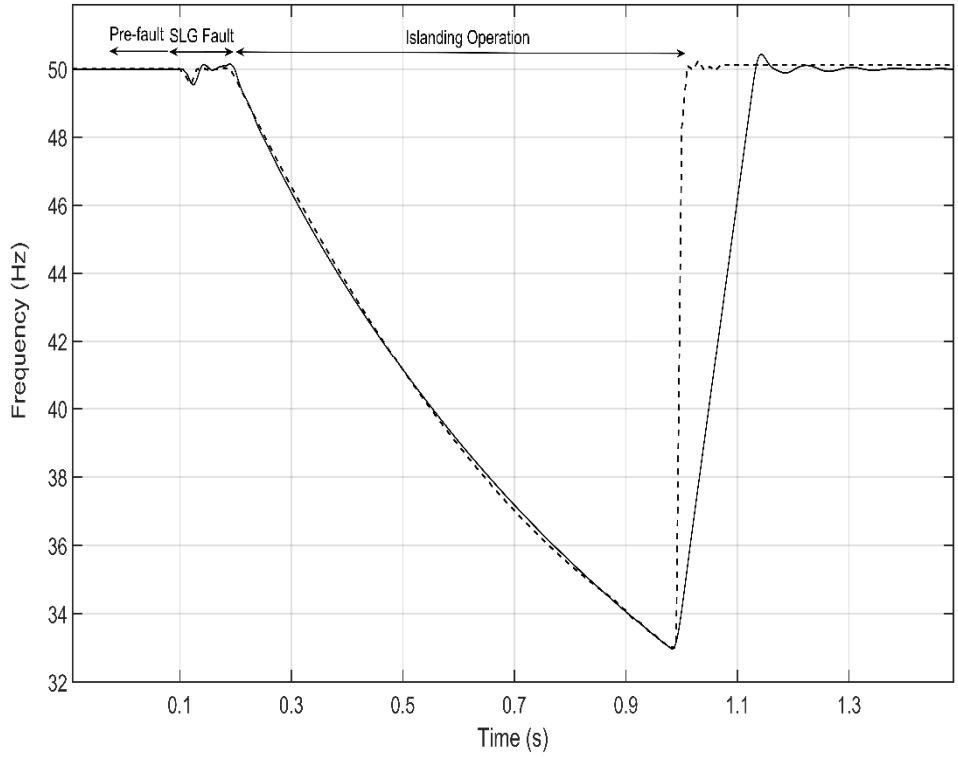

(**a**)

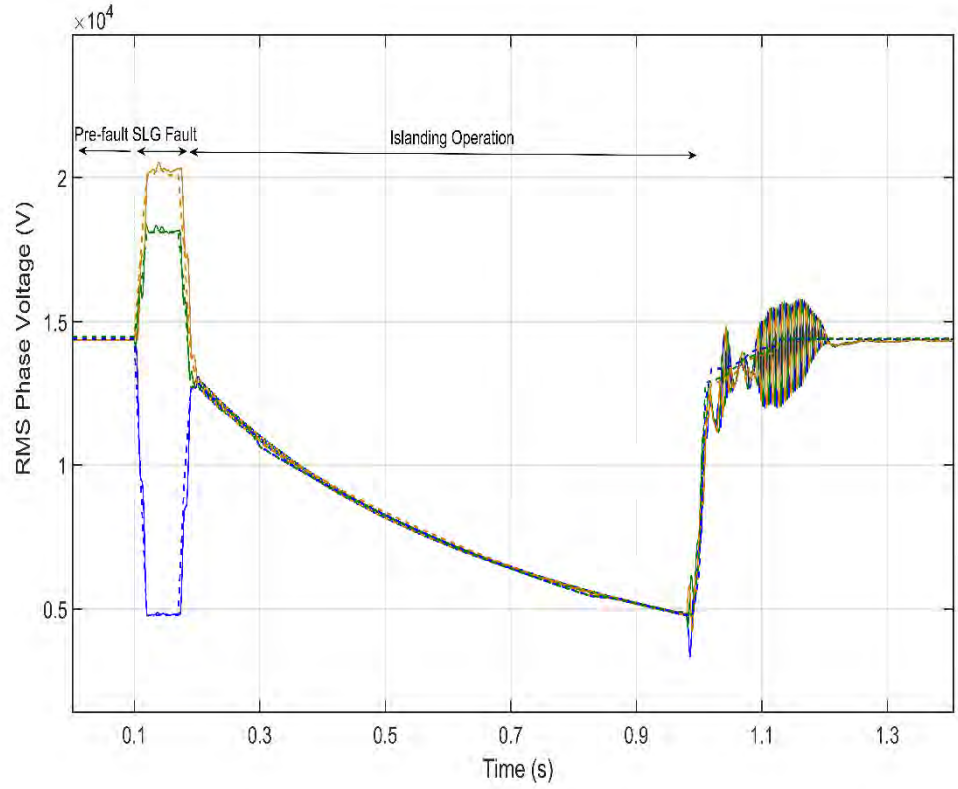

(**b**)

Figure 7.4: Validation of Event IV.

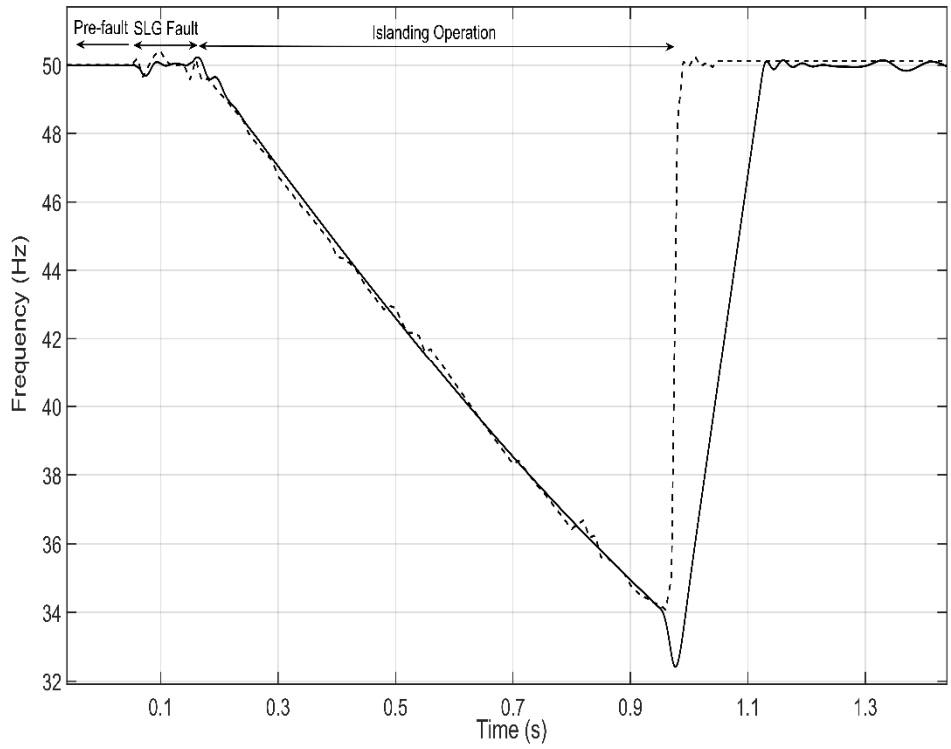

(**a**)

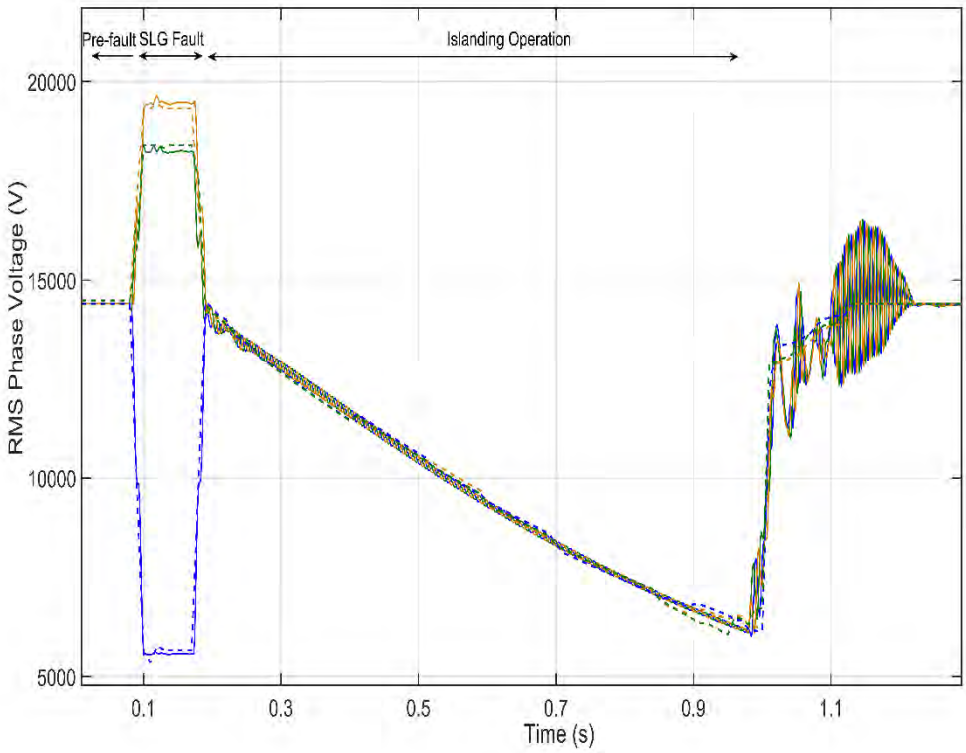

(**b**)

Figure 7.5: Validation of Event V.

7.4 Validation of Event III

Frequency: Figure 7.3a shows that the simulation frequency profile approaches the recorded frequency satisfactorily during the event. Thus, at t = 1.1s, the frequency is 40.8 Hz for both simulation result and field measurement. Pre-fault active-power of Feeder A loads is 980 kW.

Voltage: Figure 7.3b displays the three-phase voltages of a permanent fault. Firstly, the SLG fault (Phase a) that occurs in the Feeder A is fed by the main utility during 90 ms; the IM continue feeding this SLG fault after the CB has opened. It is noticeable that this type of event is highly risky for a DN; the IM is extending the time of fault after the CB operation. In this case, the voltage decreases fast, so when the CB reclosing takes place after 1.5 s (1.3 s after the fault clearing), the island has been de-energized. As for the frequency validation, voltage value before the reclosing is lower than in Event II due to the large deceleration when the IM is feeding the SLG fault.

7.5 Validation of Event IV

Frequency: In figure 7.4a the frequency comparison value is depicted. One-cycle before the CB recloses the circuit, the frequency is 33 Hz for both simulation and field measurement. It should be noted that by analysing the frequency of this event, as predicted after computing the period between voltage zero-crossings before the CB reclosing, the measurement observed in Figure 6.6b contained a slight measurement error. The active-power drawn by Feeder A loads at the time the event occurs was 850 kW.

Voltage: Figure 7.4b compares the three-phase voltages: simulation results are depicted in solid lines while field measurements are in dashed lines. The event starts in pre-fault conditions until the single line-to-ground (SLG) fault occurs in phase b at 0.1 s and is cleared within 90 ms. After the CB clearing, the islanding lasts 810 ms, meanwhile, at the time CB recloses the circuit, phase voltage reaches 6.2 kV in both simulation and measurements. Moreover, as can be seen in Figure 7.4b, the simulated voltages at PCC_2 during the fault (i.e., the voltage sag and both voltage swells) approach the field measurements with high accuracy, which again evidence not of the model but the feasibility of the fault location and resistance fault ($R_f = 5\ \Omega$) predicted in the previous section. Thus, phase voltages for both simulation and field measurements during the fault are; $V_a = 20.1$ kV, $V_b = 4.8$ kV and, $V_c = 18.24$ kV.

7.6 Validation of Event V

Frequency: In figure 7.5a, the frequency comparison value is depicted. One-cycle before the CB recloses the circuit, and the frequency is 34.1 Hz where the simulation accuracy can be seen. For this particular event, the pre-fault active-power of the Feeder A loads is 700 kW.

Voltage: Figure 7.5b compares the three-phase voltages: simulation results are depicted in solid lines whilst field measurements are in dashed lines. The event starts in pre-fault conditions until the single line-to-ground (SLG) fault takes place in line L5 for phase b at 0.1 s and it is cleared within 95 ms. After the CB clearing, the islanding lasts 810 ms, meanwhile, at the time CB recloses the circuit, phase voltage reaches 6.2 kV in both simulation and measurements. Phase

voltages for both simulation and field measurements during the fault are; V_a = 19.45 kV, V_b = 5.5 kV and, V_c = 18.25 kV.

7.6 Modelling features discussion

This section briefly details the main features of several measurement devices which have a significant impact on the model validation. In this model, both voltage and current signals are sensed through the three-phase continuous measurement block which captures the voltage and current waveforms with a sample time of 50e-6 s.

On the one hand, to obtain the RMS value, the first step is to obtain the amplitude of these signals with a phase-locked loop (PLL), and after that, dividing its value (by the square root of 2) with a gain block. To achieve such a task, we need two PLL blocks. The first PLL block (named PLL_1) obtain the waveform of the three-phase signals as an input, and the outputs, are the frequency and angular speed of these signals. Once these values are obtained, the amplitude and angle of a signal are computed through another PLL (named PLL_2) where the inputs are the three-phase signals (either voltages or currents) as well as the previously obtained frequency and angular speed from the previous PLL_1. As an output, the amplitudes and angles are obtained. The parameters used in these PLL blocks are detailed in Table 7.1 and Table 7.2, which are displayed in Figure 7.6a and 7.6b respectively.

By observing the RMS phase voltage during the validation, for all events, during the recovery (i.e., roughly between 100 and 120 ms after the CB reclosing) a slight oscillation is observed. As a result of the frequency oscillation during the recovery, an overvoltage in the RMS phase voltage is observed (e.g., see Figure 7.5a between t = 1.1 s and t = 1.21s). However, this over-voltage in the RMS value is not real, is produced due to the frequency-dependence of the PLL block. Hence, if the voltage waveform is taken into consideration instead of its computed RMS value, this voltage oscillation disappears. Accordingly, Figure 7.7 pinpoints this fact, where the voltage waveforms for both field measurements (Figure 7.7a) and simulation results (Figure 7.7b) are compared. This figure shows that, for modelling purposes, the simulation results obtained from the model match with high fidelity the recorded events in the real DN.

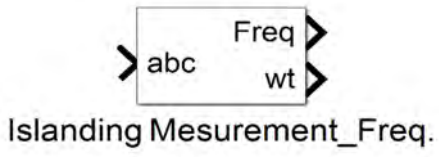

(**a**)

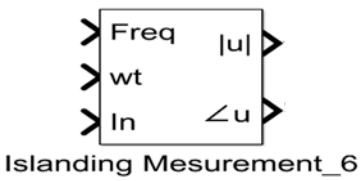

(**b**)

Figure 7.6: PLL Blocks of the Matlab model.

On the other hand, the frequency of the island is obtained from the voltage waveform through PLL_1. If one takes a look at the frequency validations, measurement values recover faster than simulations. If the time between the voltage zero-crossings during this recovery is computed, both frequencies coincide, which evidence the influence of the regulator parameters of the PLL on the frequency measurements. The values of PLL_1 and PLL_2 are both shown in Tables 7.1 and 7.2, respectively.

Table 7.1: Parameters of the PLL_1.

Parameters PLL_1	**Values**
Minimum frequency	20
Initial inputs (Phase/ Frequency)	(0 Deg./50 Hz)
Regulator gains	$K_p = 180$ $K_i = 3200$ $K_d = 1$
Time constant*(s)	1e-4
Maximum freq. derivative (Hz/s)	80
Filter cut-off frequency (Hz/s)	25
Sample time	50e-6 s

* Time constant for for derivative action.

Table 7.2: Parameters of the PLL_2.

Parameters PLL_2	**Values**
Initial frequency	50 Hz
Initial frequency	20 Hz
Initial inputs (Mag/ Degrees)	(1 pu/ 0)
Sample time	50e-6 s

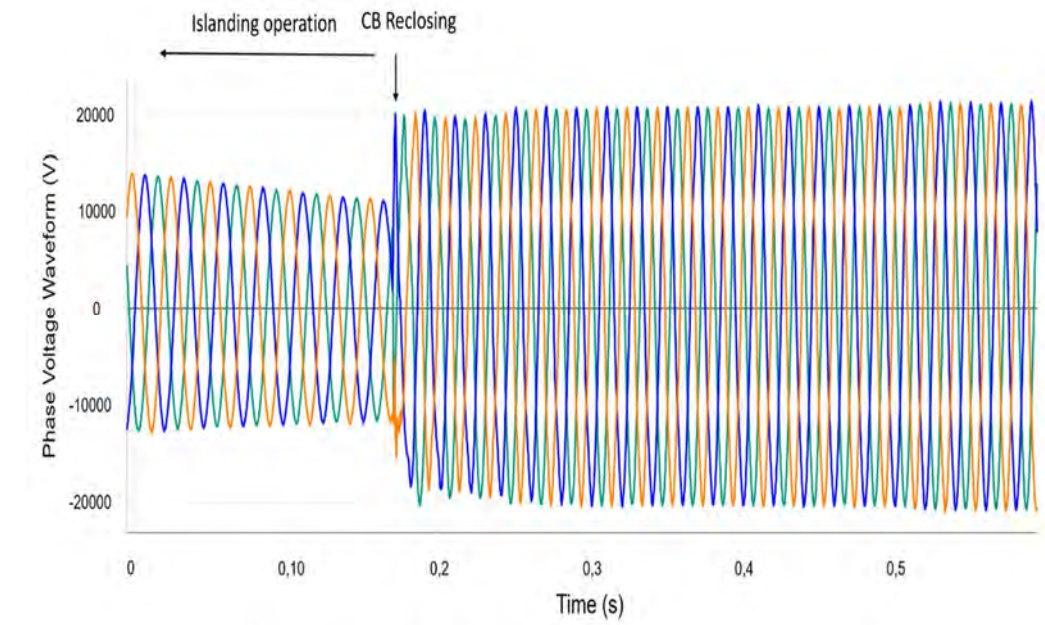

(**a**)

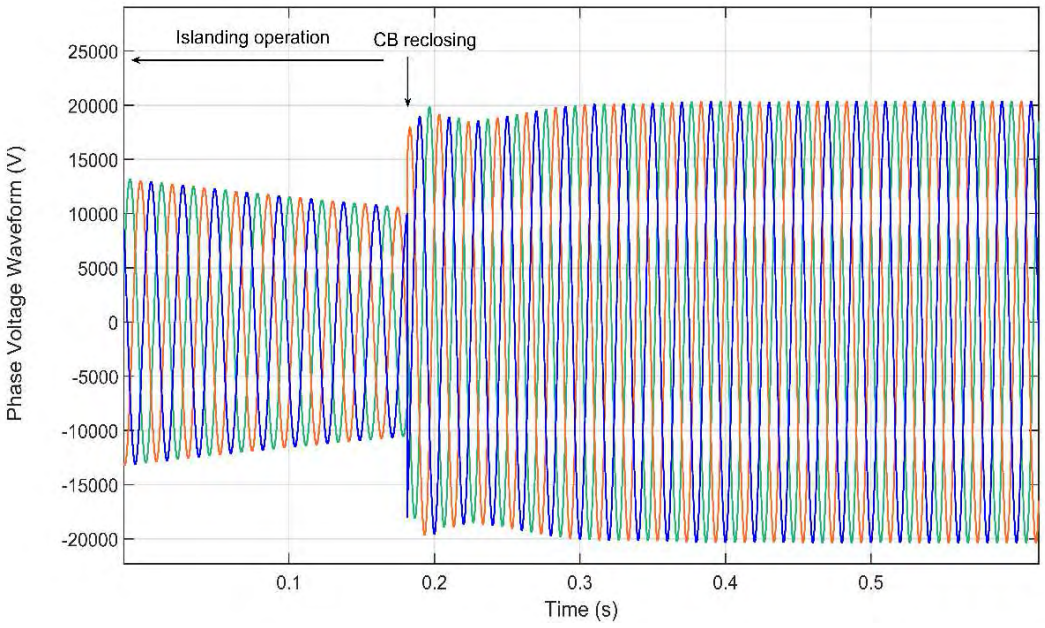

(**b**)

Figure 7.7: Phase voltage waveform comparison. (a) Field measurements; (b) Simulation results.

7.7 Conclusions

This chapter has shown and discussed the results of the model validation by comparing the simulation results of Chapter 5 with the real occurred events provided in the previous Chapter 6. The comparison is made for the three-phase voltages and frequency separately. Only voltage and frequency have been compared, given the fact that are the main parameters of interest during the IO. Although seven events have been discussed in Chapter 6, in this section, only five events have been validated. The reason is that two of them have very similar results. Therefore, it has been

considered that these five events give a close enough representative sample to prove the model dependability.

From the previously showed validations, the following aspects can be highlighted:

- By observing both voltages and frequencies for the five validated events, the fidelity of the implemented model can be observed.
- It should be stressed that this Chapter has demonstrated the high accuracy of the selected elements in the model. Particularly, loads modelling (i.e., both value and model type) was initially one of the most challenging element to model because it is random in nature. Nonetheless, as can be seen, the effectiveness of the selected model and values fitted the recorded events properly.
- It has been observed that the PID controller parameters implemented in the PLL can slightly influence the simulations results. However, with the applied settings in both PLL blocks (i.e., PLL_1 and PLL_2), it has been proven that the transient object of study has been adequately modelled and its validation gives ample evidence of it.
- Even though the field measurements are obtained from the fault recorder function in the relay which makes 32 samples/cycle and the sampling time in the simulations is much higher (50e-6 s), the comparison between them gives an acceptable representation to perform the model validation.

This chapter has proven the suitability of the implemented model and has given a thorough discussion regarding the appropriateness of the measurement devices of the model.

Chapter 8

Voltage sags during the island

8.1 Introduction

This Chapter is aimed at describing the voltage sags that occurs during the IO. Crucially, a new voltage sag topology is proposed. The function that follows the magnitude of this proposed voltage sag will be analytically modelled and further validated. As has been recalled in Chapter 3, voltage sags are a certain reduction in the RMS phase voltage during a certain period of time (e.g., typically larger than two cycles and less than 1s). The Chapter aims at contributing to the voltage sags studies.

This Chapter is organised as follows:

- The first part gives a general overview of the proposed voltage sag, where the main features are briefly defined (***section 8.2***).
- Secondly, ***section 8.3*** details the analytical expression that follows the magnitude of this novel voltage sag type.
- The third part examines the voltage sag duration, as well as focuses on its recovery process once the CB recloses the circuit. See ***section 8.4***.
- Once the voltage sag has been analytically modelled, in order to prove its feasibility, the simulations carried out in chapter 5 will be used to compute the analytical expression for each sag magnitude. See ***section 8.5***.
- To provide more evidence about the validity of this new voltage sag, the previously validated events in Chapter 7 will also be used to compute the analytical expression for each sag magnitude. Besides, in ***section 8.6***, the relationship between the influential factors of the analysed IO in Chapter 5 (i.e., electrical loads, the load torque and the reclosing time) and the analytical expression of the voltage sag magnitude is investigated.

Lastly, the main conclusions of this chapter are provided in ***subsection 8.7***.

8.2 Main features of the new voltage sag type

As can be seen from the results in the previous Chapters 5, 6 and 7, the portion of the grid downstream the CB, remains energised before the CB reclosing due to the large induction motors.

As has been already mentioned, this IO occurs due to the IMs inertia which following the CB transiently act as generators, thus energising the grid. The process for this IO is as follows: (i) a fault occurs; (ii) after a given time, the CB opens; (iii) CB recloses after the reclosing time. Thence, between the fault inception and the fault clearing, the fault causes a voltage sag. Nonetheless, the voltage sag object of study in this Chapter is the one originated by the IMs during the period of time between the CB opening and the reclosing. Since the magnitude of a voltage sag can be categorised as constant or non-constant (e.g., see characterisation in Chapter 3), the present type object of study belongs to the second one. Therefore, the originated voltage sag during the island will be defined by its magnitude, its duration and its recovery. The analytical expression that follows the sag magnitude during the IO is defined in ***section 8.3***. Meanwhile, the duration and recovery stages are established in ***section 8.4***.

8.3 Novel voltage sag magnitude: Analytical expression

The IM stator voltage dictates the analytical expression that follows the voltage sag during the island. To obtain the expression of this voltage sag, the IM equations have to be recalled. In steady-state, the IM acts as a motor and is being supplied by the grid and running at a specific point of operation. This point of operation is defined by the mechanical load torque coupled with the rotor shaft and its mechanical speed. When a fault occurs, depending on the characteristics of the originated voltage sag, the IM will decelerate according to its severity (i.e., voltage sag magnitude and duration). The pre-islanding conditions will dictate the voltage sag magnitude during the IO. Hence, the IMs' initial kinetic energy is expressed as Equation (8.1)

$$E_{Kin\_initial} = \frac{1}{2} J_T \omega_{pre\_islanding}{}^2 \tag{8.1}$$

where $E_{Kin\_initial}$ is the initial kinetic energy before the CB opening, J_T is the total moment of inertia (considering the rotor inertia and mechanical load), and $\omega_{pre\_islanding}$ is the mechanical speed before the island is formed. Since the IMs are the only sources once the CB has opened the circuit, the voltages during the island are defined by the set of equations (4.39) of subsection 4.5.2 in Chapter 4. These equations are recalled here:

$$\begin{aligned}
V_{sd} &= (R_s + l_s \frac{d}{dt}) i_{sd} + M \frac{d\, i_{rd}}{dt} \\
0 &= (R_r + l_r \frac{d}{dt}) i_{rd} + M \frac{d\, i_{sd}}{dt} \\
0 &= M \frac{d\, i_{rd}}{dt} - l_r (\wp\, \omega_m)\, i_{rd} - M\, (\wp\, \omega_m)\, i_{sd} \\
0 - \Gamma_{load} &= J \frac{d\, \omega_m}{dt} \\
\omega_m &= \frac{d\, \theta_m}{dt} \\
V_{sd} &= i_{sd} \cdot (Z_{line} + Z_{load})
\end{aligned} \tag{8.2}$$

By solving the described set of Equations (8.2) during the island, the voltage sag magnitude between t_i and t_f can be obtained. Indeed, the voltage decay following the CB has already been observed in the previous Chapters. In such a way, the analytical expression of this sag magnitude with respect to time follows the following form:

$$V_{sag}(t) = V_{pre-fault} \cdot t^{b}; \quad \forall t \in [t_i, t_f] \tag{8.3}$$

where $V_{sag}(t)$ is the RMS phase-voltage value, the scaling factor of the equation is defined by the pre-fault RMS phase voltage, and b is a non-dimensional coefficient which dictates the rate of decay. It is crucial to highlight that the scaling factor is the $V_{pre\text{-}fault}$ if the first instant t_i is set to 1. Given the natural tendency of the IM to decelerate due to the lack of grid supply, conceptually b coefficient has to be below zero. However, note that if b has negative values close to zero, the voltage remains almost constant during the island (e.g., see scenarios I, II and III of section 5.3 in Chapter 5). Whereas, larger negative b values correspond to higher voltage drops (e.g., see scenarios IV to VII). To clearly observe such reasoning, Figure 8.1 plots the analytical function that follows the magnitude of this sag for a given b value.

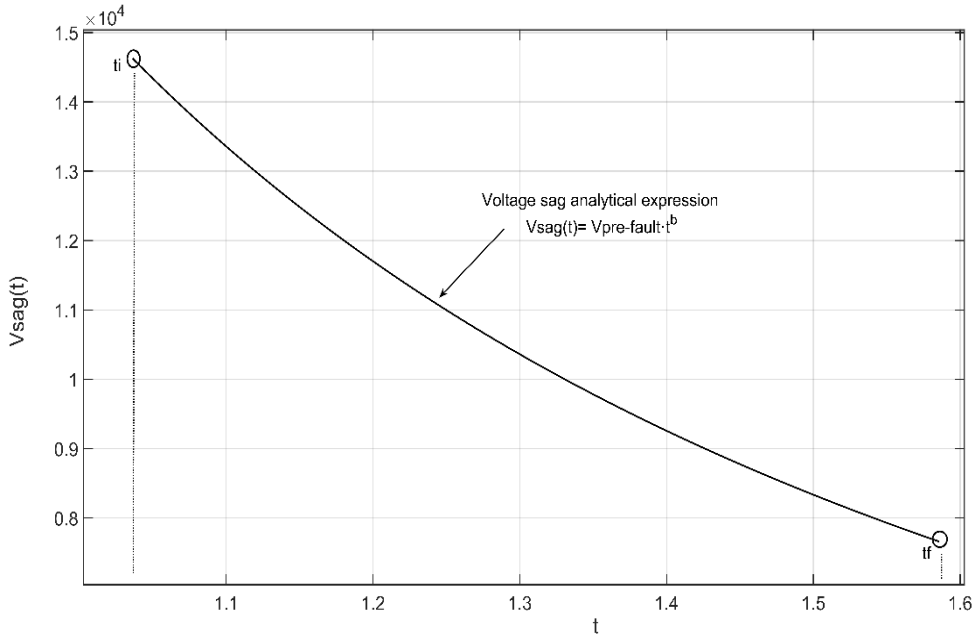

Figure 8.1: Voltage sag analytical function for a given b parameter.

As mentioned earlier, the analytical expression of the voltage sag magnitude is given by the IM stator voltages, which result from solving the differential equations in (8.2). By solving this set of equations, the non-dimensional b factor can be obtained. Particularly, in Figure 8.1, t_i = 1 s, t_f =1.5 s and, b= −1.52 s. As discussed above, this curve expression is only valid between t_i and t_f, where in fact, the voltage sag characteristic is of interest.

8.4 Voltage sag duration and recovery

8.4.1 Voltage duration

Voltage sag duration is defined as the period between the disturbance inception and its recovery; see the first plot of Figure 2.3 in Chapter 2. Typically, the voltage sag duration depends directly on the protective device's settings. However, for this particular case, the voltage sag duration depends on the preset reclosing settings. As stated before, this reclosing operation is widely implemented in DN relays, principally to avoid the need to operate the CB for non-permanent faults manually (e.g., self-extinguished faults). Commonly, DSOs set the first reclosing between 0.5 and 1 s.

8.4.2 Voltage recovery

As has been seen in Chapter 3, sags can be caused by several events (e.g., faults, induction motors starting, transformer energisation, etc.). Therefore, the recovery process may differ depending on what factor caused the sag. If the voltage sag is caused by a fault, the recovery begins when the CB clears the fault current at the zero-crossing and ends when voltage is recovered (see the discrete recovery of Chapter 3). Nevertheless, for the other disturbances, the recovery time depends on each situation.

For the voltage sag object of study, the beginning of the recovery takes place once the CB recloses the circuit. It is worth pointing out that, unlike other voltage sags, this sag recovers in two steps. The first step is due to the CB zero-crossing, which has to occur at the same instant for the three-phases, and the second stage corresponds to the time period until the voltage reaches its pre-fault value. In fact, the voltage recovery during the second step is due to the high current drawn by the IM as a result of the out-of-phase reclosing and its subsequent IM reacceleration (due to the deceleration during the IO). Two factors dictate the transient caused by the out-of-phase reclosing; the first is the difference in voltage amplitude between the grid and island, and the second is the difference in frequency between the grid and island.

8.5 Voltage sag magnitude: Simulation results

8.5.1 Overview

The main goal of this part is to obtain the analytical expression of the voltage sag magnitude for each simulated scenario in Chapter 5. Thus, since the simulations in Chapter 5 have been classified for each influential factor, the voltage sag analytical expression will also be computed here for each influential factor separately. Firstly, the originated voltage sags during the IOs in subsection 5.3 (electrical loads influence) are analysed. Secondly, the voltage sags obtained from the simulations in subsection 5.4 are evaluated (fault type influence). Thirdly, the resulting voltage sags obtained from simulations performed in subsection 5.5 (reclosing time impact), are evaluated. In fourth place, the magnitude of the voltage sags during the island from subsection 5.6 are analysed.

As an example, taking advantage of the implemented three-phase model, an additional scenario with the same conditions of Subsection 5.3 and considering the sum of electrical loads in the island 380 kW (mainly constant impedance) has been simulated. Figure 8.2 shows the obtained measurements during this simulation (only phase a is showed) where the RMS phase voltage one-cycle before the CB reclosing is 8 kV. In that Figure, the following stages can be identified; (i) the pre-fault situation before t = 0.8 s, (ii) the voltage sag due to the SLG between t = 0.8 s and t = 1 s, (iii) the proposed voltage sag which occurs between t = 1 s and t = 1.58 s and lastly, (iv) the recovery process between t = 1.58 s and t = 1.72 s. The solid black line represents the simulation results, whereas the solid blue line represents the analytical function which describes the sag magnitude. Additionally, the solid blue double arrows are also added to show the voltage sag magnitude decrease between t_i (t = 1.05 s) and t_f (t = 1.58 s).

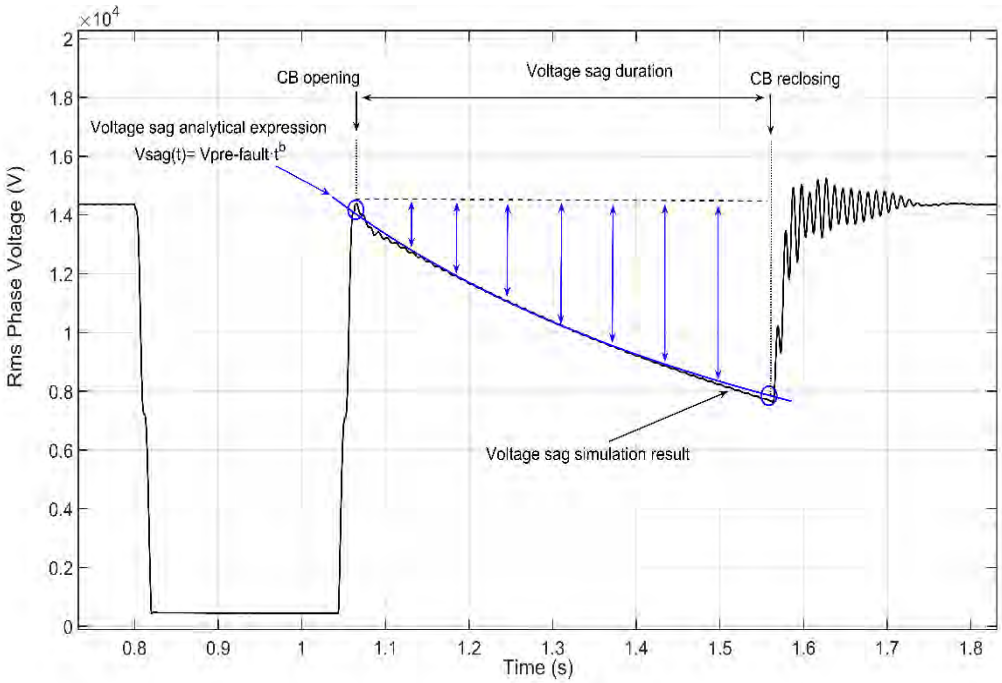

Figure 8.2: Comparison between the voltage sag analytical expression and simulation results.

8.5.2 Simulation results

Voltage sags for different load scenarios

In subsection 5.3 of Chapter 5, the influence of the electrical loads which remain during the island at the time the fault occurs has been investigated. Thus, by taking advantage of these simulations (i.e., those showed in Figures 5.2 to 5.8), the non-dimensional factor *b* can be obtained. The pre-fault phase-voltage value in equation (8.3) is set to 14.4 kV.

Figures 5.2 to 5.8 of Chapter 5 illustrate that fact that in scenarios where the amount of loads which remain within the island is low, the voltage drop during the island is negligible, see for instance scenarios I, II and III. Consequently, the voltage reduction in these scenarios cannot be considered as a voltage sag. Moreover, for these particular scenarios, *b* value is almost zero.

Given the above assumption, the voltage sag magnitude will only be analysed and discussed for scenarios IV to VII. For a better understanding, the Figures of Chapter 5 will be shown again, thus achieving a clear idea about the function that follows the voltage sag magnitude. Given the negligible unbalance between phases, in these voltage comparisons, only one phase is displayed (phase a).

- *Voltage sag obtained from Scenario IV*

The phase voltage measurements obtained for Scenario V in subsection 5.3.1, are shown in Figure 8.3. As can be seen in that Figure, the phase voltage one-cycle before the CB reclosing is 11.1 kV. Figure 8.4 shows a comparison between the phase-voltage showed in the previous Figure and the analytical expression that follows the magnitude of this voltage sag. For this scenario, the coefficient *b* proved to be -0.61.

- *Voltage sag obtained from Scenario V*

The phase voltage measurements obtained for Scenario V in subsection 5.3.1, are shown in Figure 8.5. As can be seen in that Figure, the phase voltage one-cycle before the CB reclosing is 9.8 kV.

Figure 8.6 shows a comparison between this voltage value and the analytical expression that follows the magnitude of this voltage sag. For scenario V, the coefficient *b* proved to be -0.87.

- *Voltage sag obtained from Scenario VI*

The phase voltage measurements obtained for Scenario VI in subsection 5.3.1, are shown in Figure 8.7. From that Figure, it is seen that the phase voltage one-cycle before the CB reclosing is 8.39 kV. Figure 8.8 shows a comparison between this voltage value and the analytical expression that follows the magnitude of this voltage sag. For this scenario, the coefficient *b* proved to be -1.316.

- *Voltage sag obtained from Scenario VII*

The phase voltage measurements obtained for Scenario VII in subsection 5.3.1, are shown in Figure 8.9. As can be seen in that Figure, the phase voltage one-cycle before the CB reclosing is 6.1 kV. Figure 8.10 shows a comparison between this voltage value and the analytical expression that follows the magnitude of this voltage sag. For scenario V, the coefficient *b* proved to be -2.06.

Table 8.1: Summary of the voltage sag parameters for each simulated scenario.

Scenario*	**V*[1]** **(kV)**	**b**
I	13.7	-0.1
II	13	-0.25
III	12.4	-0.38
IV	11.1	-0.61
V	9.8	-0.87
VI	8.31	-1.31
VII	6.19	-2.06

* This notation belongs to the scenarios of Subsection 5.3.1.

*[1] RMS Phase voltage (for phase a) one-cycle before the reclosing.

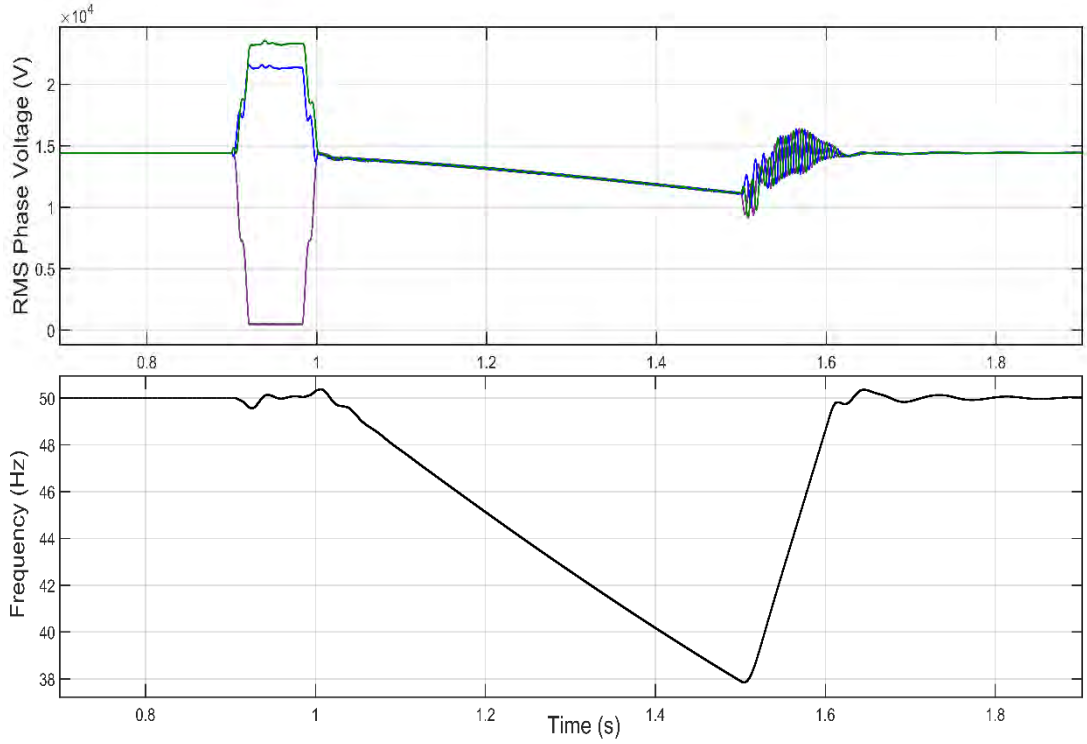

Figure 8.3: Results obtained from Scenario IV of subsection 5.3.1 in Chapter 5.

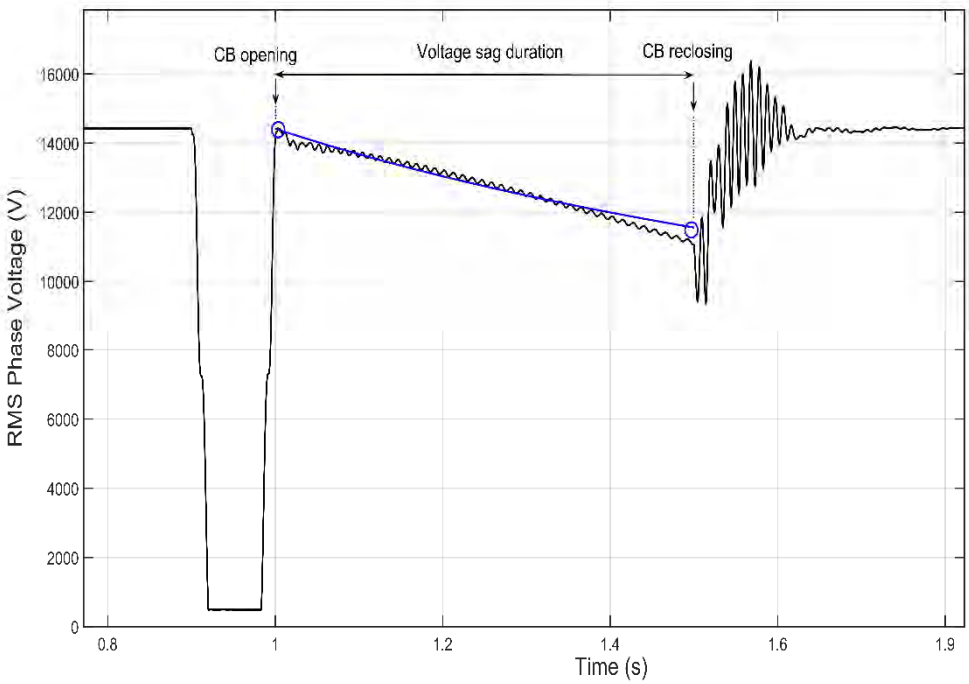

Figure 8.4: Voltage sag magnitude analytical function and simulations of scenario IV.

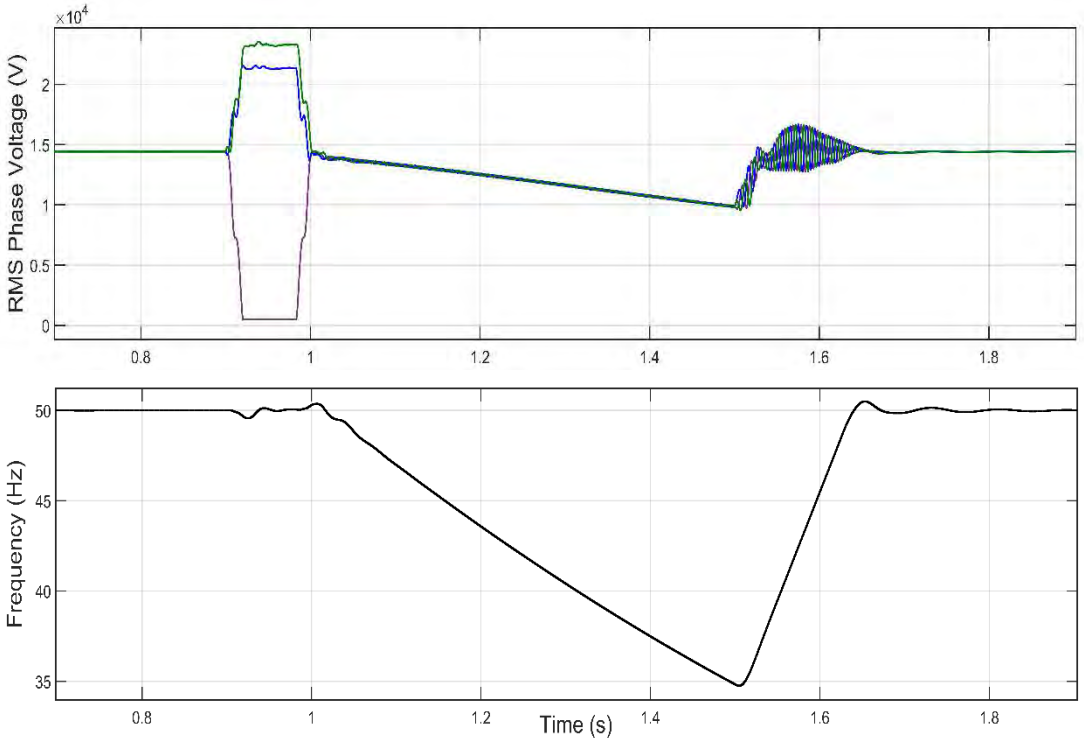

Figure 8.5: Results obtained from Scenario V of subsection 5.3.1 in Chapter 5.

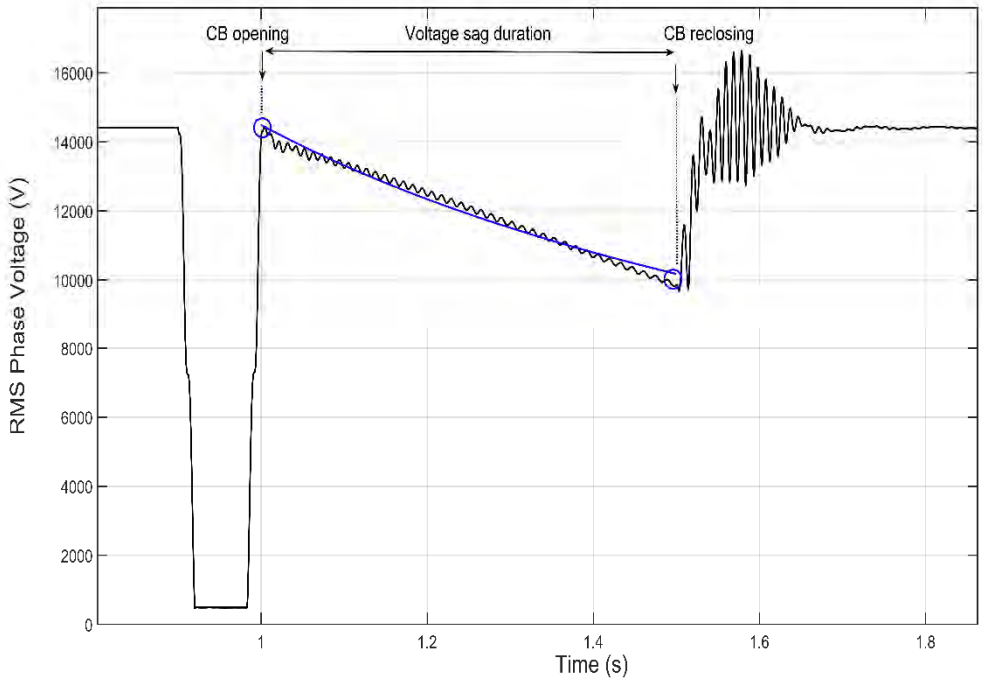

Figure 8.6: Voltage sag magnitude analytical function and simulation of scenario V.

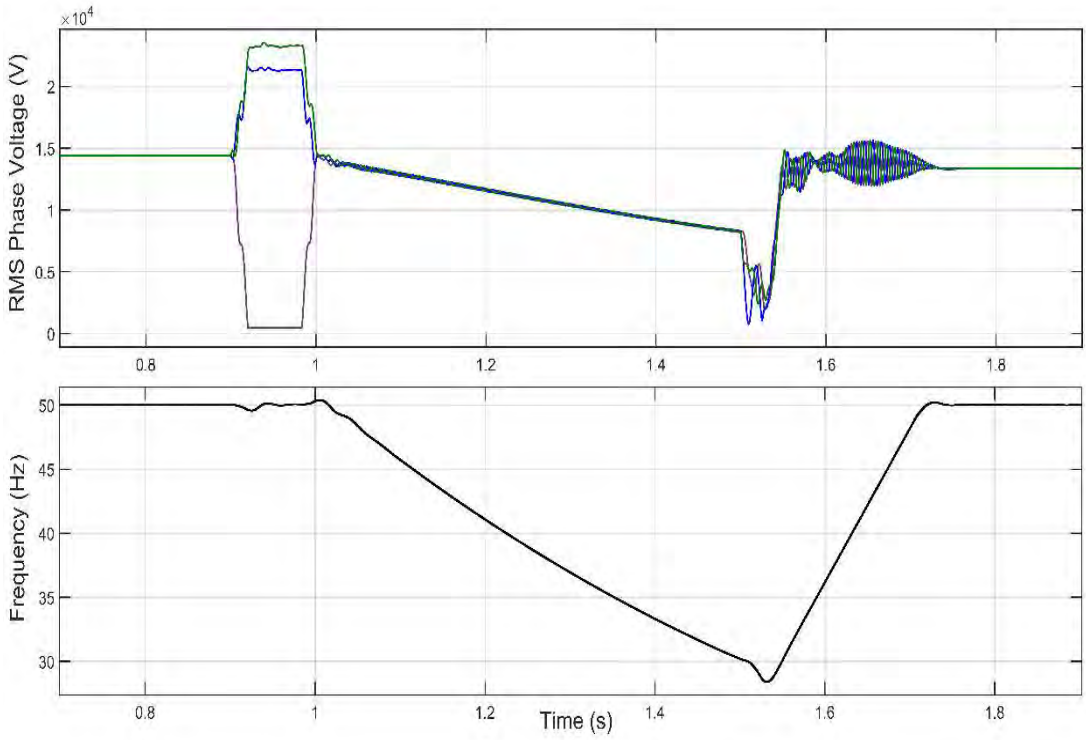

Figure 8.7: Results obtained from Scenario VI of subsection 5.3.1 in Chapter 5.

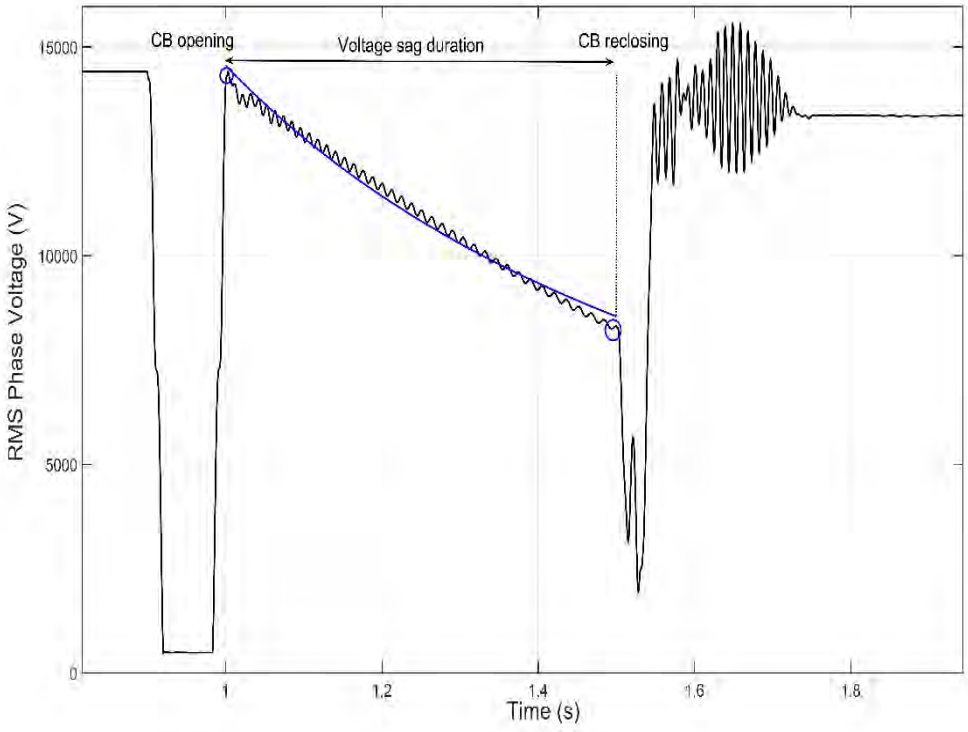

Figure 8.8: Voltage sag magnitude analytical function and simulations of scenario VI.

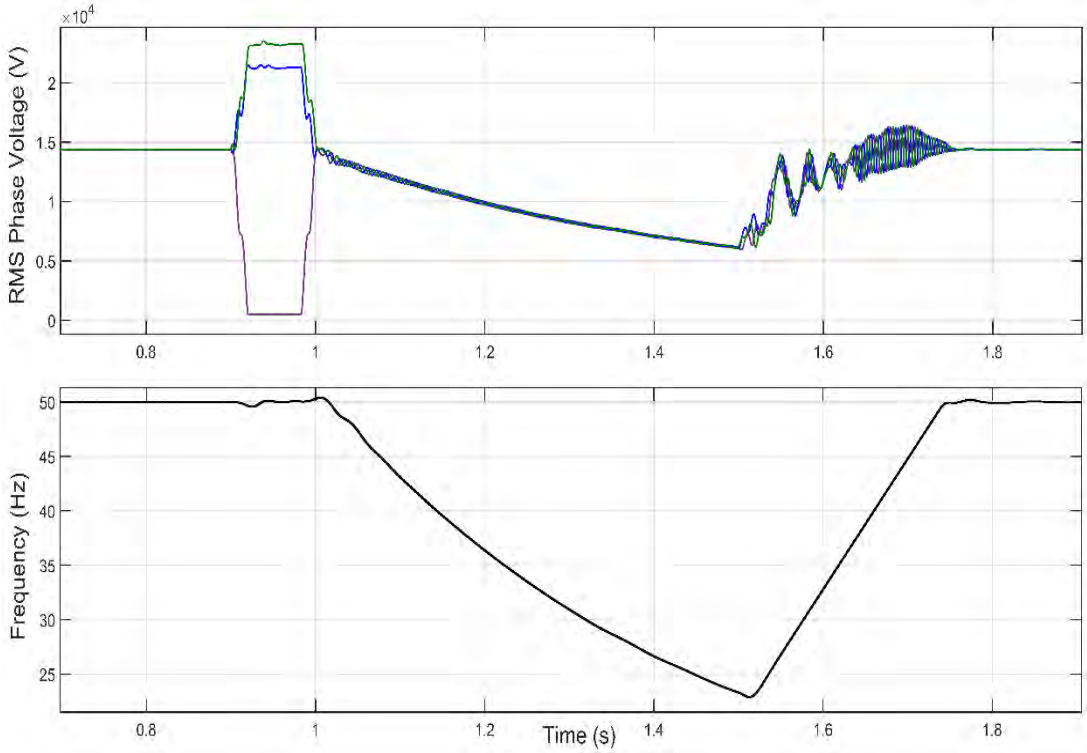

Figure 8.9: Results obtained from Scenario VI of subsection 5.3.1 in Chapter 5.

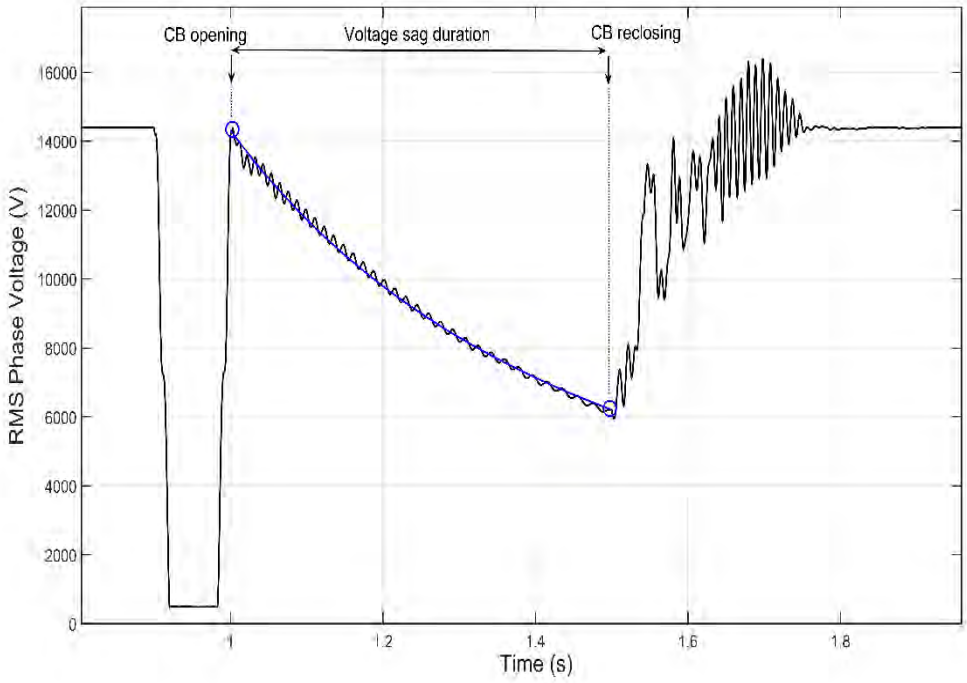

Figure 8.10: Voltage sag magnitude analytical function and simulation of scenario VI.

Voltage sags for different fault types

In subsection 5.4 of Chapter 5, the influence of the type of fault that caused the CB operation before the islanding has been investigated. Since the voltage sag that occurs during the IO for an SLG fault has been already discussed in the previous subsection, this part aims to examine the voltage sag that occurs during the island for the rest faults. The results obtained from these simulations (i.e., those showed in Figures 5.18 to 5.21) have been used to assess the voltage sags during these IOs. As concluded in chapter 5, depending on the duration and severity of the fault that caused the CB operation (i.e., the duration and magnitude of the voltage sag due to the fault), voltage and frequency during the island are highly influenced. The analysed scenarios are as follows; LLL, LLG, LL, and LLLG. In order to help the reader, these Figures of Chapter 5, are renumbered and displayed again. Thus, Figures 5.18 to 5.21 are now Figures 8.11 to 8.14. All these Figures show the voltage sag during the island (i.e., between t = 1s and the CB reclosing (t = 1.5 s)

- *Island caused by a LLL fault (Scenario V in subsection 5.4)*

Figure 8.11 display the magnitude of the voltage sag caused during the island. Immediately following CB clearing (t = 1s), the voltage drops with respect to the voltage value during the fault. However, the RMS phase voltage recovers (equally for the three-phases) from the 7.3 kV at the beginning of the event to 8.49 kV when the CB recloses (at t = 1.5 s). The magnitude of this sag changes during the island, from (0.5 pu) to (0.58 pu). Due to this recovery, the voltage sag that occurs during the island is categorized as non-constant.

- *Island caused by a LLG fault (Scenario VI in subsection 5.4)*

Figure 8.12 shows the voltage sag caused has a magnitude of 0.83 pu, which remains constant during the island. Thus, the magnitude of this sag can be classified as constant.

- *Island caused by a LL fault (Scenario VII in subsection 5.4)*

In Figure 8.13, it can be seen that the voltage sag caused during the island has a magnitude of 0.88 pu, which remains constant during the island. As for the previous case, the magnitude of this sag can be classified as constant.

- *Island caused by a LLLG fault (Scenario VIII in subsection 5.4)*

Figure 8.4 illustrates the magnitude of the voltage sag caused during the island. Immediately following CB clearing (t = 1s), the voltage drops with respect to the voltage value during the fault. However, the RMS phase-voltage recovers during the island from the 11.3 kV at the beginning of the event to 12.3 kV when the CB recloses (at t = 1.5 s). Due to this voltage recovery during the island, this sag can be categorised as non-constant.

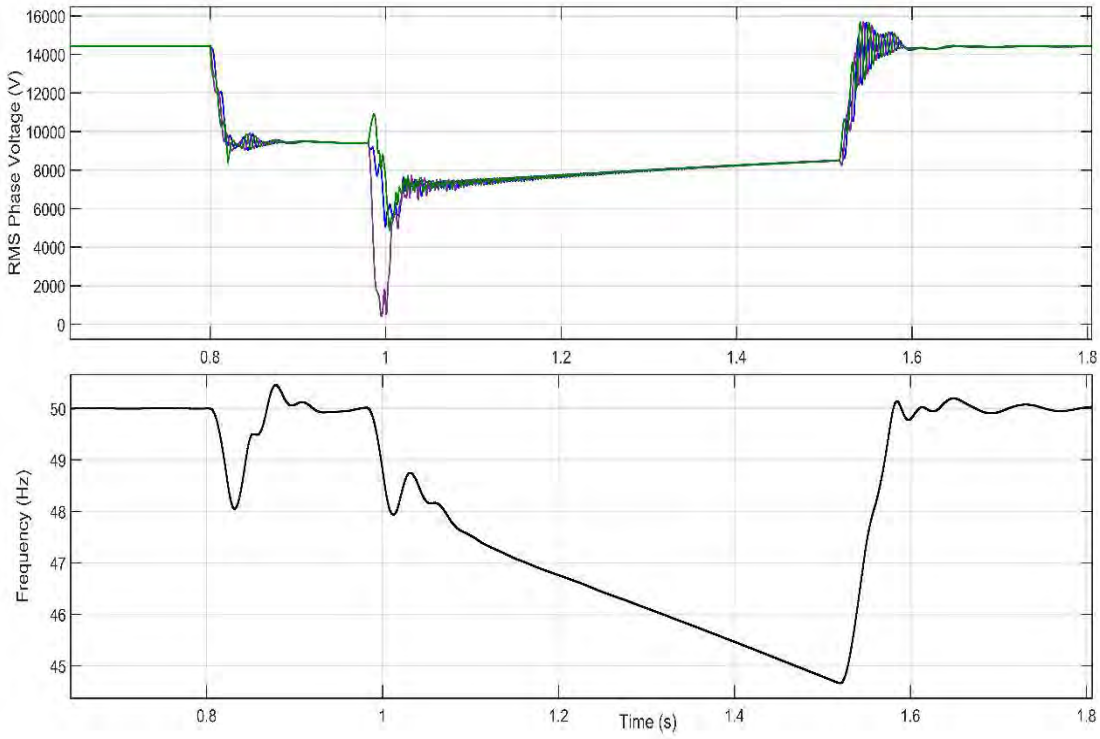

Figure 8.11: Island caused by a LLL fault.

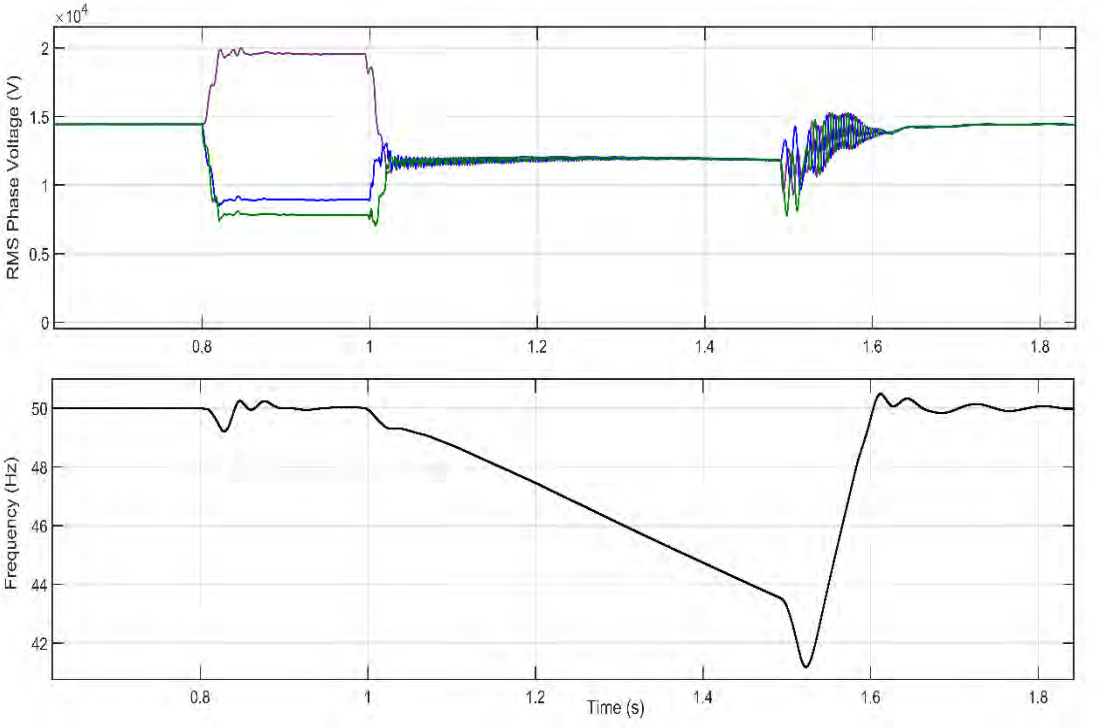

Figure 8.12: Island caused by a LLG fault.

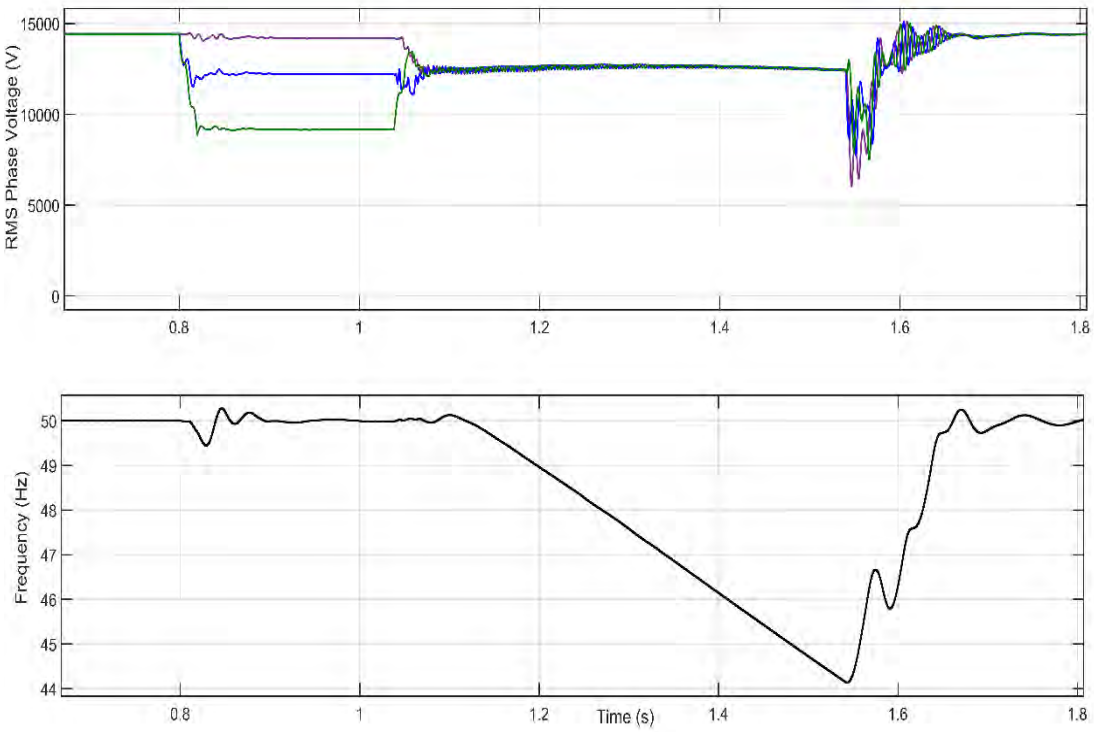

Figure 8.13: Island caused by a LL fault.

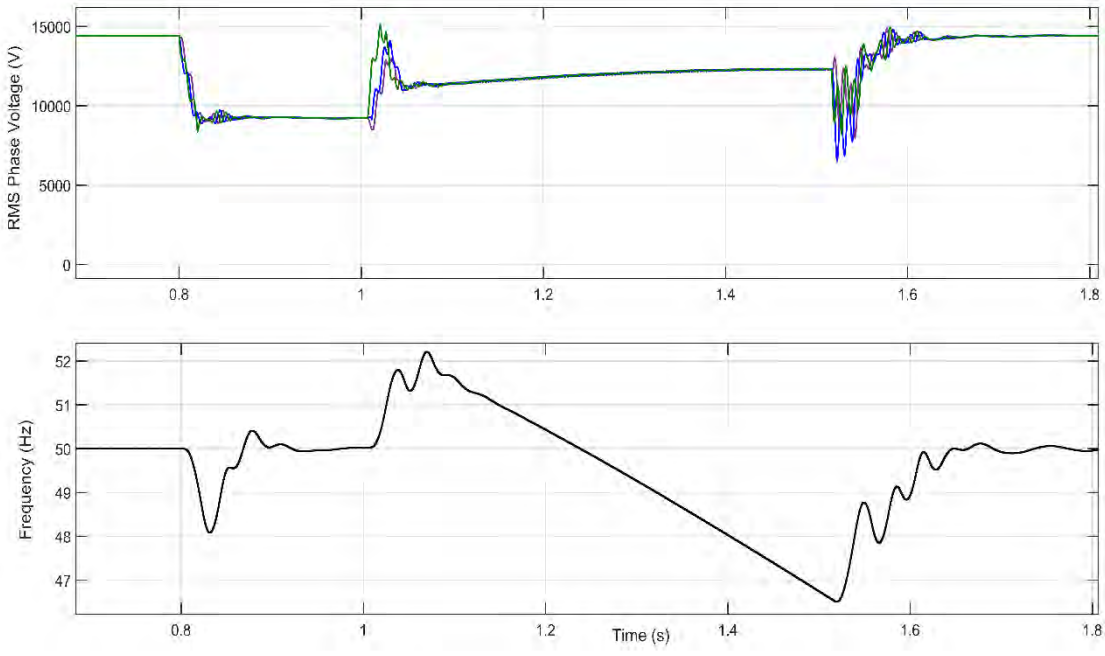

Figure 8.14: Island caused by a LLLG fault.

Simulations results with different reclosing times

In subsection 5.5 of Chapter 5, the impact of the reclosing time implemented in the relay has been investigated, and as expected, the larger is this time, the larger is the drop in voltage and frequency

during the island. This part is focused on describing the voltage sag that occurs during the island for different reclosing times. As has been observed, the magnitude of the voltage sag decreases with time, meanwhile, the curve that follows this magnitude proved to be the same. To observe such effect, see Figure 8.15, where, even though three times are implemented (t_1= 0.5 s, t_2= 0.8 s and t_3= 1 s) and the voltage decreases from one time to the next, the function which defines the voltage sag is the same. This function is plotted in blue, whereas the voltage obtained from simulation with T_1 is displayed with a dashed-black curve, T_2 is displayed with a dotted-black curve and, T_3 is displayed with a dashed-dotted-black curve.

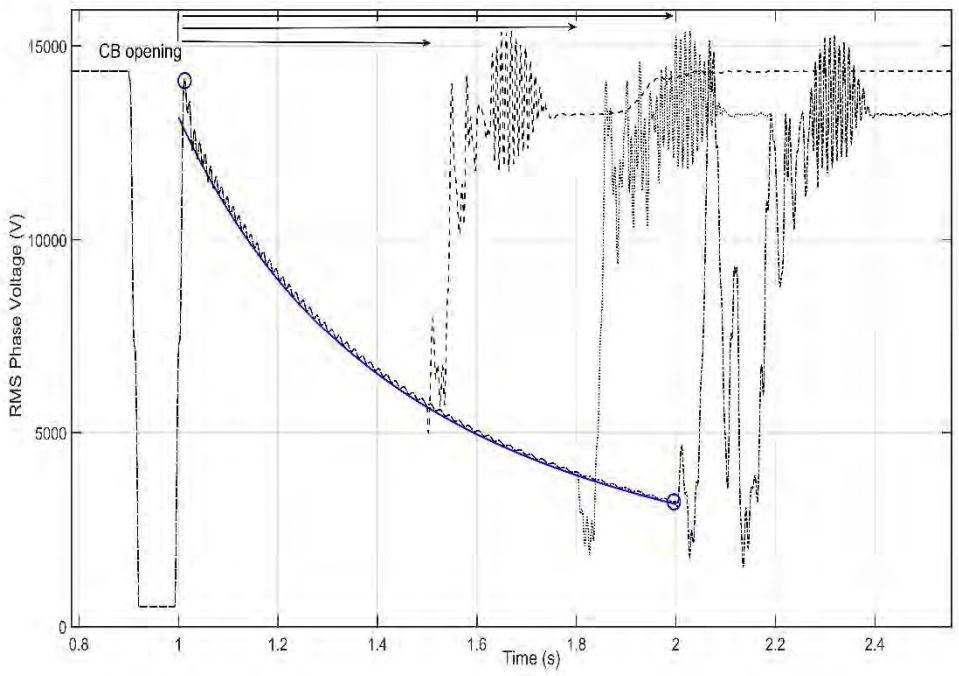

Figure 8.15: Voltage sag magnitude analytical expression for different reclosing times.

Simulations results with different load torques

In subsection 5.6 of Chapter 5, the impact of the load torque coupled with the IM rotor shaft has been investigated. From these simulations, it has been found that, as expected, the larger is the load torque, the larger is the drop in voltage and frequency during the island. Furthermore, by comparing these results with those obtained in some particular scenarios in subsection 5.3, voltage and frequency appear to be similar.

This similarity between results has been identified in four cases. Particularly, given the same reclosing time (t = 0.5 s) and fixing the active-power of loads in the island to 80 kW, the voltage obtained in Scenario II of subsection 5.3.1, shows the same voltage as the scenario I of subsection 5.6. Scenario V of subsection 5.1.3 is very close to scenario II of 5.6. The voltage in scenario III during the simulations for the load torque influence is between scenarios V and VI of subsection 5.13. The last scenario of the load torque influence (scenario IV) provides exactly the same voltage values in comparison with scenario VII of subsection 5.1.3.

Since the previously mentioned events are very similar, it is not necessary to reassess them to obtain the same voltage sag magnitude.

8.6 Voltage sag validation

This section is aimed at determining the analytical expressions that follow the magnitude of the voltage sag that occurs during the island for the seven validated events in Chapter 7. For that matter, the parameter *b* required to compute the analytical expression (8.3) for each voltage sag magnitude is provided in Table 8.2. It has to be underscored that, for the sake of brevity, the values obtained from each scenario will not be displayed in Figures. Note that, Table 8.2 is a modified version of Table 6.1, where the sixth column provides the coefficient *b* of each sag magnitude.

Table 8.2: List of the occurred events with the voltage sag magnitude coefficient.

Event	Beginning	Ending	Fault type	Fault location	b	P (MW)	V* (kV)
1	17:01:09.776	17:01:10.636	SLG	Node 8	-1.25	0.52	8.58
2	07:44:39.544	07:44:40.354	SLG	Node 5	-1.17	0.45	9
3	04:10:35.580	04:10:36.880	LLG/SLG	Node 8	-	0.8	0
4	18:14:54.263	18:14:55.128	SLG	Line 5	-2.03	0.77	6
5	17:13:58.281	17:13:59.096	SLG	Node 7	-2.6	0.85	5
6	09:52:38.440	09:52:39.395	SLG	Node 7	-	1.3	3.5
7	11:49:04.702	11:49:05.456	SLG	Line 5	-2.73	0.87	4.75
8	16:04:15.667	16:04:16.607	LLG/SLG	Node 7	-	1.21	-
9	12:24:19.550	12:24:20.469	SLG	Line 6	-2	0.7	6.2

8.7 Conclusions

This chapter has investigated the voltage sags that occur during the IO under several scenarios. Since in Chapter 5 the simulated scenarios were divided into four groups considering each influential factor, the present voltage sags evaluation has been organized according to that classification; (i) power of loads in the island, (ii) the type of fault that originated the island, (iii) the reclosing time and, (iv) load torque. By analysing the full range of voltage sags obtained in this Chapter, the following points can be stressed:

- This Chapter has evaluated the voltage during the island under several conditions and has concluded that a new voltage sag can be categorised. Due to the lack of supply following the CB clearing operation, voltage decays with time during the island, and therefore, the magnitude of this voltage sag is considered as non-constant. Thus, this voltage sag enhances the voltage sags with non-constant magnitude provided in Chapter 3.
- By considering the results in 8.5.2, the high fidelity of the predicted analytical function has been demonstrated. Note that for scenarios where the sum of all electrical loads in the island is low, the voltage drop during the island is negligible, and consequently it makes no sense to compute any function to model a voltage sag. Importantly, it has been observed that the

proposed function to model the voltage sag magnitude proved valid for any tested scenario only if the IO is caused by a SLG. On the other hand, if another fault originates the island, the voltage sag magnitude does not follow this function. For instance, it is seen that during the two-phase faults (both LLG or LL faults), the voltage remains constant at a specific value during the fault, whereas, for the three-phase faults (either LLL or LLLG) the voltage recovers during the island.

- For the proposed voltage sag, the other features such as duration and recovery have also been defined. The duration of this voltage sag depends on the reclosing time, which commonly ranges between 0.5 s and 1.3 s. Secondly, the recovery takes place in two steps, where the first coincides with the CB reclosing. The second step begins with this CB reclosing and ends when the voltage is recovered.
- It has been observed that the reclosing time has no effects into the function that follows the voltage sag magnitude. The larger is the reclosing time, the larger is the voltage drop, but the function is the same.
- The dependability of the proposed analytical expression to model this voltage sag, have been demonstrated by taking advantage of the already validated scenarios in Chapter 7.

By carefully observing the obtained results, the main goal of this Chapter has been accomplished. Thus, a new voltage sag has been analytically modelled and subsequently validated by both simulations and real measurements.

Chapter 9

Islanding detection

9.1 Introduction

By observing the results of the previous Chapters 5, 6 and 7, it has been proven that, even with no generation units, due to large induction motors, an IO may occur in a distribution network. Therefore, during the time period between the CB fault clearing and its reclosing operation (i.e., roughly between 0.5 s and 1s) the induction motors are energising the grid, thus forming an island.

Indeed, IOs are generally expected in case DG units energise the grid following the CB operation. Nevertheless, the current approach is slightly different and utterly unexpected for the DSO. As stated in Chapter 2, in order to prevent unintended IOs, several DSO guidelines force the DG to trip after the occurrence of the fault. Essentially, the obligation to remove these DG units is because the DSO does not supervise these islands. Among the available guidelines, a very useful one is the IEEE Std. 1547, which forces the DG to trip before 2 s after the loss of mains has occurred. In IOs with DG, the balance between the generation capacity and the amount of loads plays a pivotal role, thereby, both voltage and frequency during the island depend on this relationship. Conversely, for the island object of study in this thesis, voltage and frequency during the island are influenced by four factors. These factors have been cited several times in the text and are listed again; (i) the power drawn by the loads which remain in the island, (ii) the type of fault that originated the CB opening, (iii) the load torque coupled with the IM and lastly (iv), the reclosing time.

As has been stated earlier, to prevent these undesired events, ID methods can be classified into three main types (e.g. active-based methods, passive-based methods and communication-based methods). Focusing on the passive-based methods, its guiding principle is based on using the available local measurements at the target position where the source is located. At this point, it is worth recalling the most common parameters used in the passive-methods, which fundamentally, are the following ones: the rate-of-change of frequency (ROCOF), the rate of change of voltage (ROCOV), under/over voltage (UVP/OVP), under/over frequency (UFP/OFP), the rate-of-change of active and reactive power (ROCOP/ROCOQ) or the vector surge (VS) protection. Other ID indicators have been proposed in the available literature, see for instance [9.1-9.2]. However, only the previously mentioned parameters will be used in this thesis, which in turn, are the most commonly used for these purposes [9.3-9.6].

As a result of the aforementioned, the main goal of this Chapter is to implement a technique which merges several passive-based methods used for ID with an additional criterion. The latter has been implemented to fulfil the maximum efficiency in islanding detection. Besides, the most used indicators in the passive-based ID methods will be tested and discussed to make a comparison with the proposed hybrid islanding detection method (HIDM). To obtain the tripping times for both the passive-based methods and the HIDM, several scenarios will be simulated using the Matlab/Simulink model described in Chapter 4.

This Chapter is organised as follows:

- A brief review of the main used settings in the passive-based ID methods is done in ***section 9.2***.
- The proposed algorithm is described in ***section 9.3***.
- In ***subsection 9.4***, the results obtained from the performed simulations are shown. In it, a thorough discussion regarding the resulting tripping times for each simulated scenario is provided. Moreover, the evidence required to support this new technique has been obtained by testing both islanding and non-islanding scenarios.

Eventually, the main conclusions of this chapter are summarised in ***section 9.5***.

9.2 Passive-based methods review

As has been dscribed above, the local measurements are the cornerstone of a passive-based method. Nevertheless, with the sensed variables at the target position, several indicators can be computed. This section reviews the main principles of some passive-based ID methods that will be used in the hybrid technique proposed in this thesis. It is essential to mention that the ID has been the subject of many research studies; see, for instance, [9.7]. The most common indicators are listed down below:

1. *Under/Over Frequency* (81*U*/81*O*)

Frequency values are usually captured every cycle, at voltage zero-crossing. The classical frequency thresholds for a 50 Hz system are 50.5 Hz for over-frequency values and 49.5 Hz for under-frequency values. As a rule of thumb, relays generate a trip signal with a delay after any of these thresholds has been exceeded. Both under/over frequency protection can be implemented using either a time curve or a fixed time. The tripping time can be adjusted between 0.16 s for the highest deviation, and 300 s for the minimum deviation; see [9.8]. For variations beyond 95% of rated the frequency, a 0.16 s fixed-time delay is used. Slight frequency deviations in transmission levels may involve frequency nuisance tripping with this method.

2. *Under/Over Voltage* (27/59)

Voltages are measured to obtain the RMS value of the phase-to-ground voltages. Commonly used voltage thresholds are set to 1.2 pu for over-voltages and 0.8 pu for under-voltages. Voltage deviation protection can be set using either a time curve or a fixed time. Typically, the delay is set to 100 ms for both over- and under-voltage protection. Nonetheless, for voltages between 1.1 pu and 1.2 pu, the time delay is set to 500 ms. A succinct assessment concerning voltage curves for ID detection is presented in [9.9].

3. *ROCOF* (81*R*)*/ROCOV*

ROCOF and ROCOV are methods based on the derivative with respect to time of respectively frequency and voltage measurements. Usually, *df/dt* is measured over a few cycles, generally

between 2 and 50, and its value is sent to a low-pass filter to remove the high-frequency harmonics. A value of 1.2 Hz/s is seen as an inadmissible frequency rate of change. This value typically ranges from 0.1 to 3.5 Hz/s; see, for instance, [9.10-9.11]. A minimum voltage supervision is also implemented in ROCOF relays; commonly 0.85 pu. In this thesis, the frequency is measured every cycle during four cycles, and the values are stored in order to compute the derivative, which is obtained with the following expression:

$$\frac{df}{dt} = \frac{(f_1 - f_5)}{\sum_{i=1}^{4} T_i} \tag{9.1}$$

where T_i is the period of each of the four cycles after the first frequency value is captured; subindices 1 and 5 refer respectively to the first and the last values that are measured to compute the derivatives. Although measurements are available for a minimum of four cycles, false tripping could occur if only four cycles were selected. Here, a 7-cycle supervision is considered; for a 50 Hz power frequency, this is a time delay of 140 ms, a widely used setting in ROCOF relays. Voltage derivative will be similarly computed as for the ROCOF relay. A typical rate-of-change of 0.25 pu/s is used with a time delay of 140 ms; however, as for the ROCOF, a 140-ms delay will be used in the present work for this derivative.

4. *ROCOP/ROCOQ* (32*R*)

The rate-of-change in both active and reactive powers is a reasonable indicator for islanding detection, considering that, except for a balanced situation, it competes favourably for a quick IO detection. The active and reactive power derivatives are computed as follows:

$$\frac{dP}{dt} = \frac{(P_1 - P_5)}{\sum_{i=1}^{4} T_i} \tag{9.2a}$$

$$\frac{dQ}{dt} = \frac{(Q_1 - Q_5)}{\sum_{i=1}^{4} T_i} \tag{9.2b}$$

Summary of settings

The settings used for each method in this particular study and the main features of each technique are summarized in Table 9.1. These settings have been adopted taking into account the settings commonly used in ID methods, like those described before, and settings based on field experience from prescribed events.

9.3 HIDM features

9.3.1 Overview

This section is aimed at detailing the performance of the proposed HIDM. Essentially, the new hybrid method merges several existing passive ID principles, reviewed in the previous section, with a directional criterion in order to achieve high accuracy and avoid false tripping events. Figure 9.1 summarises the steps to be made from the measurements needed to detect an islanding scenario. The rest of this section is dedicated to describe the variables involved in the method, the settings, and the architecture of the implemented HIDM.

Table 9.1: Parameters used in the passive-based ID methods.

ID method (ANSI/IEEE code)	**Principle**	**Settings**	**Time-delay (ms)**
81U	Under-Frequency supervision	47.5 Hz	120
81O	Over-Frequency supervision	52.5 Hz	120
27	Under-Voltage supervision	0.8 pu	120
59	Over-Voltage supervision	1.2 pu	120
ROCOF	Frequency derivative with 0.85 pu voltage supervision	1.2 Hz/s	140
ROCOV	Voltage derivative	0.25 pu/s	140
ROCOP	Active power derivative	0.3 MW/s	140

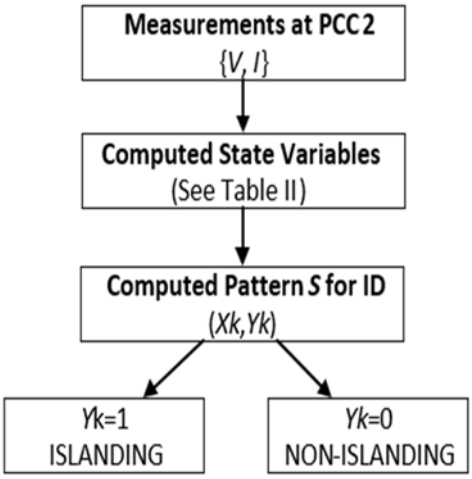

Figure 9.1: Flowchart to compute the state variables and the pattern for islanding detection.

9.3.2 Directional criterion

Directional protection is widely adopted for selectivity purposes. According to ANSI-IEEE terminology, directional power protection can be either 32P or 32Q (i.e., for active and reactive power, respectively). In addition, 32R protection can be used to prevent reverse power. The directional protection proposed in this work uses the direct-sequence angles of both voltage and current. The conditions proposed to detect IO are based on the following restrictions:

$$90 < \varphi_{I1} < 270 \tag{9.3}$$

where φ_V and φ_I are the voltage and current angles, respectively, while the subindex "1" indicates direct sequence.

The zone of actuation of this detection method is displayed in Figure 9.2, in which the angle of the direct-sequence voltage is compared with the angle of the direct-sequence current: the system will trip when the angle is between 90 and 270 degrees.

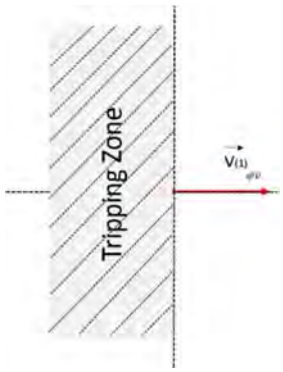

Figure 9.2: Graphical representation of the adopted directional protection.

9.3.3 Input, outputs and intermediate variables

Data analysis is one of the main tasks of the proposed method, for which the classification of local measurements is essential. This process involves two steps: the first one is focused on sensing the electrical magnitudes (independent variables); the second one provides the output (dependent variable); that is, islanding/non-islanding condition. To carry out these tasks, voltage and current values are measured every cycle (i.e. every 20 ms). The time-domain vector of the state variables is defined as follows:

$$[X^{j}_{1,k}(t)]^{T} = [x^{j}_{1,k}(t_1), x^{j}_{1,k}(t_2), x^{j}_{1,k}(t_3), \cdots, x^{j}_{1,k}(t_n)] \tag{9.4a}$$

$$[X^{j}_{2,k}(t)]^{T} = [x^{j}_{2,k}(t_1), x^{j}_{2,k}(t_2), x^{j}_{2,k}(t_3), \cdots, x^{j}_{2,k}(t_n)] \tag{9.4b}$$

$$\vdots$$

$$[X^{j}_{8,k}(t)]^{T} = [x^{j}_{8,k}(t_1), x^{j}_{8,k}(t_2), x^{j}_{8,k}(t_3), \cdots, x^{j}_{8,k}(t_n)] \tag{9.4k}$$

where is the *mth* state vector for a particular *jth* event at the *kth* target location. These forms can also be annotated by means of the following transposed 8-dimension vector expression:

$$X^{j}{}_{m,k}(t_i)^{T} = \begin{bmatrix} X^{j}{}_{1,k}(t_i) \\ \vdots \\ X^{j}{}_{8,k}(t_i) \end{bmatrix}; X^{j}{}_{m,k}(t_i) \in M_{1x8} \tag{9.5}$$

As mentioned earlier, this vector captures the time-domain variables each cycle (20 ms) during the desired period t_n. The state variables for every *jth* event at every kth location, are defined in Table 9.2; see also Fig. 9.1. Considering N events, the matrix expression of the whole range of events can be expressed as a N × 8 matrix:

$$X_k(t_i) = \begin{bmatrix} x^{1}_{1,k}(t_i) & \cdots & x^{1}_{8,k}(t_i) \\ \vdots & \ddots & \vdots \\ x^{N}_{1,k}(t_i) & \cdots & x^{N}_{8,k}(t_i) \end{bmatrix}; X_k(t_i) \in M_{Nx8} \tag{9.5}$$

Input and output variables for a given *jth* event at a *kth* target location, are stored together through the following two-dimension vector *S*:

$$S = \{(X_k, Y_k)\} \tag{9.6}$$

where Y_k is the independent vector containing a binary output for every *jth* event at a *kth* location: $Y_k = 1$ for an islanding event and $Y_k = 0$ for a non-islanding event. The state vector X_k is obtained from the measurements of the three-phase voltages and currents, (V_a, V_b, V_c) and (I_a, I_b, I_c), as shown in Figure 9.2. Crucial information derived from these inputs are the angles of the phase voltages (φ_{Va}, φ_{Vb}, φ_{Vc}) and currents (φ_{Ia}, φ_{Ib}, φ_{Ic}).

Table 9.2: State variables for ID.

Symbol	**Variable**	
x_1	ΔV	Voltage deviation (pu)
x_2	$V\varphi$	Voltage angle (Deg.)
x_3	$I\varphi$	Current angle (Deg.)
x_4	Δf	Frequency deviation (Hz)
x_5	df/dt	ROCOF (Hz/s)
x_6	dV/dt	ROCOV (pu/s)
x_7	dP/dt	ROCOP (MW/s)
x_8	dQ/dt	ROCOQ (MVAr/s)

9.3.4 Architecture

The architecture of the proposed HIDM is based on the decision tree (DT) shown in Fig. 9.3. The tree is organised as follows: firstly, the voltage and frequency magnitude deviations are measured; next, the algorithm estimates the state derivatives (*d/dt*) to avoid undesirable false-tripping operations and achieve the minimum non-detection zone (NDZ); the last step focuses on implementing the directional criterion, which assures high feasibility in preventing all scenarios, even those where voltage and frequency remain within the threshold settings.

Since a DT is a binary tree constructed by groups of datasets, the three mentioned stages are divided into several levels. To achieve the maximum precision in the settings of each level, the DT has been created by analysing a wide range of previous events captured for a two-year period in the real DN as well as considering the full range of simulated scenarios in the present study. As can be seen from Figure 9.3, the first six-level settings of the DT belong to the passive-based settings described in Table 9.1.

In order to avoid misclassification and nuisance tripping, the current HIDM consists of a seven-level DT and considers a seven-cycle parameter cluster. Besides, the DT assumes a system with multiple-feeders; three in this work. This fact underscores that disturbances on neighbour feeders can cause false-islanding detection and, consequently, false tripping. To date, most of the research studies focused on ID, have only considered one MV feeder. The present HIDM correctly deals with this issue.

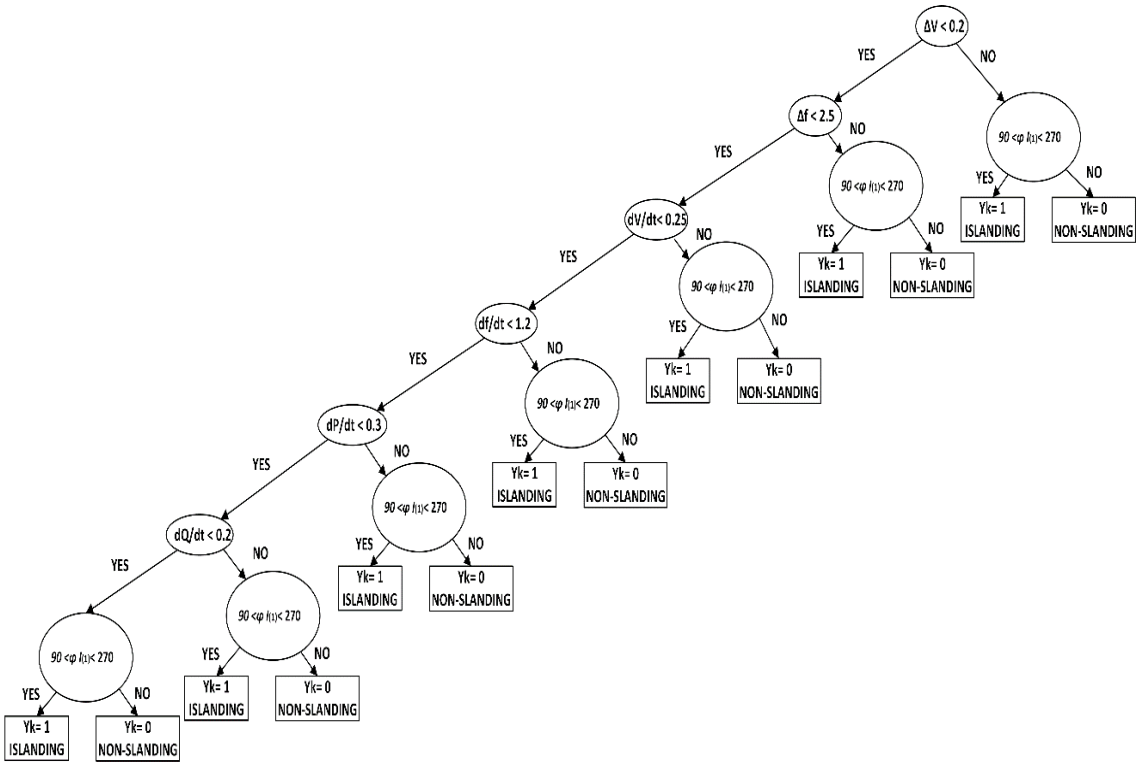

Figure 9.3: Seven-level HIDM.

Matlab implementation of the HIDM

The seven-level HIDM used to detect the IO has been implemented in the previously described model in Chapter 4.To achieve a better understanding; Figure 9.4 depicts this model with the additional blocks. As can be seen in this Figure, the HIDM block is used to trip the CB located at PCC_2 (i.e., the interconnection between the industry and the grid) where the IMs are connected. The output of the HIDM algorithm (purple-block in Figure 9.4) is sent to the CB.

On the other hand, the blue-block located at the bottom-right part of this Figure is the one which receives the independent variables (i.e., three-phase voltages and currents from measurement blocks) and compute the state variables X_k of the HIDM algorithm to obtain the dependent variable Y_k (i.e., (1) for islanding or (0) for non-islanding). Particularly, In_1, In_2 and In_3 are the three RMS phase voltages, In_4 is the frequency obtained from the voltage signal through a PLL block and, In_5 is the frequency derivative obtained from the derivative block. The latter block implements a low-pass filter to avoid high-frequency transients. Finally, In_6 and In_7 are the active and reactive powers computed through the previously obtained voltages and currents. The content of this block is detailed in the following Figure 9.5.

As stated above, the HIDM is based on a DT which merges several passive-based protective functions such as UVP/OVP (27/59), UFP/OFP (81m/81M), ROCOF (81R), ROCOV, ROCOP and ROCOQ with an additional directional criterion. As can be seen in Figure 9.5, each passive-based technique is computed in a separate block. Therefore, each one will be shown in a different Figure.

Voltage supervision is computed in one block (both under and over-voltage) and the detail of this protection is displayed in Figure 9.6. In this block, apart from the UVP and OVP, a widely adopted additional supervision criterion has been added. This supervision checks if the voltage is between 1.1 pu and 1.2 pu during 500 ms. Note that the whole range of simulated scenarios in this Chapter have been carried out with a reclosing time of 0.5 s; thereby, this makes this protective setting

incapable of tripping. However, this supervision may be really useful in scenarios with larger reclosing times.

The *Frequency supervision* is carried out for both under and over frequency through the block depicted in Figure 9.7. This protection trips for either a frequency deviation above or under the threshold and these signal is passed through a delay block aimed at applying the 120 ms delay for this supervision. Thus, if the input is true, it applies a time-delay to this signal, on the other hand, if this become false, the output is false with no time-delay. *ROCOF* protection is implemented as in Figure 9.8. It can be seen that a minimum voltage of 0.8 pu is required to trip. The ROCOV protection is implemented in a similar way as for the ROCOF, see Figure 9.9. Note that the rate of change of voltage has to exceed the threshold for the three phases.

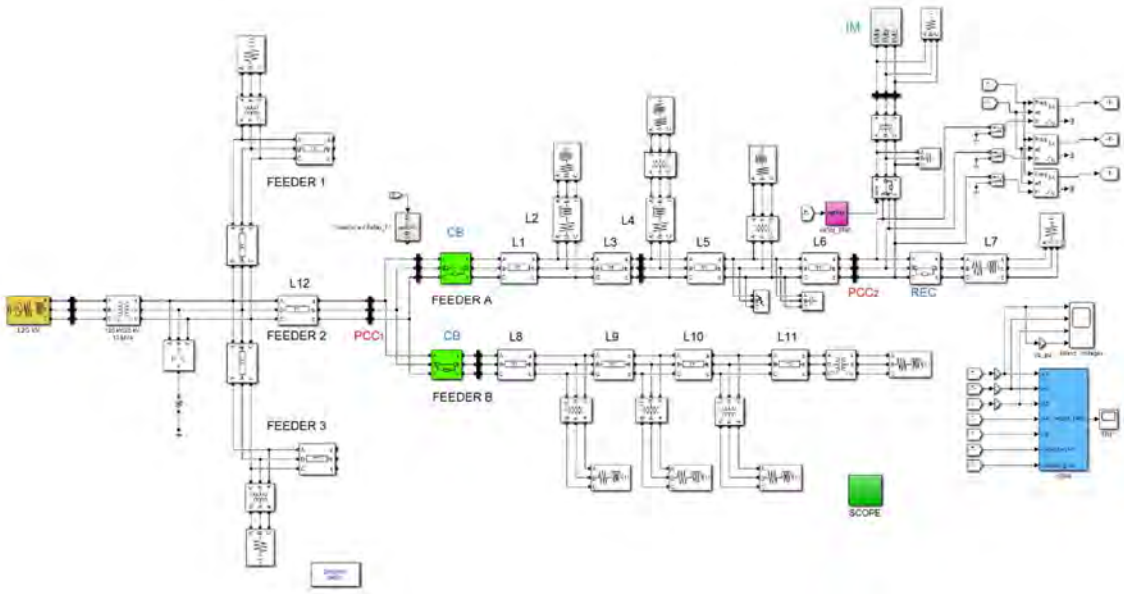

Figure 9.4: Matlab model with the proposed HIDM.

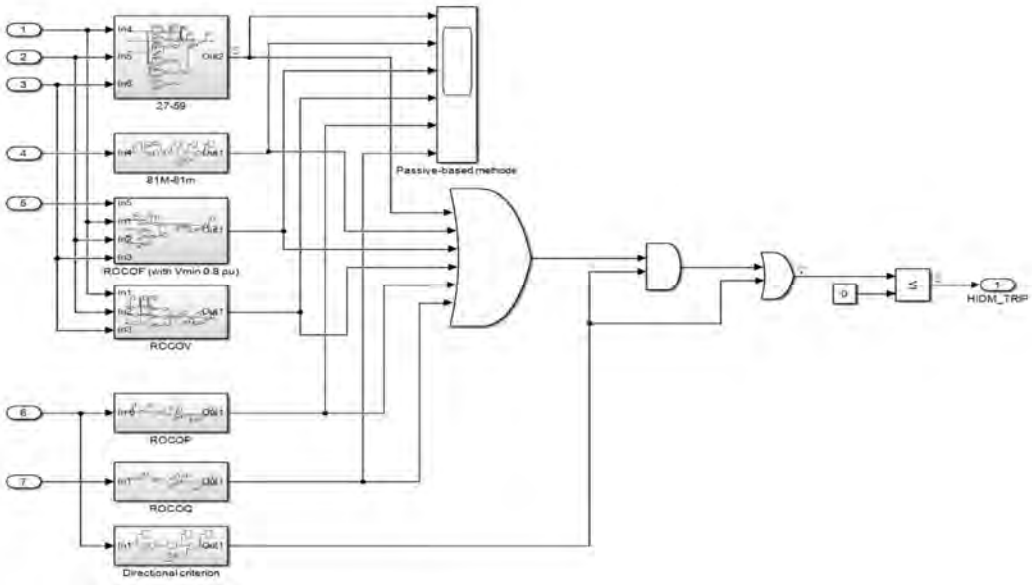

Figure 9.5: Matlab implementation of the seven-level HIDM block.

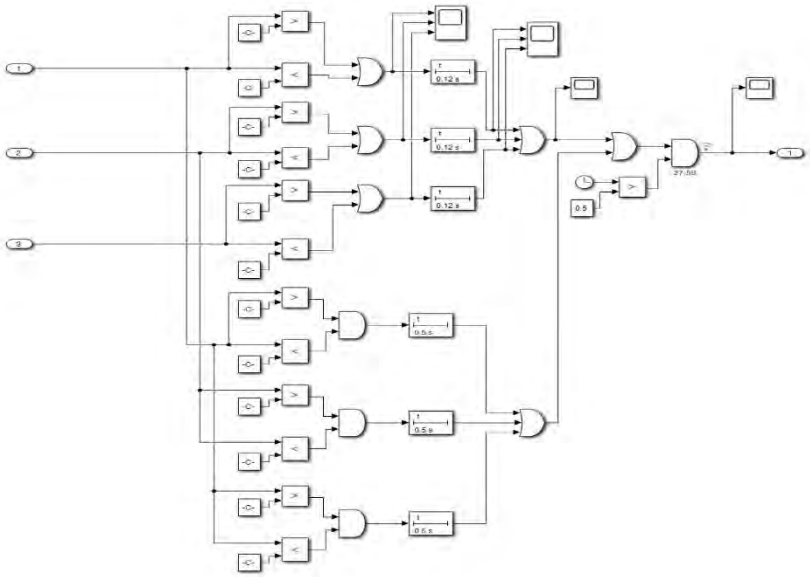

Figure 9.6: Scheme of the UVP/OVP protection.

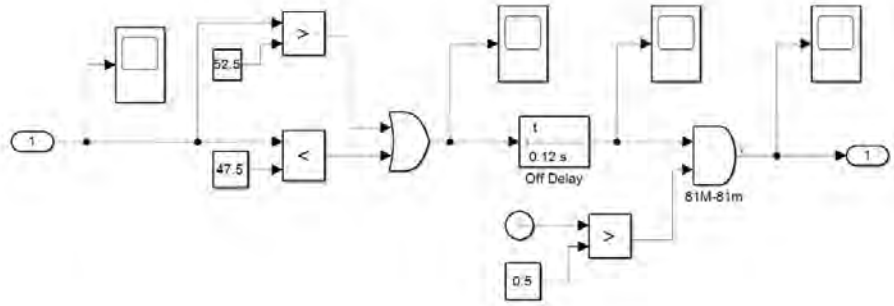

Figure 9.7: Scheme of the UFP/OFP protection.

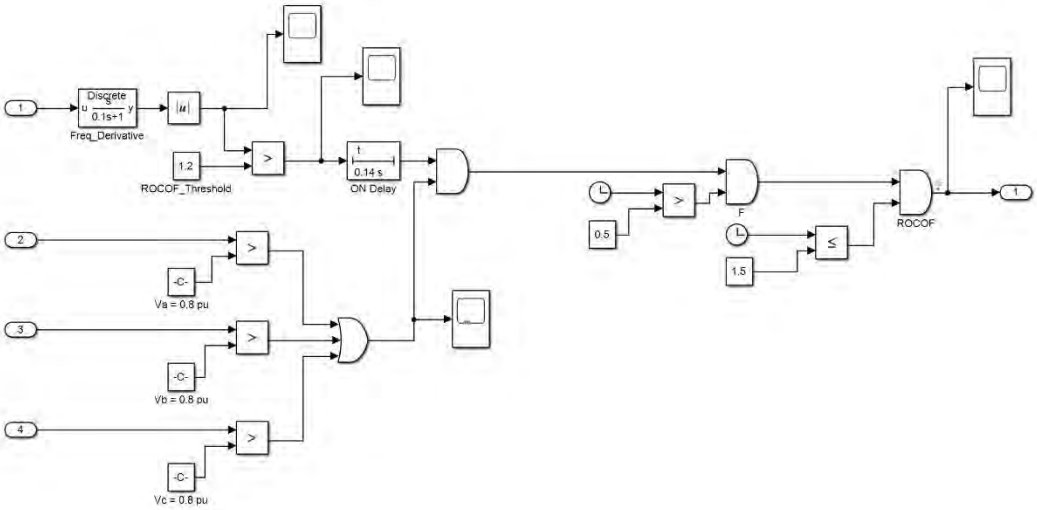

Figure 9.8: Scheme of ROCOF protection.

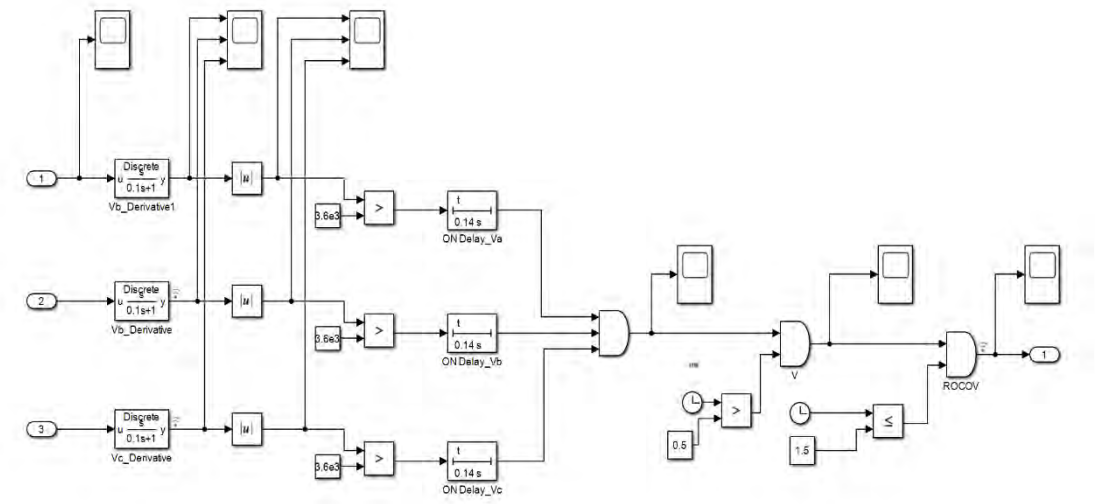

Figure 9.9: Scheme for ROCOV protection.

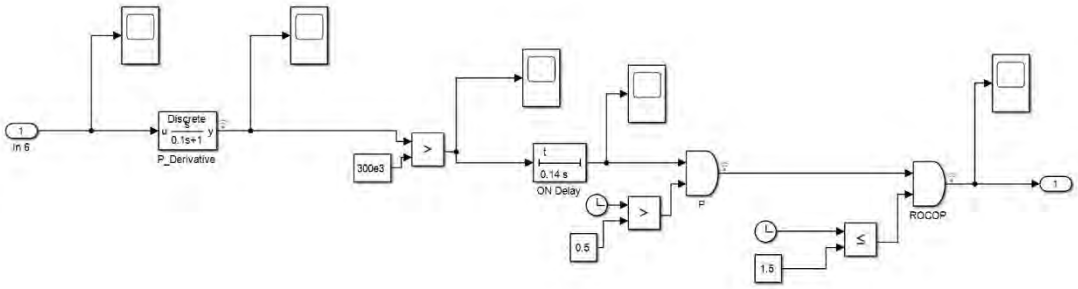

(a)

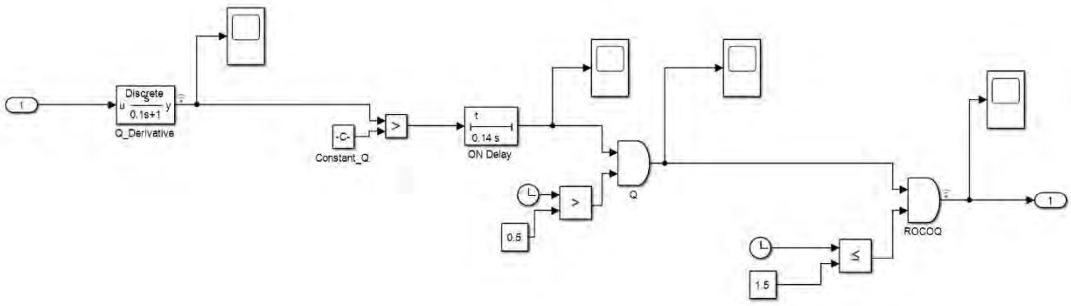

(b)

Figure 9.10: ROCOP and ROCOQ protections.

The rate of change of both active and reactive power are both computed as can be seen in Figure 9.10.

In order to avoid a false-tripping due to the initial transient when the simulation begins, the clock must be larger than 0.5s. Similarly, to prevent undesired trappings after the island, for the derivatives, the clock must be lower than 1.5 s to initiate a trip.

By observing Figure 9.5, each parameter belongs to one level of the DT, where the deviation is compared to each threshold. In the case at least one of them is exceeded, the directional criterion is then applied, and if the latter proves to be false, it is a non-islanding event. On the contrary, if the directional criterion is true, the islanding is detected and subsequently, the CB tripping is ordered. Note that if any indicator becomes true, the last stage is again the directional criterion.

By observing the last block in Figure 9.5, the obtained signal from the HIDM algorithm is compared with zero. Since a zero signal is required to open the CB, if the HIDM becomes true, this comparison allows us to obtain a zero for tripping.

9.3.5 Time constraints in islanding detection

A crucial limitation is the available time to detect the IO; as commented above, the preset reclosing time is commonly set between 0.5 s and 1 s. It is important to keep in mind that, by default, it is assumed that the substation CB will satisfactorily clear the fault. Thus, only temporary faults are considered. The mechanical time delay will last three cycles for both the substation CB (node PCC_1 in the test system; see Fig. 1) and the CB at the target position (node PCC_2). Considering the foregoing, the maximum time available to detect the IO and trip the CB at the target location may be computed as follows:

$$t_{\max} = t_{clr} + t_{rec} + t_{CB} \tag{9.8}$$

where t_{clr} is the clearing time, which, in turn, depends on the selected relay characteristic curve as well as on the sensing time, t_{rec} is the reclosing time, which is set in the relay of the head CB (PCC1), and t_{CB} is the mechanical time delay for the head CB after the relay orders the reclosing operation.

9.4 Simulations

9.4.1 Overview

This section presents the study carried out to test the performance of the proposed HIDM and compare it with the ID techniques described above. As has been seen in the previous Chapters, following the CB opening, due to the lack of supply, the equilibrium between torques is broken, the IM speed derivative becomes negative and, thereby, only the dynamic torque (i.e. the torque due to the non-zero derivative of the rotor speed) drives the machine. In order to observe the influence of each factor towards the tripping times, the simulations have been classified into three main groups. The first group focuses on analysing the impact of the loads which remain on the island at the time the fault occurs. The second group analyses the IO considering different types of faults. Lastly, the third group is aimed at determining the tripping times for both islanding and non-islanding events, thus, the dependability of the proposed method will be demonstrated.

As a general rule, considering the massive amount of signals and computed parameters obtained during the simulations, to not extend excessively the document, only the tripping times obtained for each case will be provided. However, to substantiate these tripping times, the parameters obtained from each passive-based protection will be displayed for the second case of each group, thus showing how the variables are computed. The measurements obtained from the simulations for each protective function will be organized in different figures. Hence, the first figure will show the voltage values (i.e., the three-phase voltages and its time derivatives) so as to observe the results of the UVP/OVP and ROCOV protections. The second figure will show the frequency and its derivative to observe both UFP/OFP and ROCOF protection results. In the third figure, the

active and reactive-power derivatives will be shown to observe both ROCOP and ROCOQ protection results. Lastly, a fourth figure will show the active-power to observe the effectiveness of the directional criterion. Summarising, the simulations have been divided into these three principal groups:

1. Simulations aimed at estimating the tripping times by assuming fixed fault conditions and using different feeder loads values. As assumed in the previous Chapters, the load value specified in this subsection is the sum of all LV loads that remain within the island at the time the fault occurs.

2. Simulations aimed at estimating the tripping time under different types of faults and fixing a particular value for feeder loads.

3. Islanding and non-islanding events aimed at proving the dependability of the proposed HIDM and observing the nuisance tripping of the conventional ID methods for these particular scenarios.

The hypothesis that have been considered for all scenarios are listed hereunder:

- Simulations have been performed using the described three-phase Matlab model described in Chapter 4.
- A constant impedance load model has been considered for all simulated scenarios.
- The power factor for all loads is set to 0.98 (lg.). Simulations have been carried out within the MATLAB/Simulink environment, taking advantage of the toolbox SimPowerSystems, and using a discrete mode with a fixed sample time of 50·μs.
- For all simulated scenarios, the tripping times are computed with respect to the beginning of the event.
- The simulation time is set to 2 s and the faults are initiated at 0.9 s for all scenarios.
- To observe the tripping time of each technique, the CB has been is disabled, otherwise if the CB is opened, the IMs would be removed from the grid. Hence, the obtained times belong to the time that each technique would have tripped separately. It should be noted that each technique is equipped with a time delay block (i.e., each method with its particular delay). In case the input is true (i.e., the threshold is exceeded for a particular method) this block applies a delay to the input signal, nevertheless, if this become false, the output is false with no delay. That is the reason why in some Figures, several protection functions relapse and following a certain time are again activated. However, due to the above mentioned, the tripping time is considered as the first time that a tripping signal is activated.

9.4.2 Tripping times for different feeder load scenarios

The first group of simulations are based on the following considerations:

1. A SLG fault with a fault resistance of 5 Ω occurs at node 7, the CB located at PCC_1 (header of feeder A) is set with a very inverse overcurrent curve for phase-faults (50) and extremely inverse curve for ground-faults (50N). Therefore, the fault is cleared within 100 ms.

2. The reclosing time is set to 0.5 s.

3. No mechanical load is applied to the IM.

The following four scenarios have been simulated:

- Case 1: Feeder load is set to 426 kW.

- Case 2: Feeder load is set to 75 kW.

- Case 3: Feeder load is set to 64 kW.
- Case 4: No-load scenario.

The resulting tripping times for these four cases are shown in Table 9.3. The results of both voltage (first plot) and frequency (second plot) obtained from the simulations are displayed in Figure 9.11. Besides, to demonstrate the feasibility of the tripping times summarised in this table, for each case, the resulting tripping signals are provided (see Figures 9.12-9.15). As mentioned earlier, for the sake of brevity, the obtained values of each block (i.e., each passive-based values) will only be displayed for one case, particularly case 2. Thereby, Figures 9.16-9.19 show the results obtained during the simulation of case 2.

Table 9.3: Tripping times of subsection 9.4.2.

ID method (ANSI/IEEE code)	**Case 1 (ms)**	**Case 2 (ms)**	**Case 3 (ms)**	**Case 4 (ms)**
81U	270	465	544	No Trip
81O	No Trip	No Trip	No Trip	No Trip
27	359	No Trip	No Trip	No Trip
59	No Trip	No Trip	No Trip	No Trip
ROCOF	No Trip	308	320	No Trip
ROCOV	404	No Trip	No Trip	780
ROCOP	No Trip	No Trip	No Trip	No Trip
HIDM	No Trip	No Trip	No Trip	No Trip

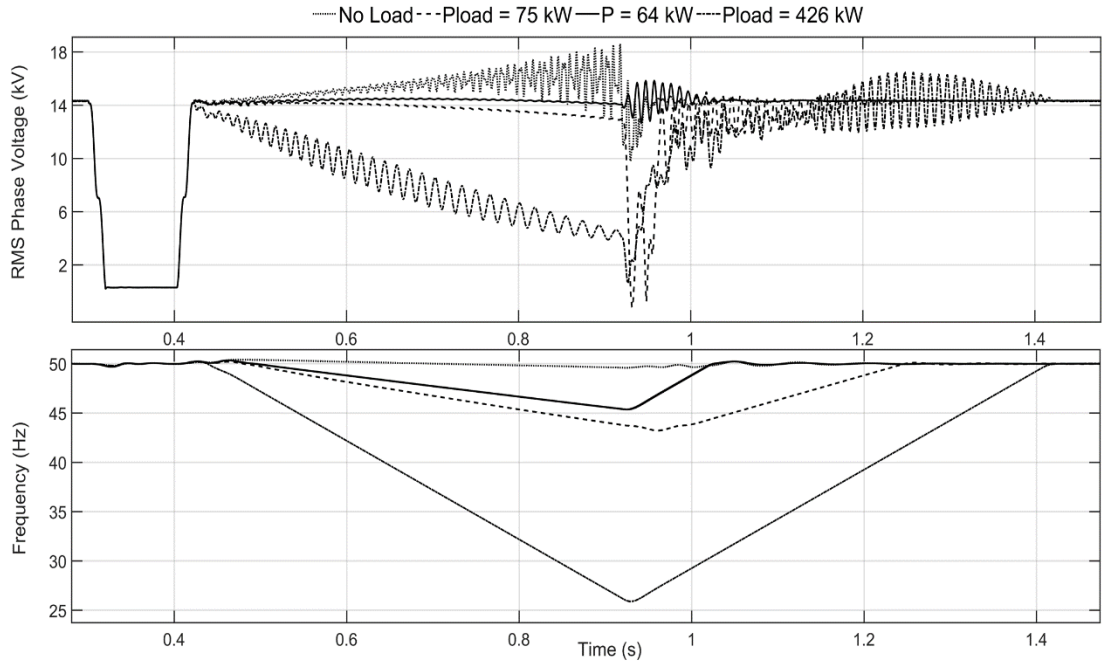

Figure 9.11: Voltage and frequency from simulations of subsection 9.4.2.

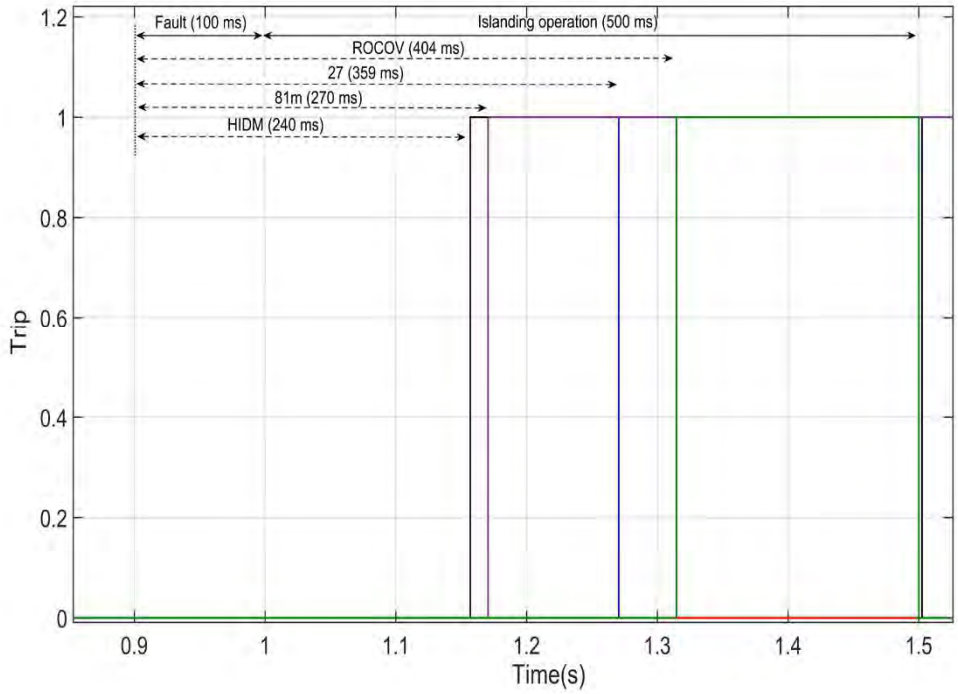

Figure 9.12: Tripping times for Case 1 of subsection 9.4.2.

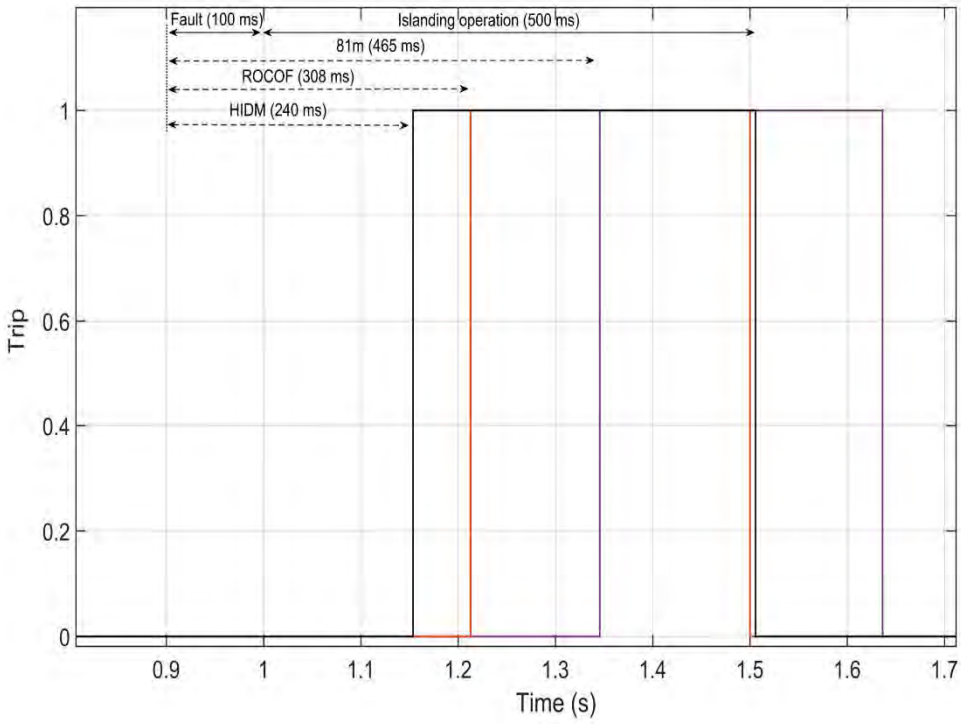

Figure 9.13: Tripping times for Case 2 of subsection 9.4.2.

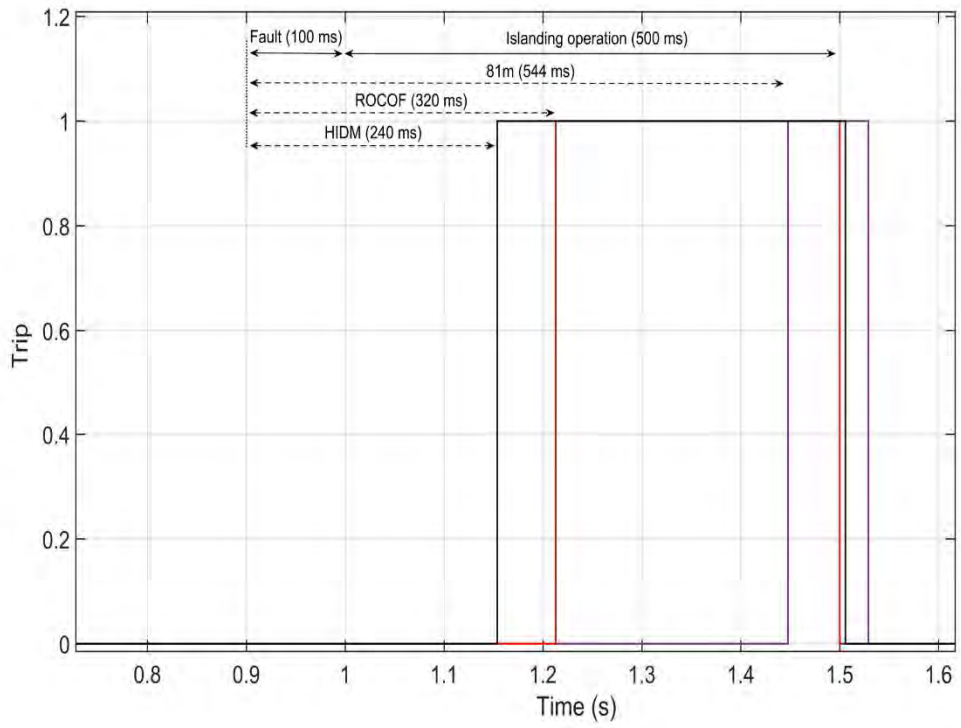

Figure 9.14: Tripping times for Case 3 of subsection 9.4.2.

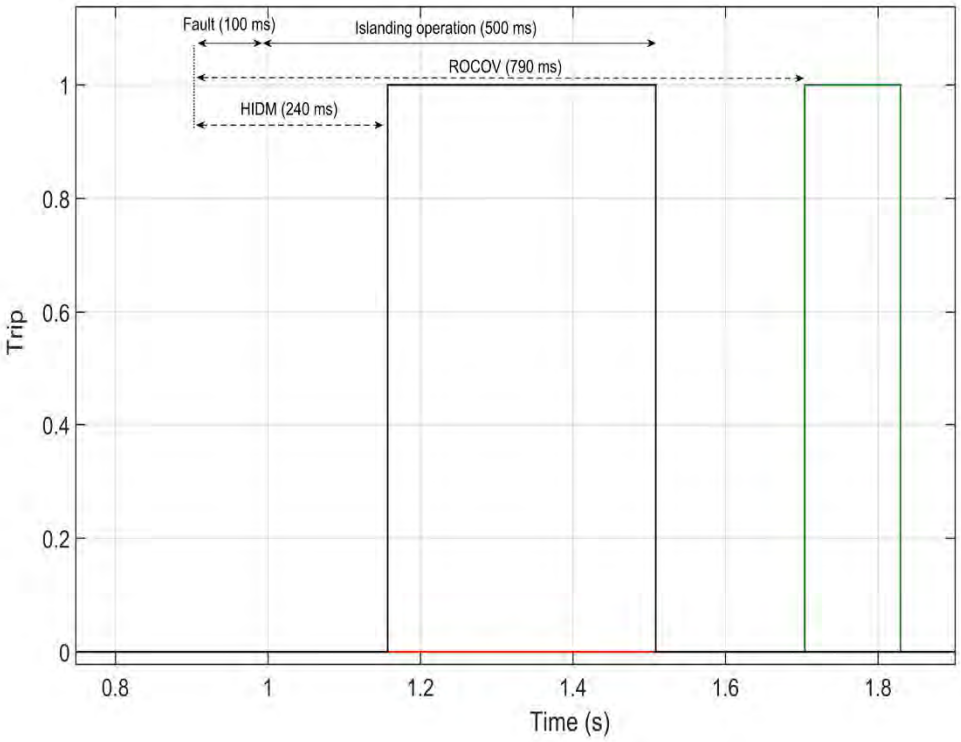

Figure 9.15: Tripping times for Case 4 of subsection 9.4.2.

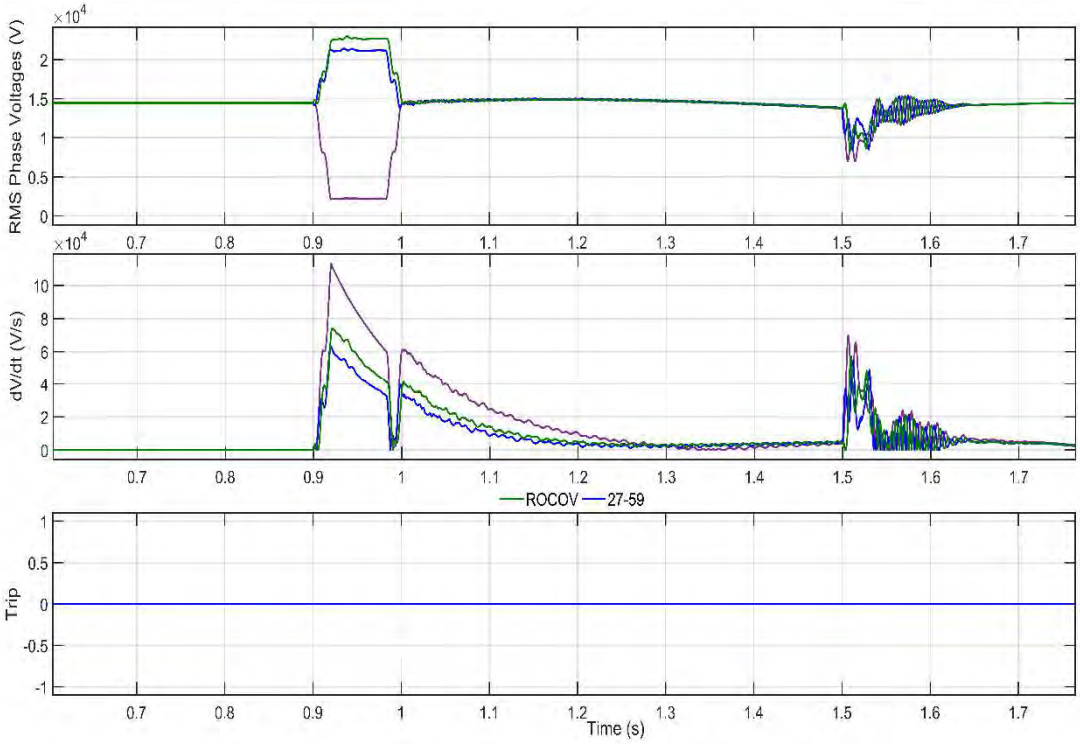

Figure 9.16: UVP/OVP and ROCOV protections results for case 2 in subsection 9.4.2.

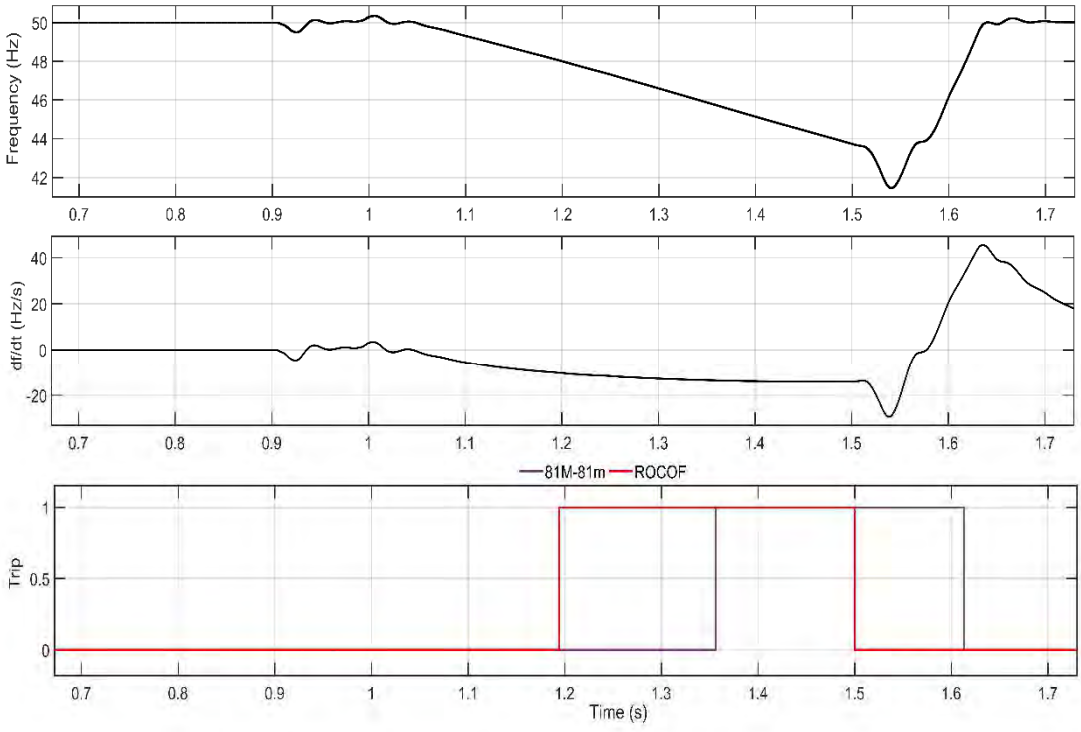

Figure 9.17: UFP/OFP and ROCOF protections results for case 2 in subsection 9.4.2.

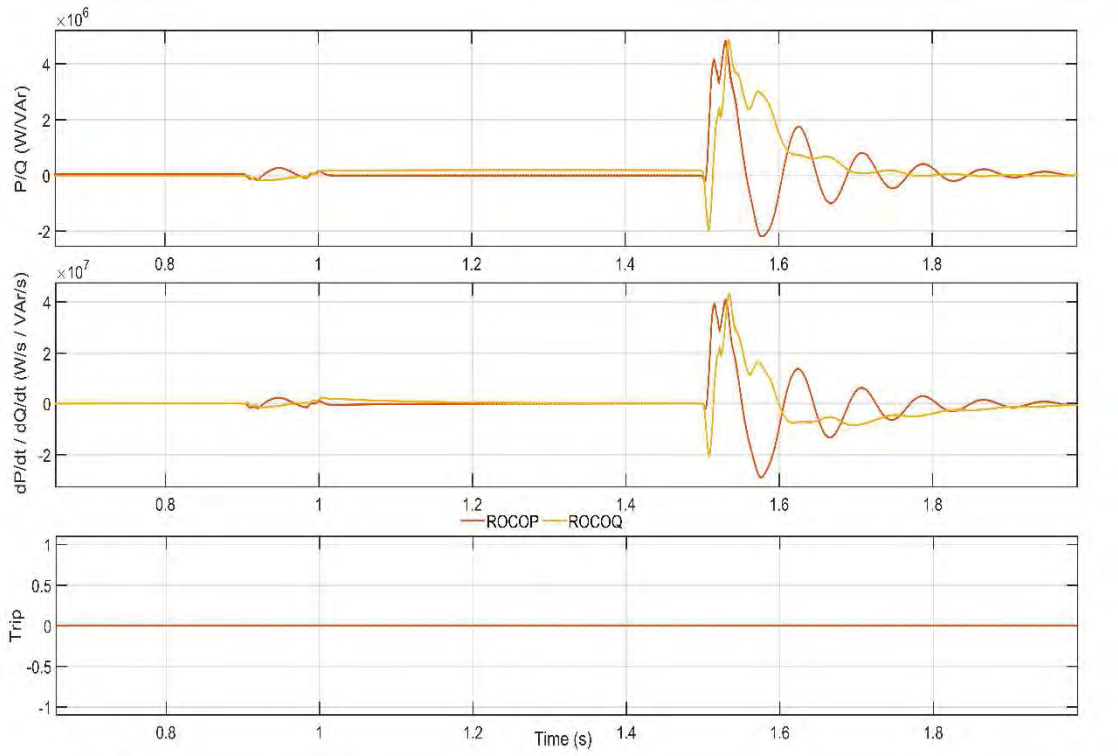

Figure 9.18: ROCOP and ROCOQ protections results for case 2 in subsection 9.4.2.

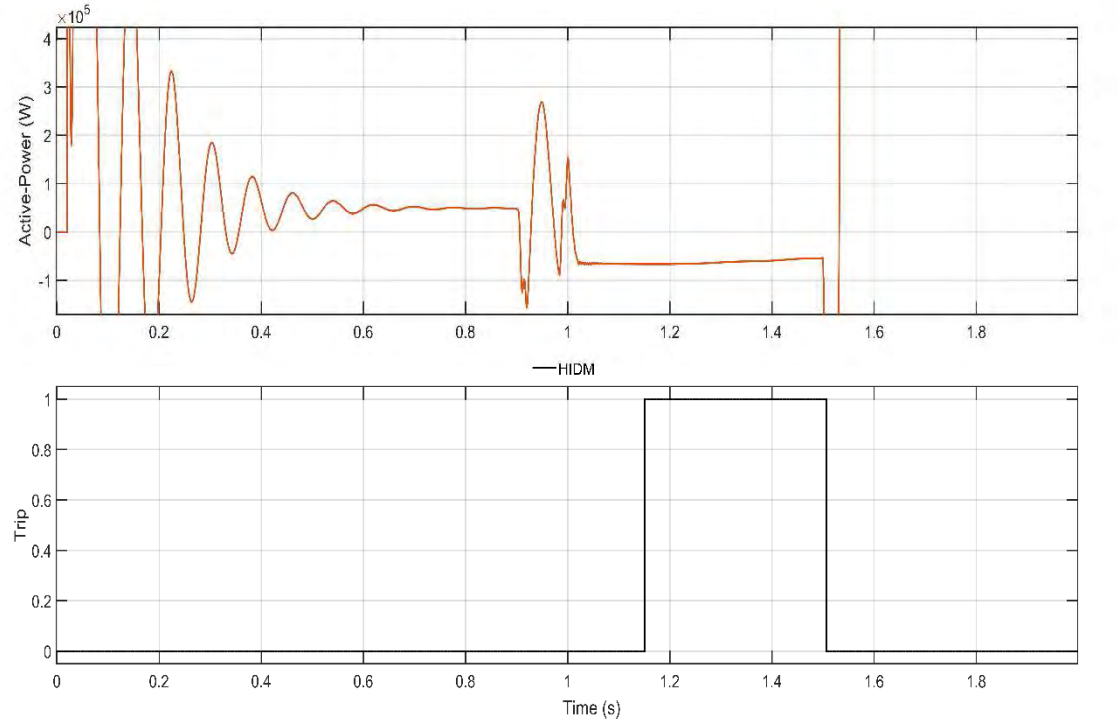

Figure 9.19: Directional criterion protection results for case 2 in subsection 9.4.2.

Results discussion

Voltage supervision only trips for under-voltage in case 1, because for the rest of cases, voltage do not exceed the established thresholds.

The UFP/OFP trips for cases 1, 2 and 3; nevertheless, in case 4, this protection does not trip.

By observing the state derivatives, ROCOF relay trips for cases 2 and 3 and does not trip for cases 1 and 4. In case 1 this protection does not generate the trip because the voltage is below 0.8 pu, whereas in case 4, the frequency remains stable at 50 Hz during the island and, its rate of change is close to zero. On the other hand, the ROCOV protection trips for cases 1 and 4, the first tripping belongs to a negative derivative (due to voltage decrease) and the second is due to a positive derivative (i.e., voltage increasing). Lastly, the rate of change of active and reactive powers do not trip neither during the fault nor during the island.

Moreover, these results reveal that, as expected, the lower is the feeder load value, the lower is the voltage and frequency deviation during the island. Remember that faults are cleared within 100 ms, which avoids tripping by UVP/OVP.

It is worth noting that in the fourth case only the HIDM is capable of undertaking such task within the time constraint.

9.4.3 Tripping times for different types of faults

The second study aims at estimating the tripping times when different types of faults originate the island. The fault position is always node seven and all faults are simulated with a resistance value of 5 Ω. Moreover, the following hypothesis have been considered for all cases:

1. The sum of all LV feeder loads is set to 200 kW.
2. IM is under no-load torque at the time the fault occurs.
3. A clearing time of 200 ms is assumed. Nevertheless, it is essential to keep in mind that the fault current depends on the type of fault, and for the same protection settings and curves, this time may slightly vary. The used curves in these simulations are those described in subsection 4.3.5 of Chapter 4.

The main goal of this section is to study the resulting tripping times when the island is caused by different types of faults. Thus, each case belongs to a particular type of fault:

- Case 1: SLG fault.
- Case 2: LL fault.
- Case 3: LLG fault.
- Case 4: LLL fault.

The resulting tripping times are shown in Table 9.4 whilst in Figure 9.20, the resulting phase voltage (first plot), IM mechanical speed (second plot) and, frequency (third plot) are depicted.

Additionally, for each case, the tripping times are represented in a separate figure. In these eight figures (i.e., Figure 9.21 to 9.24), the tripping time and the duration of the event are displayed. Thereby, the effectiveness of each method can be observed.

Table 9.4: Tripping times of subsection 9.4.3.

ID method (ANSI/IEEE code)	**Case 1 (ms)**	**Case 2 (ms)**	**Case 3 (ms)**	**Case 4 (ms)**
81U	412	466	474	620
81O	No Trip	No Trip	No Trip	No Trip
27	120	120	120	120
59	120	No Trip	120	No Trip
ROCOF	362	No Trip	No Trip	No Trip
ROCOV	146	No Trip	142	143
ROCOP	No Trip	No Trip	No Trip	No Trip
HIDM	No Trip	No Trip	No Trip	No Trip

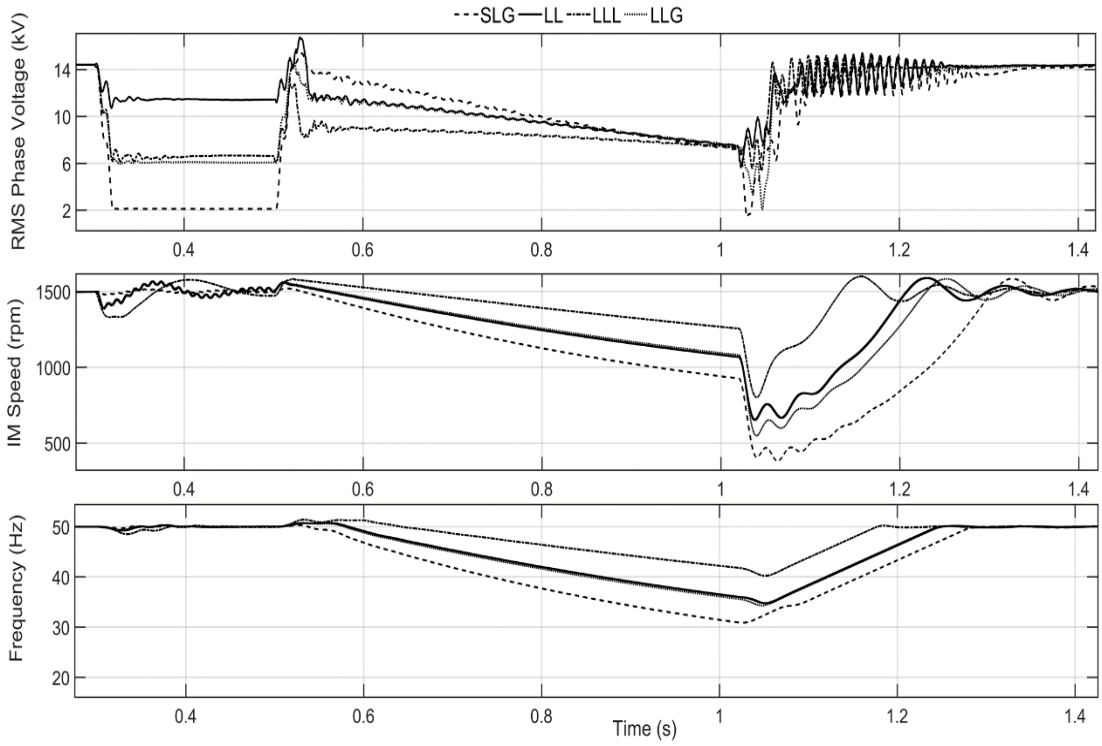

Figure 9.20: Voltage, mechanical speed and frequency from simulations of subsection 9.4.3.

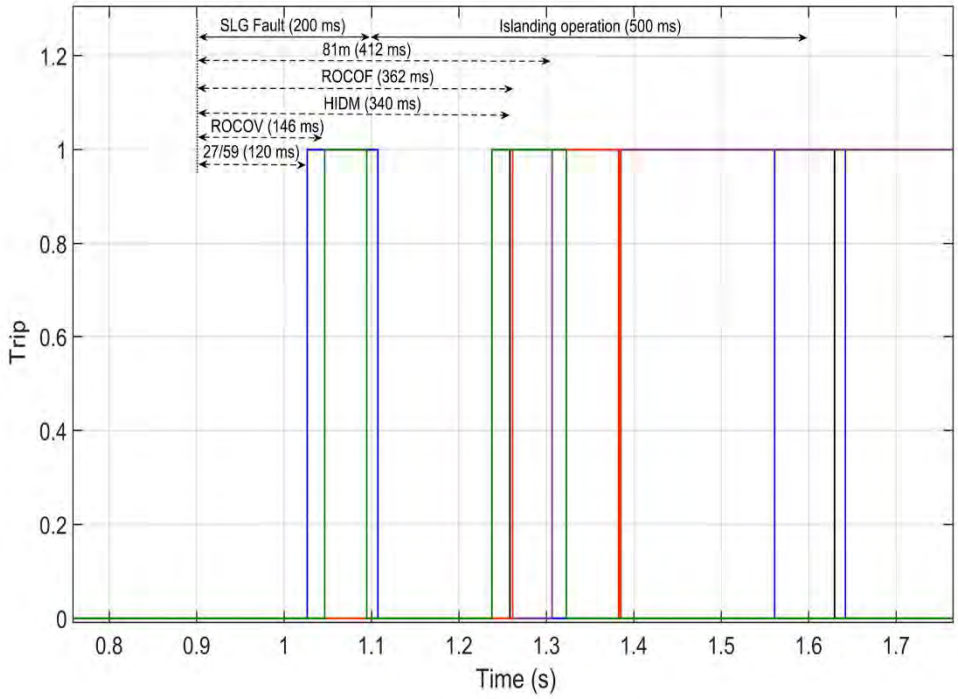

Figure 9.21: Tripping times for Case 1 of subsection 9.4.3.

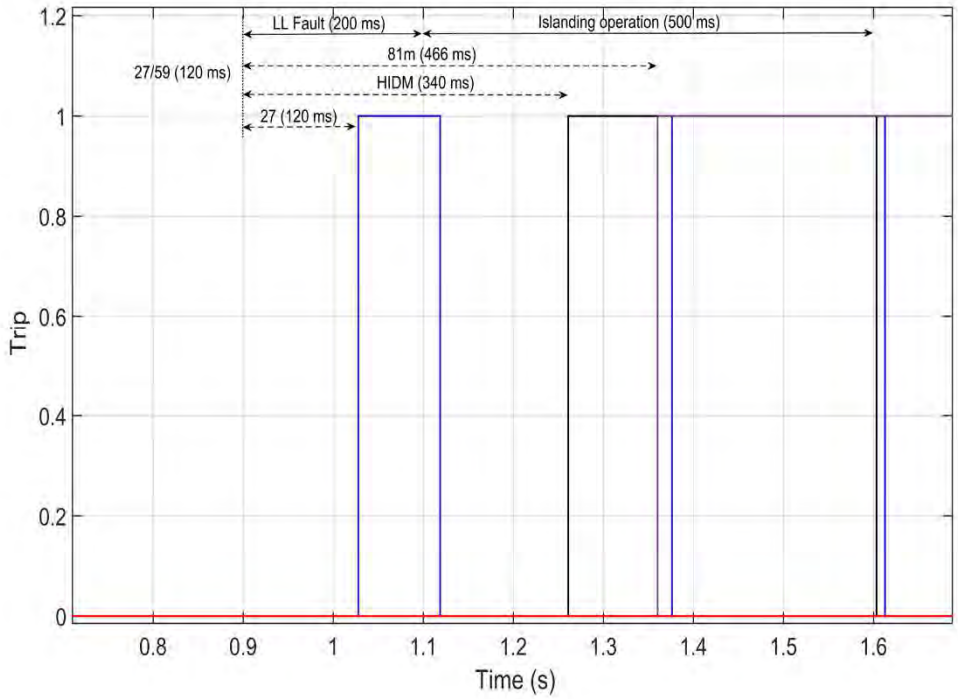

Figure 9.22: Tripping times for Case 2 of subsection 9.4.3.

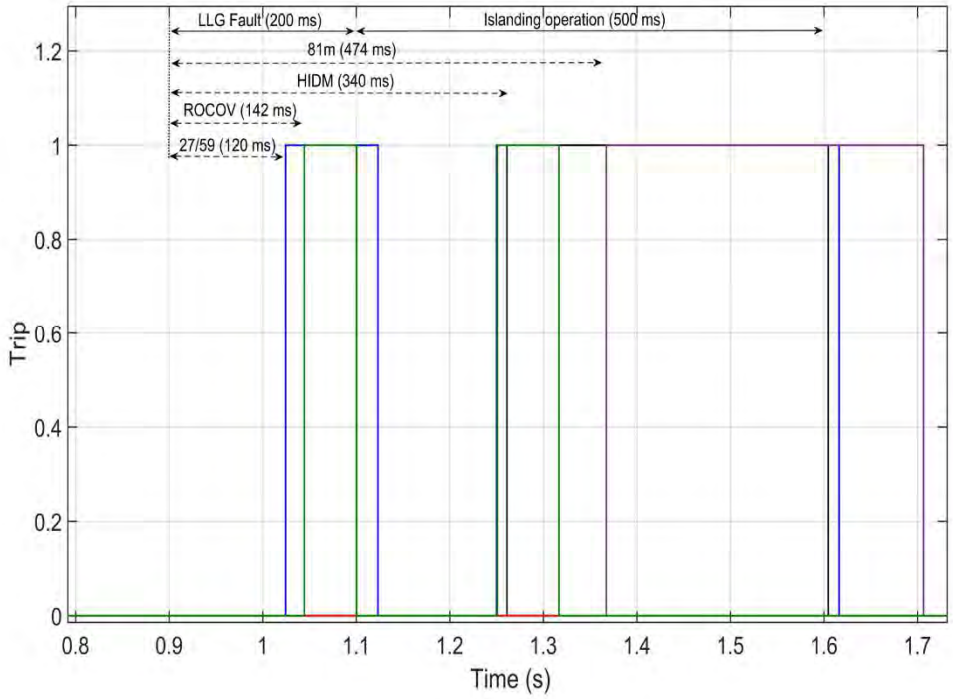

Figure 9.23: Tripping times for Case 3 of subsection 9.4.3

.

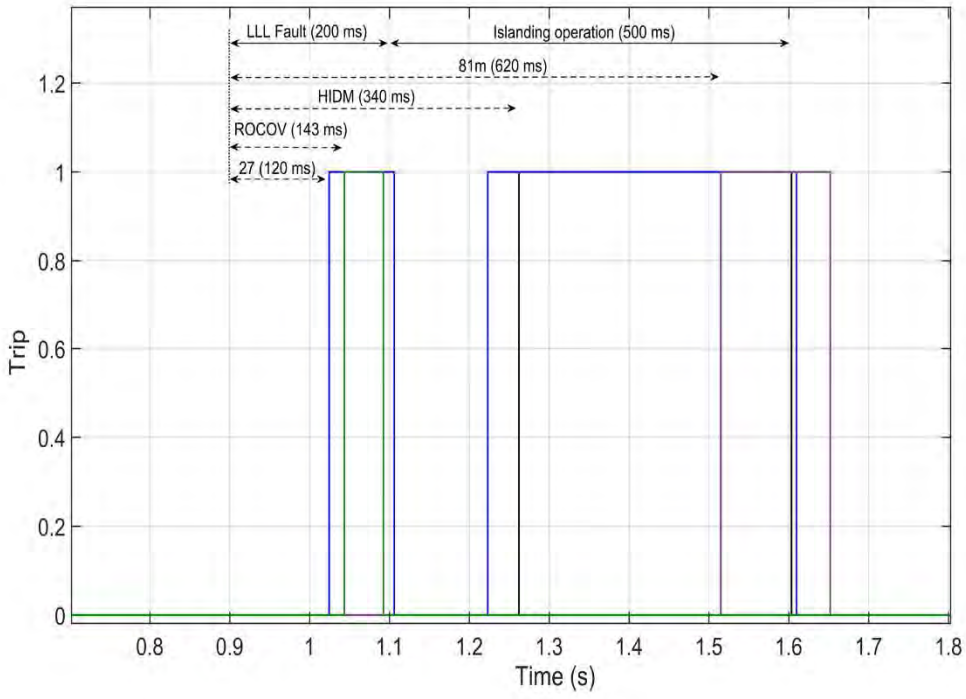

Figure 9.24: Tripping times for Case 4 of subsection 9.4.3.

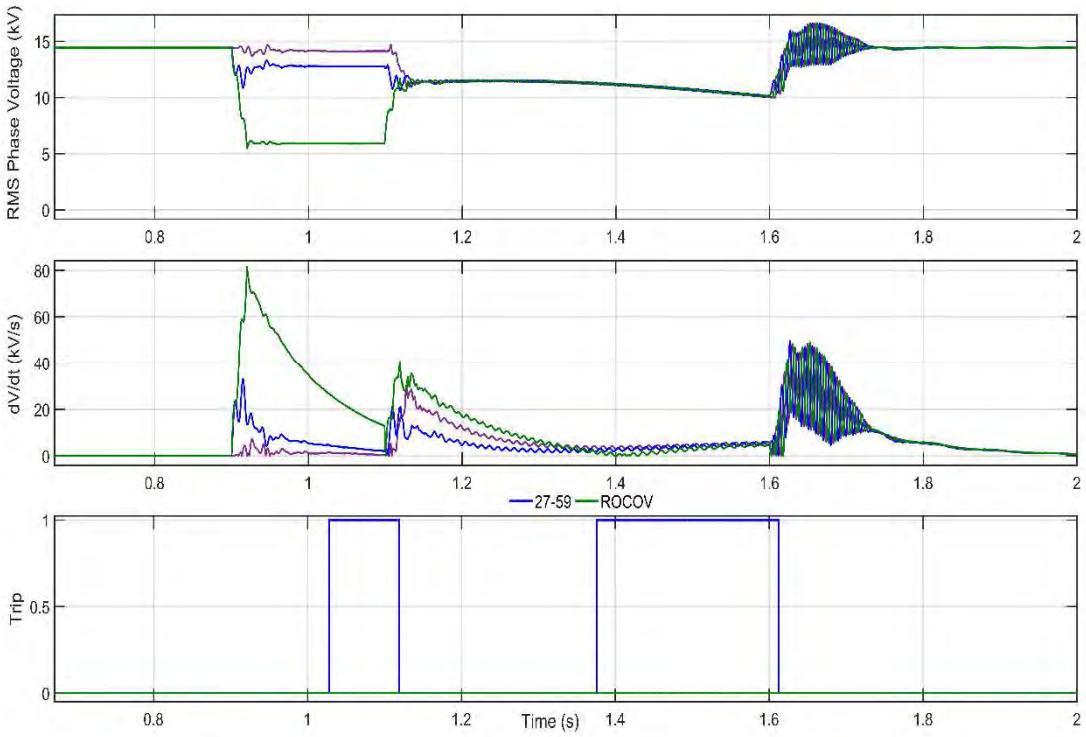

Figure 9.25: UVP/OVP and ROCOV protections results for case 2 in subsection 9.4.3.

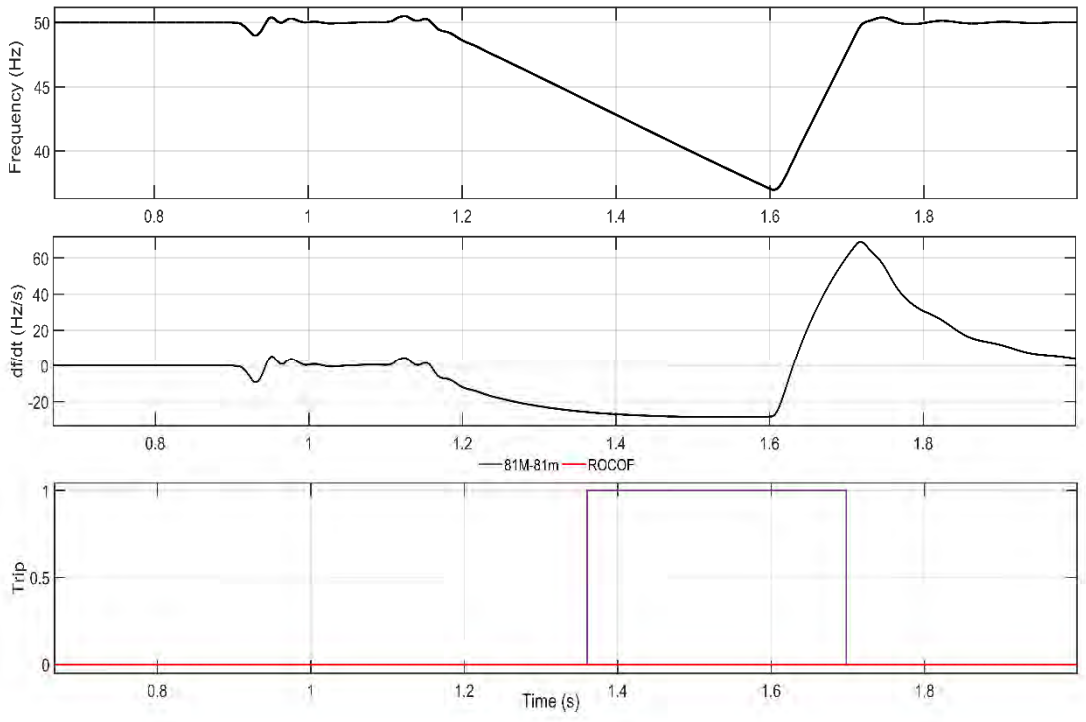

Figure 9.26: UFP/OFP and ROCOF protections results for case 2 in subsection 9.4.3.

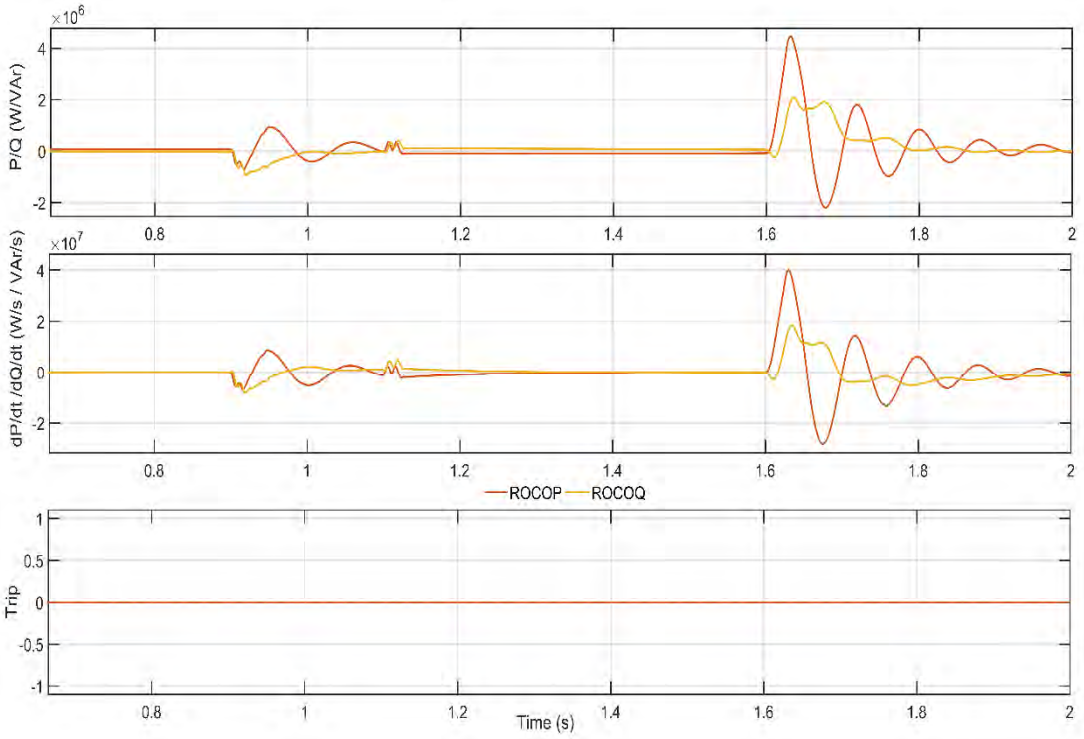

Figure 9.27: ROCOP and ROCOQ protections results for case 2 in subsection 9.4.3.

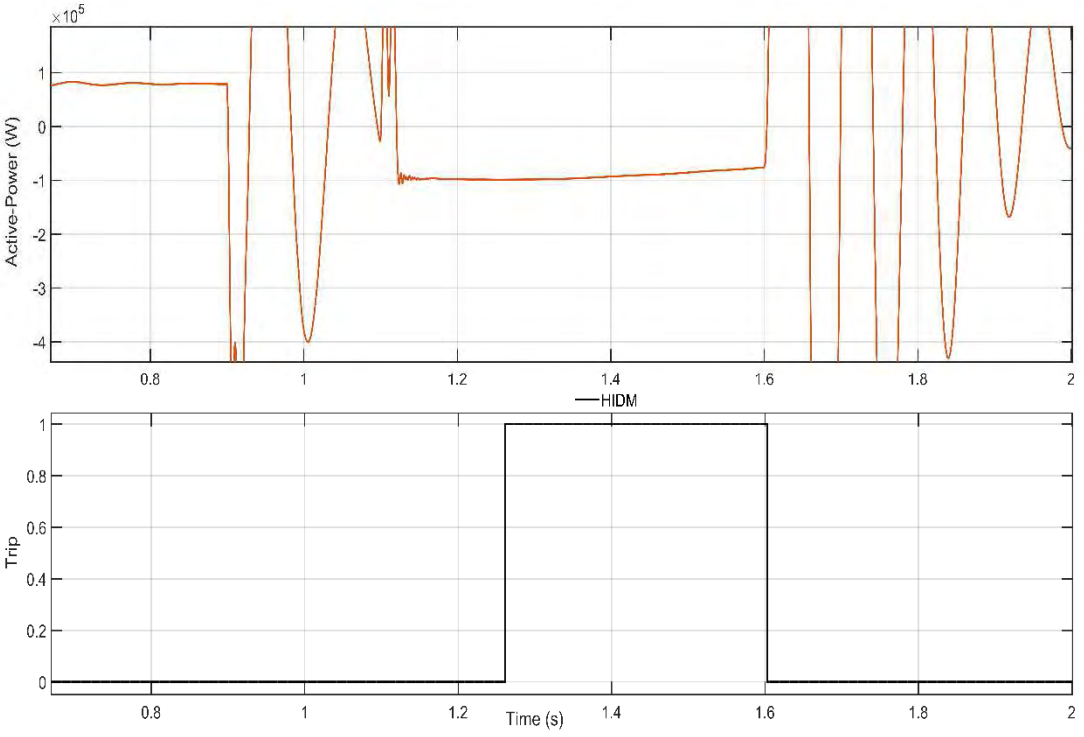

Figure 9.28: Directional criterion protection results for case 2 in subsection 9.4.3.

Results discussion

From these results, it is observed that the type of fault plays a pivotal role, and depending on the severity of the fault, the IM post-fault reacceleration affects the frequency during the IO. Thus, the highest reacceleration takes place for the LLL faults, whereas the lowest one occurs for the SLG faults. As a consequence, the frequency drop during the island, as expected, is lower than the one caused by a SLG. A proof of this effect is that the larger tripping for UFP protection takes place for a LLL fault.

The clearing time also plays a significant role. In this case, the tripping time of the substation protection is set to 200 ms, which makes the UVP at the target location to trip before the substation clearing time. Moreover, due to the originated voltage sag, ROCOV protections also trip if the clearing times are larger than 140 ms, which causes nuisance tripping for faults upstream the CB located at PCC_1. It is noteworthy to mention that ROCOV tripping is initiated if the rate of change of voltage exceeds the threshold for the three phases. Therefore, no ROCOV tripping occurs in the second case (LL fault); however, for the rest of the cases it trips in approximately 140 ms. Figures 9.25-9.28 provide evidence of how these tripping times are obtained.

Another interesting insight is the post-fault voltage recovery; the voltage caused by SLG faults recovers rapidly. Meanwhile, those caused by three-phase faults recover more slowly.

9.4.4 Testing the NDZ capabilities of the HIDM

All the case studies analyzed in previous sections assume an islanding scenario caused by a fault located upstream the PCC. Actually, the voltage at the IM location can exhibit deviations caused by events, located at neighbour feeders and even at the transmission system, that do no create an islanding condition. In order to better analyse the performance of the proposed HIDM, new scenarios have been simulated. First, some situations in which an islanding scenario does not occur:

- Case 1: Three-phase voltage sag with 0.9 pu voltage drop and 400 ms duration produced by IMs starting located at the same MV feeder.
- Case 2: Solid SLG fault at an MV-neighbor feeder (Feeder 1) and cleared in 300 ms.
- Case D3: Progressive frequency drop due to a lack of active-power generation as a consequence of a fault at the HV transmission system. The MV level experiences a sag of 0.3 pu voltage drop and 180 ms duration, whereas frequency decreases 2.5 Hz within 2 s.
- Case 4: LLL fault with a resistance of 5 Ω at an MV-neighbor feeder (Feeder B) and cleared in 300 ms.
- Case 5: Solid SLG fault at the transmission network which is cleared in 250 ms; MV grid experiences a sag type C.

The list of tested islanding events are detailed hereafter:

- Case 6: SLG fault with a 5 Ω resistance applied at node 7, feeder load is set to 320 kW, reclosing time 500 ms, no mechanical load torque, and 100 ms clearing time.
- Case 7: SLG fault with a 5 Ω resistance applied at node 7, feeder load is set to 53 kW, reclosing time 500 ms, no mechanical load torque, and 100 ms clearing time.

- Case 8: SLG Fault with a 10 Ω resistance applied at node 12, feeder load is set to 30 kW, reclosing time 500 ms, no mechanical load torque, and 100 ms clearing time.

Table 9.5 provides the tripping times obtained from the simulations for each passive-based technique as well as for the HIDM. Besides, for each case, the obtained tripping signals are represented in a separate figure. Therefore, in these eight figures (i.e., Figure 9.29 to 9.37), the tripping time and the duration of the event are displayed. By observing these results, the effectiveness of each method can be observed, which correctly discriminates between both islanding and non-islanding events.

Table 9.5: Summary of the tripping times obtained from simulations for islanding and non-islanding events.

ID method (Ansi/IEEE)	**Case 1 (ms)**	**Case 2 (ms)**	**Case 3 (ms)**	**Case 4 (ms)**	**Case 5 (ms)**	**Case 6 (ms)**	**Case 7 (ms)**	**Case 8 (ms)**
81U	No Trip	No Trip	No Trip	No Trip	No Trip	290	558	625
81O	No Trip	No Trip	No Trip	No Trip	No Trip	No Trip	No Trip	No Trip
27	No Trip	120	120	No Trip	120	432	No Trip	No Trip
59	No Trip	120	No Trip	No Trip	No Trip	No Trip	No Trip	No Trip
ROCOF	No Trip	No Trip	140	No Trip	No Trip	252	310	No Trip
ROCOV	No Trip	140	140	140	No Trip	415	No Trip	No Trip
ROCOP	238	No Trip	No Trip	No Trip	No Trip	No Trip	No Trip	No Trip
HIDM	238	No Trip	No Trip	No Trip	No Trip	No Trip	No Trip	No Trip

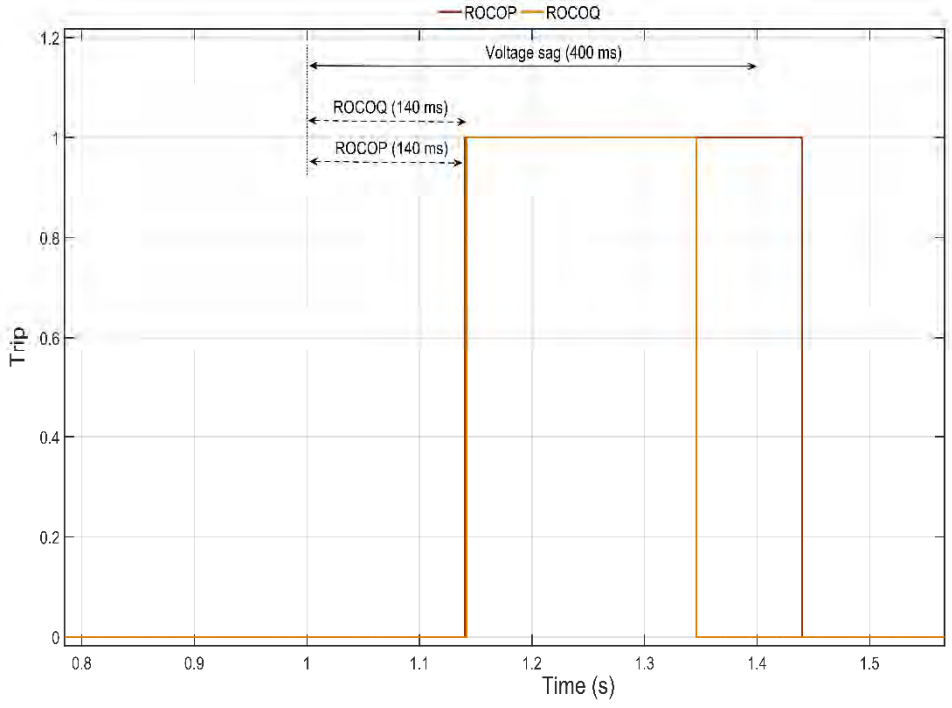

Figure 9.29: Tripping times for case 1 of subsection 9.4.4

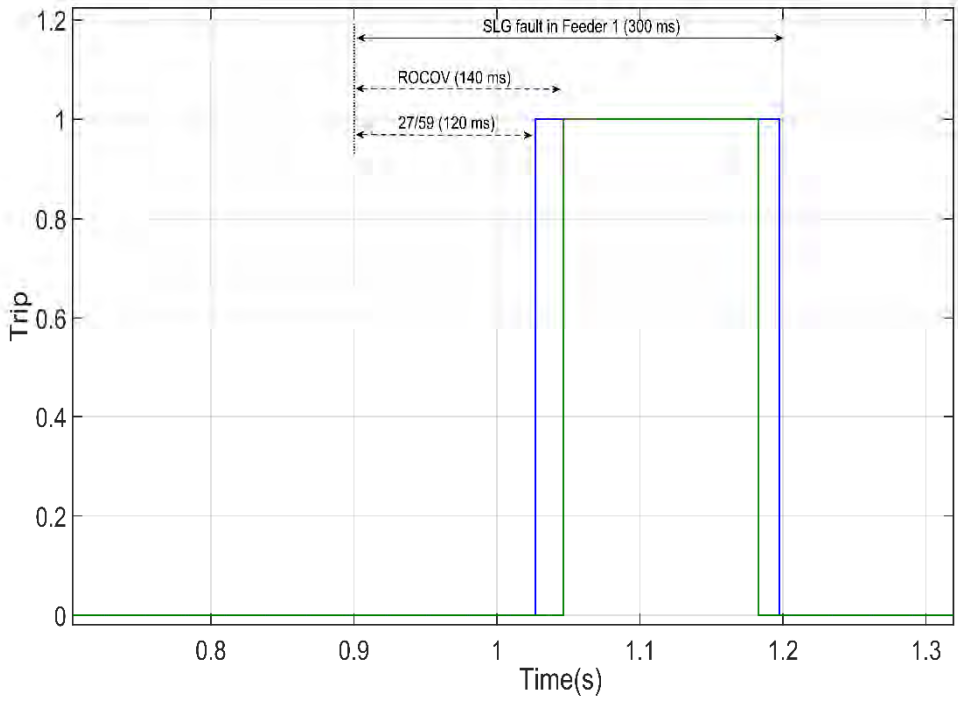

Figure 9.30: Tripping times for case 2 of subsection 9.4.4.

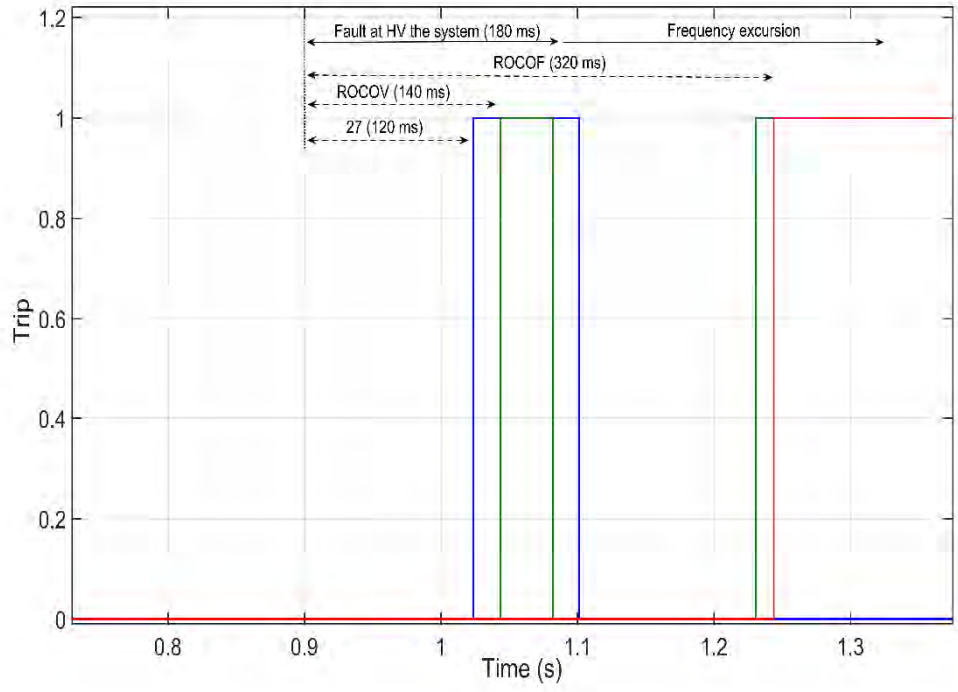

Figure 9.31: Tripping times for case 3 of subsection 9.4.4

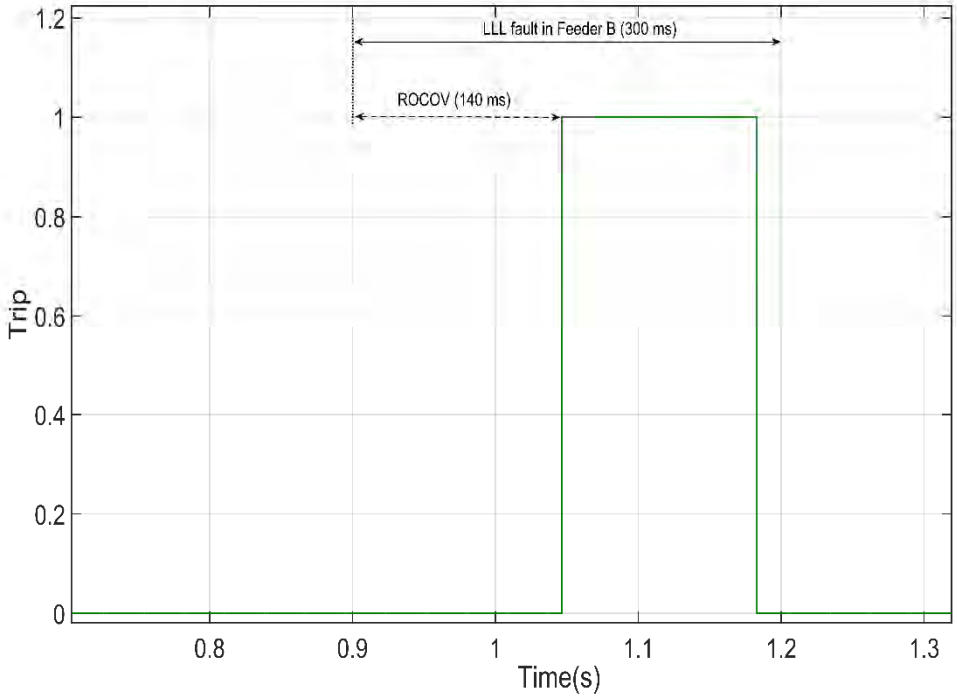

Figure 9.32: Tripping times for case 4 of subsection 9.4.4.

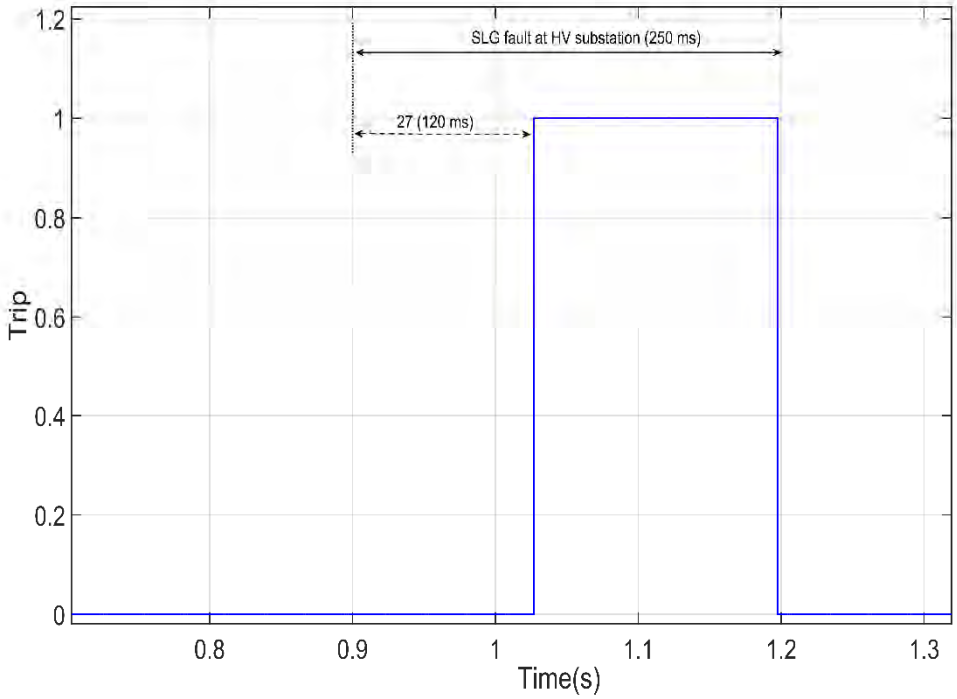

Figure 9.33: Tripping times for case 5 of subsection 9.4.4

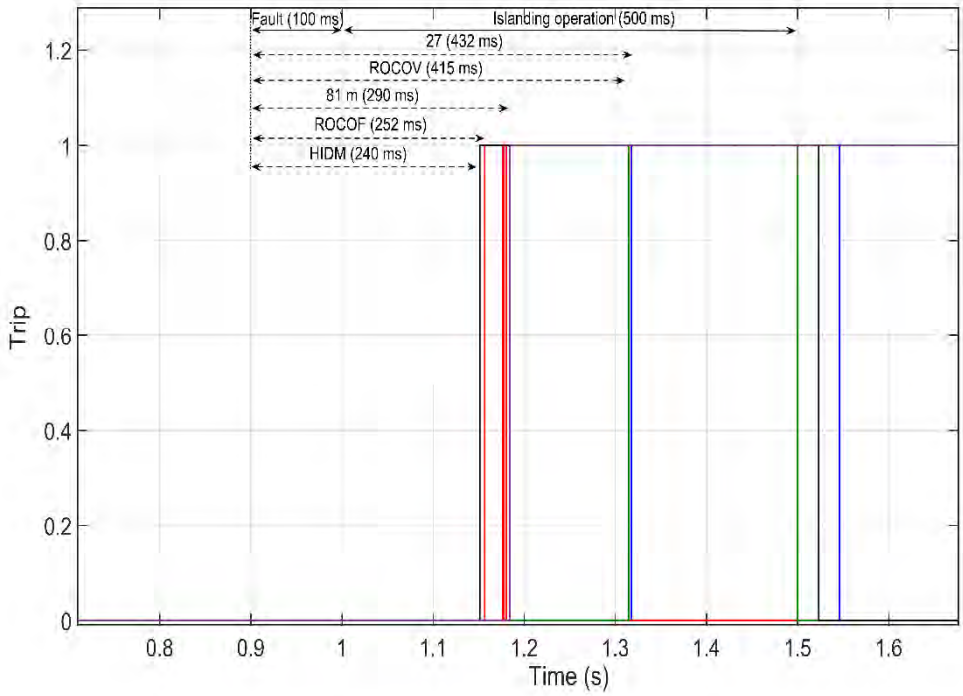

Figure 9.34: Tripping times for case 6 of subsection 9.4.4.

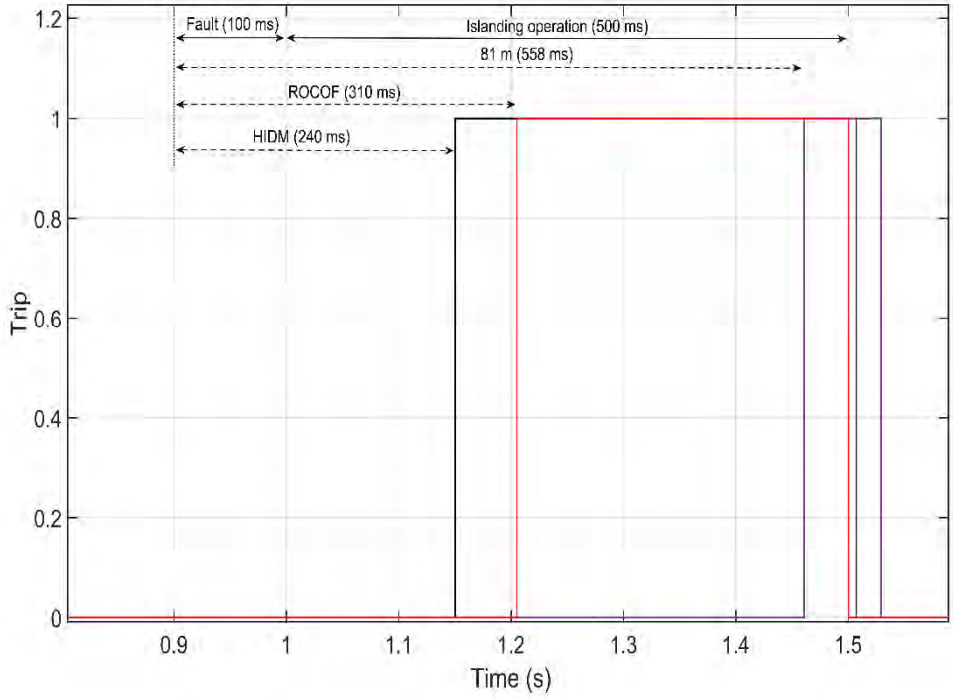

Figure 9.35: Tripping times for case 7 of subsection 9.4.4.

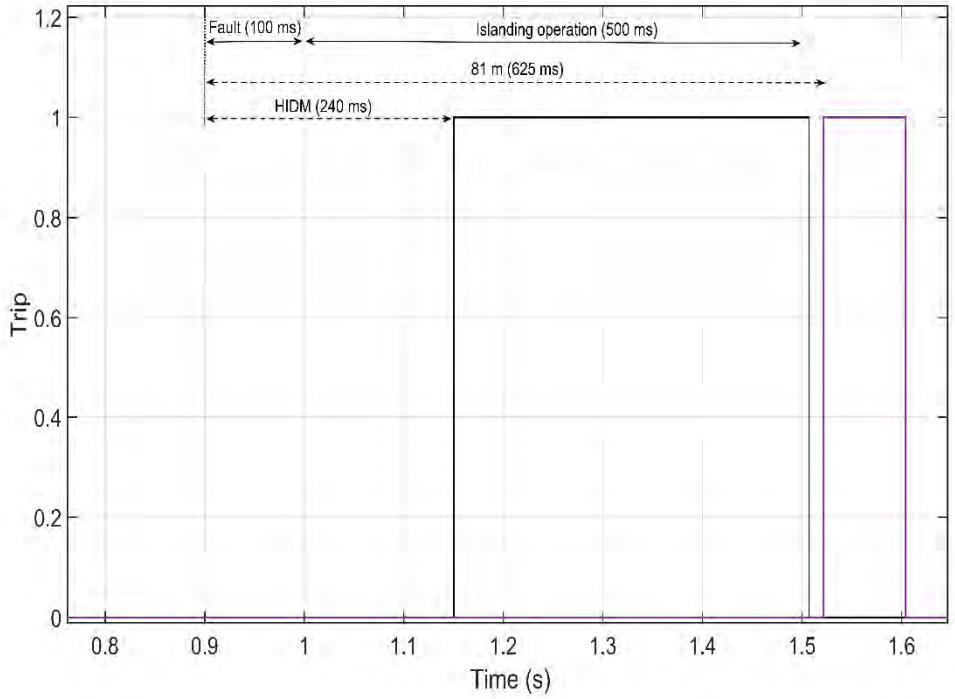

Figure 9.36: Tripping times for case 8 of subsection 9.4.4.

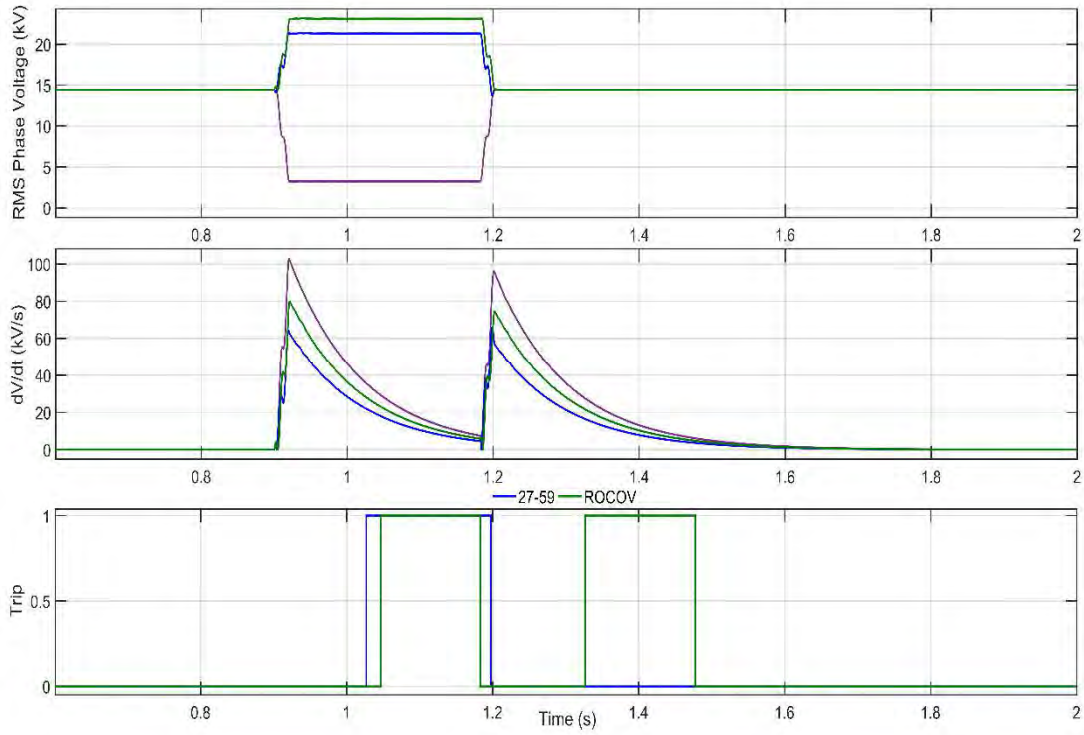

Figure 9.37: UVP/OVP and ROCOV protections results for case 2 of subsection 9.4.4.

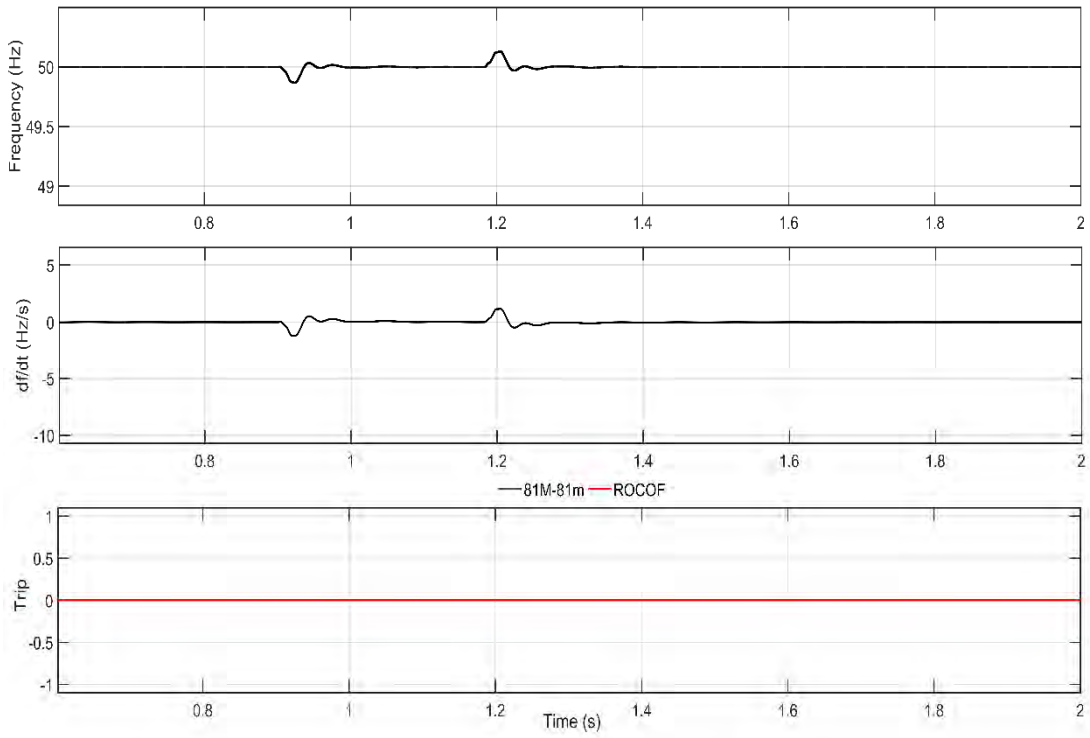

Figure 9.38: UFP/OFP and ROCOF protections results for case 2 of subsection 9.4.4.

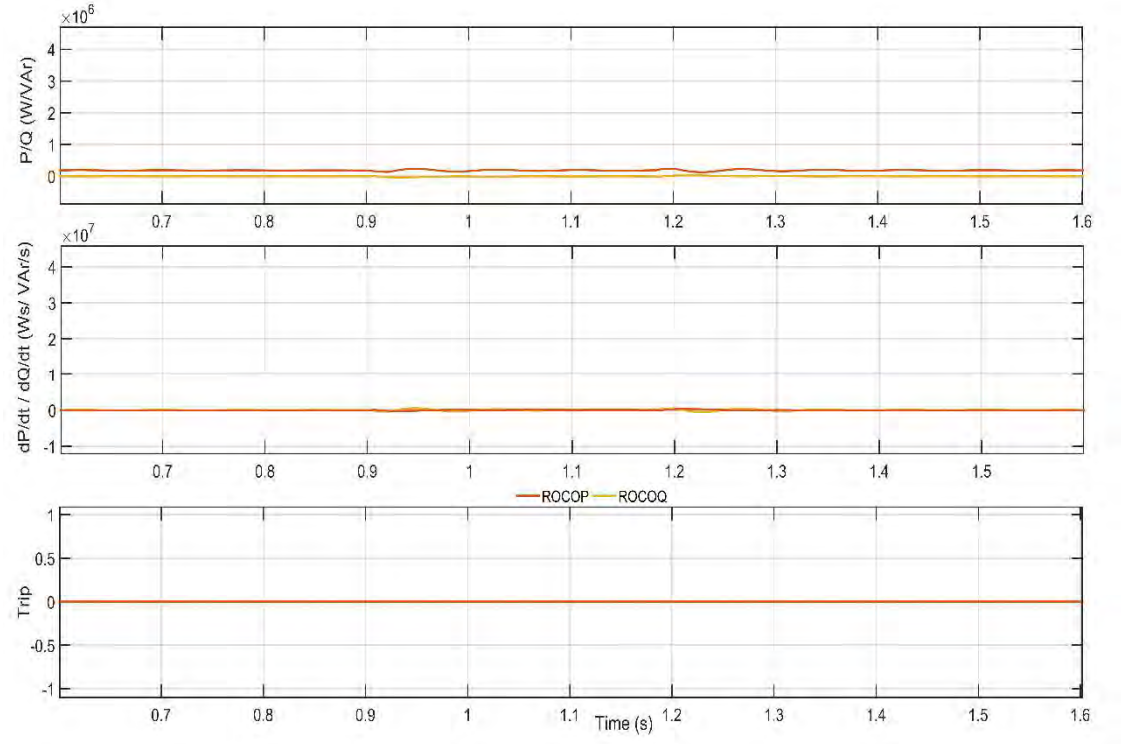

Figure 9.39: ROCOP and ROCOQ protections results for case 2 of subsection 9.4.4.

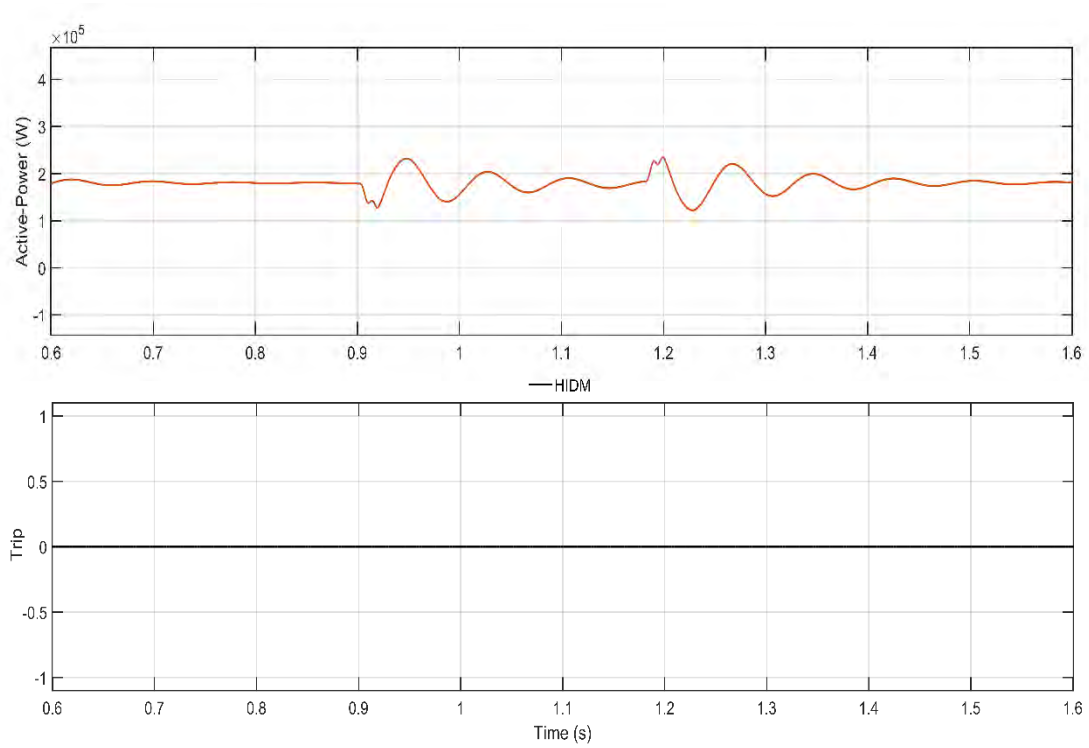

Figure 9.40: Directional criterion protection results for case 2 of subsection 9.4.4.

Results discussion

As can be seen from Table 9.4, for the non-islanding events (i.e., cases 1 to 5), at least, two passive-based methods trip, which evidences a missoperation. As an example, both UVP and ROCOV trip for faults upstream the CB located at PCC_2 which occurs for cases 2 to 5. However, as can be seen, the HIDM does not trip during these scenarios.

On the other hand, during islanding events (i.e., faults at the same feeder where the IMs are located) the fastest tripping time is achieved by the HIDM, meanwhile, due to the low deviation in either voltage or frequency, several techniques ID missoperate. Particularly, in case 8, it can be observed that, except for HIDM, no other passive method is capable of tripping within the required time constraint. The analysed events prove that the proposed algorithm correctly discriminates between islanding and non-islanding events.

9.5 Conclusions

This chapter has proposed a new technique to detect the islanding operations that have been analyzed in the previous Chapters. The architecture, the main features and the settings of this tool have been defined. To observe the effectiveness of this ID hybrid method, a wide range of scenarios have been simulated according to three main groups, where in each one, different hypothesis are considered. This method merges several passive-based methods with an additional criterion to enhance the ID.

Based on the results obtained from the simulations, some interesting aspects can be pinpointed:

- Given the number of simulated scenarios, it can be concluded that some damage to the grid and to the IMs can result during unintentional IOs. Therefore, fast tripping performance is required.
- During islanding events (i.e., the ones which imply the opening the CB of feeder A) if the amount of load level in the island is low, the ID becomes a significant challenge because voltage and frequency do not exceed the thresholds of the most common ID techniques within the time constraint. Nevertheless, for larger load levels in the island, most of the available ID indicators will trip correctly.
- All the simulated scenarios assume a situation in which the IMs are operating without mechanical load at the moment the fault occurs. Although this can be seen as a non-realistic scenario, it also represents the worst scenario in which IMs will act as generators.
- By observing the simulated non-islanding events (i.e., faults upstream the CB at PCC_1), it transpires that both voltage protections (UVP/OVP) and ROCOV untimely trip.
- Even though the passive-based ID methods can be adjusted with other thresholds closer to the rated values, it has to be underscored that doing that; more untimely tripping operations will occur. For instance, the typical voltage settings for UVP and OVP are set to 0.8 pu and 1.2 pu with a delay of 100 ms and voltage between 1.1 and 1.2 pu with a time delay of 500 ms. If these settings are replaced with more restrictive values, these methods will untimely trip for disturbances such as voltage sags due to induction motor starting, capacitors switching over-voltages or voltage drops during transformer energisation.

A significant conclusion of this Chapter, is that the implemented HIDM exhibits high robustness and feasibility: it can discriminate between IO and non-IO events, which guarantees that the IO would be cleared before any rapid reclosing from the DN could take place. Moreover, it proved to be the fastest method in detecting the island when compared with the available passive-based ID methods.

9.6 References

[9.1] S. Raza, H. Arof, H. Mokhlis, H. Mohamad, and H. A. Illias, "Passive islanding detection technique for synchronous generators based on performance ranking of different passive parameters," *IET Gener. Transm. Distrib.*, vol. 11, no. 17, pp. 4175–4183, 2017.

[9.2] N. K., S. A. Siddiqui, and M. Fozdar, "Hybrid islanding detection method and priority-based load shedding for distribution networks in the presence of DG units," *IET Gener. Transm. Distrib.*, vol. 11, no. 3, 2017.

[9.3] H. H. Zeineldin and J. L. Kirtley, "A simple technique for islanding detection with negligible nondetection zone," *IEEE Trans. Power Deliv.*, 2009.

[9.4] T. Ghanbari, H. Samet, and F. Hashemi, "Islanding detection method for inverter-based distributed generation with negligible non-detection zone using energy of rate of change of voltage phase angle," *IET Gener. Transm. Distrib.*, vol. 9, no. 15, 2015.

[9.5] K. El-arroudi, G. Joós, and I. Kamwa, "Intelligent-Based Approach to Islanding Detection in Distributed Generation," *IEEE Trans. onPower Deliv.*, vol. 22, no. 2, pp. 828–835, 2007.

[9.6] S. R. Samantaray, K. El-arroudi, G. Joós, and I. Kamwa, "A Fuzzy Rule-Based Approach for Islanding Detection in Distributed Generation," *IEEE Trans. Power Deliv.*, vol. 25, no.

3, pp. 1427–1433, 2010.

[9.7] S. Li, K. El-Arroudi, G. Joós, and A. J. Rodolakis, "Islanding protection of multiple distributed resources under adverse islanding conditions," *IET Gener. Transm. Distrib.*, vol. 10, no. 8, pp. 1901–1912, 2016.

[9.8] J. C. M. Vieira, W. Freitas, W. Xu, and A. Morelato, "Performance of frequency relays for distributed generation protection," *IEEE Trans. Power Deliv.*, 2006.

[9.9] J. C. M. Vieira, D. S. Correa, W. Freitas, and W. Xu, "Performance curves of voltage relays for islanding detection of distributed generators," *IEEE Trans. Power Syst.*, vol. 20, no. 3, pp. 1660–1662, 2005.

[9.10] O. Raipala, A. S. Makinen, S. Repo, and P. Jarventausta, "An Anti-Islanding Protection Method Based on Reactive Power Injection and ROCOF," *IEEE Trans. Power Deliv.*, vol. 32, no. 1, pp. 401–410, 2017.

[9.11] J. C. M. Vieira, W. Freitas, W. Xu, and A. Morelato, "Efficient coordination of ROCOF and frequency relays for distributed generation protection by using the application region," *IEEE Trans. Power Deliv.*, vol. 21, no. 4, pp. 1878–1884, 2006.

Chapter 10

General Conclusions and future work

10.1 General conclusions

As has been stated above, IOs occurs when a portion of the network remains energised after being removed from the main grid, and this situation has been considered as an abnormal scenario by the DSOs. IOs in DNs have elicited interest among researchers and DSOs in the recent years; essentially, the main reason for this interest lies in how to prevent them. Up until now, these IOs were expected only in the presence of distributed generation (DG) units, which following the CB disconnection, continue energising this portion of the network. Nonetheless, the main accomplishment of this thesis is the assessment of an IO where there are no DG resources, but large induction motors. This IO begins with the CB fault clearing and ends when this CB recloses the circuit to restore the supply. As a matter of fact, due to its inertia, the motors transiently act as generators between the CB opening and its reclosing, thus energising the island. Therefore, the cornerstone of the present doctoral thesis is the evaluation of this particular unintentional IO.

Chapter 4 has provided an accurate model based on the real grid where the field measurements have been obtained. The mathematical equations of each element of the model are also detailed. By observing those equations, several factors were expected to be influential for the IO. Particularly, these possible influential factors are as follows; the power drawn by the amount loads which remain in the island, the load torque coupled with the motors, the reclosing time and the type of fault that originated the island. In the subsequent Chapters, the influence of such expected factors has been demonstrated.

Once the model has been developed in Chapter 4, the main objective of the subsequent Chapters 5, 6 and 7 have been to carry out its validation. Since a model validation is a crucial task for the accurate simulation of transient events, the best way to perform a model validation is to compare field or lab recordings and simulation results. Therefore, the first step of the model validation lies in simulations (*Chapter 5*), where a wide range of scenarios have been tested. The second step focuses on displaying the field measurements obtained from real occurred events (*Chapter 6*). Lastly, the obtained results from the two previous stages are compared in *Chapter 7*.

Considering the above, the results of *Chapters 5*, *6* and *7* illustrate the following conclusions:

- It has been found that the feeder loads which remain connected within the island at the time the fault occurs play a pivotal role in this transient and dictate the survivability of the island. As expected, the lower is this value, the smaller are voltage and frequency

deviations during the island. It can be seen that the hypotheses of neglecting the frequency-dependence in load modelling by considering mainly active-power loads, approaches satisfactorily the field measurements. A noteworthy aspect regarding the load modelling is that, unfortunately, only two devices were available (locations PCC_1 and PCC_2) and therefore, there were no measurements at load nodes. However, by virtue of the obtained results in Chapter 7, the model selected for each load provides a close enough simulation result to that obtained from measurements. Besides, given the fact that the occurrence of the events is random in time, the model validation has considered several load conditions, which is one of the most challenging tasks to fulfil in load modelling.

- Since the type of load torque decelerates the machine during the island, the higher is this value, the higher is the deceleration during the island and therefore, the higher is the voltage drop and frequency excursion during the IO. However, most of the simulated scenarios assume a situation in which the IMs are operating without mechanical load at the moment the fault occurs. Although this can be seen as a non-realistic scenario, it also represents the worst scenario in which IMs will act as generators.
- As expected, the larger is the reclosing time, the larger is the island duration. This fact makes that, in turn, large voltage drops and frequency excursions occur during the IO.
- It has been found that depending on the type of fault that originated the CB operation, both voltage and frequency during the island are highly influenced. Since the motors are the only source during the island, the frequency of the island is dictated by the motors mechanical speed. An interesting insight is that the larger is the post-fault reacceleration (i.e., depending on the during-fault deceleration), the lower is the frequency excursion during the island. This fact is especially observed in severe disturbances such as three-phase faults close to the motors.
- By observing both voltage and frequency comparisons in each event of Chapter 7, the high accuracy achieved in the model has been demonstrated.

Once the model has been already validated, and the dependability of this IO has been proven, two major studies are of interest. The first is focused on the voltage sag that occurs during the island, which is explored in Chapter 8. The second is aimed at implementing a suitable tool to prevent this IO and is explored in Chapter 9.

Chapter 8 contributes to the present Power Quality studies, where a new voltage sag topology has been defined. The main features of this sag are as follows; its magnitude is non-constant, its duration depends on the reclosing time, and its recovery takes place in two-stages. Crucially, the curve that follows the non-constant magnitude has been analytically modelled and subsequently validated with several recorded events.

Considering the previously mentioned aspects, it is apparent that, in order to guarantee the power quality and safety, these IOs have to be detected and the motors have to be tripped in the minimum time possible. In this vein, *Chapter 9* has analysed the passive-based ID methods used in the presence of DG resources and has compared these results with the proposed HIDM.

From these results, it can be clearly seen that the fastest method in detecting this type of island is the HIDM, which provides evidence of its dependability. But, a crucial aspect is that under certain conditions of load where voltage and frequency do not exceed the typical ID thresholds, the only method capable of tripping with the required time constraints is the HIDM.

To sum up, the main contributions of this thesis can be summarized into three main points:

- The first accomplishment of this thesis lies in the model development, which has been successfully achieved.

- As a second main accomplishment, this thesis has contributed to the voltage sag studies. The new voltage sag topology that occurs during the island has been defined, analytically modelled and further validated.
- The third contribution focused on implementing a new technique to prevent these IOs, and based on the obtained results, it proved to be really effective for ID purposes.

Finally, it can be stated that this thesis has successfully contributed to improve the current research on distribution network studies in terms of islanding operations. Nevertheless, and perhaps even more importantly, it has also contributed to solve real problems identified in a distribution network, which underscores its high value in practical engineering.

10.2 Future work

As seen in the previous section, the studied IOs were categorised as unintentional, and therefore, naturally the objective of the DSOs is to avoid these type of events. This may, in fact, be the starting point for future research, where instead of avoiding IOs, these operations can be seen as a valuable resource for the DSO. Based on this premise, the following points will summarise the future research:

- Although some efforts have been done by the research community towards the intentional islanding operations in wide-area power systems, an interesting point to take into consideration for future research is to test these techniques into DNs. The main advantage of fostering such intentional islanding operations in distribution networks is, essentially, to reduce the time and number of interruptions, thus increasing grid reliability. Actually, with the rapid proliferation of the DG based on renewable energies embedded in the DNs such as rooftop PV or other types of DG, these units can be an asset to enhance grid resilience. Moreover, apart from the DG units, other tools will be of utmost importance to achieve successful results in the aforementioned intentional islands, for example; energy storage, smart meters, SCADA systems or state estimators. On the other hand, techniques such as demand-response or local energy markets, will undoubtedly, be benefited if these intentional operations are feasible.
- Additionally, even though some reliability studies carried out with DG operating in grid-connected mode provided fruitful results in the past, these studies can now be repeated by using these intentional islands.

By considering the previous points, it is clear that there is a lot of work to do towards the so-called active distribution networks.